UC San Diego
UC San Diego Electronic Theses and Dissertations

Title

Synthesis, Design, and Cytotoxicity of Organoferrous Anticancer Agents

Permalink

https://escholarship.org/uc/item/4dk1c7nz

Author

Hoong, Christina

Publication Date

2017

Peer reviewed|Thesis/dissertation

eScholarship.org Powered by the California Digital Library
University of California

UNIVERSITY OF CALIFORNIA, SAN DIEGO

Synthesis, Design, and Cytotoxicity of Organoferrous Anticancer Agents

A dissertation submitted in partial satisfaction of the requirements for the degree
Doctor of Philosophy

in

Chemistry

by

Christina Hoong

Committee in Charge:

Professor Joseph M. O'Connor, Chair
Professor Stephen B. Howell
Professor Patricia Jennings
Professor Charles L. Perrin
Professor Emmanuel Theodorakis

2017

Copyright

Christina Hoong, 2017

All rights reserved.

The Dissertation of Christina Hoong is approved, and it is acceptable in quality and form for publication on microfilm an electronically:

Chair

University of California, San Diego

2017

TABLE OF CONTENTS

Chapter IV. Delivery of Benzoylferrocene Using Nanoparticles and Peptide Recognition Targets 161

LIST OF FIGURES

LIST OF TABLES

LIST OF SCHEMES

LIST OF ABBREVIATIONS

Chemical Abbreviations
(– indicates covalent substituent)
B: general base
Cp: cyclopentadienyl
D/ –d: deuterium
DCM: Dichloromethane
DMF: N,N-dimethylformaimide
DMSO: dimethyl sulfoxide
Fc: ferrocene
Fc$^+$: ferrocenium
L: metal ligand
MeCN: acetonitrile
–Ph: phenyl, –C_6H_5
TFA: Trifluoroacetic acid
THF: tetrahydrofuran

Experimental/Spectroscopic
δ: chemical shift
η^x: x atoms π bound to metal
λ: wavelength
d: doublet
ESI: electrospray ionization
FTIR: fourier transform infrared spectroscopy
hν: light
HRMS: high resolution mass spectrometry
J: coupling constant
m: multiplet
NMR: nuclear magnetic resonance spectroscopy
q: quartet
rt: room temperature
s: singlet
t: triplet
TLC: thin layer chromatography
TOF: time of flight
uv: ultraviolet radiation

Parameter Units
Å: Angstrom
°C: degree Celcius
h: hour
Hz: Hertz
cm^{-1}: wavenumber
V: electron volt
K: Kelvin
L: liter
M: molar
m: meter
min: minute
mol: mole
ppm: parts per million
s: second

ACKNOWLEDGEMENTS

To my advisor, Professor Joseph O'Connor: immense thanks for your guidance and support and always having your door open to me as I navigated the frustrations and hardships of my project. Thanks for the guidance of my committee members Professors Stephen Howell, Patricia Jennings, Emmanuel Theodorakis (ET), and especially Professor Charles Perrin for all his invaluable insight during group meetings during my time here. I am also extremely grateful to Dr. Marissa Aubrey, a previous graduate student in the lab, for her patience and mentorship navigating the difficulties of this project. I am also grateful to Dr. María Proetto in the Gianneschi group for teaching me about tissue culture technique, and Dr. Mia Huang from the Godula group for her insightful discussions about various biochemical techniques. I would like to thank Dr. Mohand Melaimi for his help with cyclic voltammetry experiments, Dr. Anthony Mrse (UCSD NMR Facility) for his assistance with running difficult NMR experiments, Dr. Yongxuan Su (UCSD MS Facility) for his assistance with mass spectrometry measurements, and Dr. Paterno Castillo and Chris MacIssac (SIO) for their assistance with ICP-OES experiments. Thanks to Dr. Matt Thompson in the Gianneschi group for assistance with the peptide synthesizer. Thanks to all past and present members of the O'Connor lab, Marissa Aubrey, Stephen Cope, Ryan Holland, Kate Veccharelli, Pengjin Qin, Pauline Olsen, Han Steger, and Lian Wang for their scientific insight and keeping lab fun. Also, thanks to Ryan Holland and Pengjin Qin for assistance in obtaining crystal structures. Special thanks to my undergraduates John Poolos and Kai Silkwood for helping with scale up reactions so that I material to work with when attempting new reactions. A huge thanks to Angie Kim, a previous graduate student in the Sailor lab for collaboration on encapsulating benzoyl ferrocene in nanoparticles, the topic of Chapter IV.

Finally I am grateful for the support of all my family and friends. Without your emotional support, I wouldn’t have been able to deal with all the struggles of graduate school as I have. A tremendous thanks to my parents for always pushing me to realize my own potential, and their unwavering belief that I can accomplish great things as long as I set my mind on it. All the support they have provided for me over the years has been one of the greatest gifts given to me. And lastly, I would like to express immense gratitude for my husband, Nicholas Tiee, a fellow graduate student in the program. Thanks to his scientific insight and questioning which lead to new experiments, and assistance in techniques I was previously unfamiliar with. Thanks to his unconditional love, patience and support for ensuring I stay mentally and physically healthy in graduate school, and cooking for the both of us to ensure we are both well fed.

The material in Chapter IV contains unpublished material with co-authors: Hoong, Christina; Kim, Angie; O’Connor, Joseph. “Delivery of Benzoylferrocene Using Nanoparticles and Peptide Recognition Targets.” The dissertation author was the primary researcher and author of this material.

CURRICULUM VITAE

2012	Bachelors of Science in Chemical Biology, University of California, Berkeley
2014 San	Masters of Science in Chemistry & Biochemistry, University of California, Diego
2017	Doctor of Philosophy in Chemistry, University of California, San Diego Dissertation Title: Synthesis, Design, and Cytotoxicity of Organoferrous Anticancer Agents

PUBLICATIONS

Wang, Y-M.; Wu, J.; Hoong, C.; Rauniyar, V.; Toste, F. D. "Enantioselective Halocyclization Using Reagents Tailored for Chiral Anion Phase-Transfer Catalysis" *J. Am. Chem. Soc.* **2012**, 134 (31), 12928-12931.

Wang, Y-M.; Kuzniewski, C. N.; Rauniyar, V.; Hoong, C.; Toste, F. D. "Chiral (Acyclic Diaminocarbene)Gold(I)-Catalyzed Dynamic Kinetic Asymmetric Transformation of Propargyl Esters" *J. Am. Chem. Soc.* **2011**, 133 (33), 12972-12975.

ABSTRACT OF THE DISSERTATION

Synthesis, Design, and Cytotoxicity of Organoferrous Anticancer Agents

by

Christina Hoong

Doctor of Philosophy in Chemistry

University of California, San Diego, 2017

Professor Joseph O'Connor, Chair

Since the discovery of ferrocene in 1951 and subsequent structure elucidation in the following years, a wealth of literature is available on ferrocene functionalization. The remarkable stability of ferrocene under aqueous and aerobic conditions along with its low cost and high availability has led to widespread popularity for use in anticancer research. New methods for photodynamic therapy using ferrocenyl derivatives, possibly through the induction of ferroptosis, are explored in this research.

Chapter II details the synthesis of benzoyl ferrocene derivatives and ferrocenyl chalcones, and the determination of selective cytotoxicity in cancer cell lines. Studies showed benzoyl ferrocene derivatives internalized by cancer cells exhibited greater cytotoxicity under irradiation conditions than under dark conditions. Cytotoxicity studies regarding the photoproducts of an internalized fluorescent benzoyl ferrocene derivative indicate the fluorescent ligand is not the cytotoxic species. We therefore hypothesize that free iron(II) generated by photolysis is the cytotoxic species.

Chapter III focuses on identifying a possible mechanism of action of cell death, such as ferroptosis. A known ferroptosis inducer, ML210, was incubated with HeLa and Caov3 cells to determine compound cytotoxicity for each cell line. Interestingly, ML210 caused cytotoxicity in Caov3 cells, but not in HeLa cells. HeLa cell lines were therefore used for initial studies of concurrent treatment of ML210 and 4-pentylbenzoylferrocene. Addition of 31.25 nM of ML210 with 4-pentylbenzoyl ferrocene concurrently in HeLa cells resulted in greater cytotoxicity in the light than either compounds induced independently.

Chapter IV focuses on using nanoparticles as a drug delivery carrier. Benzoyl ferrocene, which is not internalized in HeLa cells, was encapsulated in two types of porous silicon nanoparticles. One type of nanoparticle contained the iRGD peptide targeting agent, while the other did not. Using porous silicon nanoparticles to deliver a higher payload of benzoyl ferrocene into lung carcinoma A549 cells resulted in greater toxicity under irradiation conditions than dark conditions. However, cells treated with benzoyl ferrocene encapsulated by nanoparticles containing iRGD peptide targeting agent exhibited a smaller ratio between light and dark toxicities than that of nanoparticles without iRGD. Thus, increasing drug payload with the iRGD peptide is less desirable for potential use for photodynamic therapy.

Chapter I

Introduction to Organoferrous Anticancer Agents and Ferroptosis

Introduction

Ferrocene – one of the most well-known organometallic complexes – was discovered serendipitously in 1951 by Kealy and Pauson while they were attempting to synthesize fulvalene using ferric chloride and cyclopentadienylmagnesium bromide.[1] Shortly thereafter, Miller, Tebboth, and Tremaine isolated ferrocene from an attempt to prepare amines from saturated or unsaturated hydrocarbons and nitrogen using the dinitrogen-reduction catalyst first prepared by Haber.[2] Reaction of cyclopentadiene and N_2 at 300 °C and atmospheric pressure resulted in ferrocene. While both groups reported on the synthesis of ferrocene, neither had correctly determined what the structure of this chemically stable compound was. Pauson and Kealy proposed that one carbon of the cyclopentadiene was connected to iron such that it was a FeR_2 type structure (Scheme 1.1), which was later determined to be incorrect.

Scheme 1.1. Pauson and Kealy's proposed ferrocene structure.[1]

Subsequent structure elucidation by Wilkinson, Rosenblum, Whiting, and Woodward challenged Pauson and Kealy's originally proposed structure – suggesting instead that iron was bound η^5 to both cyclopentadienide ligands (Figure 1.1).[3] They also coined the term ferrocene, since studies indicated a similar chemical behavior to aromatic molecules such as benzene. Fischer and Pfab also independently proposed the same structure for ferrocene.[4] These discoveries soon lead to a series of rapid advancements in metal and hydrocarbon interactions, advancing the field of modern organometallic chemistry, and garnering a Nobel Prize commendation for Fischer and Wilkinson in 1973.[5]

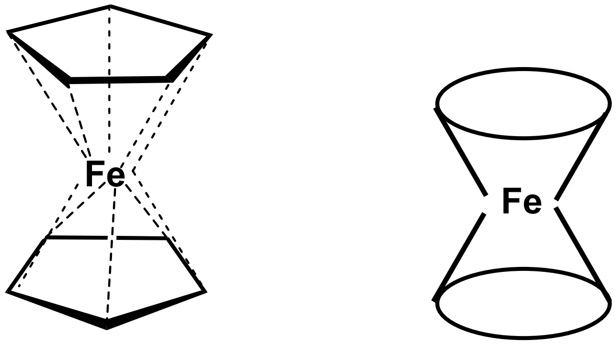

III **IV**

Figure 1.1. Woodward's (III) and Fischer's (IV) proposed ferrocene structure.[3-4]

Since that time, a wealth of literature on ferrocene functionalization has become available, in part due to the stability of the sandwich complex in aqueous and aerobic media. The stability of ferrocene, as well as its low cost and high availability, has led to widespread popularity in usage for anticancer research.[6-9] Herein we discuss the biological activity of ferrocenyl antitumor compounds, the storage, transport, and reactivity of iron in biological systems, and potential strategies for delivery of new ferrocenyl derivatives as a method for anticancer therapeutics.

A. Biological Activity of Ferrocene and Derivatives

One of the earliest ferrocene derivatives used for biological activity was in the 1970s with the development of ferrocerone (**V**, Figure 1.2) for the treatment of anemia in the former USSR.[10] The antitumor activity of ferrocenyl complexes was first studied in the late 1970s by Brynes and co-workers who reported on the activity of ferrocenyl compound **VI** and other derivatives against lymphocytic leukemia P-388 in mice.[11] The antitumor activity of these compounds were low, but significant enough to demonstrate that incorporation of the ferrocenyl moiety might provide a compound with enhanced antitumor activity. Since this time, several ferrocenyl complexes have been developed and evaluated in terms of their anticancer properties.

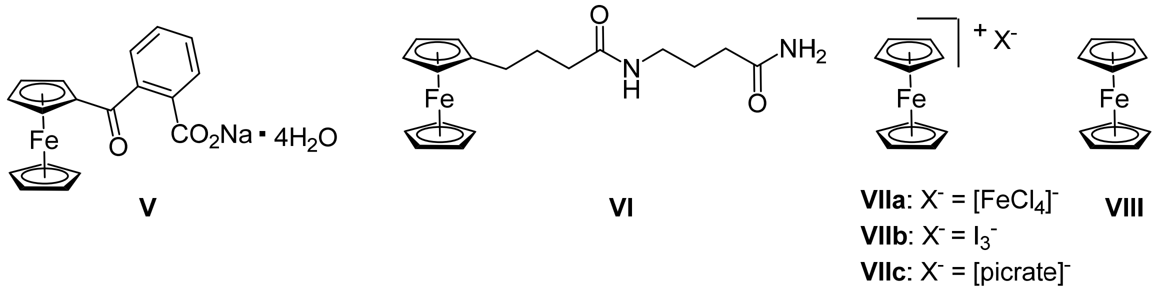

Figure 1.2. Select ferrocenyl derivatives with biological activity.[10-12]

In 1984, Köpf-Maier, Köpf, and Neuse reported on the anticancer potential of ferrocenium salts **VII**.[12] The salts **VIIa-c**, were independently shown to cure female CF1 mice with Ehrlich ascites tumors (EAT) when injected as part of a physiological saline solution. Survival rates of up to 100% for the mice were achieved depending on the dose and the particular Fc$^+$ **VII** salts administered. They also tested ferrocene (**VIII**), which did not exhibit any anticancer activity, demonstrating that the neutral ferrocene complex lacks antitumor efficacy against EAT. Up until the 1990s, it was hypothesized that ferrocene derivatives could be used as prodrugs that undergo oxidation to the more toxic ferrocenium complex in biological environments dependent on the local potential of the organelles.[13] However, a mechanism of ferrocenium toxicity was not reported until 1997, when a landmark discovery by Tamura and Miwa demonstrated that ferrocenium compounds could affect DNA cleavage *in vitro* by generating hydroxyl radicals (•OH), speculated to occur through a Fenton mechanism.[14] Three years later, Osella and co-workers demonstrated that DNA from cells treated with ferrocenium salts was also fragmented, suggestive of iron-mediated DNA strand cleavage.[15] The authors also performed electron spin resonance (ESR) measurements to positively identify a hydroxyl radical spin trap adduct in aqueous solutions.[15] These studies have paved the way for development of ferrous anticancer agents by conjugating ferrocenyl moieties to biologically-active biomolecules in the hope of discovering a more selective drug.

The antimalarial complex ferroquine (**IX**, Figure 1.3) was first identified as an alternative drug for malarial treatment,[16] as malaria parasites have developed resistance to drugs such as chloroquine (**X**) and artemisinin (**XI**), rendering these drugs ineffective. Ferroquine (**IX**) was found to be active against both chloroquine-sensitive and chloroquine-resistant strains of malarial species *Plasmodium falciparum*. Ferroquine **IX** remains a lead compound currently undergoing phase II clinical trials.[7] Numerous studies on the structure-activity relationship (SAR) of ferroquine have been conducted (more than 120 derivatives have been tested), but none have demonstrated greater activity than **IX**.[17]

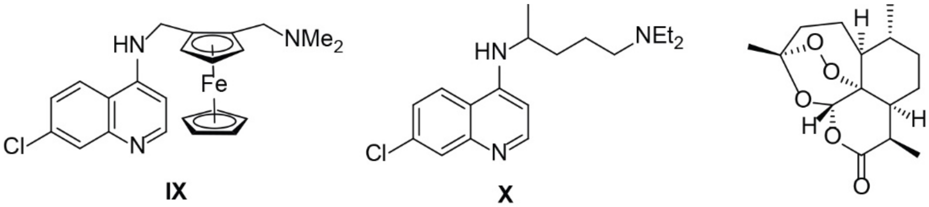

IX

X

XI

Figure 1.3. Antimalarial complexes.[16]

Concurrent with the discovery of antimalarial drug **IX** was the discovery of ferrocifen (**XII**)[18] – a ferrocenyl analogue of tamoxifen (**XIII**, Figure 1.4) – by Jaouen and co-workers. Compound **XIII** is a leading chemotherapeutic for patients with hormone-dependent estrogen receptor α-positive (ERα$^+$). In the body, compound **XIII** undergoes oxidation to the metabolic product hydroxytamoxifen (**XIV**), which competes with native molecules to bind ERα**,** repressing estradiol-mediated DNA transcription in tumor cells and subsequently causing cell death.[19] It has become clear that replacement of the phenyl group of **XIII** with a ferrocenyl group makes a better drug candidate, as the ferrocenyl analogues **XII** and **XV** were demonstrated to be highly active against ERα$^+$ and ERα$^-$ (hormone-independent breast cancer cells).[18] Compound **XIV** is known to be active against ERα$^+$ cells and inactive against ERα$^-$-type cells, so activity of the ferrocenyl tamoxifen derivatives for ERα$^-$ cell-lines is extremely significant. One-third of all breast cancers are ERα$^-$ type, which are untreatable by hormone therapy with selective estrogen receptor modulators such as **XIII** and **XIV**. Another significant factor in selecting chemotherapeutics is the expression of ERα, which may become down-regulated under repeated **XIII** treatment, leading to the decreased efficacy of the **XIV** metabolite.

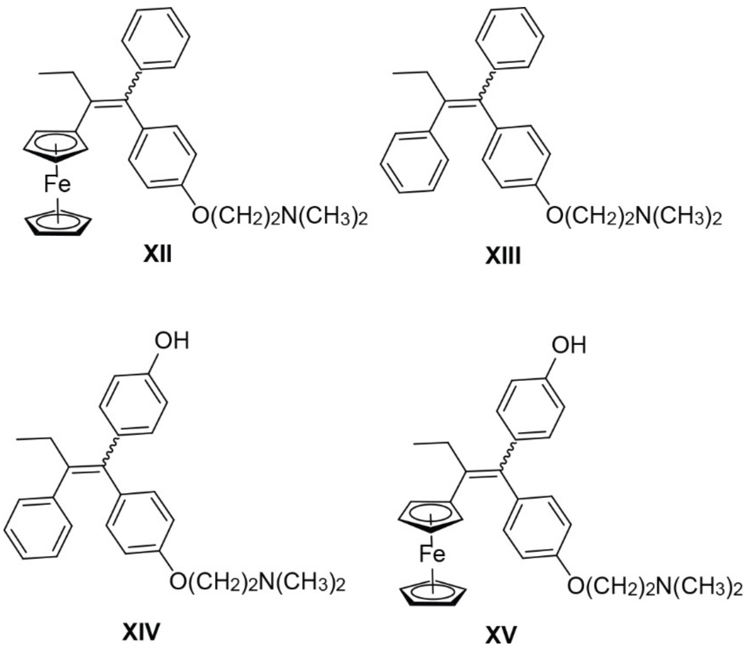

Figure 1.4. Breast cancer targets.[18-19]

More recent research by Jaouen's group in 2009 lead to the development of ferrocene-based antitumor agents for treatment of prostate cancer.[20] The progression of prostate cancer is promoted by testosterone (**XVI**, Figure 1.5) and its metabolite dihydrotestosterone (**XVII**). The development of anti-androgens that can competitively bind to cell receptors to prevent binding of **XVI** and **XVII** could therefore be a strategy for anticancer therapeutics. Jaouen's group synthesized the ferrocenyl analogs **XVIII** and **XIX** by using an ethyne linker to join the ferrocene and hormone functional groups. While the ferrocenyl compounds **XVIII** and **XIX** showed low affinity for receptor binding, there was strong antiproliferative effects found on the hormone-independent PC-3 prostate cancer cell line.[20]

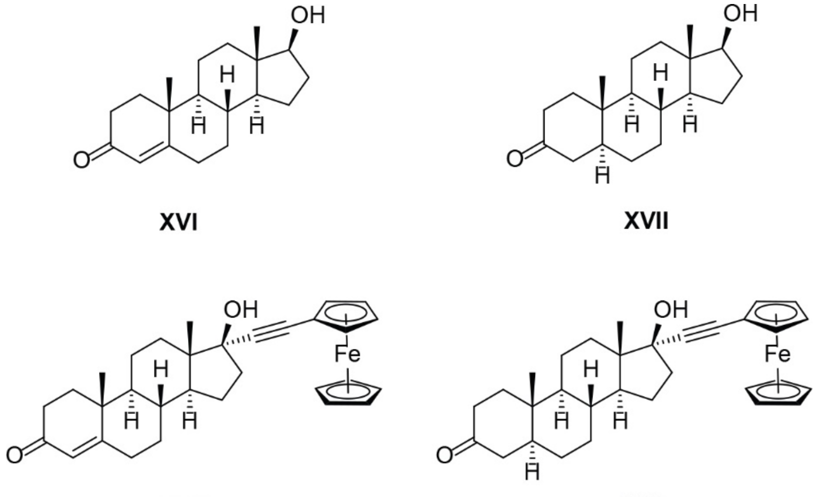

XVI **XVII**

XVIII **XIX**

Figure 1.5. Testosterone derivatives and ferrocenyl mimics for treatment of prostate cancer.[20]

Another common strategy for development of ferrous anticancer agents has been to conjugate the ferrocene moiety to biomolecules that could target specific cellular locations in the hopes of making a more selective drug. Compound **XX** (Figure 1.6), synthesized by Kenny and colleagues, was designed to contain three key parts: a peptide target to deliver the cytotoxic species to the cells, the redox-active iron core, and a conjugated aromatic linker to lower the oxidation potential (58 mV relative to Fc/Fc^+), making it easier for ferrocenium ion formation to generate hydroxyl radicals *in vitro*.[21-22] Compound **XX** was found to be highly cytotoxic, with an IC_{50} value of 620 nM in human lung carcinoma H1299 cells.

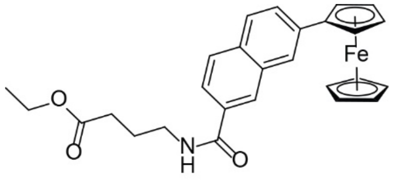

XX

Figure 1.6. Kenny and coworker's reported iron complex with toxicity in H1299 cells.[21]

Given the known redox potential of iron in cells, research efforts have also focused on creating ferrocenyl derivatives that target DNA, by generation of highly damaging hydroxyl radicals.[23] Ong and colleagues prepared **XXI** (Figure 1.7), a ferrocenyl scaffold covalently linked to acridine, a known DNA intercalator.[24] Compound **XXII** was synthesized as a control, as it lacked the ability to intercalate with DNA. While compound **XXI** was found to be highly cytotoxic to the four cancer cell lines tested, compound **XXII** was inactive.[24] Another strategy designed to target DNA was to synthesize ferrocenyl compounds that could inhibit topoisomerase, an enzyme responsible for unwinding and rewinding DNA in preparation for replication. It was hypothesized that since cancer cells are rapidly dividing, there would be elevated levels of topoisomerase IIβ, allowing for a more selective approach to target cancer cells.[25] Kondapi and coworkers found that compounds **XXIII** and **XXIV** (Figure 1.7) demonstrated significant inhibition of topoisomerase IIβ.[25]

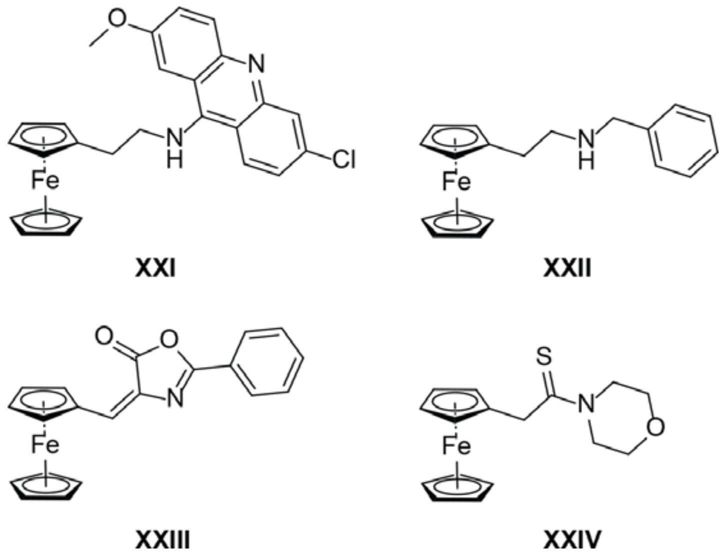

XXI XXII XXIII XXIV

Figure 1.7. DNA targets with a ferrocenyl scaffold.[23-25]

In summary, the discovery of ferrocenium salts with anticancer properties – which are proposed to work via generation of reactive oxygen species – has paved the way for development of ferrocenyl analogues for antitumor agents.[9] A common method for the synthesis of ferrocene-based anticancer complexes is substitution of a phenyl ring for the more lipophilic ferrocene species, with the hope that a change in the shape or biological distribution will increase the drug's antitumor properties.[26-27] Another strategy involves conjugation of the ferrocene complex to biomolecules to enhance pharmacospecificity – the targeting of a specific location within the cell.[20,24-25] Both these methods have led to a large number of new iron-based anticancer compounds with varying degrees of success. Currently, the iron-containing drug ferroquine (**IX**) is undergoing phase II clinical trials for FDA approval for treatment against malaria.[28] The fact that ferrocene derivatives may induce antiproliferative effects by formation of reactive oxygen species generated from the iron center is a huge field of interest, and one which allows for exploitation of novel cytotoxicity pathways.

B. Photochemistry of Benzoyl Ferrocene

Given the redox-active nature of successful ferrocenyl anticancer complexes mentioned in section **A**, we wondered if free iron(II) could be delivered into cancer cells with spatiotemporal control by photochemical activation of benzoyl ferrocene derivatives to release free inorganic iron(II). Once iron(II) was released from the ligands, it could participate in detrimental Fenton chemistry within the cells to generate cytotoxic reactive oxygen species (section **D**).

The first publication regarding the photoactivity of benzoyl ferrocene (**XXV**) and 1,1'-dibenzoyl ferrocene (**XXVI**, Figure 1.8) was reported by Tarr and Wiles, who demonstrated that both compounds were stable in the dark for weeks, while exposure to wavelengths of light identical to either one of their absorption bands at 470 nm and 354 nm lead to rapid decomposition.[29] These absorptions were attributed to the presence of the conjugated carbonyl group, as it was found to be drastically different relative to ferrocene. The absorption bands were tentatively assigned as a metal-to-ligand charge transfer.[29] Ferrocene derivatives without the carbonyl conjugation to the cyclopentadienyl ring were found to be photoinert, leading the authors to speculate on a unique interaction between the iron center and neighboring carbonyl group as being responsible for photoactivity.

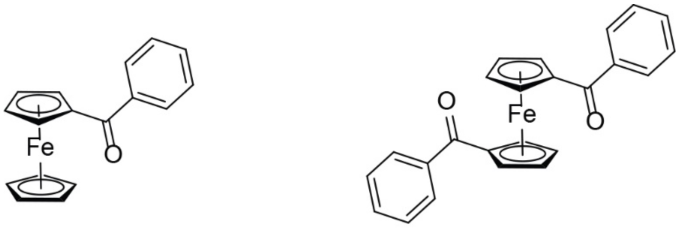

XXV **XXVI**

Figure 1.8. Benzoyl ferrocene (**XXV**) and 1,1'-dibenzoyl ferrocene (**XXVI**).

The decomposition of benzoyl ferrocene was found to be slow in CCl4 and rapid in water-methanol mixtures.[29] The only products from the decomposition were methyl benzoate and a poorly characterized iron-containing solid, which was suspected to be ferrous benzoate on the basis of UV-Vis spectroscopy. While the authors remarked that any proposed mechanism was highly speculative, they suggested that this decomposition was due to the initial activation of the carbonyl by hydrogen-bonding to the protic solvent. This was followed by a low energy metal-to-ligand charge transfer generating ferrocenium salt **XXVII** (Scheme 1.2).

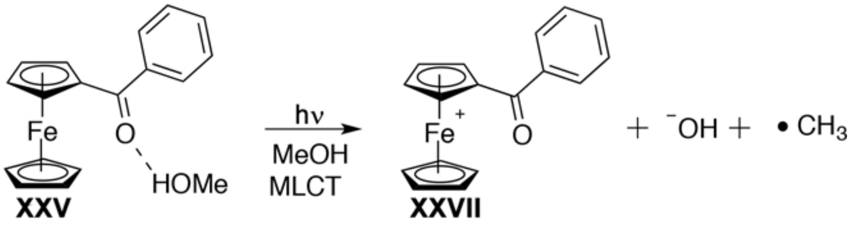

Scheme 1.2. Tarr and Wiles mechanism of decomposition for **XXV**.[29]

Ali, Cox, and Kemp also studied the photochemical decomposition of **XXV**, and reported in 1972 and 1973 that **XXV** also decomposed in wet polar aprotic solvents, such as DMSO, DMF, and pyridine.[30,31] The authors monitored the reaction by Infrared (IR) spectroscopy, and reported that upon photolysis, the IR absorption for the starting benzoyl ferrocene **XXV** at 1638 cm^{-1} was replaced by new carbonyl stretches at 1538 and 1364 cm^{-1}, which were assigned to a carboxylate group. An attempt to monitor the reaction by proton NMR specroscopy yielded frustrating results, as there was formation of solids in the NMR tube, but there was evidence for formation of free cyclopentadiene, and iron-bound cyclopentadiene. Treatment of the crude product mixture with HCl afforded benzoic acid in 50% yield, which was identified by mass spectroscopy, IR spectroscopy, and melting point analysis. Based on the data, the authors assigned the photoproduct as the iron complex **XXVIII** (Scheme 1.3) and cyclopentadiene ligand (**XXIX**).[31]

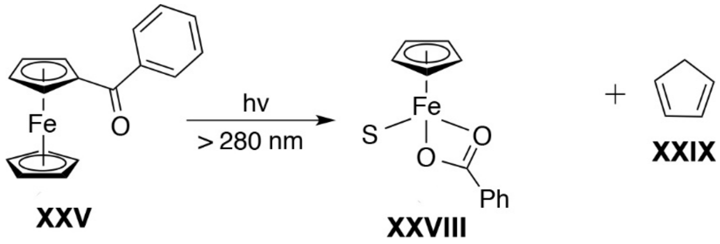

Scheme 1.3. Photoproducts of benzoyl ferrocene as reported by Ali, Cox, and Kemp (S = solvent).[30,31]

Independent studies by Bozak and Javaheripour in the same year lead to further evidence on the photodecomposition of compound **XXV** in methanol.[32] They reported that the photolysis of **XXV** results in iron-cyclopentadienyl ring cleavage caused by the dissociative charge transfer bands at 370 and 480 nm.[32] After light exposure of **XXV** in methanol for 30 minutes, they observed benzoylcyclopentadienyl anion (**XXX**), which was then protonated by solvent to give the neutral ligand **XXXI** (Scheme 1.4). This was in contrast to Ali, Cox, and Kemp's report, which had not identified any debenzoylated products. Treatment of the crude reaction with 1,10-phenanthroline indicated the presence of iron(II) by colorimetric analysis. After isolating the organic products, gas chromatography-mass spectrometry (GCMS) analysis detected **XXXI**, cyclopentadiene (**XXIX**), and Diels-Alder adducts of cyclopentadiene.

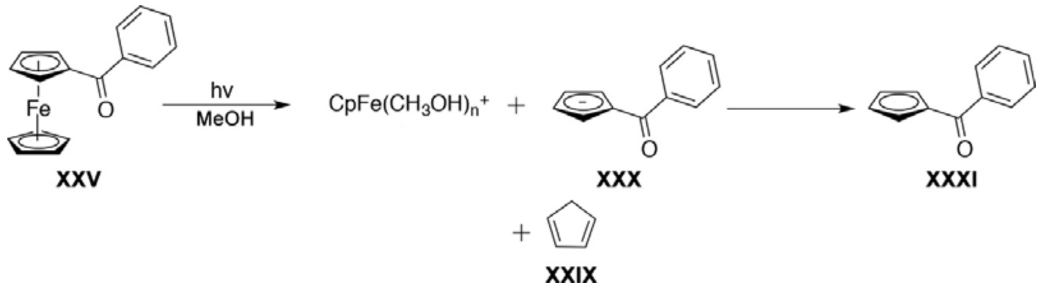

Scheme 1.4. Bozak and Javaheripour's photodecomposition of XXV.[32]

More recently, Kutal's lab proposed that the enhanced UV-Vis absorptivity and photoactivity of **XXV** resulted from mixing of the metal-to-ligand charge transfer (MLCT) character with the low energy excited states of the metallocene compound. The MLCT character in the excited state was described by Kutal as accruing to resonance structure **XXV***, wherein the conjugated carbonyl draws electron density away from the iron and toward the ligand, similar to early observations by Tarr and Wiles.[33-35]

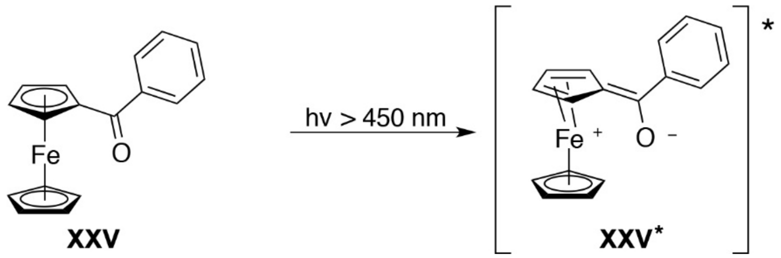

Figure 1.9. Kutal's reported excited state of **XXV**.[33]

When exposed to visible light in methanol or acetonitrile, compound **XXV** would rapidly dissociate to form the anion **XXX**, which would be protonated by solvent to form **XXXI** –consistent with Bozak and Javaheripour's observation. The half-sandwich complex **XXXII** was also formed by a series of our own proposed ring-slippages (Scheme 1.5). Detection of cyclopentadiene **XXIX** lead to a proposed mechanism involving ring-slippage of **XXXII** to give solvent-ligated iron(II) and the anion **XXXIII**, which would protonate in solvent to form **XXIX**.

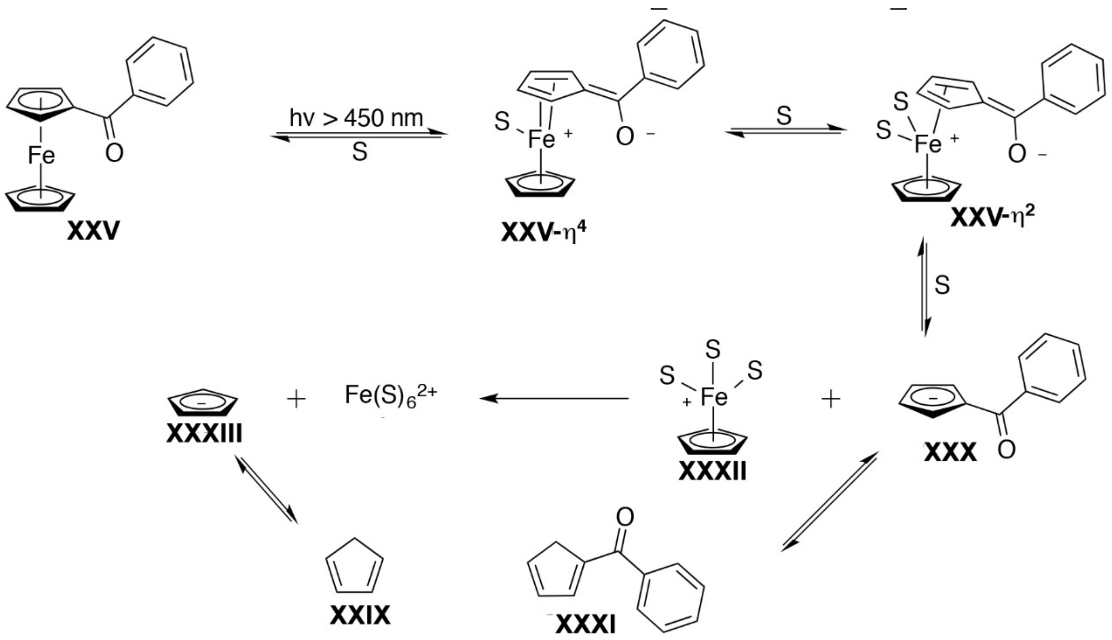

Scheme 1.5. Kutal's decomposition with our speculated mechanism of action (S = solvent).[33-35]

With this background knowledge on the photochemistry of benzoyl ferrocene, we set out to design benzoyl ferrocene derivatives which could be used as antitumor agents by utilizing its photochemical properties to deliver free iron(II) with spatiotemporal control.

C. Storage and Transport of Cellular Iron and Reactive Oxygen Species

Nature has developed elegant mechanisms for cellular storage of free iron, as elemental iron has crucial functions in cells.[36] Iron can act as a redox component of proteins and is integral to vital biological process that require electron transfer. Iron is also intimately involved in numerous essential biological functions, including oxygen transport, oxidative phosphorylation, DNA biosynthesis and drug metabolism.[37] The ability of iron to undergo redox reactions between its ferric and ferrous states is largely responsible for the biologic significance of iron.[38] This characteristic of iron redox activity that is beneficial to cells can also be detrimental if there is excess labile iron; excessive amounts of free iron are also responsible for iron toxicity.[38] Most cytoplasmic iron is in its ferrous form, which can easily donate an electron, leading to the formation of free radicals.[38] For example, when ferrous ion reacts with endogenous H_2O_2, it undergoes the Fenton reaction to product toxic hydroxyl radicals.[38] The donation of an electron from ferrous ion may also result in the peroxidation of lipids, leading to oxidative damage of DNA and other macromolecules.[37] The human body requires 25 mg of iron daily for various biological functions, and while 12-18 mg are typically consumed daily, only 1-2 mg of dietary iron is absorbed by the intestine.[39-40] As a result of its necessity – and its sometimes routine dietary unavailability – cells have developed elaborate systems to ensure adequate iron levels for biological function, while also precluding iron overload.

Due to the redox-active nature of iron, the transportation of iron from the intestines – where it is absorbed – to other areas, is a tightly-controlled process (Figure 1.10). Ferroportin (Fpn), the only known iron exporter to date, is regulated by the master iron regulatory hormone, hepcidin, which acts as a negative regulator of cytoplasmic iron.[41] When the cytoplasmic iron level is too high, hepcidin binds to Fpn. The iron-laden exporter protein is phosphorylated, endocytosed, and degraded (Figure 1.11). When iron needs to be transported to other areas, it is released by Fpn and oxidized to its ferric state by hephaestin (Figure 1.10). Once oxidized, iron is transferred to the iron transport protein transferrin (Tf) for circulation.[39-40]

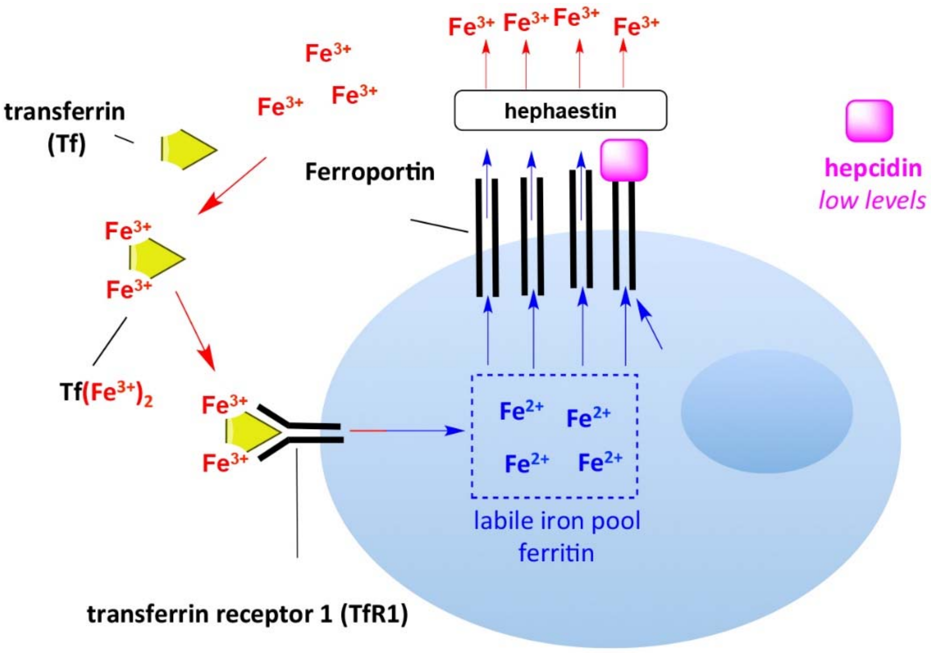

Figure 1.10. Iron transport and storage in cells.[40,42]

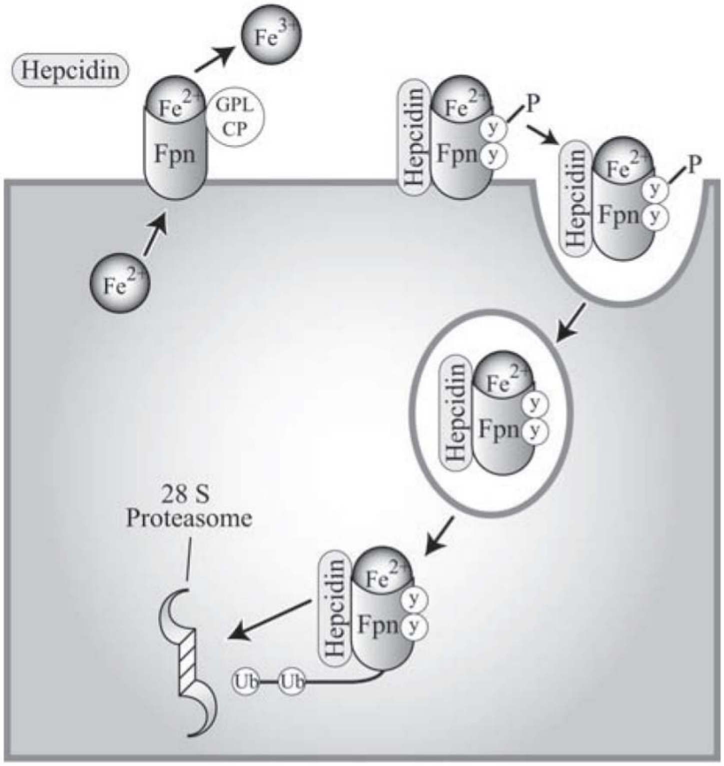

Figure 1.11. Figure from review article detailing the mechanism of hepcidin regulation of ferroportin (Fpn).[40] When hepcidin is unable to bind to Fpn, the iron is released and oxidized. When hepcidin binds to Fpn, it is endocytosed and degraded by proteasome.[40]

Iron bound to transferrin (Tf) circulates in the plasma until it is delivered to cells. Transferrin readily binds to two iron ions, forming a diferrous iron-transferrin complex, $Tf(Fe^{3+})_2$.[43] Each iron in Tf is coordinated to four amino acid residues (histidine, aspartate, and two tyrosines), as well as a labile carbonate ligand (Figure 1.12). Once $Tf(Fe^{3+})_2$ has reached its destination, it binds to the transferrin receptor (TfR) and is endocytosed into the cells. The low pH in the intracellular environment causes Tf to release ferric ion by protonation of the labile carbonate ligand.[44]

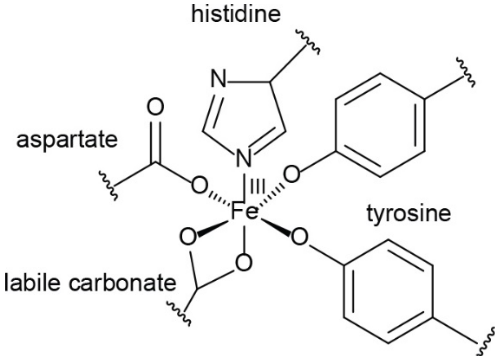

Figure 1.12. Coordination sphere for ferric ion in Tf.

Once released in a cell, iron(II) enters the labile iron pool, where it is either incorporated into proteins or sequestered in order to avoid detrimental redox chemistry.[40] Ferritin, the major iron storage protein, stores up to 4,500 iron atoms (as Fe^{3+}) and is found in the cytoplasm, nucleus, and mitochondria.[39] If iron is depleted, ferritin degradation is mediated by lysosomes, resulting in an increased concentration of iron in the labile iron pool.[39-40]

A high iron concentration in the labile iron pool can cause cellular damage by generation of reactive oxygen species.[45-47] One mechanism for iron toxicity is through Fenton chemistry, where iron(II) reacts with hydrogen peroxide to form hydroxide and hydroxyl radical (Figure 1.13).[48] Once generated, the highly reactive hydroxyl radical will immediate participate in detrimental free radical chemistry with the nearest biomolecule, such as the cell membrane or DNA. In biological systems, the ferrous ion can be regenerated by superoxide-mediated one-electron reduction of ferric ion to ferrous ion, in a catalytic cycle known as the Haber-Weiss cycle (Figure 1.13).[48]

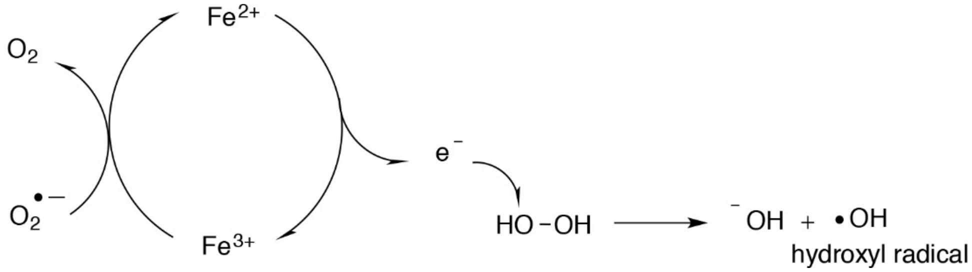

Figure 1.13. Potential mechanism of disruptive iron redox chemistry in cells.[49]

Iron(II) can also directly react with the phospholipid membrane, resulting in phospholipid peroxidation (Figure 1.14).[39] Phospholipid peroxidation can also be initiated by formation of a hydroxyl radical. Following radical initiation, a hydrogen atom in the allylic position can be abstracted from the fatty acid chain, generating a radical on the carbon atom. This carbon atom can then react with molecular oxygen to generate a peroxy radical.[39]

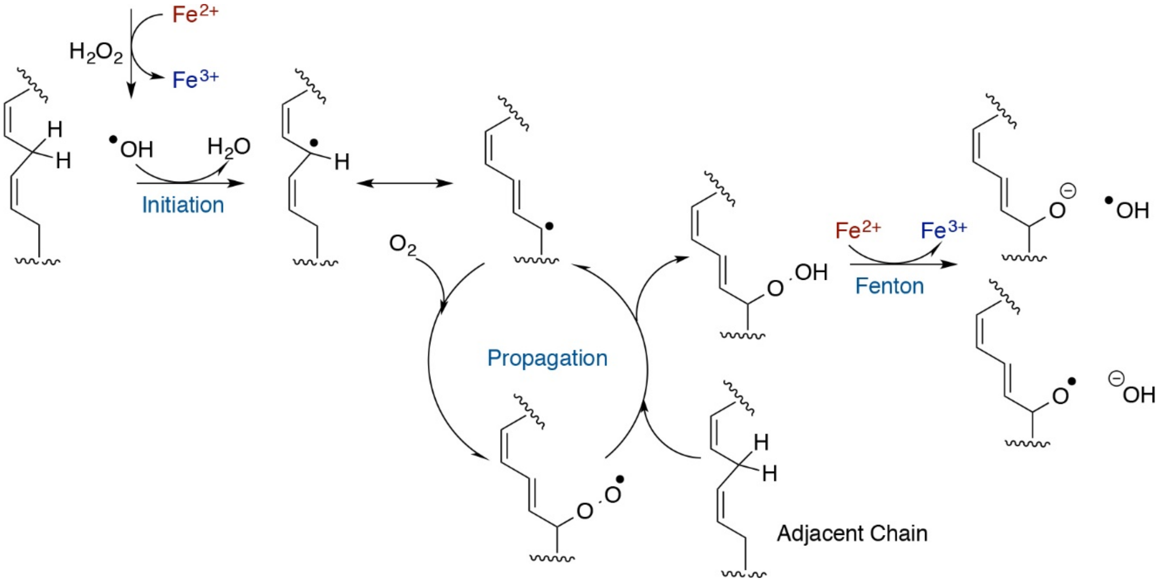

Figure 1.14. Proposed mechanism of phospholipid peroxidation.[49]

We proposed to utilize the redox potential of iron as an essential feature in the design and synthesis of new organometallic chemotherapeutics. We hypothesized that the cellular recognition of iron could be bypassed by masking competent iron-labilizing compounds as covalent iron-containing molecules; in particular by employing quantum-efficient benzoyl ferrocene derivatives. After cellular uptake, we plan to utilize the photochemical properties of benzoyl ferrocene to release free iron(II), thereby killing cancer cells by generation of reactive oxygen species (ROS) in a spatially- and temporally-controlled fashion. Ideally, our chemotherapeutic molecules will also be multimodal, featuring cytotoxic or cytotoxicity-enhancing agents in both the labilized ligand, and in the potentially catalytic features of ROS-generating iron(II). A design feature we hope to include in our chemotherapeutics is the incorporation of components in the iron ligand set that – once labilized – can disrupt cellular processes that protect against iron-overload and/or act as a cytotoxic agent independently.

D. Photodynamic Therapy

Photodynamic therapy (PDT) is a clinically approved therapeutic procedure involving administration of a photosensitizing agent followed by irradiation at a wavelength corresponding to the absorbance band of the sensitizer.[50] The photosensitizer is normally nontoxic, however, in the presence of oxygen, can lead to direct tumor cell death by reaction to produce reactive oxygen species. PDT is not a new concept; researchers have observed that combination of light and certain chemicals could induce cell death more than 100 years ago.[50] Oscar Raab, a German medical student, accidently discovered the beginning foundations for PDT research in 1900. He found that infusaria, a microorganism, when treated with light in the presence of acridine, a fluorescent dye, resulted in rapid cellular destruction.[51] Also in 1900, J. Prime reported that epileptic patients treated with eosin, a red fluorescent dye that is a brominated derivative of fluorescein, developed dermatitis in sunlight-exposed areas.[52] Later, in 1903, Herman Von Tappeiner and A. Jesionek applied eosin to skin tumors and treated it with white light. They termed this phenomenon 'photodynamic action'.[53] These early experiments led to more research on combinations of reagents and light, which led to modern PDT.

PDT involves two essential components that are nontoxic individually but which combine to initiate a cytotoxic photochemical reaction in an oxygen-dependent manner. After the photosensitizer is administered and localized in a target cell or tissue, the treatment area is irradiated at a specific wavelength in order to activate the photosensitizer.[54] After promoting the photosensitizer to an excited state, it can transfer energy to molecular oxygen, generating reactive oxygen species (ROS) – such as singlet oxygen and free radicals – that are toxic to cells (Figure 1.15).

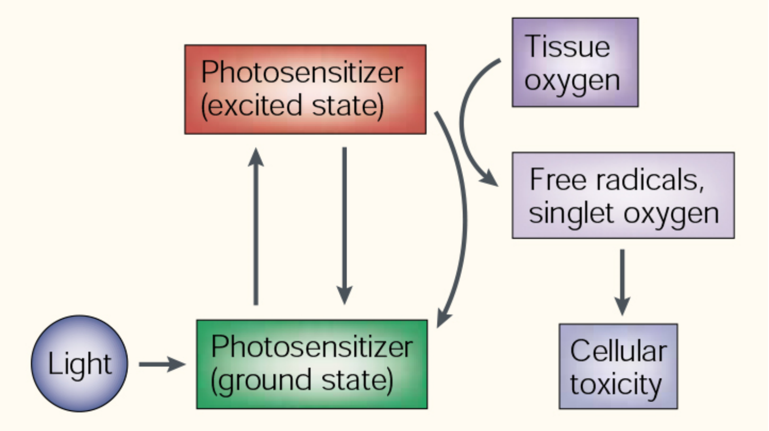

Figure 1.15. Figure from review article illustrating the mechanism of action of PDT as detailed in this section.[50]

There are two types of mechanisms for PDT. After the photosensitizer is transformed from the ground state into the activated excited state, it can undergo two kinds of reactions, Type I or Type II.[55] In a Type I reaction, the activated photosensitizer can react directly with nearby biomolecules, such as hydrogen peroxide or the cell membrane, to transfer a hydrogen atom to form a radical (Figure 1.16). The radicals generated through direct interaction can react with oxygen to form oxygenated products, such as the lipid peroxidation compound shown in Figure 1.14. In a Type II reaction, the activated photosensitizer can transfer energy directly to oxygen to form singlet oxygen (Figure 1.16). Singlet oxygen is a highly toxic reactive oxygen species.[56] Both Type I and Type II reactions can occur simultaneously, however, the ratio is dependent upon the type of photosensitizer used, the concentration of oxygen and other biomolecules in the cells, and the affinity of the photosensitizer to nearby biomolecules.[56] Only cells that are close to areas of photosensitizer cations are directly affected by PDT due to the short half-life and high reactivity of reactive oxygen species that are generated.[57]

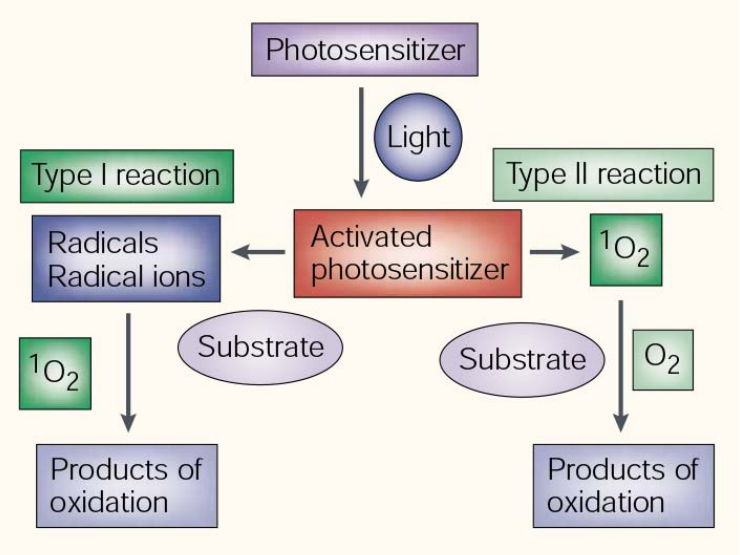

Figure 1.16. Figure from review article of Type I and Type II reactions in photodynamic therapy.[50]

We hope to use a new approach to photodynamic therapy by using *in situ* generated iron(II) as a catalyst in biological systems. After activating benzoyl ferrocene derivatives using light to generate free iron(II), it can produce reactive oxygen species in cells, either through electron donation to nearby biomolecules or by participation in cellular Fenton chemistry by oxidation to iron(III). Iron(III) can also be reduced to iron(II) in cells in a Haber-Weiss cycle, generating catalytic iron(II) (as detailed in Section C). In this way, we hope to generate a catalyst that continues to function in the absence of light.

E. Ferroptosis

Ferroptosis is a recently recognized form of non-apoptotic cell death.[58] It is characterized by iron-dependent lipid peroxidation distinct from apoptosis, necrosis, autophagy, and other forms of cell death. It is morphologically characterized by the presence of smaller than normal mitochondria with condensed mitochondrial membrane densities.[58] Ferroptosis can be triggered by small molecules which inhibit the glutathione biosynthesis pathway, system x_c^-, or the glutathione-dependent antioxidant enzyme, glutathione peroxidase 4 (GPx4).[59] Cancer cells with high level RAS-RAF-MEK pathway activity or p53 expression may be sensitive to ferroptosis.[60-62]

Ferroptosis-inducers were discovered before the concept of ferroptosis was invented by the Stockwell group in 2012. In 2003, the Stockwell lab reported that erastin (Figure 1.17) was lethal toward human engineered RAS oncogene fibroblasts (BJeLR), but not the isogenic wild-type counterparts.[60] Later in 2008, the Stockwell lab also reported that Ras-selective small molecules, RSL3 and RSL5, selectively killed BJeLR cells in a similar manner to erastin.[61] While cell death induced by RSL3 was found to share similar features with erastin-mediated ferroptosis, RSL3 and erastin induce ferroptosis through different mechanisms.[58,61] Erastin was found to induce ferroptosis through inhibition of system x_c^-,[58] the glutamate/cysteine antiporter system in cells.[63-64] Inhibition of system x_c^- results in depletion of intracellular cysteine, which is essential for glutathione synthesis. Glutathione depletion causes loss of cellular antioxidant capacity, such that generation of lipid ROS leads to cell death. RSL3 was reported to directly inhibit GPx4 enzyme activity.[59] Inhibition of GPx4 generates elevated levels of ROS, leading to ferroptosis.

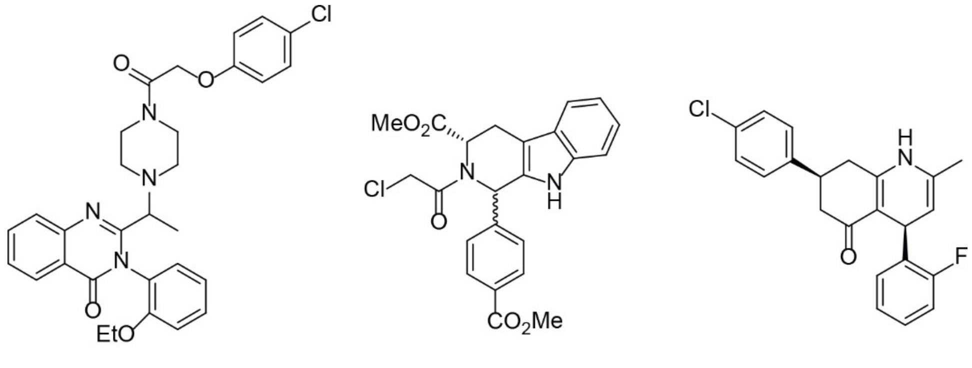

erastin **RSL3** **RSL5**

Figure 1.17. Selected structures of ferroptosis inducers.[60-61]

Further studies by the Stockwell lab have also identified ferroptosis inhibitors. Lipophilic antioxidants such as ferrostatin-1 and α-tocopherol (Figure 1.18), as well iron chelators have been identified as strong suppressors of erastin-induced cell death.[65] This suggests that reactive oxygen species, likely lipophilic in nature, were involved in the cell death process. More recently, Stockwell *et al*. has found that mitochondrial-targeted nitroxide, such as XJB-5-131, is a potent inhibitor of ferroptosis.[66] Scheme 1.6 illustrates a schematic of ferroptosis inducers such as RSL3, which inhibits GPx4, and erastin, which inhibits system x_c^-, both leading to indirect inhibition of GPx4. Treatment with iron chelators and antioxidants such as ferrostatin-1 can inhibit ferroptosis by inhibiting lipid ROS (Scheme 1.6).

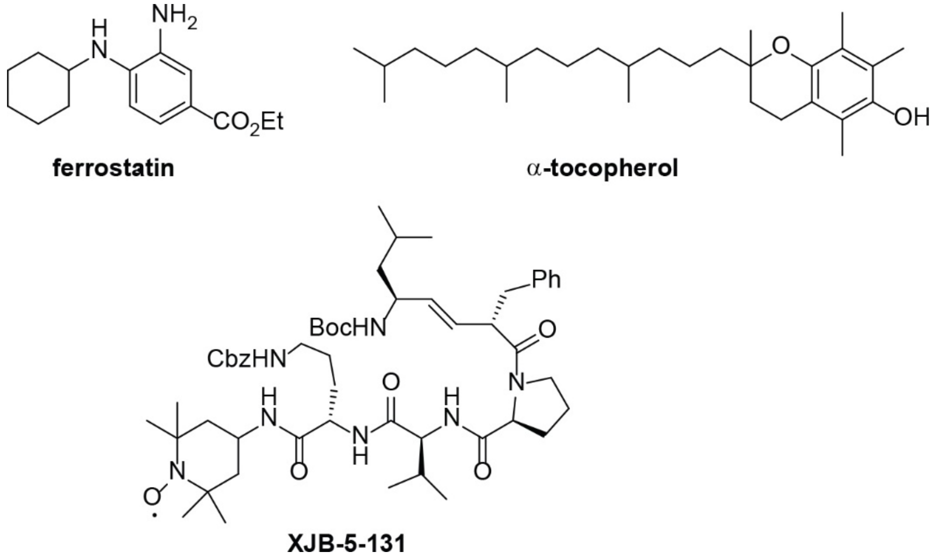

Figure 1.18. Structures of selected ferroptosis inhibitors.

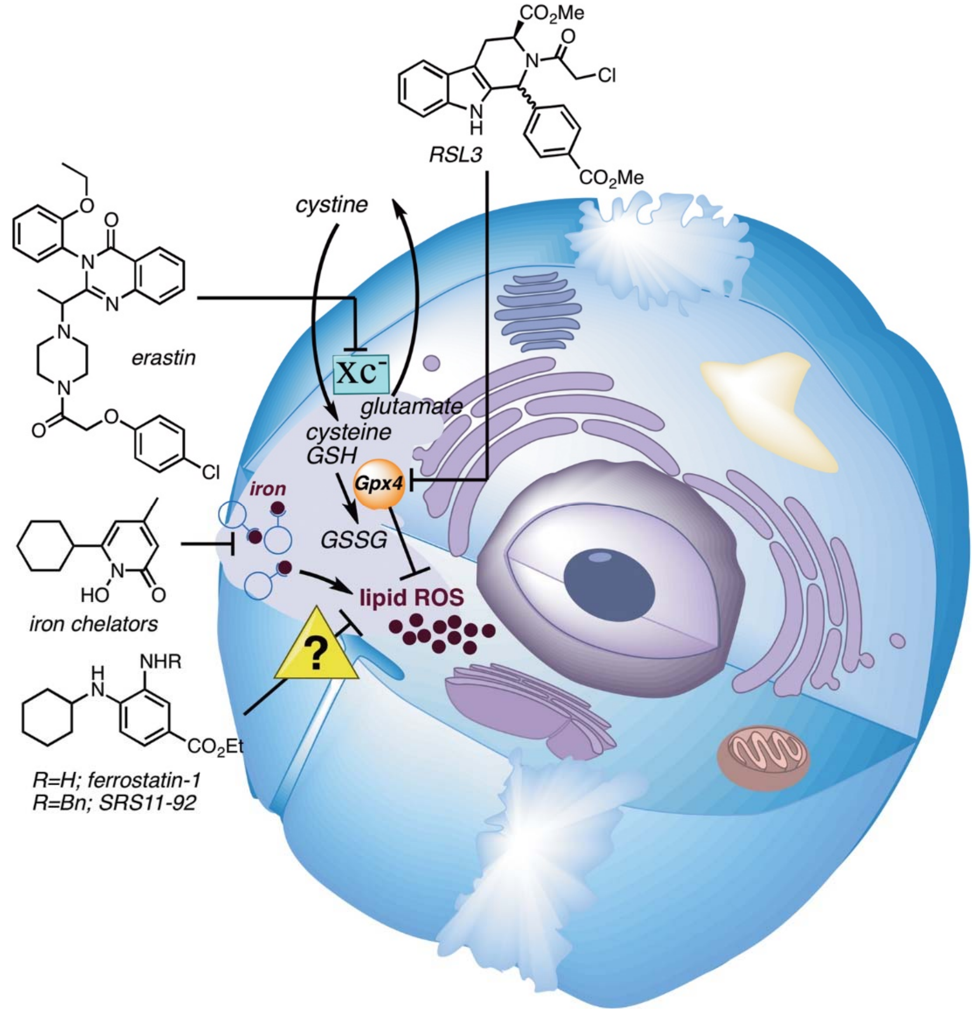

Scheme 1.6. Illustration of ferroptosis in a cell, with RSL3 and erastin inducing ferroptosis, while iron chelators and ferrostatin-1 prevent ferroptosis by inhibiting lipid ROS. If GPx4 is not induced, it can inhibit lipid ROS by production of glutathione (GSH), which oxidizes to glutathione disulfide (GSSG) after interaction with ROS.[66]

F. Nanoparticles as a Drug Delivery Vehicle

Nanotechnology has started to play an important role in the field of medicine, and more specifically in the development of anticancer therapeutics.[67-68] For example, nano-formulated chemotherapeutic agents are used to treat metastatic ovarian cancer and AIDS-related Kaposi's sarcoma, as well as advanced breast, lung, and pancreatic cancers.[69-71] A large variety of nanoparticles demonstrating potential in treatment and diagnosis have been developed.[72-75] In particular, porous silicon nanoparticles (pSiNPs) are of interest in biomedical research because of their low toxicity and high potential for evading conventional side effects.[76]

The size and shape of porous silicon nanoparticles play a role in both *in vivo* and *in vitro* behavior; therefore, calibrated uniform particles are desired for chemotherapeutic use.[77] Pharmacokinetics is linked to the nanoparticle degradation rate, which depends on the surface chemistry, which is also strongly correlated to size and shape. Cellular internalization and cytotoxicity have been reported as influenced by nanoparticle size.[78] The circulation time of nanoparticles in the blood stream has been found to be longer for nanoparticles in the range of 20-200 nm.[79]

Silicon is the trace metal with the highest levels in the human body, as the total silicon content in a 70 kg adult is approximately 1 g.[80] This demonstrates silicon's biocompatibility in living organisms, and its nontoxic behavior. Porous silicon nanoparticles in humans can be completely degraded into orthosilicic acid, a nontoxic, bioavailable form of silicon in the body;[81-82] the orthosilicic acid thus generated can be efficiently excreted from the human body through renal clearance.[76]

Porous silicon nanoparticles are an ideal drug carrier due to the ability to graft and functionalize silicon with other molecules in large amounts by different surface chemical modifications such as hydrosilylation, silanisation, and hydrocarbonization, to name just a few.[83] This versatility of pSiNPs permits targeted and controlled drug release within tumor cells.[84] The nanostructure and porosity of pSiNPs allow for efficient loading of anticancer drugs, small molecules, enzymes, proteins, antibodies and small interfering RNA molecules or other species.[85-87] The pSiNPs are also useful for encapsulating hydrophobic drugs which can increase their application efficacy.[84] Interest in pSiNPs is also due to easy handling and cost-efficient synthesis through simple electrochemical anodization of crystalline silicon.[88] We hope to utilize these properties of pSiNPs to encapsulate benzoyl ferrocene derivatives for delivery to cancer cells.

G. RGD as a peptide target

The RGD peptide sequence (Figure 1.19) has been demonstrated to target the αv-integrins, which are over expressed in tumor vasculature.[89-91] RGD-based peptide targeting agents have been successfully used to deliver drugs, imaging agents, viruses, and nanoparticles.[92-95] However, tumor parenchymal penetration and high drug payload delivery remain major challenges. Initial studies to overcome these challenges were performed by a phage screening method to identify peptides.[96] Ruoslahti's group found that internalized RGD (iRGD) demonstrated both superior tumor parenchymal penetration and higher payload delivery.[96]

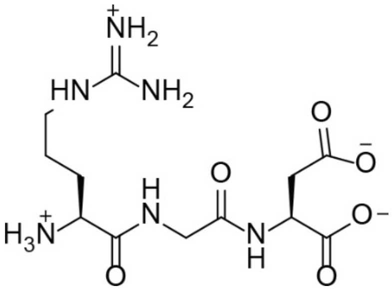

Figure 1.19. RGD peptide sequence.

The iRGD is a cyclic 9-amino acid structure consisting of the sequence CRGD[K/R]GP[D/E]C (Figure 1.20). The peptide contains two critical sequences that enable the higher penetrability, leading to better payload delivery. The first is the integrin-binding RGD peptide sequence, which can mediate the first binding of iRGD to $\alpha_v\beta_3$ or $\alpha_v\beta_5$ integrins, both of which are preferentially overexpressed in tumor cells.[89-90] After binding of the iRGD peptide to the integrins, proteolytic cleavage releases the C-terminal

CRGDK peptide sequence (also known as the CendR motif), which interacts with the neuropilin-1 (NRP-1) receptor. This second critical sequence resulting from proteolytic cleavage and binding to NRP-1 triggers the endocytic transcytosis pathway in tumor cells.

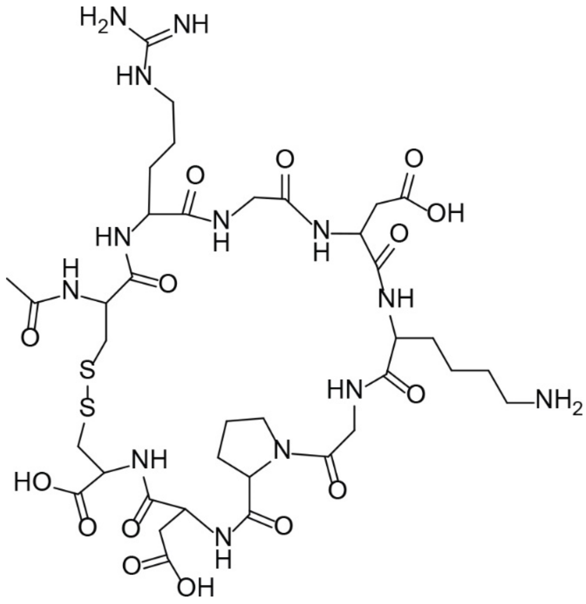

Figure 1.20. iRGD peptide sequence CRGDKGPDC.

H. Project Proposal

In light of the previously described literature precedents, we propose to esign and synthesize benzoyl ferrocene derivatives that can photochemically generate cytotoxic reactive oxygen species in tumor cells. The use of photochemical activation to release iron(II) after cellular uptake allows for enhanced spatiotemporal control. Part of the synthetic design includes benzoyl ferrocene derivatives which are biologically inactive under dark conditions, but cytotoxic upon treatment with light, as in photodynamic therapy. We wish to investigate iron redox-driven cytotoxicity in tumor cells as a novel alternative to traditional photodynamic therapy. While previous literature regarding photochemical decomposition of benzoyl ferrocene was conflicting, both Bozak[32] and Kutal[33] reported formation of free iron(II) and complete dissociation of both ligands upon photochemical decomposition of **XXV**. Marissa Aubrey, a previous graduate student in the O'Connor lab, carried out photochemical studies on the decomposition of 4-pentylbenzoyl ferrocene (Figure 1.21), and obtained results which were in line with those of Bozak and Kutal.[97] Based on these previous results, we believe that the free iron(II) generated *in situ* would cause cell death by generation of toxic radicals and reactive oxygen species through the Haber-Weiss cycle (Figure 1.22).

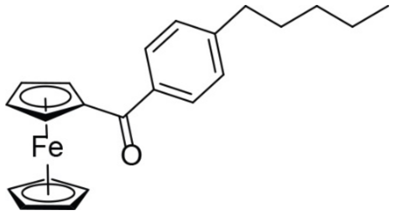

Figure 1.21. Structure of 4-pentylbenzoyl ferrocene.

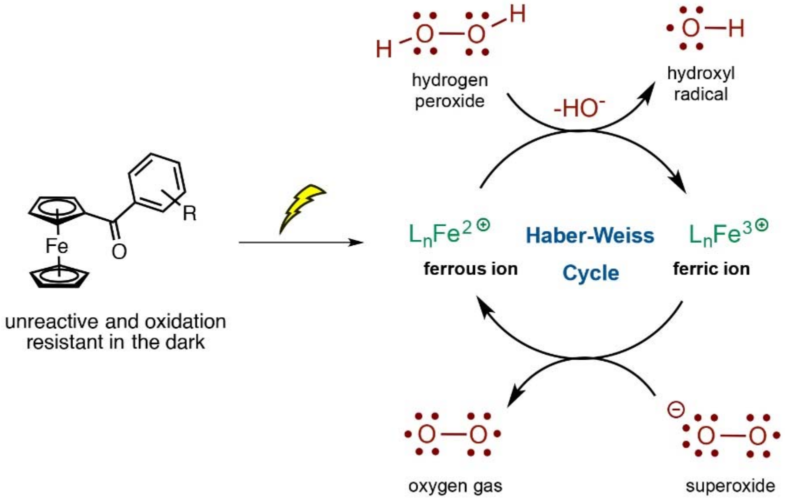

Figure 1.22. Generation of free iron(II) by light for *in situ* redox in cells in the Haber-Weiss cycle.[97]

By triggering generation of free iron(II) *in situ*, we hypothesize that the overload of iron in cells will induce ferroptosis by generation of ROS, which can lead to lipid peroxidation. In this way, we can create a more general cancer treatment to induce ferroptosis, compared to compounds such as ML210 and erastin, which shut down the

GPx4 pathway in *RAS* oncogenic mutated cancer cells.[58-59] We also wish to utilize porous silicon nanoparticles to deliver benzoyl ferrocene derivatives to tumor cells, functionalizing with iRGD peptide targeting agent to determine if the greater payload results in greater light toxicity.

I. References

1. Kealy, T. J.; Pauson, P. L. *Nature*, **1951**, *168*, 1039-1040.

2. Miller, S. A.; Tebboth, J. A.; Tremaine, J. F. *J. Chem. Soc.* **1952**, *74*, 2125-2126.

3. Wilkinson, G.; Rosenblum, M.; Whiting, M. C.; Woodward, R. B. *J. Am. Chem. Soc.* **1952**, *74*, 2125-2126.

4. Pfab, W.; Fischer, E. O. *Z. Anorg. Allg. Chem.* **1953**, *274*, 316-322.

5. Werner, H. *Angew. Chem. Int. Ed.* **2012**, *51*, 6053-6058.

6. Ornelas, C. *New J. Chem.* **2011**, *35*, 1973-1985.

7. Gasser, G.; Ott, I.; Metzler-Nolte, N. *J. Med. Chem.* **2011**, *54*, 3-25.

8. Braga, S. S.; Silva, A. M. S. *Organometallics*, **2013**, *32*, 5626-5639.

9. Patra, M.; Gasser, G. *Nature Rev. Chem.* **2017**, *66*, 1-12.

10. Nesmeyanov, A. N.; Bogomolova, L. G.; Viltcheskaya, V. Ferrocerone. US Patent 119 365 (1971).

11. Fiorina, V. J.; Dubois, R. J.; Brynes, S. *J. Med. Chem.* **1978**, *21*, 393-395.

12. Köpf-Maier, P.; Köpf, H.; Neuse, E. W.; *J. Cancer Res. Clin. Oncol.* **1984**, *108*, 336-340.

13. Neuse, E. W.; Kanzawa, F. *Appl. Organomet. Chem.* **1989**, *4*, 19-26.

14. Tamura, H.; Miwa, M. *Chem. Lett.* **1997**, *26*, 1177-1178.

15. Osella, D.; Ferrali, M.; Zanello, P.; Laschi, F.; Fontani, M.; Nervi, C.; Cavigiolio, G. *Inorg. Chim. Acta*. **2000**, *306*, 42-48.

16. Biot, C.; Glorian, G.; Maciejewski, L. A.; Brocard, J. *J. Med. Chem.* **1997**, *40*, 3715-3718.

17. Dubar F. et al The antimalarial ferro. *ACS Chem. Biol.* **2012**, *6*, 275-287.

18. Top, S.; Tang, J.; Vessières, A.; Carrez, D.; Provot, C.; Jaouen, G. *Chem. Commun.* **1996**, *8*, 955-956.

19. Schatzschneider, U.; Metzler-Nolte, N. *Angew. Chem. Int. Ed.* **2006**, *45*, 1504-1507.

20. Top, S.; Thibaudeau, C.; Vessières, A.; Brulé, E.; Bideau, F.; Joerger, J. M.; Plamont, M. A.; Samreth, S.; Edgar, A.; Marrot, J.; Herson, P.; Jaouen, G. *Organometallics*. **2009**, *28*, 1414-1424.

21. Mooney, Á.; Corry, A. J.; O'Sullivan, D.; Rai, D. K.; Kenny, P. T. M. *J. Organomet. Chem.* **2009**, *694*, 886-894.

22. Mooney, Á.; Corry, A. J.; Ní Ruairc, C.; Mahgoub, T.; O'Sullivan, D.; O'Donovan, N.; Crown, J.; Varughese, S.; Draper, S. M.; Rai, D. K.; Kenny, P. T. M. *Dalton Trans*. **2010**, *39* 8228-8239.

23. Epton, R.; Hobson, M. E.; Marr, G.; *J. Organomet. Chem.* **1978**, *149*, 231.

24. Ong, C.-W.; Jeng, J.-Y.; Juang, S.-S.; Chen, C.-F. *Bioorg. Med. Chem. Lett*. **1992**, *2*, 929-932.

25. Vashisht Gopal, Y. N.; Jayaraju, D.; Kondapi, K. Arch. Biochem. Biophys. **2005**, *438*, 206-216.

26. Jastroch, M.; Divakaruni, A. S.; Mookerjee, S.; Treberg, J. R.; Brand, M. D. *Essays Biochem*. **2010**, *47,* 53-67.

27. Nguyen, A.; Top, S.; Pigeon, P.; Vessières, A.; HIllard, E. A.; Plamont, M. A.; Huché, M.; Rigamonti, C.; Jaouen, G. *Chem. A. Eur. J.* **2009**, *15*, 684-696.

28. McCarthy, J. S.; Rückle, T.; Djeriou, E.; Cantalloube, C.; Ter-Minassian, D.; Baker, M.; O'Rourke, P.; Griffin, P.; Marquart, L.; Hooft van Huijsduijnen, R.; Möhrle, J. J. *Malaria J.* **2016**, *15*, 469-475.

29. Tarr, A. M.; Wiles, D. M. *Can. J. Chem.* **1968**, *46*, 2725-2731.

30. Ali, L. H.; Cox. A.; Kemp, T. J. *J. Chem. Soc. Chem. Commun.* **1972**, 265-266.

31. Ali, L. H.; Cox, A.; Kemp, T. J. *J.C.S. Dalt.* **1973**, *46*, 2725.

32. Bozak, R. E.; Javaheripour, H. *Chem. Ind.* **1973**, 696.

33. Yamaguchi, Y.; Kutal, C. *Inorg. Chem.* **1999**, *38*, 4861-4867.

34. Ding, W.; Sanderson, C. T.; Conover, R. C.; Johnson, M. K.; Amster, I. J.; Kutal, C. *Inorg. Chem*. **2003**, *42*, 1532-1537.

35. Yamaguchi, Y.; Ding, W.; Sanderson, C. T.; Borden, M. L.; Morgan, M. J.; Kutal, C. *Coord. Chem. Rev*. **2007**, *251*, 515-524.

36. Torti, S. V.; Torti, F. M. *Nat. Rev Cancer*. **2013**, *13*, 342-355.

37. Hentze, M. W.; Muckenthaler, M. U.; Andrews, N. C. *Cell* **2004**, *102*, 15048-15052.

38. Papanikouloau, G.; Pantopoulous K. *Toxicol Appl Pharmacol*. **2005**, *202*, 199-211.

39. Crichton, R. *Iron Metabolism*; 3rd ed.; Wiley: West Sussex U. K., 2009.

40. MacKenzie, E. L; Iwasaki, K.; Tsuji, Y. *Antioxid. Redox Signal*. **2008**, *10*, 997-1030.

41. Vulpe, C. D.; Kuo, Y. M.; Murphy, T. L; Cowley, L.; Askwith, C.; Libina, N.; Gitschier, J.; Anderson, G. J. *Nat. Genet.* **1999**, *21*, 195-199.

42. Figure modified from Professor O'Connor's figure from presentation.

43. Ponka, P.; Beaumont, C.; Richardson, D. R. *Semin. Hematol.* **1998**, *35*, 35-54.

44. MacGillvray, R. T. A.; Moore, S. A.; Chen. J. Anderson, B. F.; Baker, H.; Luo, Y.; Bewley, M.; Smith, C. A.; Murphy, M. E. P.; Wang, Y. Mason, A. B.; Woodworth, R. C.; Brayer, G. D.p Baker. E. N. *Biochemistry* **1998**, *37*, 7919-7928.

45. Liou, G.-Y.; Storz, P. *Free Radic. Res.* **2010**, *44,* 479-496.

46. Ray, P. D.; Huang, B.-W.; Tsuji, Y. *Cellular Signaling.* **2012**, *24*, 981-990.

47. Holmström, K. M.; Finkel, T. *Nat. Rev. Mol. Cell Biol.* **2014**, *15*, 411-421.

48. Koppenol, W. H. *Redox Report*. **2001**, *6*, 229-234.

49. Figures obtained from Marissa's thesis. Aubrey, M. 'Organoferrous Antitumor Agents', PhD thesis, University of California San Diego, San Diego, CA.

50. Dolmans D. E.; Fukumura, D.; Jain, R. K. *Nature Reviews Cancer*. **2003**, *3*, 380-387.

51. Raab, O. *Zeitung Biol.* **1990**, *39*, 524–526.

52. Prime, J. *Les accidents toxiques par l'eosinate de sodium* (Jouve and Boyer, Paris, 1900).

53. von Tappeiner, H. & Jodlbauer, A. *Die sensiblilisierende Wirkung fluoreszierender Substanzer Gesammte Untersuchungen uber die photodynamische Erscheinerung* (Voger, F. C., Leipzig, 1907).

54. Henderson, B. W.; Dougherty, T. J. *Photochem. Photobiol.* **1992**, *55*, 145-157.

55. Allison R. R.; Moghisi, K. *Clin. Endosc.* **2013**, *46*, 24-29.

56. Weishaupt, K. R.; Gomer, C. J.; Dougherty, T. J. *Cancer Res.* **1976**, *36*, 2326-2329.

57. Moan, J.; Berg, K. *Photchem. Photobiol* **1991**, *53*, 549-553.

58. Dixon, S. J.; Lemberg, K. M.; Lamprecht, M. R.; Skouta, R.; Zaitsev, E. M.; Gleason, C. E.; Patel, D. N.; Bauer, A. J.; Cantley, A. M.; Yang, W. S.; Morrison, B.; Stockwell, B. R. *Cell*. **2012**, *149*, 1060-1072.

59. Yang, W.S.; SriRamaratnam, R.; Welsche, M. E.; Shimada, K.; Skouta, R,; Viswanathan, V. S.; Cheah, J. H.; Clemons, P. A.; Shamji, A. F.; Clish, C. B.; Brown, L. M.; Girotti, A. W.; Cornish, V. W.; Schreiber, S. L.; Stockwell, B. R. *Cell*. **2014**, *156*, 317-331.

60. Dolma, S.; Lessnick, S. L.; Hahn, W. C.; Stockwell, B. R. *Cancer Cell*. **2003**, *3,* 285-196.

61. Yang, W. S.; Stockwell, B. R. *Chem. Bio.* **2008**, *15*, 234-245.

62. Jiang, L.; Kon, N.; Wang S. J.; Su, T.; Hibshoosh H.; Baer, R.; Gu, W. *Nature*. **2015**, *520*, 57-62.

63. Bannai, S.; Kitamura, E. *J. Biol. Chem.* **1980**, *255*, 2372-2376.

64. Bridges, R. J.; Natale, N. R.; Patel, S. A. *Br. J. Pharmacol.* **2012**, *165*, 20-34.

65. Yagoda, N.; von Rechenberg, M.; Zaganjor, E.; Bauer, A. J.; Yang, W. S.; Fridman, D. J.; Wolpaw, A. J.; Smukste, I.; Peltier, J. M. Boniface, J. J.; Smith, R.; Lessnick, S. L.; Sahasrabudhe, S.; Stockwell, B. R. *Nature*. **2007**, *447*, 864-868.

66. Krainz, T.; Gaschler, M. M.; Lim, C.; Sacher, J. R.; Stockwell, B. R.; Wipf, P. *ACS Cent. Sci*. **2016**, *2*, 653-659.

67. Ferrari, M. *Nat Rev. Cancer*. **2005**, *5*, 161-171.

68. Serda, R. E.; Godin, B.; Blanco, E.; Chiappini, C. Ferrari, M.; *Biochim. BIophys. Acta, Ge. Subj.* **2011**, *1810*, 317-329.

69. Treat, J.; Greenspan, A.; Forst, D.; Sanchez, J. A.; Ferrans, V. J.; Potkul, L. A.; Woolley, P. V.; Rahman, A. *J. Natl. Cancer Inst.* **1990**, *82*, 1706-1710.

70. Gradishar, W. J. *J. Clin. Oncol.* **2005**, *23*, 7794-7803.

71. Shen, H.; You, J.; Zhang, G.; Ziemys, A.; Li, Q.; Ba, L.; Deng, X.; Erm, D. R.; Liu, X.; Li, C.; Ferrari, M. *Adv. Healthcare Mater*. **2012**, *1*, 84-89.

72. Huang, H.-C.; Barua, S.; Sharma, G.; Dey, S. K.; Rege, K. *J. Controlled Release*. **2011**, *155*, 344-357.

73. Van de Ven, A. L.; Kim, P.; Haley, O.; Fakhoury, J. R.; Adriani, G; Schmulen, J.; Moloney, P.; Hussain, F.; Ferrari, M.; Liu, X.; Yun, S.-H.; Decuzzi, P. *J. Controlled Release*. **2012**, *158*, 148-155.

74. Liu, Z.; Liu, J.; Wang, R.; Du, Y.; Ren, J.; Qu, X. *Biomaterials*. **2015**, *56*, 206-218.

75. Shi, P.; Liu, Z. Dong, K.; Ju, E.; Ren, J.; Du, Y.; Li, Z.; Qu, X. *Adv. Mater.* **2014**, *26*, 6635-6641.

76. Park, J-H.; Gu, L.; von Maltzahn, G.; Ruoslahti, E.; Bhatia, S. N.; Sailor, M. J. *Nat. Mater.* **2009**, *8*, 331-336.

77. Stojanovic, V.; Cunin, F.; Durand, J. O.; Garcia, M.; Gary-Bobo, M. *J. Mater. Chem. B.* **2016**, *4*, 7050-7059.

78. Qin, Z.; Joo, J.; Gu, L.; Sailor, M. J. *Part. Part. Syst. Charact.* **2014**, *31*, 252-256.

79. Alhmoud, H.; Delalat, B.;Elnathan, R.; Cifuentes-Rius, A.; Chaix, A.; Rogers, M.-L.; Durand, J.-O. Voelcker, N. H. *Adv. Funct. Mater.* **2015**, *25*, 1137-1145.

80. Osminkina, L. A.; Tamarov, K. P.; Sviridov, A. P.; Galkin, R. A.; Gongalsky, M. B.; Solovyev, V. V.; Kudryavtsev, A. A.; Timoshenko, V. Y. *J. Biophotonics*. **2012**, *5*, 529-535.

81. Canham, L. T. *Nanotechnology*. **2007**, *18*, 186704.

82. Tzur-Balter, A.; Gilert, A.; Massad-Ivanir, N.; Segal, E. *Acta Biomater*. **2013**, *9*, 6208-6217.

83. Wu, E. C.; Andrew, J. S.; Cheng, L.; Freeman, W. R.; Pearson, L.; Sailor, M. J. *Biomaterials*. **2011**, *32*, 1957-1966.

84. Wang, C.-F.; Mäkilä, E. M.; Kaasalainen, M. H.; Liu, D.; Sarparanta, M. P.; Airaksinen, A. J.; Salonen, J. J.; Hirvonen, J. T.; Santos, H. A. *Biomaterials.* **2014**, *35*, 1257-1266.

85. Kaaslaainen, M.; Rytkönen, J.; Mäkilä, E.; Närvänen, A.; Salonen, J. *Langmuir*. **2015**, *31*, 1722-1729.

86. Kinsella, J. M.; Ananda, S.; Andrew, J. S.; Grondek, J. F.; CHien, M.-P.; Scadeng, M.; Gianneschi, N. C.; Ruoslahti, E.; Sailor, M. J. *Adv. Mater.* **2011**, *23*, H248-H253.

87. Hasanzadeh Kafshgari, M.; Alnakhli, M.; Delalat, B.; Apostolou, S.; Harding, F. J.; Mäkilä, E.; Salonen J. J.; Kuss, B. J.; Voelcker, N. H. *BIomater. Sci.* **2015**, *3*,1555-1565.

88. Sailor, M. J. *Porous Silicon in Practice – Preparation, Characterization and Application, XII.,* 2011.

89. Pierschbacher, M. D.; Ruoslahti, E. *Nature*. **1984***, 309*, 30-33.

90. Eliceiri, B. P.; Cheresh, D. A. *Curr Opin Cell Biol.* **2001**, *13*, 563-568.

91. Rouslahti, E. *Matrix Biol.* **2003**, *22*, 459-465.

92. Curnis, F.; Gasparri, A.; Sacchi, A. Longhi, R.; Corti, A. *Cancer Res*. **2004**, *64*, 565-571.

93. Sipkins, D. A.; Cheresh, D. A.; Kazemi, M. R.; Nevin, L. M.; Bednarski, M. D.; Li, K. C. *Nat Med*. **1998**, *4*, 623-626.

94. Wickham, T. J. *Gene Ther*. **2000**, *7*, 110-114.

95. Murphy, E. A.; Majeti, B. K.; Barnes, L. A.; Makale, M.; Weis, S. M.; Lutu-Fuga, K.; Wrasidlo, W.; Cheresh, D. A. *Proc. Natl. Acad. Sci. U S A*. **2008**, *105,* 9343-9348.

96. Sugahara, K. N.; Tessalu, T.; Karmali, P. P.; Kotamraju, V. R.; Agemy, L.; Girard, O. M.; Hanahan, D.; Mattrey, R. F.; Ruoslahti, E. *Cancer Cell*. **2009**, *16*, 510-520.

97. Aubrey, M. 'Organoferrous Antitumor Agents', PhD thesis, University of California San Diego, San Diego, CA.

Chapter II

Cytotoxicity of Ferrocenyl Derivatives and Possible Mechanism of Action

A. Introduction

Organometallic drugs are increasingly popular anticancer drug candidates.[1-4] In particular, the use of ferrocene and its derivatives in medicinal applications has become a very popular research area.[5-6] The anticancer potential of ferrocene derivatives was first studied in the late 1970s by Brynes and co-workers who reported the antitumor activity of ferrocenyl compound **1** (Figure 2.1).[7] In 1984, Kopf-Maier and co-workers reported that ferrocenium salts **2a** and **2b** were active against Ehrlich ascites tumor (EAT) and Rauscher leukemia virus (RLV) respectively, whereas ferrocene **3** displayed no anti-tumor efficacy against EAT.[8] While the mechanism of action for **2** was not known at the time, follow up studies by various groups have suggested that ferrocenium salts **2** generate radicals through the Fenton pathway, causing DNA damage and cell apoptosis.[9-12] Of all the ferrocene derivatives studied for cancer therapy, the ferrocifen derivatives (**4**) have been most widely studied, with very promising results for breast cancer.[13-14] In 1996, Jouen *et al.* first coupled ferrocene to the active metabolite tamoxifen to make the antitumor compound hydroxyferrocifen **4**.[15] Recent studies of the mechanism of action for **4** suggests a reactive oxygen species (ROS) pathway that leads to cell death.[16]

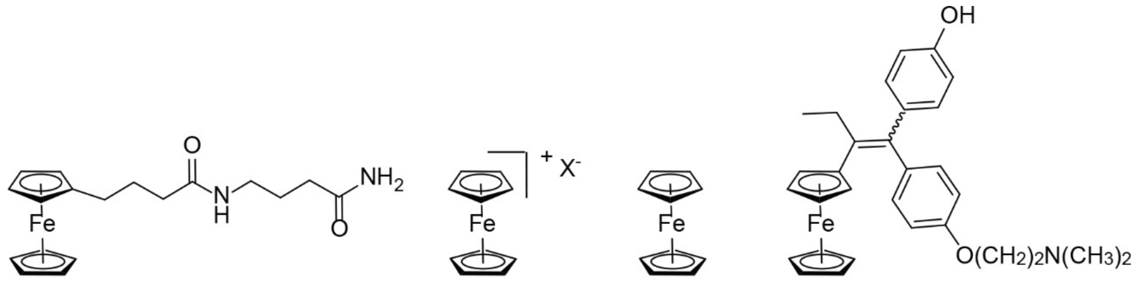

1

2a: $X^- = [FeCl_4]^-$
2b: $X^- = I_3^-$

3

4

Figure 2.1. Select ferrocene derivatives with biological studies.[7,8,15]

Ferrocene-based antitumor agents are attractive drug candidates due to iron being an inexpensive metal relative to other transition metals – such as platinum – as well as their relative air-stability and ease of synthesis. It is due to these reasons that the O'Connor lab has been interested in investigating a new method using ferrocene derivatives and light to trigger selective death in cancer cells. A fundamental precedent for our work is found in studies by Kutal reporting that benzoyl ferrocene (**5**) undergoes photochemical loss of the organic ligands to give solvated iron(II) upon irradiation at 546 nm in acetonitrile or methanol (Figure 2.2).[17-19] Kutal and co-workers attributed the unique photochemical activity of **5** to the metal-to-ligand charge transfer (MLCT) in low energy excited states wherein the benzoyl cyclopentadienyl is labilized by slipping η^5 to η^4, creating an open coordination site and formal positive charge on the iron, and also making the metal center susceptible to nucleophilic attack by solvent as shown in Figure 2.2. The **5**-η^4 intermediate can expel the solvent and re-form the sandwich complex, or dissociate the remaining cyclopentadienyl ligand to give free iron(II) as shown in Scheme 2.1. By utilizing the photochemical properties of benzoyl ferrocene, we hypothesized that we could disrupt iron homeostasis in cells, which would eventually lead to cell death.

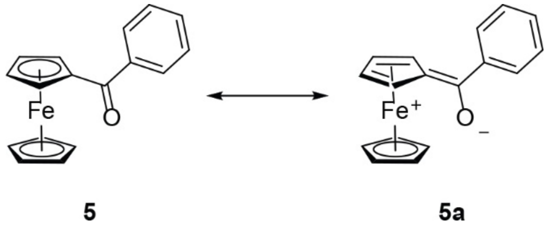

Figure 2.2. Benzoyl ferrocene resonance illustrating the ring slippage from η^5 to η^4.

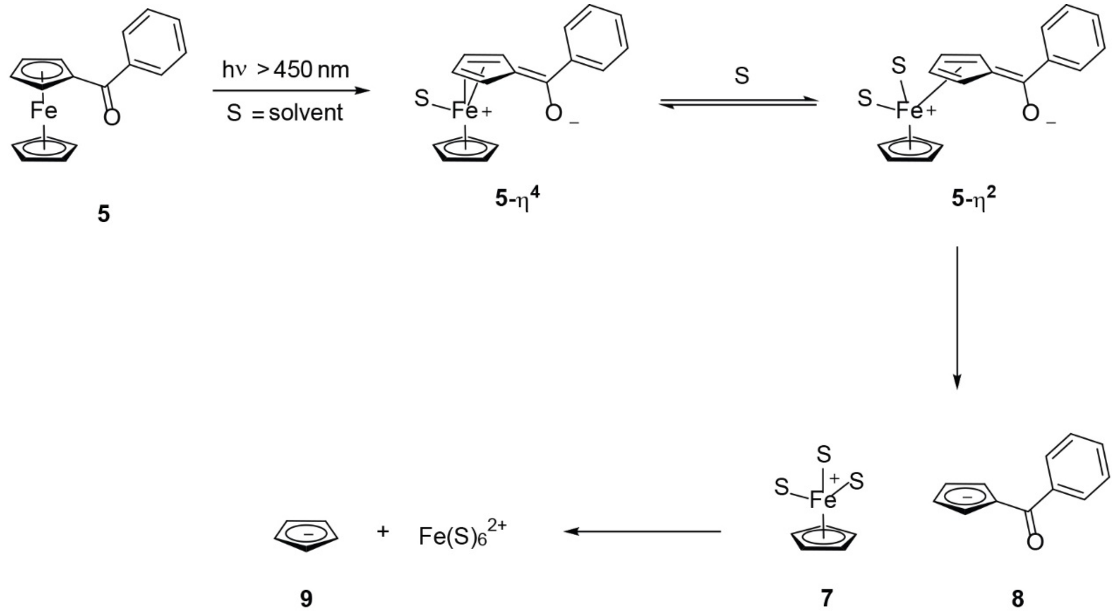

Scheme 2.1. Proposed mechanism of ring slippage to photochemical dissociation of benzoylferrocene.[17]

Iron homeostasis is a highly regulated process in mammalian cells due to both its essential and potentially toxic effects. The redox chemistry of iron is useful enzymatically and crucial for cell metabolism, proliferation, and growth.[20] However, this ability to gain and lose electrons can lend itself to potentially destructive free radical generation. Iron(II) can partake in Fenton chemistry in cells, wherein iron(II) is oxidized to iron(III) upon reaction with endogenous H_2O_2. The oxidized iron(III) can then react with endogenous superoxide to reduce back to iron(II) and oxygen, leading to a catalytic redox of iron in the Haber-Weiss reaction (Figure 2.3).[21-22] Formation of the hydroxyl radical (•OH) can cause damage to lipids, proteins and DNA.[23]

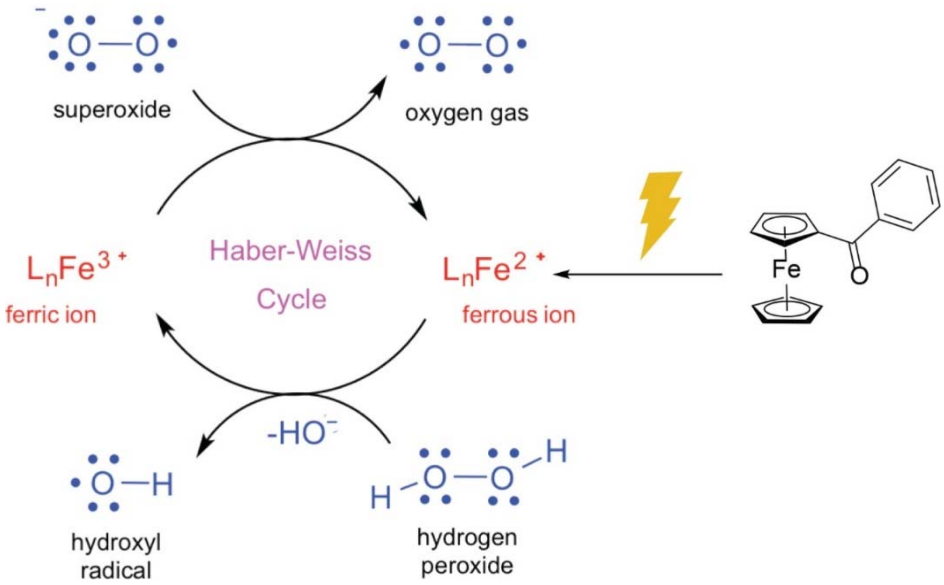

Figure 2.3. Photochemical generation of free iron(II) *in situ* in cells and catalytic formation of detrimental reactive oxygen species.

We propose that by masking iron(II) as benzoyl ferrocene derivatives, we could spatiotemporally disrupt cellular iron homeostasis by treating the cells with our organoferrous complex, followed by irradiation to release free iron(II). The photo-generated iron(II) in cells could then catalyze the conversion of endogenous hydrogen peroxide to hydroxyl radical, eventually leading to cell death. We further hypothesized that the relatively electron-deficient benzoylferrocene derivatives would not participate in detrimental redox chemistry, thus leading to an increase of cytotoxicity under irradiation conditions as compared to non-radiative conditions.

Initial biological studies in our laboratory have illustrated that benzoyl ferrocene (**5**), 4-pentylbenzoyl ferrocene (**10**), 4-cyclohexylbenzoyl ferrocene (**11**), and 2,6-dichlorobenzoyl ferrocene (**12**) are cytotoxic (Figure 2.4).[24] Compound **6** and **7** showed the largest difference between light and dark toxicity, whereas compound **5** and **8** have no difference in cytotoxicity under light or dark conditions. Herein, our goals were to: (1) synthesize a benzoyl ferrocene derivative such that we had greater cytotoxicity difference between irradiation and dark conditions (ideally with no toxicity under dark conditions); (2) determine if the benzoyl ferrocene derivatives are uptaken by the cancer cells; and (3) determine whether the iron or the photolyzed ligand was the toxic species.

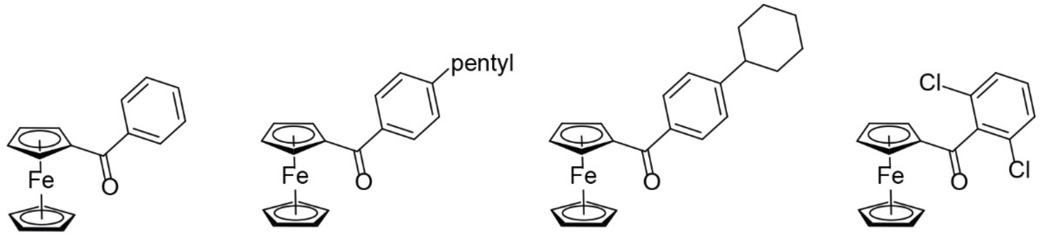

5 **10** **11** **12**

Figure 2.4. Previously determined cytotoxicity of benzoyl ferrocene derivatives.

B. Results

1. Synthesis of Benzoyl Ferrocene Derivatives

Marissa Aubrey, a previous graduate student in the O'Connor lab, had previously synthesized a library of benzoyl ferrocene derivatives and tested them in cancer cell lines, with compounds **10** and **11** showing particular promise. Table 2.1 illustrates the cytotoxicity values of compounds **5**, **10**, **11**, and **12** wherein light IC_{50} values indicate cells irradiated with light 24 h after addition of compound to the cells. Dark IC_{50} values indicate cells that were left in the incubator without treatment by irradiation. Compounds were originally studied in HeLa and lung carcinoma A549 cell lines.

Table 2.1. Previously reported cytotoxicity values in HeLa and A549 cell lines

	Light IC_{50} (μM)		**Dark IC_{50} (μM)**	
Entry	**Hela**	**A549**	**HeLa**	**A549**
5	30.8	43.5	33.5	41.5
10	12.8	9.5	57.9	49.0
11	8.7	6.8	>40*	>40*
12	40.5	33.2	47.1	36.1

*IC_{50} value could not be determined due to solubility constraints. However, no cytotoxicity was observed up to the solubility limit.

With the observation that pentyl derivative **10** was a promising lead, we hypothesized that if we placed a triphenylphosphine mitochondrial targeting unit[25-26] on benzoyl ferrocene, we could increase cytotoxicity and lower the IC_{50} value. Synthesis of compound **15** was accomplished by first synthesizing 4-(chloromethyl)benzoyl ferrocene (**13**) from ferrocene and 4-methylchlorobenzoyl chloride in a Friedel-Crafts acylation, which proceeded in 61% yield. Treatment of compound **13** with triphenyphosphine had no reaction, so we converted the chloride of **13** to iodo-analogue **14** by reaction with NaI in acetone at room temperature overnight. Compound **14** was reacted with triphenylphosphine in diethyl ether with precautions to exclude oxygen, which afforded the triphenylphosphine benzoyl ferrocene derivative **15** in 50% yield.

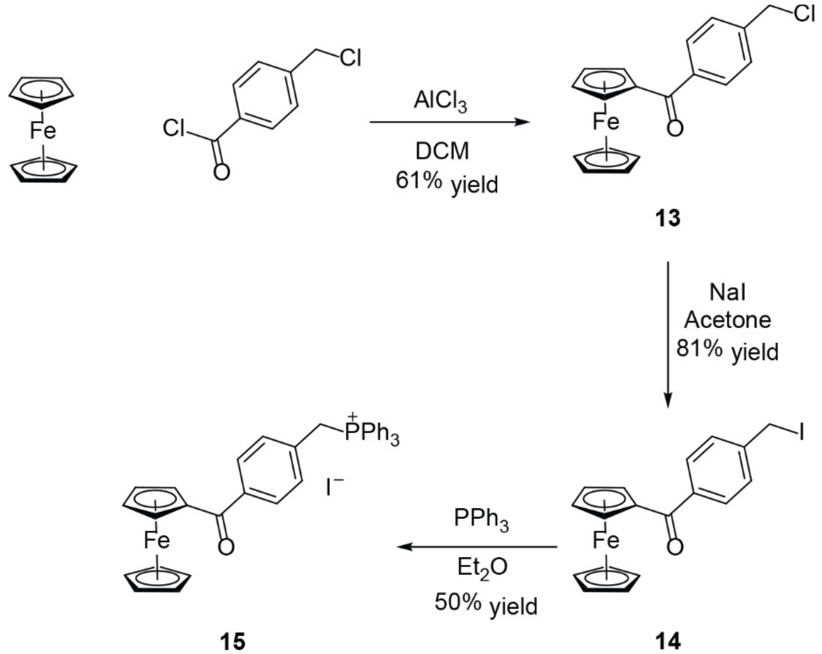

Scheme 2.2. Synthesis of mitochondrial target compound **15**.

We also synthesized and determined the cytotoxicity of several bis-substituted benzoyl ferrocenes, as they are more electron withdrawing in character, and are known to have a higher quantum yield for ligand dissociation.[27] Compound 1,1'-(bispentyl)benzoyl ferrocene (**16**) was synthesized by performing a Friedel-Crafts acylation on ferrocene using at least two equivalents of 4-pentylbenzoyl chloride. 1,1'-(bistriphenylphosphinemethyl)benzoyl ferrocene (**19**) was synthesized using at least two equivalents of 4-(chloromethyl)benzoyl chloride to afford compound **17**. The chloride derivative was then treated with NaI in acetone to afford compound **18**, which when further treated with triphenylphosphine in diethyl ether gave compound **19** in 21% combined yield over the three steps.

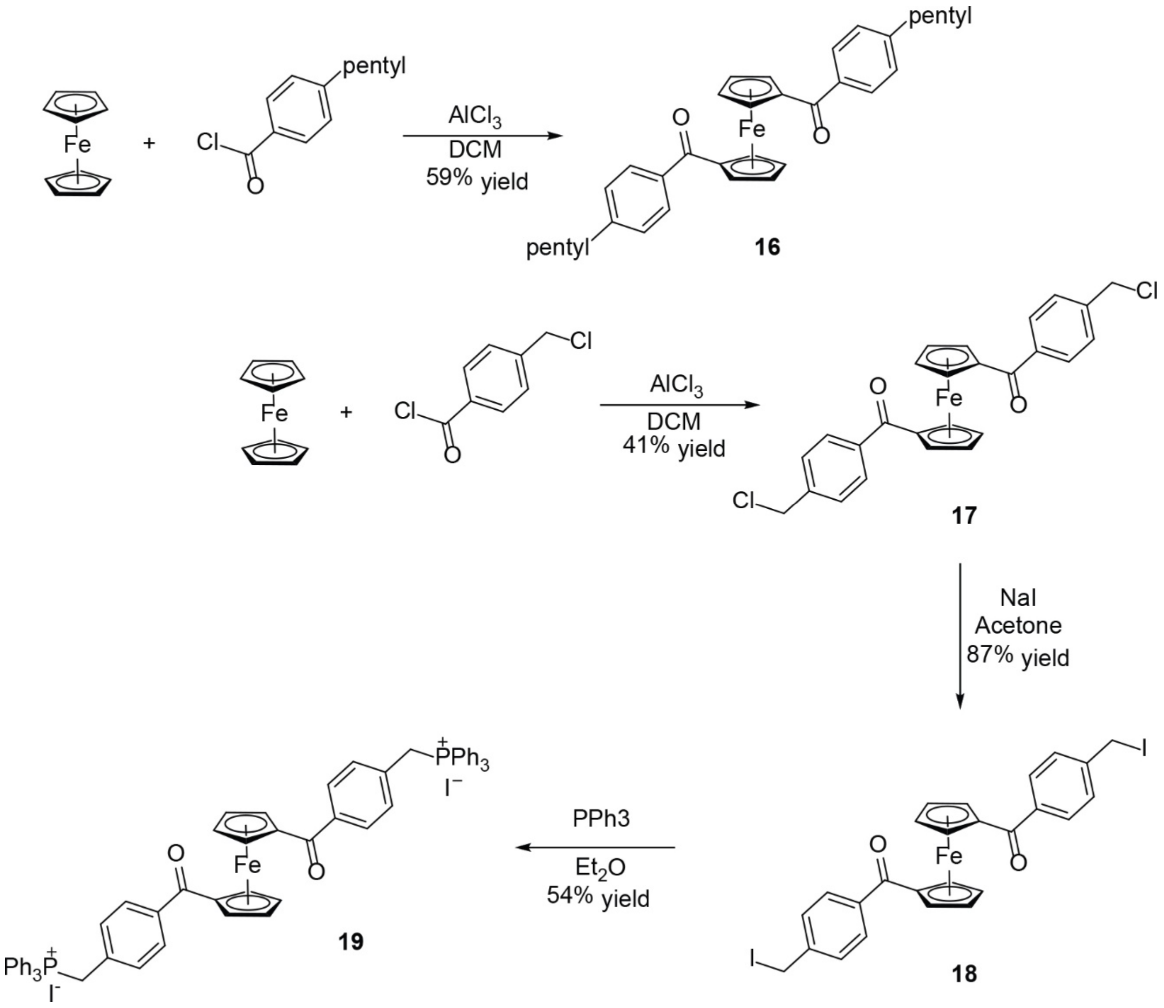

Scheme 2.3. Synthesis of compound **16** and **19**.

In order to elucidate whether the liberated ligand(s) or free iron(II) was the cytotoxic species in cells, we pursued several benzoyl ferrocene derivatives that incorporate a fluorescent tag. Our initial approach to this synthesis was to conjugate fluorescein to the iron compound, as fluorescein is a very common imaging agent for confocal microscopy and a relatively inexpensive dye.[28] Fluorescent compound **20** was synthesized from compound **14** and treated with fluorescein sodium salt in THF and refluxed overnight. Due to the poor yield (<1%) of the **13** to **20** with fluorescein sodium salt, we looked into conjugating other fluorescent dyes.

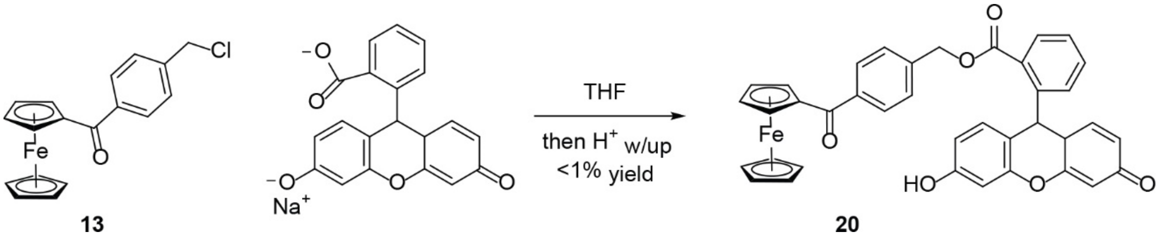

Scheme 2.4. Synthesis of fluorescein conjugated benzoyl ferrocene **20**.

At the suggestion of Professor Tor in the Chemistry and Biochemistry Department at UCSD, we looked into synthesizing fluorescent derivatives with 4-chloro-7-nitrobenzo-2-oxa-1,3-diazole (NBD-Cl).[29] Treatment of NBD-Cl with primary amine **21** affords the NBD fluorescent benzoyl ferrocene derivative **22** such that we can image and determine if our compound is taken up by cells.[30] Primary amine **21** was synthesized in 84% yield from chloride **13** by treatment of aqueous ammonia in THF and MeOH.

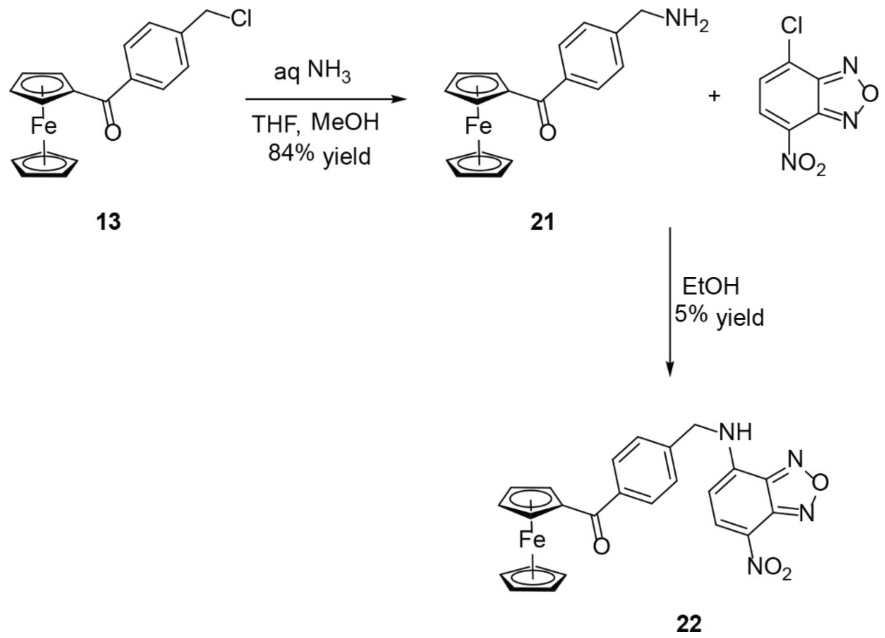

Scheme 2.5. Synthesis of NBD-benzoyl ferrocene derivative **22**.

2. Cytotoxicity Studies of Compounds 10, 15, 16, 19 and 22

With a few functionalized benzoyl ferrocene derivatives in hand, we tested *in vitro* cytotoxicity in cervical HeLa, lung carcinoma A549, and ovarian Caov3 cancer cell lines as indicated below. Our standard protocol consists of two separate 96-well plates prepared such that one can test irradiation conditions while the other remained in the dark in the incubator as a control. A standard protocol is illustrated in **Scheme 2.6** to show timeline of our assays.

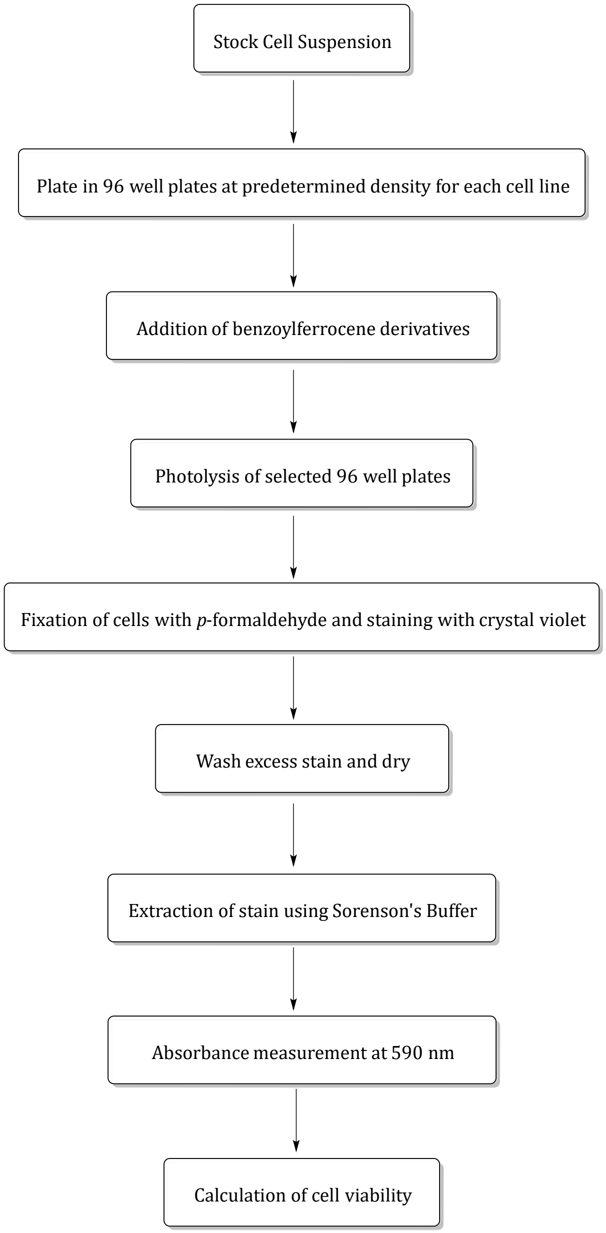

Scheme 2.6. Standard protocol for cytotoxicity using crystal violet assay.

The compounds were diluted in DMSO, with the amount dependent upon the concentration used. Six varying concentrations per compound per trial in order to create an IC_{50} curve. We need to obtain at least two concentration points with greater than 90% cell death, two points with less than 90% cell death, and two points in between in order to plot and calculate IC_{50} values in OriginPro 8.0 software. A set-up of the 96-well microtiter plate is illustrated in **Figure 2.5**.

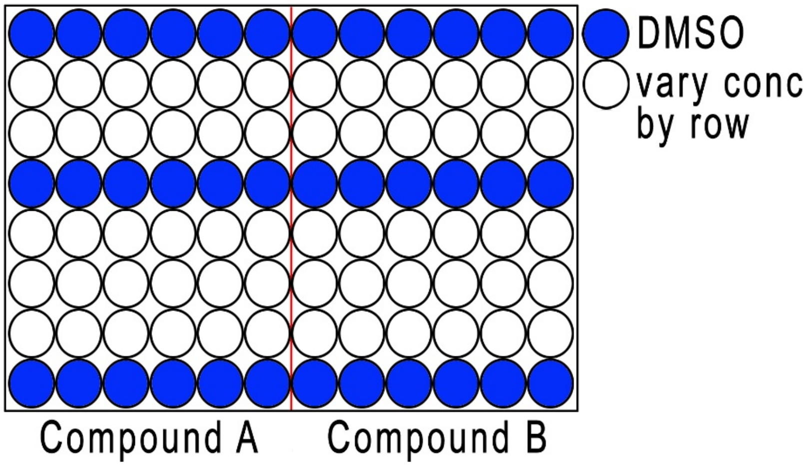

Figure 2.5. Set-up of 96-well plate for cytotoxicity assays.

One day (24 h) after seeding the cells at a density specific to their cell line in 96-well plates, our compounds were added. After incubation for 24 h, one of the plates was covered with a 455 nm longpass filter and placed under a light source[24] for 3 h, while the other plate was maintained in the incubator in the dark. After 48 h of irradiation, cytotoxicity was determined using crystal violet assay methods,[31] as explained in the experimental section. The UV-Vis absorbance at 590 nm was used to calculate the percentage of cell viability at each compound concentration using **Equation 2-1**. Each test was performed independently in at least triplicate for each compound, on different days over the course of at least one month.

Equation 2-1: $\text{Average Absorbance}_{\text{drug containing wells}}/\text{Average Absorbance}_{\text{control wells}}$

Marissa had originally tested pentyl compound **10** in HeLa and A549 cell lines, but due to the lack of readily available A549 cells, we first tested newly synthesized pentyl complex **15**, triphenylphosphine derivative **16**, bis(pentyl) complex **19**, and NBD-fluorescently tagged compound **22** using the HeLa cell line. While mitochondrial targeting compound **15**, showed slightly better IC_{50} values at 5.8±0.3 μM compared to **10**, the compound has nearly the same toxicity in the dark with an IC_{50} value of 12.4±2.7 μM. Compound **16** exhibited an IC_{50} value of 16.8±2.3 μM under light conditions and no cytotoxicity in the dark up to the solubility limit of 100 μM. Cytotoxicity of complex **19** has yet to be determined, but we know that HeLa cells treated with 2.5 μM of **19** exhibits more than 90% cytotoxicity. Cytotoxicity assays of fluorescent compound **22** indicate an IC_{50} value of 31.2±0.9 μM in the light, and approximately 63% cell viability at the solubility limit of 100 μM in the dark. Compound **22** was also photolyzed before addition into cells in order to test the cytotoxicity of the unbound ligands. We knew from previous studies that free inorganic iron(II) is not cytotoxic due to cytotoxicity studies with $FeSO_4$ up to 200 μM, so we were not concerned about any adverse effects of free iron(II) in solution before addition to cells. Treatment of HeLa cells with the photoproducts of **22** led to no cytotoxicity. Later confocal microscopy images demonstrates that the dissociated fluorescent ligand had internalized into the cells. This result is very promising as it indicates the toxicity of the compound is most likely due to the generation of free iron(II) instead of the ligand. All IC_{50} values are listed in Table 2.2 for ease of comparison.

Table 2.2. Cytotoxicity of compounds **10**, **15**, **16**, **19** and **22**

	Light IC_{50} Values (μM)			**Dark IC_{50} Values (μM)**		
Entry	**HeLa**	**A549**	**Caov3**	**HeLa**	**A549**	**Caov3**
10	12.8±1.8	9.5±2.7	10.9±2.3	57.9±5.0	49.0±6.7	71.0±4.5
15	5.8±0.3	n.d.	n.d.	12.4±2.7	n.d.	n.d.
16	16.8±2.3	n.d.	1.8±0.2	>100	n.d.	>100
19	<2.5	n.d.	n.d.	<2.5	n.d.	n.d.
22	31.2±0.9	n.d.	n.d.	>100*	n.d.	n.d.

n.d. – values were not determined as cytotoxicity was not tested in these cell lines.
*exhibited 63% cell viability at 100 μM.

Table 2.2 Cytotoxicity of compounds **10**, **15**, **16**, **19** and **22** continued.

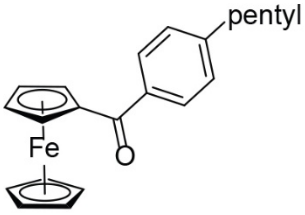

10

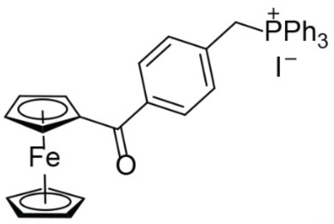

15

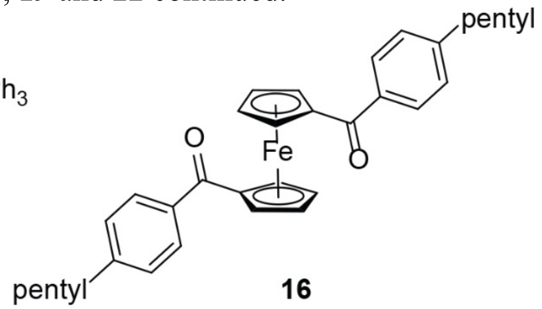

16

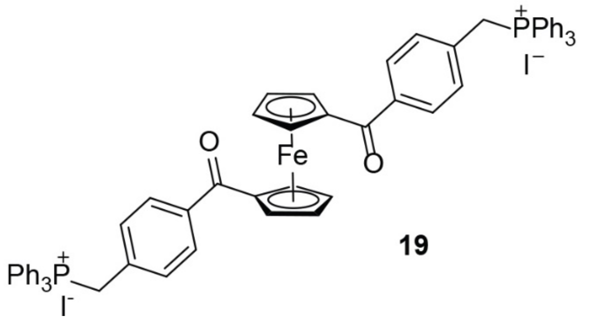

19

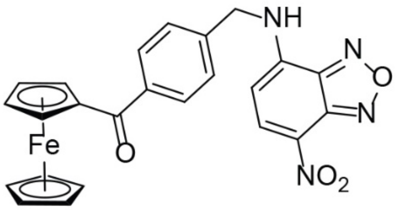

22

We decided to test compounds **10** and **16** in ovarian Caov3 cells lines because we want to compare to the cytotoxicity of normal ovarian cell lines in the future. Compound **10** exhibited a greater ratio of light and dark IC_{50} values in Caov3 cell lines than in HeLa and A549, with 10.9±2.3 μM and 71.0±4.5 μM respectively. The same trend held true for compound **16** as the IC_{50} value under irradiation conditions was 1.8±0.2 μM, and no cytotoxity up to 100 μM in the dark. Figures 2.6 – 2.9 illustrate the IC_{50} graph of compounds **10**, **15**, **16**, and **22** created in OriginPro 8.0 software.

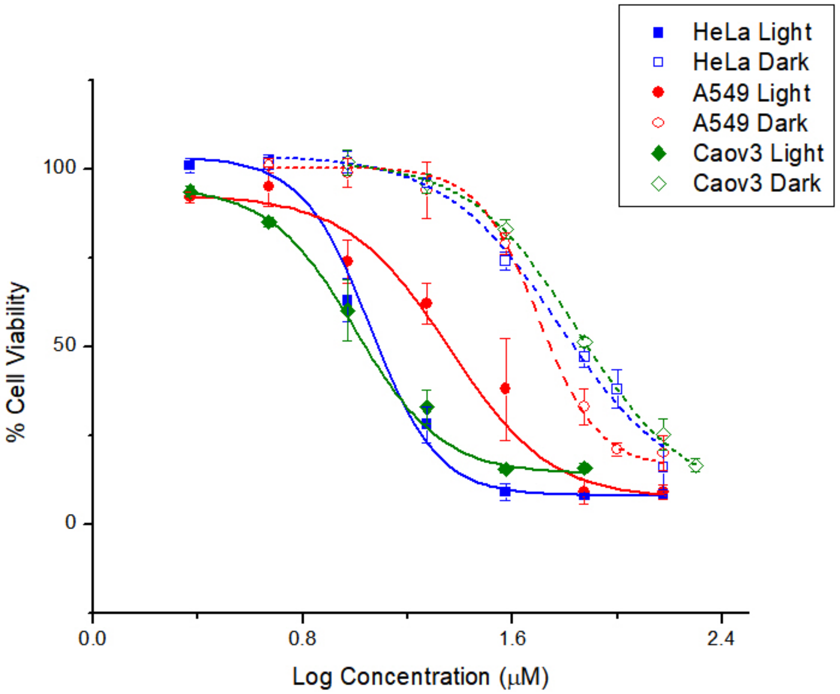

Figure 2.6. IC50 graph of pentyl derivative **10**.

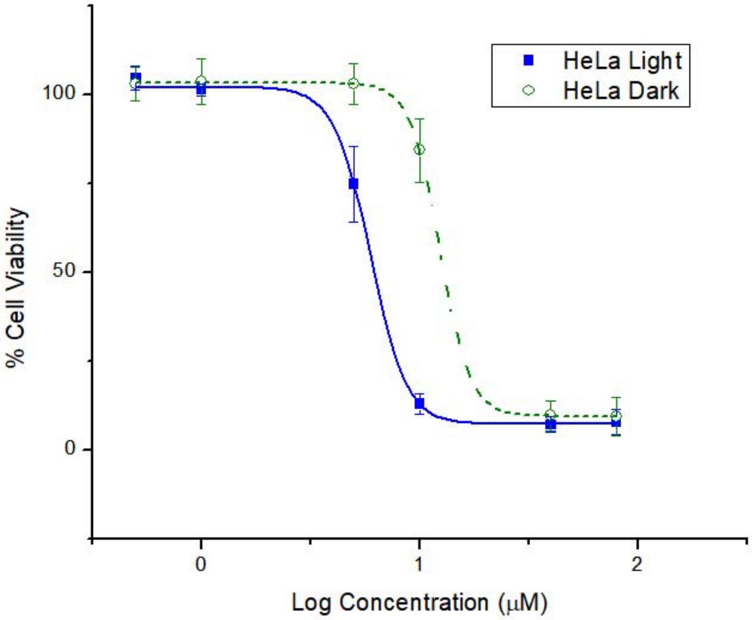

Figure 2.7. IC50 graph of triphenylphoshine derivative **15**.

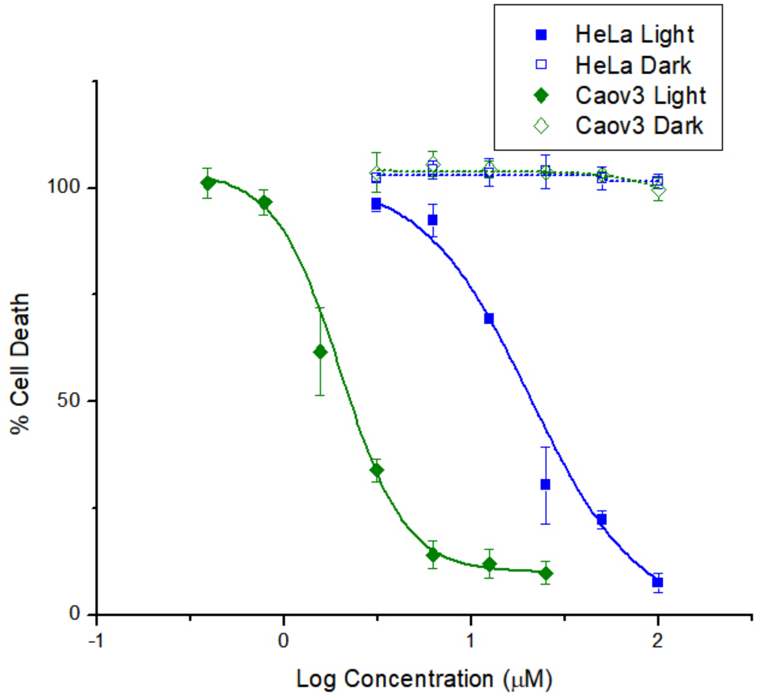

Figure 2.8. IC_{50} graph of bis(pentyl) derivative **16**.

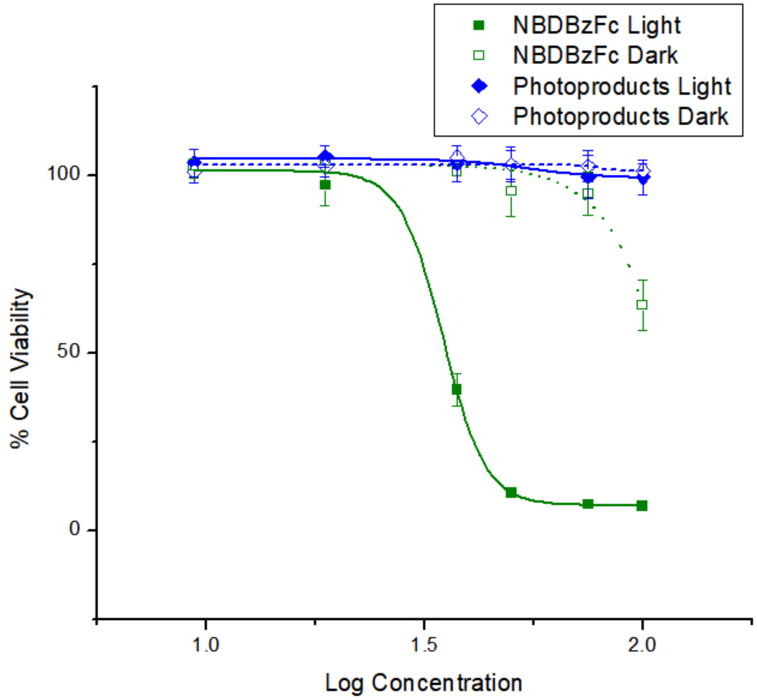

Figure 2.9. IC_{50} graph of NBD fluorescent tagged complex **22**.

3. Confocal Microscopy Studies

NBD fluorescent complex **22** was synthesized in order to image the compound inside the cells using confocal microscopy techniques.[32] HeLa cells were seeded in a 4-chamber 35 mm glass bottom dish. Compound **22** and the photolyzed products of compound **22** (which contains the free fluorescent ligand) were added 24 h after seeding. After another 24 h, the medium was removed and the cells were rinsed three times with DPBS. The cells were then fixed with 4,6-diamidino-2-phenylindole, dihydrochloride (DAPI)[33] in order to stain and differentiate the nucleus from the rest of the cells for imaging. Cells were imaged with a confocal microscope with excitation at 358 nm and emission at 461 nm for DAPI and excitation at 465 nm and emission at 535 for compound **22** and freed fluorescent ligand.

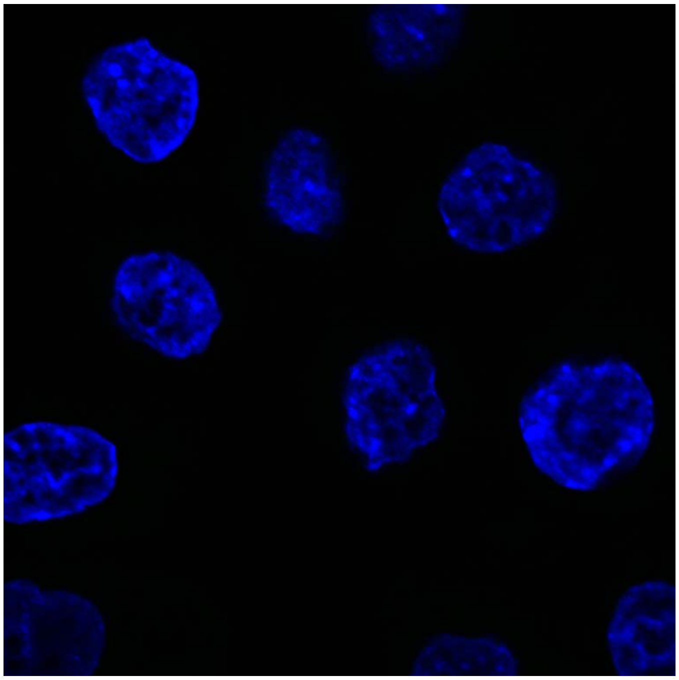

Figure 2.10. Confocal microscopy images of control HeLa cells left in the dark incubator.

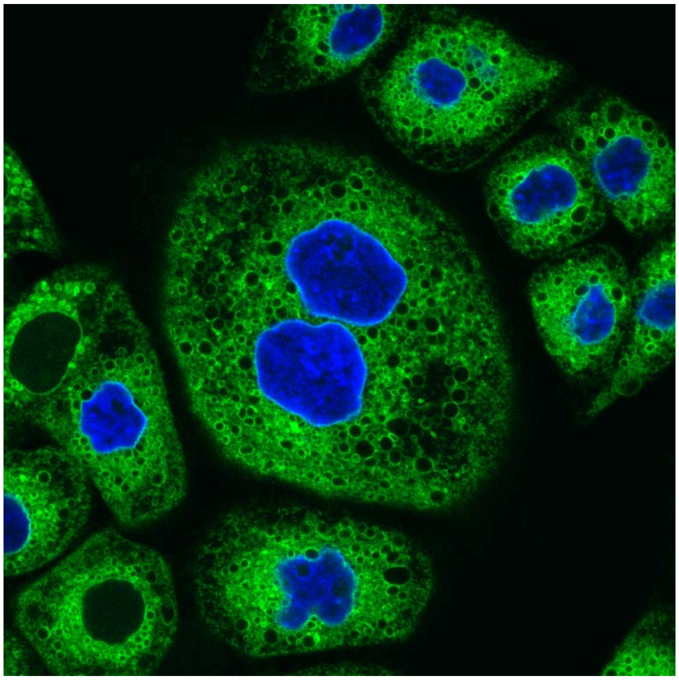

Figure 2.11. Confocal microscopy image of HeLa cells and internalization of fluorescently tagged compound **22** grown in the dark incubator.

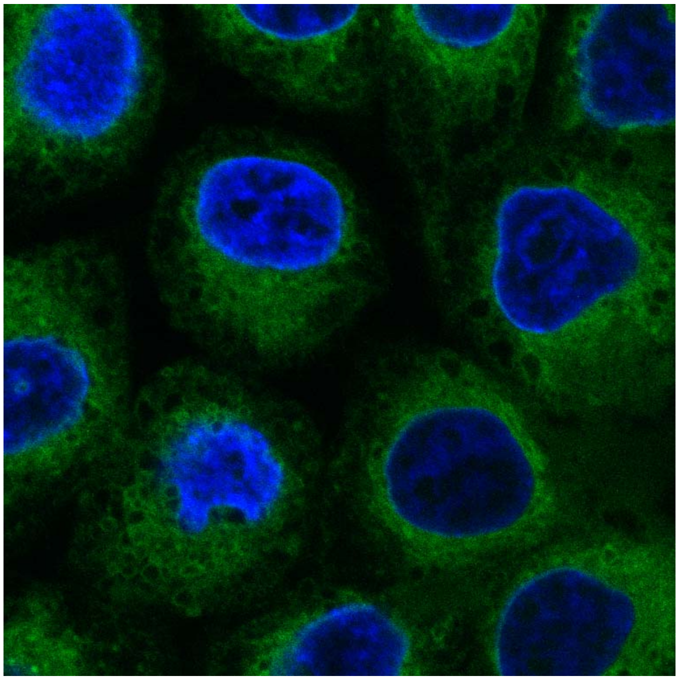

Figure 2.12. Confocal microscopy image of cells treated with labilized benzoyl cyclopentadienide ligand from compound **22**.

As seen in Figures 2.10-2.12, the control cells do not have any green fluorescence after merging green and blue channels, whereas compound **22** and liberated fluorescently-tagged cyclopentadiene compound **22** are uptaken by the cells. Combined with cytotoxicity assay data, these studies suggest that the cytotoxicity of **22** is due to the free iron(II) generated upon irradiation rather than the liberated ligands, as treatment with the photodecomposition products containing the liberated ligands does not affect a cytotoxic response.

4. TEM Image Studies

While confocal microscopy shows that our fluorescent compound is entering cells, the resolution is not sensitive enough to see the organelles or minuscule changes within a cell. We have chosen to use transmission electron microscopy (TEM) techniques in order to image cells at a much higher resolution and sensitivity.[34] HeLa cells were seeded on multiple sterile petri dishes at a density of 5×10^7 cells/well. Cells were then independently treated with benzoyl ferrocene (**5**), 4-pentylbenzoyl ferrocene (**10**), 2,6-dichlorobenzoyl ferrocene (**12**), triphenylphosphine derivative **15**, 1,1'-bis(4-pentyl)benzoyl ferrocene (**16**), and NBD-fluorescently tagged complex **22**, 24 h after seeding. After 24 h of compound addition, media was removed with a pipet and gently washed three times with DPBS, then immersed in Karnovsky's fixative (2.5% glutaraldehyde and 2% paraformaldehyde in 0.15 M sodium cacodylate buffer, pH 7.4). After samples were embedded on copper grids, the cells were imaged using TEM.

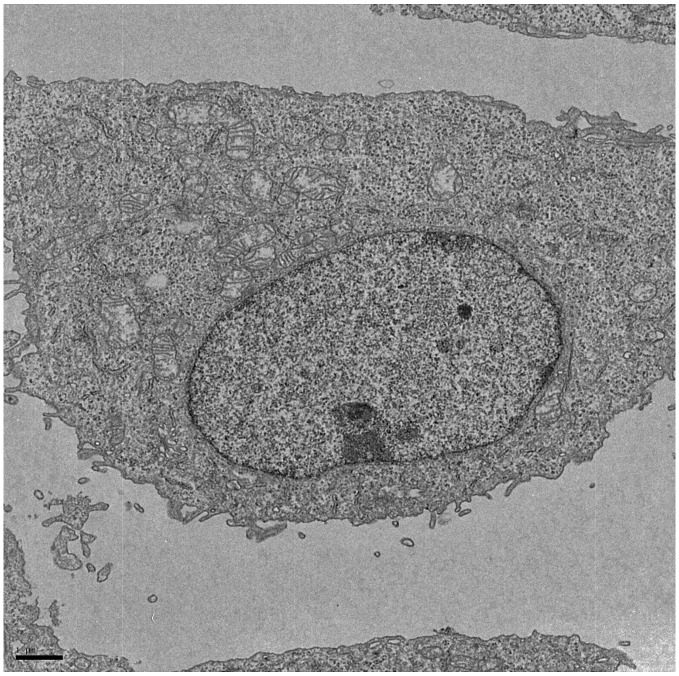

Figure 2.13. TEM image of control HeLa cells.

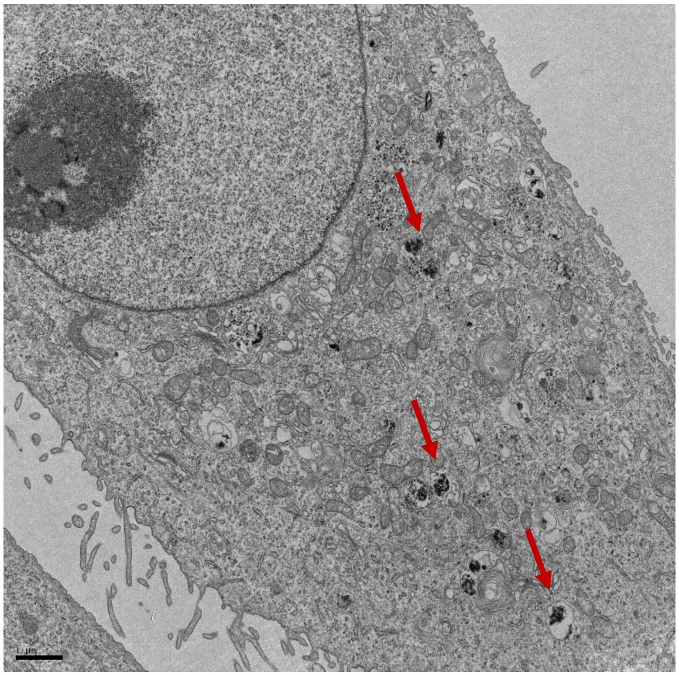

Figure 2.14. TEM image of pentyl derivative **10.**

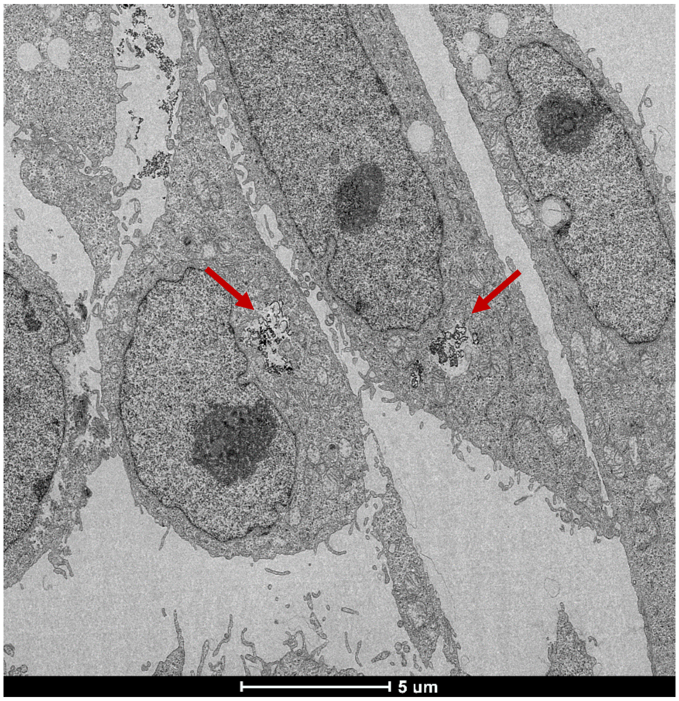

Figure 2.15. TEM image of triphenylphosphine derivative **15**.

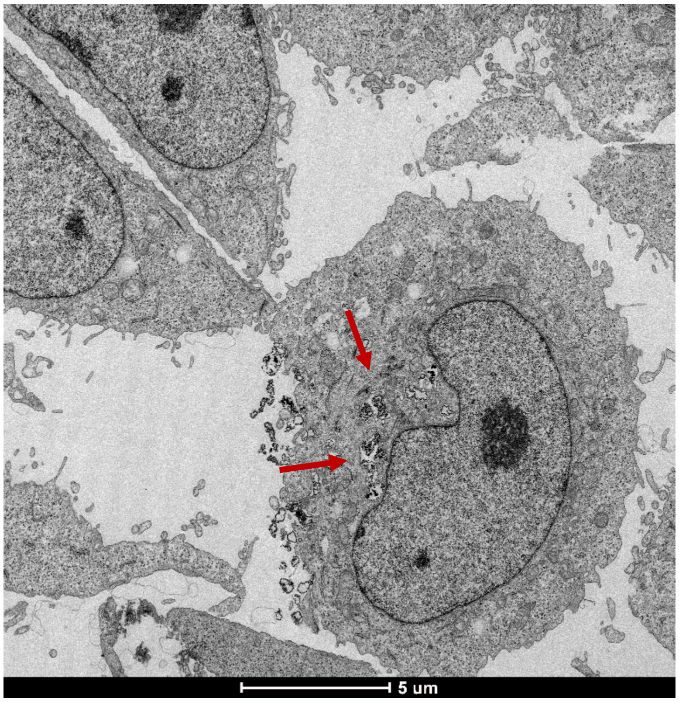

Figure 2.16. TEM image of bis(pentyl) derivative **16**.

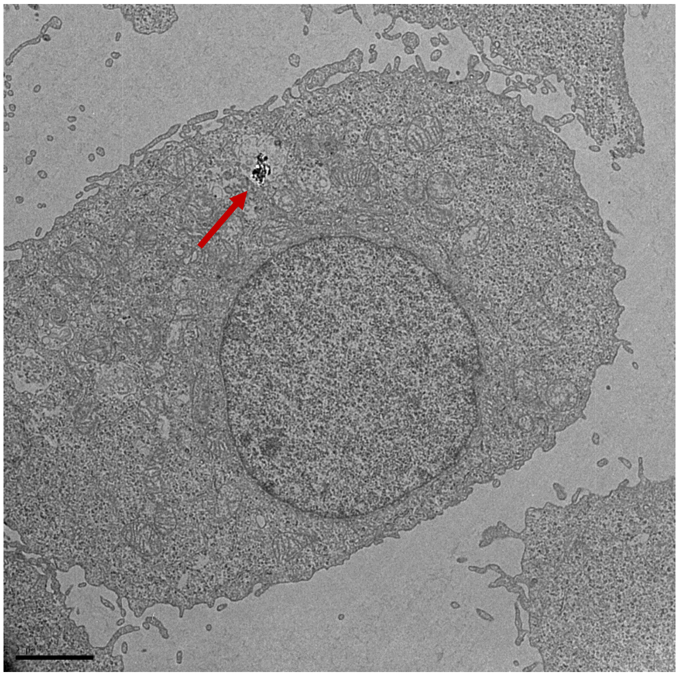

Figure 2.17. TEM image of NBD-tagged complex **22**.

TEM images of the control cell show the phenotype of HeLa cells that were not treated with compound (Figure 2.13). In comparison, cells treated with various compounds show abnormalities; vacuoles containing black particles are shown in Figures 2.14-17. Interestingly, cells treated with benzoyl ferrocene (**5**) and 2,6-dichlorobenzoyl ferrocene (**12**) looked like normal HeLa cells, whereas cells treated with pentyl derivative **10**, triphenylphosphine derivative **15**, bis(pentyl) derivative **16**, and NBD-fluorescently tagged complex **22** displayed pockets of vacuoles (illustrated with red arrows) containing black particles within a 0.5 – 1.0 μm range, possibly our endocytosed compounds. There seems to be a slight correlation between amount of foreign black particles and the cytotoxicity of the complex. The NBD-tagged complex **22**, which exhibits lower cytotoxicity, did not display as many vacuoles of black particles as pentyl derivative **10**, triphenylphosphine derivative **15**, and bis(pentyl) derivative **16**, in HeLa cells as apparent in the TEM images.

5. Iron Uptake Studies

The amount of iron accumulated in HeLa cells following treatment with pentyl derivative **10**, bispentyl deriative **16** and $FeSO_4$ were determined by relating the concentration of iron in cell lysates to the cellular protein concentration. As a control, HeLa cells were not treated with any compound. We utilized inductively coupled plasma optical emission spectrometry (ICP-OES) to detect iron concentration due to the instrument's sensitivity and low detection limit.

HeLa cells were grown in a 150 cm^2 flask until nearly confluent, and then treated with 12 μM solution of each compound in FBS-free media for either 2 or 24 h. The control flask was prepared with an identical concentration of DMSO, since it was necessary to dissolve compound **10** and **16** in DMSO as there is limited solubility in water. The flasks containing $FeSO_4$ also included identical concentrations of DMSO in order to keep conditions consistent. The cells were then harvested for iron and protein analysis. Protein content was determined by the Bradford method.[35] Following lyophilization and treatment with concentrated HNO_3, iron concentration was quantified by ICP-OES, at the UCSD-SIO facility ran by Pat Castillo with assistance from Chris MacIsaac. Experiments were performed in triplicate during different days over a range of a month.

Table 2.3. Average ratio of iron concentration compared to control

Compound	Avg Ratio to Control (Std Dev)
Control	1
$FeSO_4$ 2 h	2.9 (0.5)
$FeSO_4$ 24 h	9.6 (0.6)
Compound 10 2 h	9.7 (0.8)
Compound 10 24 h	11.6 (1.6)
Compound 16 2 h	51.0 (6.3)
Compound 16 24 h	55.0 (10.4)

As anticipated from cytotoxicity studies, the iron content of cells treated with 12 μM concentration of bis(pentyl) derivative **16** had a significantly higher ratio compared to control, with an average uptake of 51 times more iron in 2 h and 55 times more iron in 24 h. However, there was not much difference in iron uptake between incubating the cells with compound **16** for 2 h or 24 h. HeLa cells treated with monopentyl derivative **10** exhibited approximately 10 times more iron after 2 h and 12 times more after 24 h, as compared to control cells. Similar to compound **16**, compound **10** also exhibits no notable iron uptake between 2 h and 24 h. HeLa cells treated with 12 μM of $FeSO_4$ indicates an uptake of approximately 3 times more iron compared to control cells after 2 h or 9 times more iron uptaken after 24 h. While the cells uptake free iron(II), previous cytotoxicity studies in HeLa cells indicated no cell death up to 1 mM, we hypothesize that the cells must have a mechanism to deal with free iron(II) such that it does not participate in detrimental redox chemistry. Aubrey's previous ICP-OES studies of benzoyl ferrocene (**5**) with 60 μM indicated that there was no iron uptaken, so we hypothesize that benzoyl ferrocene is causing cytotoxicity extracellularly, perhaps by affecting the lipid membrane.

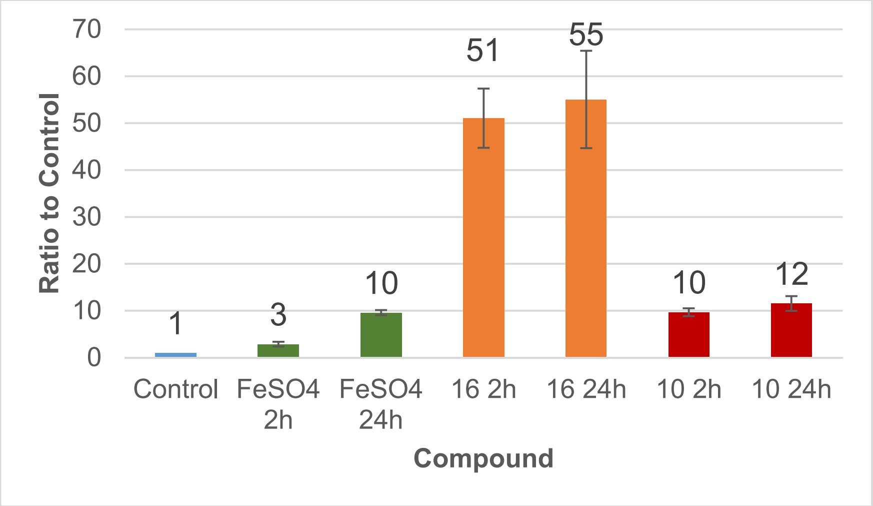

Figure 2.18. Graph comparison of iron uptake for compounds **10**, **16**, and $FeSO_4$.

6. Cytotoxicity of bispentyl derivative 16 with iron chelators and antioxidants

After confirmation that free iron(II) from our photolyzed benzoyl ferrocene derivatives was the most likely cause of cytoxicity, possibly by generation of reactive oxygen species, we decided to test if we could 'rescue' the cells by treating it with an iron chelator. This idea came up in part due to reading a paper by the Chris Chang group wherein they were probing labile iron pools with fluorescent chelators.[36] The Chang group used bathophenanthroline disulfonate to chelate free iron to determine if there was a decrease in their Green/FRET ratio. We sought to test whether addition of bathophenanthroline would cause less cytotoxicity in HeLa cells when added in conjunction with our benzoyl ferrocene derivative. Under our current cytotoxicity mechanistic hypothesis, chelation of free iron should decrease apparent cell death in cells treated with bathophenanthroline disulfonate. Initial cytotoxicity studies with bis(pentyl) complex **16** in HeLa cells were ran since it had the greatest ratio of light to dark cytotoxicity and **16** was our most promising candidate.

Cyotoxicity assays were run under standard protocols, the only difference would be the addition of 100 μM of bathophenanthroline disulfonate (BPS) 4 hours or 7 hours before photolysis. The molarity of bathophenanthroline was determined by running cytotoxicity assays, and a concentration was picked such that there was no cell death, limiting the cytotoxic interference of bathophenanthroline. Cytotoxic assays demonstrated a higher cell viability when BPS was added 7 h prior to photolysis, so with these conditions in hand, the experiment were ran in triplicate. The IC_{50} values with **16** could not be determined due to cell viability around 34% at the solubility limit of 100 μM. We estimate the IC_{50} value to be around 50 μM as the average cell viability was determined as 49% at that concentration. Table 2.4 lists the cytotoxicity data.

Table 2.4. Cytotoxicity of compound **16** with independent treatment of bathophenanthroline and α-tocopherol

Entry	**Estimated IC_{50} (μM) HeLa Light**	**IC_{50} (μM) HeLa Dark**
16 + BPS	~50	>100
16 + α-tocopherol	>100	> 100

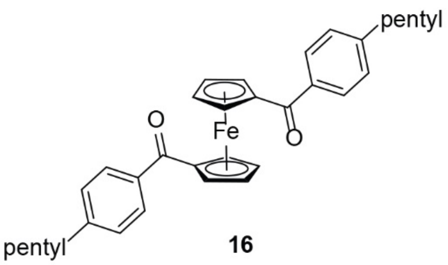

16

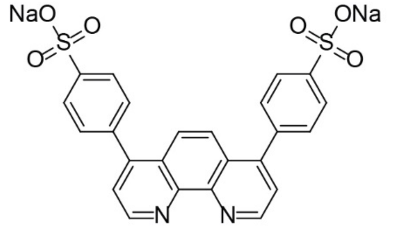

bathophenanthroline disulfonate (BPS)

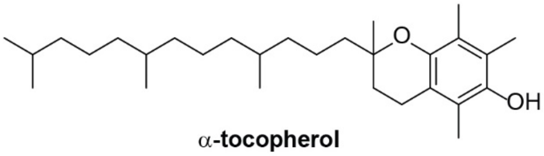

α-tocopherol

We hypothesized that since free iron(II) can generate reactive oxygen species in cells, we could neutralize the effect of benzoyl ferrocene derivative **16** by treating the cells with an antioxidant such as α-tocopherol, which is a relatively inexpensive. After running cytotoxicity assays with α-tocopherol and determining no cytotoxicity up to 1 mM, we treated HeLa cells with various concentrations of compound **16** and a constant 100 μM of α-tocopherol at the same time through standard procedures. Our initial hypothesis of neutralizing the effect of compound **16** proved correct as there was 98-100% cell viability when HeLa cells were treated with both α-tocopherol and compound **16** under both irradiative and dark conditions.

7. Ferrocenyl Chalcones

In our quest to find optimal ferrocenyl derivatives, we sought to test ferrocenyl chalcones due to their ease of synthesis and the speculation that the conjugated properties would lead to a greater absorbance wavelength. Previous literature has also reported on the biological activity of ferrocenyl chalcones in nematodes.[37] The general synthesis of ferrocenyl chalcones is straightforward, and consists of an aldol condensation of ferrocene carboxyaldehyde and the corresponding acetone derivative. Figure 2.19 illustrates the ferrocenyl chalcones synthesized for cytotoxicity assays.

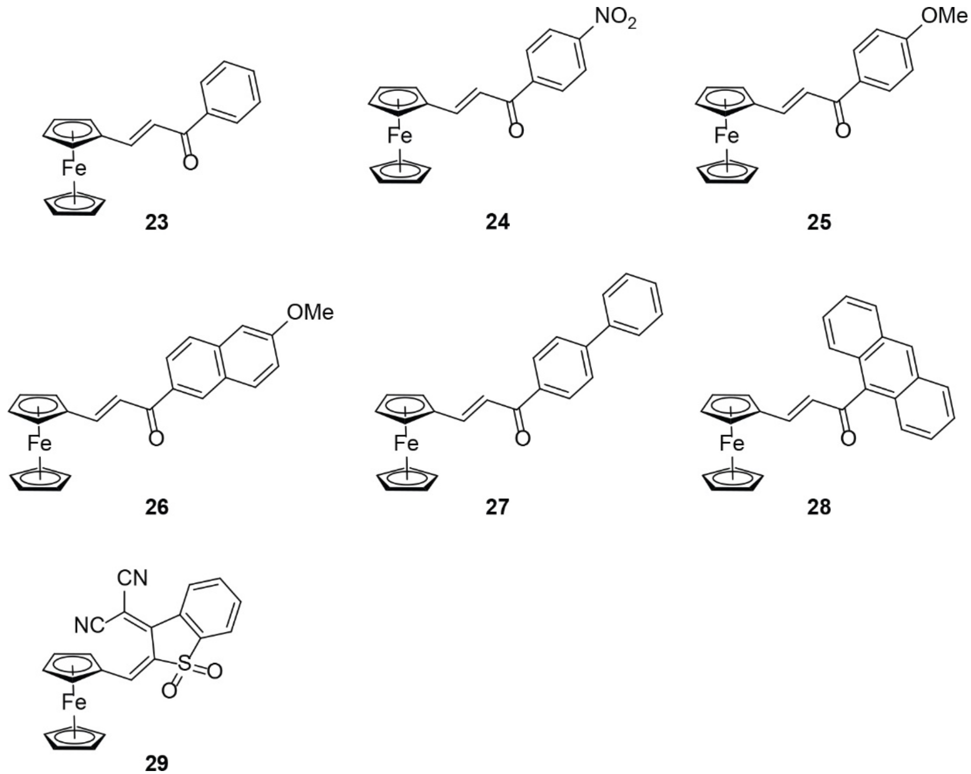

23 **24** **25** **26** **27** **28** **29**

Figure 2.19. Ferrocenyl chalcones synthesized.[37,38]

The only deviation is compound **29**, wherein we used a benzothiophene derivative starting material and the product is not a ferrocenyl chalcone; however the mechanism and condensation reaction is analogous. Unfortunately, our hypothesis of the conjugation in ferrocenyl chalcones lending to compound absorption at a longer wavelength was not true as most of these compounds absorbed around 510 nm, which is not significantly better than benzoyl ferrocene derivatives absorbing around 490 nm. Compound **24** exhibited the highest λ_{max} value at 537 nm, which we have attributed to the incorporation of a nitro group. Compound **28** exhibited a λ_{max} value of 503, which we found surprising considering the conjugated system. X-ray crystallography data (next section) clears up the confusion by illustrating that the pi-system in the anthracene ring is actually perpendicular to our ferrocenyl chalcone moiety. However, while the ferrocenyl chalcones did not have a significantly higher absorption, benzothiophene derivative **29** turned out to have a much greater absorbance at 670 nm.[38]

Table 2.5. UV-Vis absorbance values

Compound	UV-Vis (nm)
23	505
24	537
25	502
26	506
27	505
28	503
29	670

Cytotoxicity assays were run on compounds **23-29** in HeLa cells. Only compounds **23**, **28**, and **29** exhibited any biological activity in HeLa cell lines. Compound **23** has an IC_{50} value of 30.3±6.1 μM under irradiation conditions while exhibiting no cytotoxicity up to its solubility limit of 75 μM under dark conditions. While the light IC_{50} value was not ideal, the lack of cytotoxicity in the dark was very promising, so we ran assays on the rest of or ferrocenyl chalcones. Compound **28** exhibited an IC_{50} value of 9.9±2.3 μM in the light and no toxicity in the dark up to the solubility limit of 25 μM, which turned out to be one of the more promising candidates. Compound **29** has very similar IC_{50} values in the light and dark, 10.8±1.8 and 11.3±1.8 respectively, which indicates that the compound is toxic, without irradiation.

Table 2.6. IC_{50} values of select ferrocenyl chalcones

Compound	HeLa Light (μM)	HeLa Dark (μM)
23	30.3±6.1	>75
28	9.9±2.3	>25
29	10.8±1.8	11.3±1.8

8. X-Ray Crytallographic Analyses

X-ray quality crystals of compounds **18**, **19**, and **28** were grown by slow diffusion of hexanes into DCM. Refinement (full data tabulated in Appendix) gave the structures shown in **Figures 2.20 – 2.22**. Selected bond distances and angles are listed in **Table 2.7**.

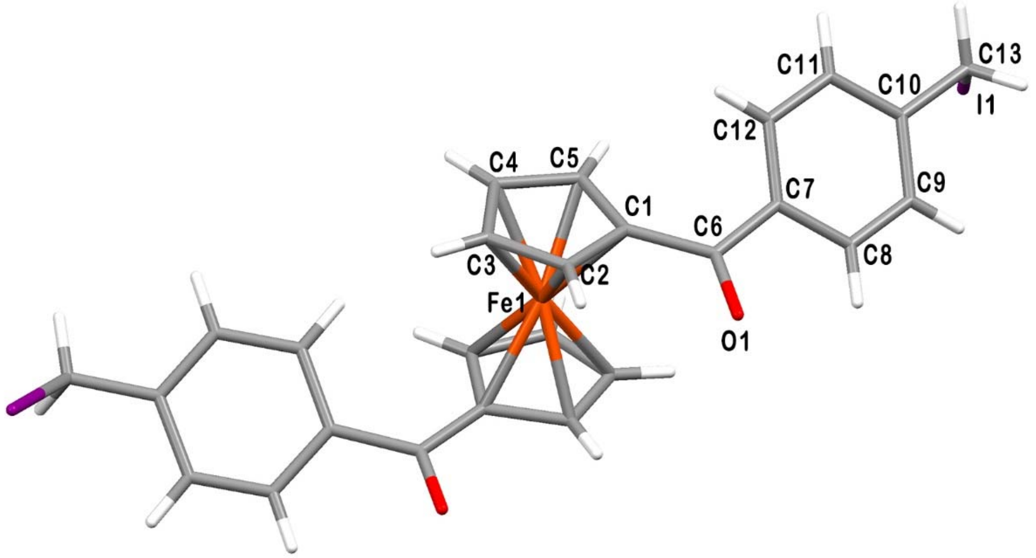

Figure 2.20. X-ray crystal structure of compound **18**.

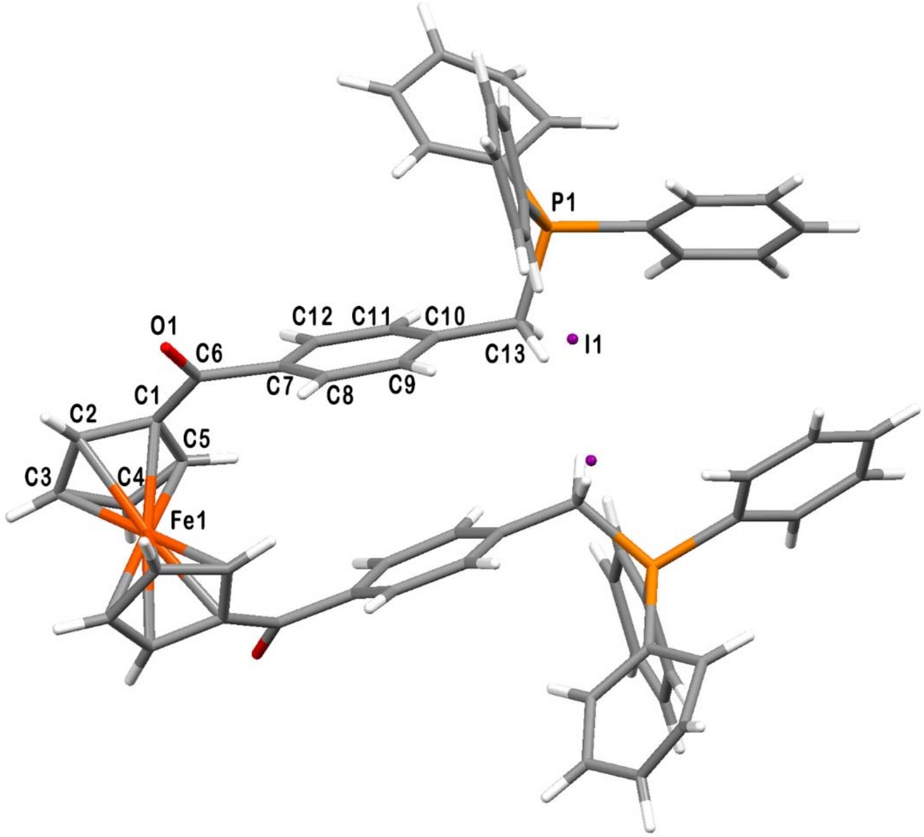

Figure 2.21. X-ray crystal structure of compound **19**.

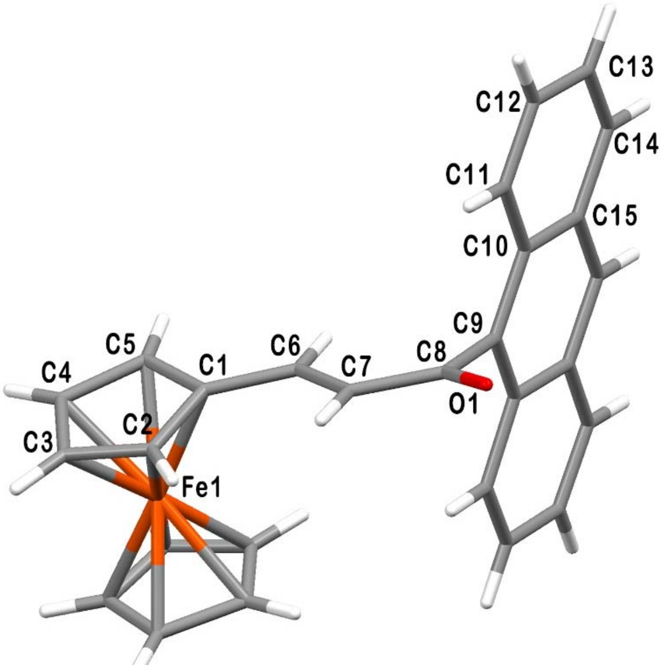

Figure 2.22. X-ray crystal structure of compound **28.**

Table 2.7. Selected metrics for X-ray crystal structure of **18**, **19**, and **28**.

Compound	C2-C1-C6-O1 (°)	O1-C8-C9-C10 (°)
18	10.80	n.a.
19	-6.52	n.a.
28	n.a.	-70.96

n.a. – not applicable

C. Discussion

Cellular metabolism is a complex process with a highly evolved mechanism that can sense ferrous and ferric ion levels in the local environment, allowing for sensitive control of iron homeostasis.[39-40] Much of the ferrocene-based antitumor literature feature mimics of known organic drugs, synthesized and tested with hopes that addition of a ferrocenyl moiety can modify the lipophilicity in order to enhance biological activity.[5] The appeal of utilizing ferrocene-based anticancer drugs is twofold: (1) iron is fairly nontoxic up to a certain limit compared to other transition metal drugs such as platinum, and (2) iron(II) can be oxidized to iron(III) by endogenous hydrogen peroxide to generate the highly toxic hydroxyl radical via the Fenton Reaction (**Equation 2-2**). The hydroxyl radical is a highly toxic species due to its rapid abstraction of hydrogen atoms from the nearest biomolecule – which could be either the lipid bilayer or the nucleus or other biomolecules – resulting in cell death.[41-43]

Equation 2-2: $Fe^{2+} + H_2O_2 \rightarrow Fe^{3+} + \bullet OH$

Based on what is currently known about iron homeostasis in biological systems, and inspiration from Kutal's work on benzoyl ferrocene, we set out to design and optimize new iron-based organometallic complexes for a new mode of photodynamic therapy. By masking iron(II) as an organometallic sandwich complex, we speculated that we could bypass cellular recognition of iron. We hypothesized that in the absence of light, the electron-withdrawing ligands would stabilize the electron-deficient central iron atom from oxidation. Following cellular uptake of the ferrocene derivatives in cancer cells, exposure to visible light (>450 nm) would trigger the release of solvated iron(II) from the appended ligand set. While iron(II) is nontoxic by itself due to the highly-evolved cellular mechanism that deals with excess free iron in the cell, we speculated that we could sneak an excess of iron into a cell by masking the metal as a covalent compound. The nature of the appended ligand set on the iron would play a role in the lipophilicity of the molecule and may increase cellular uptake, and it could also play a role in promoting cell death independently of the iron. Once accumulation of the iron complex was accomplished intracellularly, irradiation of the targeted tumor cells would facilitate molecular decomposition, releasing free iron(II). Untargeted biological tissues would also uptake the synthesized molecular iron complexes and have a potential excess of iron, but these covalent iron compounds would exist as benign molecules without effect until photoactivated, thus affecting a measure of spatiotemporal control that could prove to be an effective treatment in an oncological setting. By utilization of photodynamic therapy, we could promote the sudden and rapid onset of a huge increase (50 times increase with 12 μM of **16**) in cellular iron, creating conditions for the rapid and perhaps catalytic generation of reactive oxygen species that could promote cellular apoptosis. Iron(II) can rapidly react with endogenous hydrogen peroxide, generating the highly toxic hydroxyl radical, or react directly with oxygen in an electron-transfer reaction to generate iron(III) and superoxide. Superoxide in cells can be broken down by the enzyme superoxide dismutase into hydrogen peroxide and oxygen[43], which would provide the necessary reagents for the Fenton reaction, even in the absence of endogenous hydrogen peroxide.[41] In this way, the organoferrous complexes can release ferrous catalysts that can be continually regenerated by reaction with endogenous ROS species in the Haber-Weiss cycle within cells. This mode of action utilizing the photochemical properties of ferrocenyl derivatives can lend itself to a new photodynamic therapy pathway.

Photodynamic therapy (PDT) began in the 1960s after Lipson and Baldes reported on a porphyrin mixture compound developed by Schwartz wherein the compound contained phototherapeutic potentials.[44-46] Since then, studies on photosensitizers and PDT have proliferated.[47] Traditional PDT involves excitation of a ground state photosensitizer (PS) to generate a short-lived photoexcited state that can undergo two types of reactions.[48] In a Type I reaction, the excited PS undergoes a direct redox reaction with the substrate to give a radical anion that readily reacts with oxygen to form ROS species such as superoxide anion. This can further generate hydrogen peroxide and hydroxyl radical. The excited PS can also abstract a hydrogen atom from nearby biomolecules, leading to oxygenated products. In a Type II reaction, the triplet excited state PS transfers energy directly to molecular oxygen, generating a highly toxic singlet oxygen species which oxidizes nearby biomolecules easily, such as unsaturated lipids.[49-50] The half-life of singlet oxygen in the cell is very short (< 0.05 μs) which accounts for its small radius of action (0.02 μm). Under traditional PDT, continuous irradiation is required for generation of the cytotoxic species. In contrast, we envision our organoferrous complexes as being longer-lived ferrous catalysts capable of ROS-generation even after irradiation conditions, which would proceed via the Haber-Weiss reaction (Figure 2.3), and which could continue to function even in the absence of further irradiation (Figure 2.23).

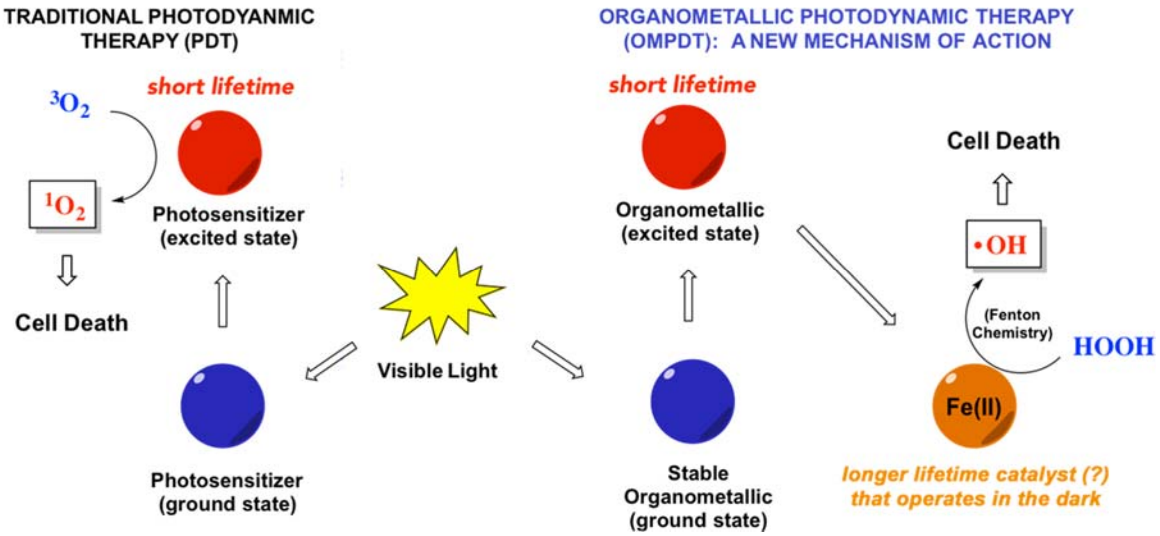

Figure 2.23. Traditional PDT and a new mechanism for PDT.

With these precedents in mind, Marissa Aubrey first synthesized a variety of benzoyl ferrocene derivatives.[24] She had determined that 4-pentylbenzoyl ferrocene (**10**) and 4-cyclohexylbenzoyl ferrocene (**11**) were the most promising candidates for PDT antitumor treatment, however, there were still many questions left unanswered. Why were certain benzoyl ferrocenes exhibiting similar cytotoxicity under light and dark conditions? Were these compounds being uptaken by cells? Is cytotoxicity due to free iron(II) or the ligand(s)? Can we synthesize more efficacious ferrocenyl derivatives? These were some questions we had set out to answer by synthesizing more derivatives, running cytotoxicity assays, imaging cells and running iron uptake studies.

Cytotoxicity assays were performed on compounds **15**, **16,** **19**, and **22** (shown below Table 2.8) initially in HeLa cells in order to compare to lead compounds **10** and **11** as well as compounds **5** and **12**. **Table 2.8** lists all the compounds for ease of comparison, with the exception of compound **19** because an IC_{50} value was not determinable. Regarding compound **19**, we do know that the compound is highly toxic as it had 90% cell death at a concentration of 2.5 μM; however, such and such prevented the determination of precise

IC50 values for this particular complex. Cytotoxicity assays were then performed in Caov3 cells with compounds **10** and **16,** as compound **16** presented as the best lead compound determined from the HeLa cell studies. Compounds **10**, **11**, **16** and **22** exhibited a huge difference between light and dark toxicity (from 3-fold difference for **22** to 55-fold difference for **16**), whereas compounds **5**, **12**, and **15** do not display any significant differences between light and dark conditions.

Table 2.8. Cytotoxicity of benzoyl ferrocene derivatives

	Light IC_{50} Values (μM)			**Dark IC_{50} Values (μM)**		
Entry	**HeLa**	**A549**	**Caov3**	**HeLa**	**A549**	**Caov3**
5	30.8 (3.8)	43.5 (2.0)	n.d.	33.5 (5.2)	41.5 (2.7)	n.d.
10	12.8 (1.8)	9.5 (2.7)	10.9 (2.3)	57.9 (5.0)	49.0 (6.7)	71.0 (4.5)
11	8.7 (2.3)	6.8 (2.4)	n.d.	>40	>40	
12	40.5 (2.5)	33.2 (4.3)	n.d.	47.1 (3.1)	36.1 (5.2)	
15	5.8 (0.3)	n.d.	n.d.	12.4 (2.7)	n.d.	n.d.
16	16.8 (2.3)	n.d.	1.8 (0.2)	>100	n.d.	>100
22	31.2 (0.9)	n.d.	n.d.	>100*	n.d.	n.d.

n.d. – values were not determined as cytotoxicity was not tested in these cell lines. *exhibited 63% cell viability at 100 μM.

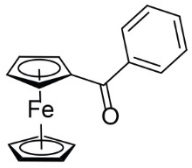

5

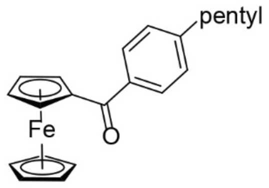

10

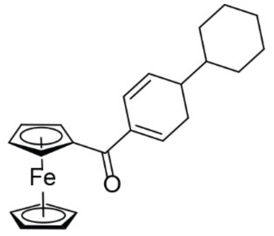

11

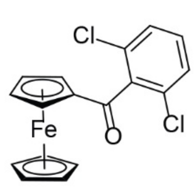

12

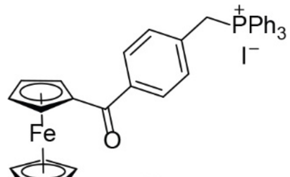

15

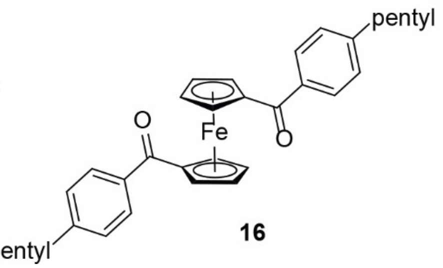

16

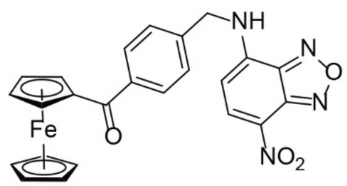

22

After running these assays, we suspected that certain benzoyl ferrocenes were not getting into the cells as the light and dark cytotoxicity was the same, or some other mechanism was predominant which caused it to differ it from the compounds that exhibit a huge difference in dark vs. light toxicity. We speculate that the triphenylphosphine derivative **15** does not have a huge difference between light and dark cytotoxicity because it contains a mitochondrial targeting substituent, and the highly sensitive redox environment of the mitochondria is disrupted by this iron complex, leading to cell death even in the dark.[25,51] To elucidate why benzoyl ferrocene (**5**) and 2,6-dichlorobenzoyl ferrocene (**12**) exhibit no cytotoxic difference between dark and irradiation conditions (here forth referred to as phototoxicity ratio), whereas compounds **10** and **11** do have a marked difference in phototoxicity, Marissa ran lipophilicity studies on those compounds to determine if the cells were lipophilic enough to cross the cell membrane barrier.[24] In the lipophilicity studies, standards with known lipophilicity values were plotted against retention values using HPLC analysis. This gave a standard linear plot such that the unknown lipophilicity values of compounds **5**, and **10-12** could be determined. The lipophilicity values along with the phototoxicity ratio are listed in **Table 2.9**.

Table 2.9. Lipophilicity (Log P) and Phototoxicity Ratios

Compound	Log P	$IC_{50\text{-dark}}/IC_{50\text{-light}}$
5	3.3	1.1
10	5.62	4.5
11	5.54	>4.6*
12	3.86	1.2

*$IC_{50\text{-dark}}$ value was not able to be determined due to solubility limit of 40 μM.

As we see from Table 2.9, there is a correlation between having a higher lipophilicity and an increase in phototoxicity ratio. We speculated that since benzoyl ferrocene (**5**) and 2,6-dichloro complex **12** have a phototoxicity ratio of approximately 1, with lipophilicity values of around 3 and 4, they might not be entering the cells. It is possible that benzoyl ferrocene **5** and the dichloro substituent **12** is causing antiproliferative activities on the outside cellular membrane. Pentyl complex **10** and cyclohexyl compound **11** both have higher lipophilicity values and have an increase in phototoxicity, which we hypothesized is due to both compounds crossing the cell membrane leading to detrimental redox chemistry, more so in the light than in the dark. We suspect that the cause of cell death in the dark with pentyl derivative **10** could be due to the highly oxidative environments of cancer cells[23,52] which could have oxidized the benzoyl ferrocene derivative. Compound **10** has an $E_{1/2}$ potential of 0.251 V[24] compared to the harder-to-oxidize bis(pentyl) derivative**16** which has an $E_{1/2}$ potential of 0.441 V[24] and exhibits no dark cytotoxicity up to 100 μM. This higher oxidation potential and lack of dark cytotoxicity for the bis(pentyl) derivative **16** is logical as there are now two electron-withdrawing groups on our ferrocene derivative. We suspect that there may be an oxidation potential number somewhere between 0.251 V and 0.441 V such that the compound will not oxidize in the cells until triggered by photodecomposition.

In order to validate our hypothesis that benzoyl ferrocene (**5**) and 2,6-dichlorobenzoyl ferrocene (**12**) were not entering cells, while pentyl derivative **10** was, we wanted to utilize transmission electron microscopy (TEM) to examine possible changes inside the cell. Newly synthesized compounds triphenylphosphine derivative **15**, bis(pentyl) derivative **16**, and NBD-fluorescently tagged **22** were also used in TEM studies. HeLa cells were grown on petri dishes for 24 h before addition of compounds. The compounds were then incubated independently at a concentration below their dark IC_{50} to ensure that cells were alive for imaging. After imaging, cells treated with benzoyl ferrocene (**5**) and 2,6-dichlorobenzoyl ferrocene (**12**) exhibited normal characteristics compared to the control HeLa cells treated with no compounds. However, cells treated with pentyl complex **10**, triphenylphosphine derivative **15**, bis(pentyl) complex **16** and fluorescently tagged compound **22** deviated from the control. HeLa cells treated with those four compounds had varying amounts of foreign black particles enclosed in vacuoles. We speculate that those black particles could be our compound that was endocytosed into the cells and aggregated together. Interestingly, cells that displayed greater amounts of products inside the vacuoles of cells, have a rough correlation to greater cytotoxicity. Compounds **10**, **15**, and **16** showed greater amounts of material in vacuoles inside the cells whereas compound **22** did not exhibit as much, which corresponds to their greater toxicity compared to **22**. The results from our TEM imaging indicate that the compounds endocytosed by the cell lead to higher phototoxicity values than benzoyl ferrocene (**5**) and 2,6-dichlorobenzoyl ferrocene (**12**).

Besides using TEM imaging to visualize cellular changes after addition of the ferrocene derivatives, we employed confocal microscopy as an additional analytical tool. One limitation of TEM imaging is an inability to visualize cellular changes if the molecular weight for the benzoyl complexes is too low. We sought to discriminate between ligand-promoted cell death and iron-promoted cell death. If ligand-induced cell death could be ruled out, then *in situ* generated Fe(II) would be implicated as the causative ROS-generating species responsible for cell death. In order to determine if the ligand was the cytotoxic species, we first determined the phototoxicity ratio of NBD-fluorescently tagged complex **22**, which turns out to be greater than 3.2, as there was no dark cytotoxicity up to the solubility limit of 100 μM. We then sought to compare those results to the cytotoxicity of the fluorescent ligand of compound **22**. We examined the cytotoxicity of the photo-decomposition products generated upon photolysis of **22**. NBD fluorescently tagged complex **22** was photolyze 3 h before addition to HeLa cells. Previous NMR studies performed by Marissa Aubrey on 4-pentylbenzoyl ferrocene (**10**) confirmed Kutal's experiments which indicated that the benzoyl ferrocene ligands cleanly photodissociate from the iron center.[17,24] We suspected that the free iron(II) in the photoproduct would not interfere with cytotoxicity, as previous cytotoxicity with $FeSO_4$ indicated no biological activity. The standard cytotoxicity assay protocol was employed for HeLa cells treated with the photoproducts of **22**, and the results indicated no biological activity. To ensure that the fluorescent ligands of the photolyzed products were entering the cell, and to confirm nontoxicity of the ligand, we utilized confocal microscopy to image cells treated with the fluorescent photoproduct of **22**. Figure 2.12 illustrates that the fluorescently tagged ligands are indeed uptaken by the cells when compared to control cells in Figure 2.10. Confocal images of compound **22** (Figure 2.11) also indicated that the benzoylferrocene derivative was taken up by the cells. We do not know whether the free cyclopentadiene ligand is endocytosed by the cell. However, we were unconcerned about cyclopentadiene as a cytotoxic species as previous reports indicate LC_{50} values of 230 μM for mouse inhalation and 590 μM for rat inhalation.[53] Cytotoxicity assays ran on benzoyl ferrocene derivatives did not exceed a concentration of 100 μM. We therefore conclude from the confocal microscopy images and cytotoxicity assays that the benzoyl ferrocene derivatives are taken up by the cells and that cell death is due to the release of free iron(II) rather than the action of the dissociated ligand.

To definitively determine whether our ferrocenyl complexes were entering the cells, we decided to measure the iron concentration inside cells with inductively coupled plasma atomic emission spectroscopy (ICP-OES) of select ferrous compounds. Marissa Aubrey had originally chosen benzoyl ferrocene (**5**), which exhibits a similar lipophilicity profile to 2,6-dichlorobenzoyl ferrocene (**12**), and 4-pentylbenzoyl ferrocene (**10**), which exhibits a similar lipophilicity profile to 4-cyclohexylbenzoyl ferrocene (**11**), and $FeSO_4$ to compare for extra iron accumulation in HeLa cells. We then further expanded upon this by running experiments with pentyl derivative **10**, bis(pentyl) derivative **16**, and $FeSO_4$ to compare to control HeLa cells with no compound. To account for the difference in biomass between samples, the iron concentration in the cell lysates was related to the protein concentration of each sample determined by the Bradford Assay.

We first determined the protein concentration of the cell lysates by a modified method of the Bradford assay, a common biochemical technique wherein the UV-Vis absorbance of coomassie brilliant blue dye is measured upon binding to protein.[35] In a traditional assay, a linear calibration curve is determined utilizing known protein concentration standards. The UV-Vis absorption at 590 nm is measured and plotted against the protein concentration to generate a linear standard curve. However, this method often displays considerable deviations from linearity due to spectral overlap and interference. The dye is present in several forms under the assay conditions, leading to potential absorbance maxima at 470, 590 and 650 nm. Additional deviations can occur as the concentration of the reagent decreases as more dye is bound to the protein sample. In 1996, Zor reported that the accuracy of the Bradford assay is improved significantly by reducing the background signal due to the unbound dye and dye-protein complex equilibrium.[54] Independent measurement of absorbance at 450 and 590 nm and calculation of the A_{590}/A_{450} ratio produces linearity over a wider concentration range, allowing for detection down to 50 ng of bovine serum albumin, the standard protein used for the calibration curve.

Using Zor's modification of the Bradford assay we created a standard calibration curve using bovine serum albumin solution (see Experimental section). We were then able to determine our unknown protein concentrations by utilizing the absorbance values. Once the protein concentration was determined for each unknown compound and the control HeLa cells, the concentration of iron in the cell lysates was determined by ICP-OES analysis. The iron concentration was then related to the protein concentration in each sample to determine iron accumulation in the cells. The number from the various compounds were then compared to the control cell iron concentration as a ratio. Table 2.10 lists the ratios with compounds when Marissa Aubrey ran iron uptake studies with 60 μM of iron complexes with compound incubation period of 2 h and Table 2.11 lists the ratios of recent studies with 12 μM of iron complexes with compound incubation for 2 and 24 h.

Table 2.10. Previous Iron Uptake Results by ICP-OES

Complex	Average Fe**	Ratio to Control
Control (H_2O)*	345.7	1
Control (DMF)*	325.9	1
5	415.8	1.3
10	6157	18.9
$FeSO_4$	6996	20.2

*two control cells were grown because compound **5** and **10** were diluted with DMF, while $FeSO_4$ was diluted with H_2O; control cells were treated with the same concentration of DMF or H_2O and ratios of $FeSO_4$ determined with control (H_2O) while **5** and **10** were related to control (DMF). **ng Fe/mg of protein

Table 2.11. Recent Iron Uptake Results by ICP-OES

Complex (time incubated)	Average Fe Uptake*	Ratio to Control
Control	82	1
10 (2 h)	802.03	9.7
10 (24 h)	956.42	11.6
16 (2 h)	4220.76	51.0
16 (24 h)	4550.14	55.0
$FeSO_4$ (2 h)	238.63	2.9
$FeSO_4$ (24 h)	794.48	9.6

*ng Fe/mg of protein

Aubrey had previously determined that after an incubation period of 2 h, benzoyl ferrocene had not been uptaken by the cells, whereas cells treated with pentyl derivative **10** and iron sulfate indicate a 20-fold increase. Later iron uptake studies using 12 μM of iron complexes were conducted in order to facilitate a comparison between the amount of bis(pentyl) derivative **16** relative to monopentyl complex **10** and iron sulfate. Compounds were incubated for either 2 h or 24 h, to determine whether the concentration of iron changed as cells are incubated for 24 h with the complex before photolysis, and a change could affect the best time to photolyze cells. The results indicate that for the 4-pentylbenzoyl ferrocene (**10**) and 1,1'-bis(4-pentyl)benzoyl ferrocene (**16**), there was slight, nearly negligible, increase in iron uptake between 2 h and 24 h compared to the control, whereas cellular uptake of iron sulfate was increased. The 5-fold increase of iron in bis(pentyl) derivative **16** compared to pentyl derivative **10** was surprising but expected as biological assays have indicated compound **16** is more cytotoxic than **10**. Along with TEM and confocal imaging, these iron uptake studies suggest that while benzoyl ferrocene (**5**) is cytotoxic, it is not due to intercellular redox chemistry. We hypothesize this to be true for compound (**12**) as well due to its similar lipophilicity value. We can also conclude from these iron uptake studies that bis(pentyl) derivative **16** is uptaken by cells more than pentyl derivative **10**, resulting in a more cytotoxic complex in the light. The lack of dark cytotoxicity with complex **16** suggests that while these compounds are intracellular, the high oxidation potential of the molecular complex does not allow it to participate in detrimental redox chemistry that would lead to ROS.

After obtaining evidence that the benzoyl ferrocene derivatives uptaken by the cells caused cytotoxicity due to the free iron(II), we wanted to test whether we could rescue these cells using an iron chelator or a lipid soluble antioxidant such as α-tocopherol. Cytotoxicity studies with bathophenanthroline disulfonate (BPS) and α-tocopherol were performed on lead compound **16** as it had the highest phototoxicity ratio with a decent IC_{50} value in the light with HeLa cells. The cytotoxicity results of 1,1-bis(4-pentyl)benzoyl ferrocene (**16**) with BPS indicate that while BPS is a good iron chelator, it was unable to stop the redox of all free iron generated by phototolysis. There was still 50% cell viability at a concentration of 50 μM of compound **16** and 100 μM of BPS. Optimal time and concentration to add BPS was determined such that it would not chelate to native intracellular free iron that is vital for function. This turned out to be 7 h before photolysis and 100 μM of BPS, as determined by independent cytotoxicity assays. Treatment of HeLa cells with various concentrations of compound **16** and 100 μM of α-tocopherol indicated no cell death up to 100 μM of compound **16**. We propose that the antioxidant properties of α-tocopherol[55] were able to negate the detrimental redox chemistry that free iron(II) lends itself to in cells. This further confirmed our hypothesis that ferrous ion can generate ROS in the cells that lead to cellular death.

In our quest to design a more optimal benzoyl ferrocene derivative we looked to synthesize ferrocenyl chalcones **23-28** and the mechanistically analogous compound **29**. We had hoped that extended conjugation would lead to a significant increase in UV-Vis absorption as the benzoyl ferrocene derivatives are currently absorbing around 490 nm. Most drugs for photodynamic therapy are greater than 600 nm.[56] Unfortunately, most compounds we synthesized had UV-Vis absorbance values around 500 nm, with the exception of compound **29** with an absorbance of 670 nm. Surprisingly, anthracene derivative **28** did not have a longer wavelength absorbance with its conjugated system.

However, X-ray crystal structures revealed that the anthracene moiety is not in conjugation with the rest of the ferrocenyl moiety, and instead is nearly perpendicular with a torsion angle from O(1)-C(8)-C(9)-C(10) of 71°. While these compounds did not have ideal UV-Vis absorbance values, we still decided to run cytotoxicity assays to see if there was any biological activity. Interestingly, ferrocenyl chalcone **23** and nitro derivative **28** displayed cytotoxicity values of 30.3 and 9.9 µM under irradiation conditions respectively, with no cytotoxicity in the dark up to the solubility limit of 75 and 25 µM respectively. Compound **29** displayed similar cytotoxicity values under light and dark conditions, with IC_{50} values of 10.8 µM and 11.3 µM respectively. We postulate that this could be due to cyano-functional groups, or the thiophene structure. The electronic potential could also lend itself to unwanted side reactions.

D. Conclusion

Significant progress has been made toward establishing the characteristics needed to make benzoyl ferrocenes more cytotoxic under irradiative conditions, while remaining benign under non-irradiative conditions. This improved photodynamic index is an essential feature in developing a redox-capable PDT pro-drug that could be useful and effective in clinical studies. Utilizing knowledge about the oxidation potential and lipophilicity studies, we can further design and synthesize even better molecules for PDT utilizing this new methodology. We think that if we can design a compound with an oxidation potential above 0.441 V, we would be able to proscribe the cytotoxicity of the organoferrous drugs in the dark. We speculate that there must be some cut-off oxidation potential of our derivatives between 0.251 V and 0.441 V such that benzoyl ferrocene derivatives will not lend themselves to unwanted redox chemistry until irradiation triggers the release of free iron(II). We speculate that if benzoyl ferrocene derivatives have a lipophilicity value above 5.5, it will be able to enter cells without assistance of a targeting agent. We hypothesize that there is a possible lipophilicity value between log P 3.86 and 5.54 such that the ferrous complex can cross the cell membrane.

We have illustrated in this chapter through cytotoxicity assays, TEM imaging, confocal microscopy and ICP-OES studies that the benzoyl ferrocene derivatives which are uptaken by the cells exhibit greater cytotoxicity in the light than in the dark. By tuning the properties of our benzoyl ferrocenes through different functionalization, we were able to synthesize bis(benzoyl) ferrocene derivative **16** with greater cytotoxicity in the light, and no cytotoxicity in the dark. From these experiments, it's highly possible that the cytotoxic properties of benzoyl ferrocene (**5**) and 2,6-dichloro derivative **12** are due to extracellular interactions on the cellular membrane surface, as lipophilicity values and TEM imaging indicate no cellular uptake. Iron uptake studies with benzoyl ferrocene (**5**) also indicate no extra intercellular iron when compared to the control. We hypothesize that since iron sulfate displayed no adverse biological affects to cell proliferation, the masking of iron(II) as an organometallic sandwich complex for cellular uptake is crucial to bypass cellular recognition of iron. In this way, we can spatiotemporally disrupt iron homeostasis utilizing a new method of photodynamic therapy to treat cancer cells.

While we have made great strides with the photochemical and biological activities of our benzoyl ferrocene derivatives, there are still a multitude of studies to be performed. One of our main goals is to determine the magnitude of ROS-generation in cells after photolysis and incubation of our compound in cancer cells, which is currently an active area of study. We are also planning to test our compounds *in vivo* in mice in order to determine the lethal dosage in mammalian species. It would be interesting to encapsulate our fluorescently tagged molecule **22** in porous silicon nanoparticles and track where our compound is in mice. Finally, the terminal endpoint of these studies remains the synthesis and identification of an iron(II)-generating covalent compound that displays a target wavelength of greater than 600 nm, high quantum yield, high cellular uptake, and a difference in cytotoxicity between radiative and non-radiative conditions of at least several orders of magnitude.

E. Experimentals

General Methods

All synthetic reagents were purchased from Aldrich, Fisher Scientific, or Alfa Aesar, and were used without further purification. All solvents for anhydrous reactions were obtained from Fisher scientific and dried on alumina columns prior to use. All reactions were performed under N_2 or argon using standard Schlenk techniques unless otherwise noted. Solvents used for chromatography were ACS technical grade and used without further purification. Water (18.2 μΩ/cm) was filtered through a NANOPure DiamondTM (Barnstead) water purification system before use. All ^1H NMR and ^{13}C NMR spectra were recorded on a Varian Mercury Plus 400 MHz NMR spectrometer or a Varian VNMRS NMR spectrometer equipped with a 500 MHz XSens Cold Probe. Deuterated solvents were purchased from Cambridge Isotopes. Chemical shifts are reported as δ in units of parts per million (ppm) referenced to the residual solvent peak. Coupling constants are reported as a *J* value in Hertz (Hz). High-resolution mass spectrometry analysis was performed by the UCSD Chemistry and Biochemistry Molecular Mass Spectrometry Facility on a ThermoFinnigan MAT900XL mass spectrometer with an ESI source. UV-Vis absorption spectra were collected with a Shimadzu UV 3600 and plotted using Excel. Cyclic voltammetry measurements were performed by Dr. Mohand Melaimi from the Bertrand group at UCSD at room temperature in acetonitrile under an argon atmosphere with a CH Instrument potentiostat (CHI620e) with freshly polished Pt disk working electrode, a Ag wire counter electrode, a Ag/Ag+ pseudo reference electrode, and $[nBu_4N][PF_6]$ (0.1 M) as electrolyte. Potentials were then calibrated against the Fc/Fc+ couple as an internal standard and plotted in Excel. FTIR spectra were recorded on a

Thermo-Nicolet iS10 FTIR spectrometer. Samples were prepared as a thin film using KBr, NaCl or BaF_2 windows as noted. ICP-OES analysis was obtained on a Perkin Elmer Optima 3000 DV ICP at UCSD-SIO facility ran by Pat Castillo, with assistance from Chris MacIssac.

General Procedure A: Ferrocene (5.00 g, 26.9 mmol, 1 equiv) was dissolved in anhydrous CH_2Cl_2 (107 mL, 0.25 M) in a round bottom flask equipped with a magnetic stir bar and the corresponding acid chloride (29.6 mmol, 1.1 equiv) was added via syringe. The reaction mixture was cooled to 0 °C by use of an ice bath and anhydrous $AlCl_3$ (3.75 g, 29.6 mmol, 1.1 equiv, 0.3 M) was added in three portions over a 15 min period. The dark blue solution was allowed to warm to RT slowly while stirring overnight (12 h). The reaction mixture was poured into a flask of ice water, extracted into 100 mL of CH_2Cl_2, then washed successively with 10% NaOH solution, water, and brine. The organic layer was dried over $MgSO_4$, filtered, and the solvent was removed under reduced pressure. Chromatography on SiO_2 gel with 90:10 hexanes:ethyl acetate as eluent (unless noted otherwise) led to isolation of the pure 1-benzoylferrocenes.

General Procedure B: Ferrocene (5.00 g, 26.9 mmol, 1 equiv) was dissolved in anhydrous CH_2Cl_2 (107 mL, 0.25 M) with magnetic stirring and acid chloride (59.2 mmol, 2.2 eqiuv) was added via syringe. The reaction mixture was cooled to 0 °C in an ice bath and anhydrous $AlCl_3$ (7.5 g, 59.2 mmol, 2.2 equiv) was added in three portions over a 15 min period. The dark blue solution was allowed to warm to RT while stirring overnight for 12 h. The reaction mixture was poured into a flask of ice water, extracted into 100 mL of CH_2Cl_2, then washed successively with 10% NaOH solution, water, and brine. The organic layer was dried over $MgSO_4$, filtered, and the solvent removed under reduced pressure.

Chromatography on SiO_2 gel with hexanes:ethyl acetate (80:20) as eluent led to isolation of the pure 1,1'-dibenzoylferrocenes, by ^{1}H NMR analysis.

General Procedure C: Ferrocenecarboxaldehyde (100 mg, 0.47 mmol, 1 equiv) and the corresponding ketone (0.52 mmol, 1.1 equiv) were dissolved in EtOH (4 mL, 0.12 M) and the round-bottom flask with magnetic stirring. NaOH (38 mg, 0.94 mmol, 2 equiv) dissolved in 0.6 mL of water was added via syringe. The reaction was allowed to stir overnight for 12 h at room temperature. The reaction was then filtered and the solid was collected and dried (how?). Product was determined to be pure by ^{1}H NMR spectroscopy and used without further purification.

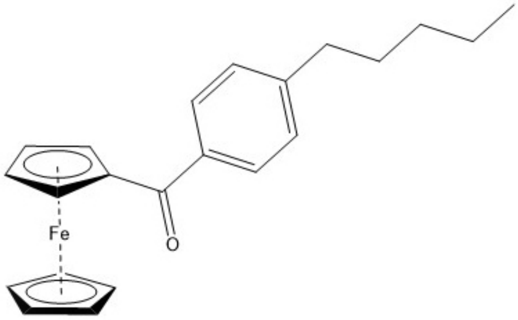

Compound 10. Prepared according to the General Procedure A using commercially available 4-pentylbenzoyl chloride. Obtained an orange solid in 76% yield. ^{1}H NMR (500 MHz; $CDCl_3$): δ 0.91 (t, $^3J_{HH}$ = 6.7 Hz, 3H, CH_3), 1.35-1.38 (m, 4H, CH_2CH_2), 1.66 (m, 2H, CH_2), 2.68 (t, $^3J_{HH}$ = 7.5 Hz, 2H, CH_2), 4.21 (s, 5H, Cp), 4.57 (s, 2H, Cp'H), 4.91 (s, 2H,Cp'H), 7.28 (d, $^3J_{HH}$ = 8.0 Hz, 2H, ArH), 7.84 (d, $^3J_{HH}$ = 8.0 Hz, 2H, ArH). $^{13}C\{^1H\}$ NMR (126 MHz, $CDCl_3$): δ 14.20, 22.68, 31.06, 31.63, 36.09, 70.34, 71.70, 72.50, 78.56, 128.39, 137.36, 147.19, 198.98. IR (BaF_2, cm^{-1}): 1163, 1291, 1376, 1442, 1558, 1616, 2849, 2992, 2945. HRMS-(ESI-TOF) (*m/z*): calcd for $[C_{22}H_{25}FeO]^+$, 361.1125; found, 361.1253.

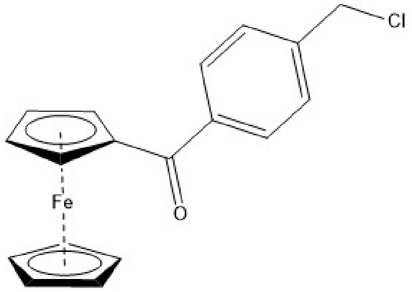

Compound 13. Prepared according to General Procedure A using commercially available 4-(chloromethyl)benzoyl chloride. Yield 6.09 g of a red solid (67%). ^{1}H NMR (400 MHz; CD_2Cl_2): δ 4.22 (s, 5H, Cp), 4.63 (t, $^3J_{HH}$ = 1.9 Hz, 2H, Cp'H), 4.69 (s, 2H, CH_2), 4.88 (t, $^3J_{HH}$ = 1.9 Hz, 2H, Cp'H), 7.52 (d, $^3J_{HH}$ = 8.3 Hz, 2H, ArH), 7.90 (d, $^3J_{HH}$ = 8.3 Hz, 2H, ArH). $^{13}C\{^1H\}$ NMR (126 MHz, CD_2Cl_2): δ 46.08, 70.55, 71.68, 73.05, 78.39, 128.75, 128.80, 140.05, 141.11, 198.26. IR (NaCl, cm^{-1}): 800, 819, 1285, 1440, 1633. HRMS-(ESI-TOF) (*m/z*): calcd for $[C_{18}H_{16}ClFeO]^+$, 339.0234; found, 339.0236.

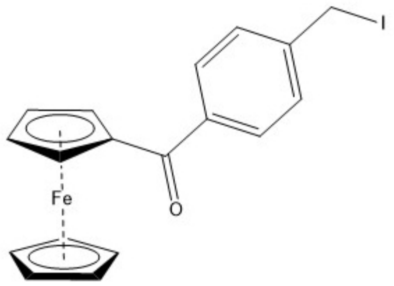

Compound 14. **Compound 13** (1.00 g, 2.95 mmol, 1 equiv) was dissolved in acetone (15 mL, 0.2M) with magnetic stirring and NaI (884 mg, 5.90 mmol, 2 equiv) was added. The reaction proceeded overnight at room temperature. Then the acetone was evaporated by rotary evaporation. The crude was then dissolved in CH_2Cl_2 and washed with brine three times. The combined organic layers were dried with $MgSO_4$, and the crude product isolated by rotory evaporation. The product was purified by column chromatography using 80:20 hexanes:ethyl acetate as eluent. Yield 1.1 g of orange solid (87%). ^{1}H NMR (400

MHz, $CDCl_3$): δ 4.21 (s, 5H, CpH), 4.51 (s, 2H, CH_2), 4.60 (t, $^3J_{HH}$ = 1.8 Hz, 2H, Cp'H), 4.90 (t, $^3J_{HH}$ = 1.8 Hz, 2H, Cp'H), 7.47 (d, $^3J_{HH}$ = 8.0 Hz, 2H, ArH), 7.84 (d, $^3J_{HH}$ = 8.0 Hz, 2H, ArH). $^{13}C\{^1H\}$ NMR (126 MHz, $CDCl_3$): δ 4.68, 70.61, 71.85, 72.99, 78.38, 128.99, 129.05, 139.47, 143.16, 198.69. IR (KBr, cm^{-1}): 819, 1288, 1446, 1635, 1690, 3031. HRMS-(ESI-TOF) (*m/z*): calcd for $[C_{18}H_{16}FeIO]^+$, 430.9590; found, 430.9588.

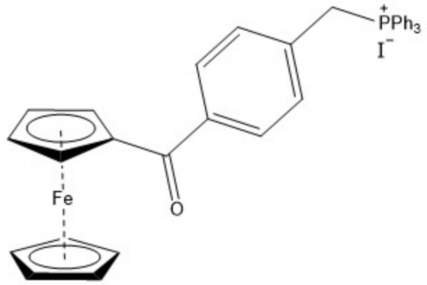

Compound 15. **Compound 14** (100 mg, 0.23 mmol, 1 equiv) was dissolved in diethyl ether (2.3 mL, 0.1M) with magnetic stirring and purged with argon. Then triphenylphosphine (315 mg, 1.2 mmol, 5 equiv) in diethyl ether (2.3 mL) was purged with argon and added in one portion. The reaction proceeded overnight at room temperature under argon. The product was then filtered to collect the yellow solid, and washed three times with diethyl ether. Yielded 80 mg of yellow solid (50%). The product was used without further purification. ^1H NMR (400 MHz, CD_3CN): δ 4.21 (s, 5H, CpH), 4.66 (t, $^3J_{HH}$ = 1.6 Hz, 2H, Cp'H), 4.77 (d, $^2J_{HP}$ = 15.6 Hz, 2H, CH_2), 4.79 (t, $^3J_{HH}$ = 1.6 Hz, 2H, Cp'H), 7.09 (d, $^3J_{HH}$ = 7.9 Hz, 2H, BzArH), 7.54 (d, $^3J_{HH}$ = 7.9 Hz, 2H BzArH), 7.61 – 7.74 (m, 12H, ArH), 7.91 (t, $^3J_{HH}$ = 7.5 Hz, 3H). $^{13}C\{^1H\}$ NMR (126 MHz, CD_3CN): δ 30.85 (d, $^2J_{CP}$ = 48.5 Hz), 71.61, 72.61, 74.41, 79.20, 129.87 (d, J_{CP} = 3.3 Hz), 130.10 (d, J_{CP} = 12 Hz), 131.58 (d, J_{CP} = 12.6 Hz), 132.07 (d, J_{CP} = 5.4 Hz), 133.09 (d, J_{CP} = 9.8 Hz), 135.64 (d, J_{CP} = 9.9 Hz), 136.80 (d, J_{CP} = 3.04 Hz), 141.18 (d, J_{CP} = 3.9Hz), 199.03. IR

(KBr, cm^{-1}): 830, 1107, 1288, 1440, 1624, 1710, 2856, 3053. HRMS-(ESI-TOF) (*m/z*): calcd for $[C_{36}H_{30}FeIOP]^+$, 565.1379; found, 565.1377.

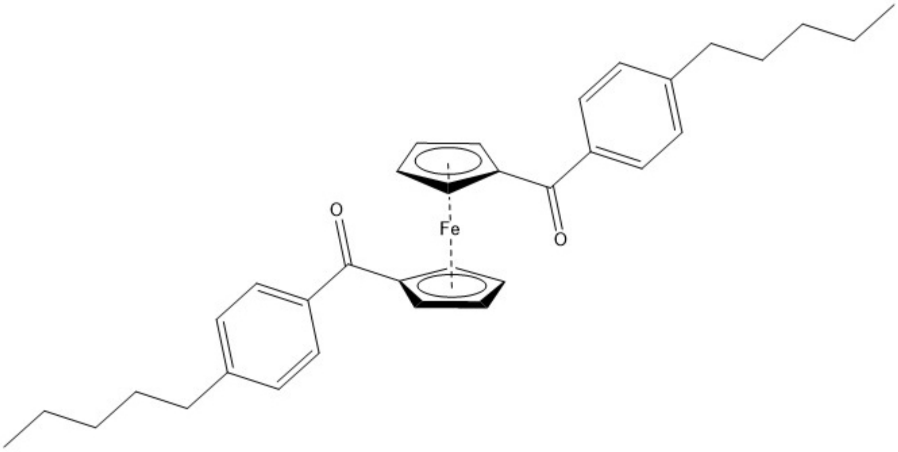

Compound 16. Prepared according to General Procedure B using commercially available 4-pentylbenzoyl chloride. Yielded a red solid (59%). ^{1}H NMR (400 MHz, CD_2Cl_2): δ 0.91 (t, $^3J_{HH}$ = 6.7 Hz, 6H, CH_3), 1.35 (m, 8H, CH_2CH_2), 1.65 (m, 4H, CH_2), 2.67 (t, $^3J_{HH}$ = 7.7 Hz, 4H, CH_2-benzylic), 4.56 (s, 4H, CpH), 4.87 (s, 4H, CpH), 7.24 (d, $^3J_{HH}$ = 8.1 Hz, 4H, aryl), 7.71 (d, $^3J_{HH}$ = 8.1 Hz, 4H, aryl). $^{13}C\{^1H\}$ NMR (500 MHz, CD_2Cl_2): δ 14.15, 22.87, 31.28, 31.85, 36.21, 73.30, 74.59, 80.22, 128.58, 128.61, 136.98, 147.87, 197.36. IR (BaF_2, cm^{-1}) 857, 1277, 1562, 1601, 1624, 2861, 2931. HRMS-(ESI-TOF) (*m/z*): calcd for $[C_{34}H_{39}FeO_2]^+$ 535.2295, found 535.2294.

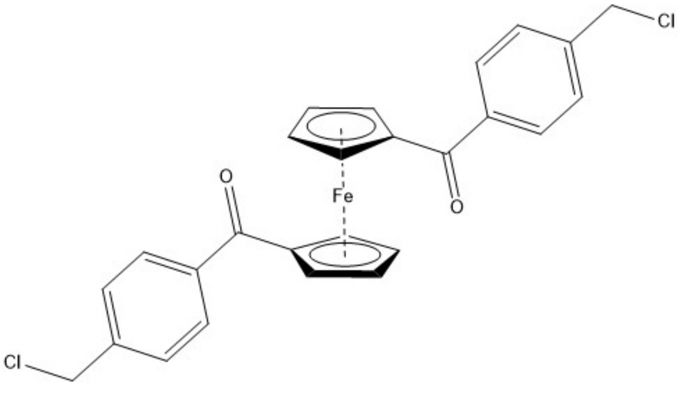

Compound 17. Prepared according to General Procedure B using commercially available 4-(chloromethyl)benzoyl chloride. Yielded a red solid (45%). ^{1}H NMR (400 MHz, CD_2Cl_2): δ 4.63-4.62 (m, 4H, CpH), 4.68 (s, 4H, CH_2Cl), 4.90-4.89 (m, 4H, CpH), 7.48 (d, $^{3}J_{HH}$ = 8.1 Hz, 4H, ArH), 7.78 (d, $^{3}J_{HH}$ = 8.1 Hz, 4H, ArH); $^{13}C\{^{1}H\}$ NMR (400 MHz, CD_2Cl_2) δ 45.87, 73.28, 74.61, 79.78, 125.04, 128.73, 139.21, 141.42, 196.89. IR (NaCl, cm^{-1}) 950, 1012, 1165, 1284, 1370, 1410, 1446, 1604, 1636, 2335, 2361. HRMS-(ESI-TOF) (*m/z*): calcd for $[C_{26}H_{20}Cl_2FeO_2Na]^+$ 513.0087; found, 513.0079.

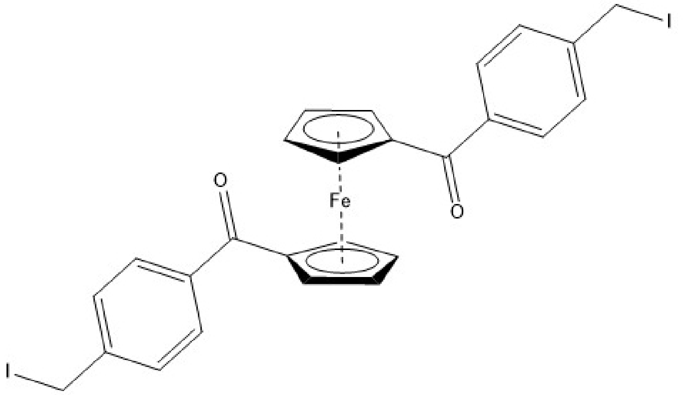

Compound 18. **Compound 17** (500 mg, 1.02 mmol, 1 equiv) was dissolved in acetone (5 mL, 0.2M) with magnetic stirring and NaI (612 mg, 4.08 mmol, 4 equiv) was added. The reaction proceeded overnight at room temperature. Then the acetone was evaporated by rotary evaporation. The crude was then dissolved in CH_2Cl_2 and washed with brine three times. The combined organic layers were dried with $MgSO_4$, and the crude product isolated by rotory evaporation. The product was purified by column chromatography using 80:20 hexanes:ethyl acetate as eluent. Yielded 600 mg of orange solid (87%). ^{1}H NMR (400 MHz, $CDCl_3$): δ 4.5 (s, 2H, CH_2I), 4.59 (t, $^{3}J_{HH}$ = 1.8 Hz, 2H, CpH) 4.90 (t, $^{3}J_{HH}$ = 1. Hz, 2H, CpH), 7.43 (d, $^{3}J_{HH}$ = 8.0 Hz, 2H, ArH), 7.71 (d, $^{3}J_{HH}$ = 8.0 Hz, 2H, ArH) . $^{13}C\{^{1}H\}$ NMR (126 MHz, $CDCl_3$): δ 29.06, 72.56, 73.86 78.85, 128.09, 128.11, 137.71,142.69,

196.42. IR (KBr, cm^{-1}): 1043, 1285, 1632, 2915, 3095, 3372. HRMS-(ESI-TOF) (*m/z*): calcd for $[C_{26}H_{21}FeI_2O_2]^+$, 674.9080; found, 674.9082. .

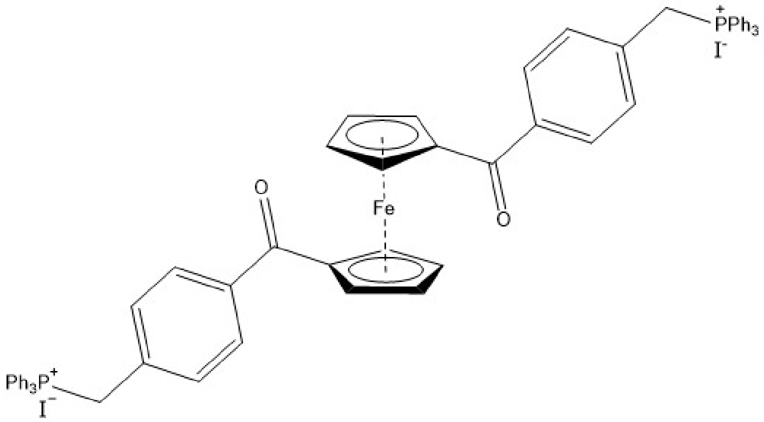

Compound 19. **Compound 18** (100 mg, 0.15 mmol, 1 equiv) was dissolved in diethyl ether (1.5 mL, 0.1M) with magnetic stirring and purged with argon. Then triphenylphosphine (393 mg, 1.5 mmol, 10 equiv) in diethyl ether (2.3 mL) was purged with argon and added in one portion. The reaction proceeded overnight at room temperature under argon. The product was then filtered to collect the yellow-orange solid, and washed three times with diethyl ether. Yielded 97 mg of yellow-orange solid (54%). The product was used without further purification. ^{1}H NMR (400 MHz, CDCl$_3$): δ 4.62 (d, $^3J_{HH}$ = 12.5 Hz, 4H, CpH), 6.07 (d, $^3J_{HP}$ = 15 Hz, 2H, CH$_2$), 7.22-7.72 (m, 16H, ArH), 7.91 (t, $^3J_{HH}$ = 11.8 Hz, 3H, ArH). ^{13}C{^{1}H} NMR (126 MHz, CD$_3$OD): δ 75.39, 76.77, 81.48, 119.40, 120.09, 130.60 (d, J_{CP} = 3.2 Hz), 132.34 (d, J_{CP} = 12.7 Hz), 133.15 (d, J_{CP} = 5.4 Hz), 136.35 (d, J_{CP} = 9.8 Hz), 137.47 (d, J_{CP} = 3.0 Hz), 141.28 (d, J_{CP} = 3.9 Hz), 199.51. IR (KBr, cm^{-1}) 849, 1110, 1629, 1707, 2845, 3048. HRMS-(ESI-TOF) (*m/z*): calcd for $[C_{62}H_{50}FeO_2P_2]^{2+}$, 472.1313; found, 472.1315.

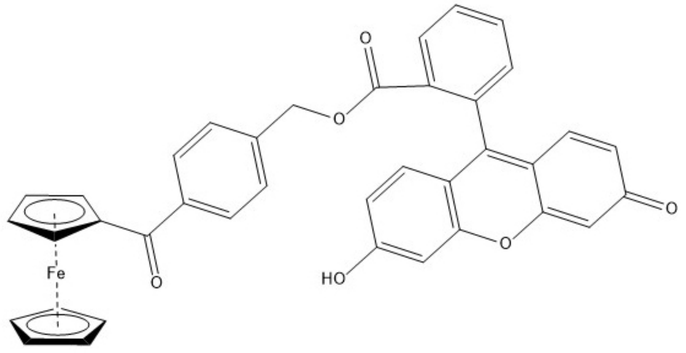

Compound 20. **Compound 13** (100 mg, 0.295 mmol, 1.00 equiv) was dissolved in THF (2.5 mL) and fluorescein sodium salt (122 mg, 0.325 mmol, 1.1 equiv) was added with water (2.5 mL). The reaction was refluxed overnight. The reaction was then quenched with 1M HCl to acidify solution. DCM was added to extract the organic compound from the aqueous layer. The combined organic layer was then washed with brine and dried with $MgSO_4$. Crude compound was purified with prep TLC with 70:30 hexanes ethyl acetate. Yielded 5 mg of a yellow-orange oil (0.8%). ^{1}H NMR (400 MHz, $CDCl_3$): δ 4.21 (s, 5H, Cp), 4.60 (t, $^3J_{HH}$ = 2.3 Hz, 2H, Cp'H), 4.91 (t, $^3J_{HH}$ = 2.3 Hz, 2H, Cp'H), 6.44 (dd, J_{HH} = 2.6, 12.4 Hz, 1H, ArH), 5,19 (s, 2H, OCH_2) 6.64 (t, $^3J_{HH}$ = 5 Hz, 1H, ArH) 6.67-6.74 (m, 2H, BzArH), 6.86 (s, 1H, ArH), 7.18 (d, $^3J_{HH}$ = 12.4 Hz, 1H, ArH), 7.53 (d, $^3J_{HH}$ = 10.9 Hz, 1H, ArH), 7.94 (d, $^3J_{HH}$ = 10.9 Hz, 1H, ArH), 8.03 (d, $^3J_{HH}$ = 9.9 Hz, 1H). IR (KBr, cm^{-1}): 822, 1085, 1178, 1444, 1611, 1733, 2924, 3301 (br). HRMS-(ESI) (*m/z*): calcd for $[C_{38}H_{26}FeO_6Na]^+$, 657.092; found, 657.0970.

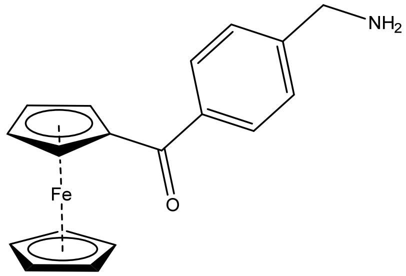

Compound 21. Compound 13 (1.00 g, 2.95 mmol, 1.00 equiv) was dissolved in THF (10 mL) and MeOH (10 mL), then aqueous ammonia (10 mL) was poured in at room temperature. The red solution was allowed to stir overnight at room temperature before using the rotory evaporator to remove the organic solvents. Aqueous solution was then treated with 2M NaOH and extracted with dichloromethane twice. The combined organic layers were dried with $MgSO_4$, and the crude product isolated by rotory evaporation. The amine was purified by SiO_2 chromatography, eluting with 5% MeOH/dichloromethane. Yielded 0.70 g of an orange solid (84%). ^{1}H NMR (500 MHz; $CDCl_3$): δ 1.85 (br s, 2H, NH_2), 3.95 (s, 2H, CH_2), 4.19 (s, 5H, Cp), 4.57 (t, $^3J_{HH}$ = 3.5 Hz, 2H, Cp'H), 4.89 (t, $^3J_{HH}$ = 3.5 Hz, 2H, Cp'H), 7.40 (d, $^3J_{HH}$ = 8 Hz, 2H, ArH), 7.87 (d, $^3J_{HH}$ = 8 Hz, 2H, ArH). $^{13}C\{^1H\}$ NMR (126 MHz, $CDCl_3$): δ 46.41, 69.66, 70.52, 71.71, 72.84, 78.50, 127.22, 128.79, 138.65, 146.89, 199.04. IR (KBr, cm^{-1}): 1044, 1108, 1163, 1285, 1377, 1443, 1563, 1632, 2848, 2915, 3095, 3373. HRMS-(ESI) (m/z): calcd for $[C_{18}H_{18}FeNO]^+$, 320.0732; found, 320.0731.

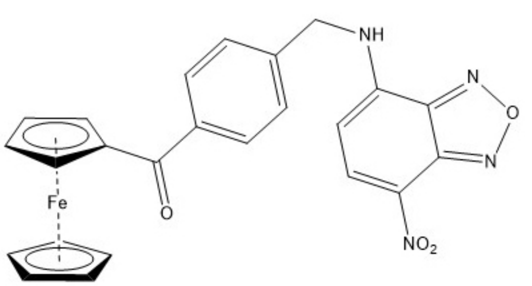

Compound 22. Compound 21 (0.20 g, 0.63 mmol, 1 equiv) was dissolved in EtOH with magnetic stirring (21 ml, 0.03 M) and 4-chloro-7-nitrobenzofurazan (NBD-Cl) was added in one portion (0.63 g, 3.2 mmol, 5 equiv). The reaction was heated to reflux overnight for 16 hours. After observance of product and decomposition of starting material by TLC, the solvent was quenched with 2M NaOH. The solution was then put on the rotary vapor to

remove EtOH. Afterwards, the product was extracted using DCM, and dried with $MgSO_4$. The product was purified by preparative TLC using PLC Silica gel 60 F254, 0.5mm plates with 70:30 hexanes:ethyl acetate as eluent. Yield 15 mg of an orange oil (5%). ^1H NMR (400 MHz, $CDCl_3$): δ 4.22 (s, 5H, Cp), 4.62 (s, 2H, Cp'H), 4.78 (d, $^3J_{HH}$ = 8 Hz, 2H, CH_2), 4.91 (s, 2H, Cp'H), 6.24 (d, $^3J_{HH}$ = 8 Hz, 1H, ArH), 6.53 (s br, 1H, NH), 7.49 (d, $^3J_{HH}$ = 8 Hz, 2H, ArH), 7.96 (d, $^3J_{HH}$ = 8 Hz, 2H, ArH), 8.50 (d, $^3J_{HH}$ = 8 Hz, 1H, ArH). $^{13}C\{^1H\}$ NMR (126 MHz, CD_3CN): δ 46.41, 70.13, 71.21, 72.76, 78.16, 99.72, 102.56, 127.21, 128.53, 137.10, 139.21, 140.30, 144.39, 144.46, 144.90, 197.86. IR (KBr, cm^{-1}): 1299, 1441, 1494, 1577, 1627, 2848, 2920, 3331.07. HRMS-(ESI-TOF) (*m/z*): calcd for $[C_{24}H_{19}FeN_4O_4]^+$, 483.0756; found, 483.0745.

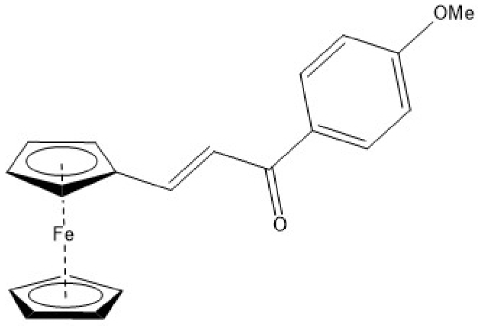

Compound 25. Prepared according to General Procedure C with commercially available acetanisole. Obtained a red solid in 83% yield. ^1H NMR (400 MHz, CD_3CN): δ 3.89 (s, 5H, Cp), 4.19 (s, 3H, OCH_3), 4.51 (t, $^3J_{HH}$ = 1.0 Hz, 2H, Cp'H), 4.72 (t, $^3J_{HH}$ = 1.0 Hz, 2H, Cp'H) 7.05, (d, $^3J_{HH}$ = 8.6 Hz, 2H, ArH), 7.31 (d, $^3J_{HH}$ = 15.2 Hz, 1H, CH), 7.68 (d, $^3J_{HH}$ = 15.2 Hz, 1H, CH), 8.04 (d, $^3J_{HH}$ = 8.6 Hz, 2H). $^{13}C\{^1H\}$ NMR (126 MHz, CD_3CN): δ 55.38, 69.14, 69.71, 71.25, 79.56, 113.84, 119.02, 130.55, 131.33, 145.15, 163.31, 187.36. IR (KBr, cm^{-1}): 841, 1032, 1260, 1585, 1649, 2923. HRMS-(ESI-TOF) (*m/z*): calcd for $[C_{20}H_{19}FeO_2]^+$, 347.0729; found, 347.0727. UV-Vis (50:50 DMF:H_2O) λ_{max}, nm: 502.

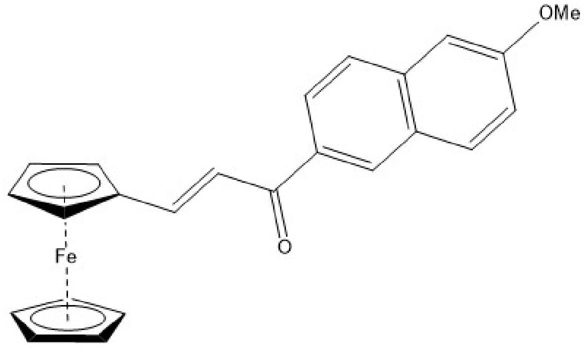

Compound 26. Prepared according to General Procedure C with commercially available 2-acetyl-6-methoxynaphthalene. Obtained a red solid in 79% yield. ^{1}H NMR (400 MHz, CD_3CN): δ 3.97 (s, 3H, CH_3), 4.23 (s, 5H, CpH), 4.55 (t, $^3J_{HH}$ = 1.8 Hz, 2H, Cp'H), 4.77 (t, $^3J_{HH}$ = 1.8 Hz, 2H, Cp'H), 7.27 (dd, $^3J_{HH}$ = 2.6 and 5.1 Hz, 1H, ArH), 7.37 (d, $^3J_{HH}$ = 2.6 Hz, 1H, ArH), 7.49 (d, $^3J_{HH}$ = 15.4 Hz, 1H, CH), 7.77 (d, $^3J_{HH}$ = 15.4 Hz, 1H, CH), 7.90 (d, $^3J_{HH}$ = 8.5 Hz, 1H, ArH), 8.00 (d, $^3J_{HH}$ = 8.5 Hz, 1H, ArH), 8.07 (dd, $^3J_{HH}$ = 1.8 and 4.3 Hz, 1H, ArH), 8.61 (s, 1H, ArH). ^{13}C{^{1}H} NMR (126 MHz, CD_3CN): δ 55.30, 69.22, 69.77, 71.39, 79.56, 106.00, 119.15, 119.61, 125.05, 127.18, 127.97, 129.68, 131.09, 137.14, 137.61, 145.66, 159.75, 188.45. IR (KBr, cm^{-1}): 849, 1024, 1479, 1574, 1624, 1646, 2850, 1956. HRMS-(ESI-TOF) (*m/z*): calcd for $[C_{24}H_{21}FeO_2]^+$, 397.0886; found, 397.0083. UV-Vis (50:50 DMF:H_2O) λ_{max}, nm: 506.

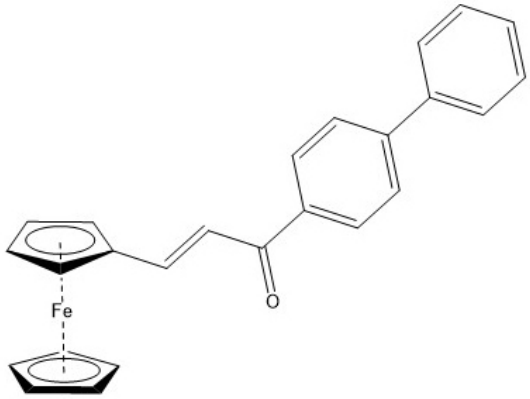

Compound 27. Prepared according to General Procedure C with commercially available 4-acetylbiphenyl. Obtained an orange solid in 80% yield. ^{1}H NMR (400 MHz, $CDCl_3$): δ 4.21 (s, 5H, CpH), 4.52 (t, $^3J_{HH}$ = 1.2 Hz, 2H, Cp’H), 4.64 (t, $^3J_{HH}$ = 1.2 Hz, 2H, Cp’H), 7.18 (d, $^3J_{HH}$ = 15 Hz, 1H, CH), 7.41 (t, $^3J_{HH}$ = 7.3 Hz, 1H, ArH), 7.49 (t, $^3J_{HH}$ = 7.3 Hz, 2H, ArH), 7.66 (d, $^3J_{HH}$ = 7.3 Hz, 2H, ArH), 7.72 (d, $^3J_{HH}$ = 7.9 Hz, 2H, ArH), 7.79 (d, $^3J_{HH}$ = 15 Hz, 1H, CH), 8.07 (d, $^3J_{HH}$ = 7.9 Hz, 2H, ArH). ^{13}C{^{1}H} NMR (126 MHz, $CDCl_3$): δ 69.39, 70.18, 71.76, 79.58, 119.39, 127.56, 127.63, 128.46, 129.30, 137.67, 140.42, 145.46, 147.11, 189.59. IR (KBr, cm^{-1}): 802, 999, 1102, 1402, 1590, 1651, 2842, 2917. HRMS-(ESI-TOF) (*m/z*): calcd for $[C_{25}H_{21}FeO]^+$, 393.0937; found, 393.0934. UV-Vis (50:50 DMF:H_2O) λ_{max}, nm: 505.

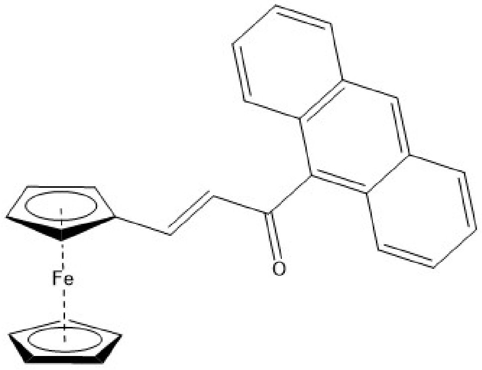

Compound 28. Prepared according to General Procedure C with commercially available 9-acetylanthracene. Obtained a purple-reddish solid in 75% yield. ^{1}H NMR (400 MHz, $CDCl_3$): δ 4.09 (s, 5H, CpH), 4.42 (t, $^3J_{HH}$ = 1.5Hz, 2H, Cp’H), 4.45 (t,$^3J_{HH}$ = 1.5 Hz, 2H, Cp’H), 6.90 (d, $^3J_{HH}$ = 15.9 Hz, 1H, CH), 7.03 (t, $^3J_{HH}$ = 15.9 Hz, 1H, CH), 7.49 (m, 4H, ArH), 7.92 (m, 2H, ArH), 8.07 (m, 2H, ArH), 8.55 (s, 1H, ArH). ^{13}C{^{1}H} NMR (126 MHz, $CDCl_3$): δ 69.26, 69.81, 72.01, 78.01, 125.56, 125.58, 126.45, 126.62, 127.99, 128.43, 128.62, 131.21, 135, 151.73, 199.87. IR (KBr, cm^{-1}): 734.78, 965.52, 1106, 1150, 1357,

1608, 1629. HRMS-(ESI) (*m/z*): calcd for $[C_{27}H_{21}FeO]^+$, 417.0937; found, 417.0936. UV-Vis (50:50 DMF:H_2O) $\lambda_{max,}$ nm: 503.

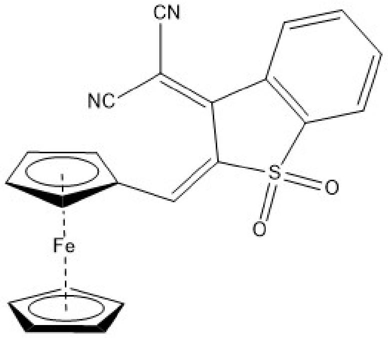

Compound 29. Prepared according to General Procedure C using commercially available 3-(dicyanomethylidene)-2,3-dihydroxybenzothiophene-1,1-dioxide with reflux overnight. Obtained a green solid in 68% yield. ^{1}H NMR (400 MHz, $CDCl_3$): δ 4.44 (s, 5H, Cp), 5.15 (d, $^3J_{HH}$ = 2.6 Hz, 4H, Cp'H), 7.82 (m, 2H, ArH), 7.95 (d, $^3J_{HH}$ = 6.8 Hz, 1H, ArH), 8.40 (s, 1H, CH), 8.81 (d, $^3J_{HH}$ = 7.7 Hz, 1H, ArH). $^{13}C\{^1H\}$ NMR (126 MHz, $CDCl_3$): δ 69.39, 73.36, 74.89, 78.41, 115.52, 115.90, 122.44, 124.94, 125.94, 129.49, 134.76, 135.17, 139.42, 146.87, 151.54, 152.47. IR (KBr, cm^{-1}): 830, 1163, 1302, 1546, 1674, 2210, 2925. UV-Vis (50:50 DMF:H_2O) $\lambda_{max,}$ nm: 670.

General Cell Culture Methods

Cell Lines and Growth Conditions: All cell lines were purchased from ATCC. HeLa, A549, and Caov-3 cells were cultivated as a monolayer cultures at 37 °C in a humidified atmosphere (95% air, 5% carbon dioxdie) in 25 cm^2 culture flasks using DMEM supplemented with FBS 5% (V/V), non-essential amino acids (1%), sodium pyruvate (1%), GlutaMax (1%), and antibiotics (penicillin/streptomycin, 1%) as growth medium. All cell seeding and manipulations were carried out in a sterile laminar flow hood unless noted otherwise. Passage into a fresh flask was done at 80-90% confluency as needed. At the time of passage, the old medium was removed by pipette and the cells were washed with 5 mL of sterile dPBS. Trypsin solution (1x) was washed gently over the cells and the flask was incubated for 10 min to detach the cells. Following treatment with trypsin, the cells were resuspended in fresh medium and a 0.2 mL aliquot of cell suspension was added to a fresh flask with new medium. All cells were passaged every 3-4 days, and no medium change was necessary.

All micro-plate UV-Vis data was collected using a PerkinElmer Health Sciences Inc., EnSpire multimode basic unit plate reader. Iron quantification was determined using a model 3000DV Perkin Elmer inductively coupled plasma-optical emission spectrometer (ICP-OES) in the laboratory of Dr. Paterno Castillo at the Scripps Institution of Oceanography. All TEM imaging was performed using a JOEL 1200EX II(JEOL, Peabody, MA) transmission electron microscope and photographed using a Gatan digital camera (Gatan, Pleasanto, CA), or viewed using a Tecnai G2 Spirit BioTWIN transmission electron microscope equipped with an Eagle 4k HS digital camera (FEI, Hilsboro, OR). Confocal microscopy images were obtained on the Olympus FV1000 Confocal with an Olympus IX81 inverted microscope incubated with CO_2 at the UCSD Microscopy Core managed by Jennifer Santini.

***In-Vitro* Cell Cytotoxicity Assays**: The cytotoxicity of the ferrocene complexes and their photoproducts were determined by the effect on growth rate as quantified by crystal violet staining at the end of drug exposure. Cells were seeded in 100 μL of DMEM media in 96-well plates at a density specific to the cell line: HeLa (3.5×10^4 cells/well), A549 (3.5×10^4 cells/well), and Caov-3 (3.5×10^4 cells/well). After incubation for 24 h at 37°C the cells were exposed to various concentrations of ferrocenyl compounds in media for 24 h. At this time, the dark plate was left in the incubator and an identically prepared plate was illuminated with a Richee 2014-SLT-CW/WW 50W Flood Light (0.031 W) for 3 hours with a 455 nm long pass filter (Pol filter 152x100x3mm GG455) resting on top of the 96 well plate. Temperature during photolysis was kept constant at 37°C using a Denville Incubloc solid aluminum block. 48 h after photolysis, the cell cultures were fixed with 4% paraformaldehyde, washed three times with DPBS, and stained with crystal violet. The absorbance at 590 nm was measured for each well using a microplate reader scanning spectrophotometer. Cytotoxicity was then determined by dividing the average absorbance values of each concentration of the drug-containing wells by the average absorbance of the control wells. Each experiment was performed in at least triplicate. IC_{50} values were calculated using OriginPro 8.0 software.

Confocal Microscopy Imaging: Cells were grown in a 35 mm glass bottom cell culture dish split into 4 chambers seeded at a density of 5.0×10^4 cells/well with 250 μL DMEM media in each chamber. Various compounds were then dissolved in 250 μL and added 24 h after into 3 chambers with the last used as a control. 24 h after addition of compound, the medium was removed with a pipet and the cells were rinsed three times with DPBS. Fix with DAPI mounting agent for 20 min covered with aluminum foil. Then observe with confocal microscope with excitation at 358 nm and emission at 461 nm for DAPI and excitation at 465 nm and emission at 535 for green fluorescent tag.

Transmission Electron Microscopy Imaging: Cells were grown on 60 x 15 mm sterile petri dishes at a density of 5×10^7 cells/well. Cells were then treated with various benzoylferrocene derivaives 24 h after seeding. 24 h after compound addition, the media was removed with a pipet and gently washed three times with DPBS, and immersed in modified Karnovsky's fixative (2.5% glutaraldehyde and 2% paraformaldehyde in 0.15 M sodium cacodylate buffer, pH 7.4) for at least 4 hours, postfixed in 1% osmium tetroxide in 0.15 M cacodylate buffer for 1 hour and stained en bloc in 2% uranyl acetate for 1 hour. Samples were dehydrated in ethanol, embedded in Durcupan epoxy resin (Sigma-Aldrich), sectioned at 50 to 60 nm on a Leica UCT ultramicrotome, and picked up on Formvar and carbon-coated copper grids. Sections were stained with 2% uranyl acetate for 5 minutes and Sato's lead stain for 1 minute. Grids were viewed using a JEOL 1200EX II (JEOL, Peabody, MA) transmission electron microscope and photographed using a Gatan digital camera (Gatan, Pleasanton, CA), or viewed using a Tecnai G2 Spirit BioTWIN transmission electron microscope equipped with an Eagle 4k HS digital camera (FEI, Hilsboro, OR).

Iron Uptake Studies

Cell Cultivation, Addition of Complexes, and Cell Harvesting: HeLa cells were cultivated as a monolayer in 75 cm^2 flasks under conditions previously described. For each drug containing flask a separate control flask was also prepared. The substances were diluted in DMF (**7**, **31**) or water ($FeSO_4$ and **21**) then added to FBS-free cell growth medium. The HeLa cells were exposed to the drug containing media for a period of 24 h then the media was removed by pipette and the cell monolayer was washed gently three times with 10 mL of warm dPBS. The cells were then treated with 3 mL of 1x trypsin for ten minutes and resuspended in 10 mL of fresh FBS-free media. The cell suspension was subsequently centrifuged at 1200 rpm (4 °C) for 5 min, and the pellets were washed twice with 10 mL of dPBS between additional centrifugation cycles. The pellets were drained 10 minutes then stored at -18 °C until analysis.

Determination of Protein Concentration: The cell pellets were homogenized in 5 mL of 0.001% Triton X-100 solution by vortexing followed by sonication (5 x 5 s). 1 mL was removed for protein quantification and the remaining 4 mL were lyophilized in preparation for iron quantification. Protein concentration was determined by the Bradford method using the commercially available Bio-Rad Protein Assay Dye Reagent Concentrate #500-0006 prepared per the manufacturer's instructions. Protein standards were prepared using human serum albumin (HSA) in 0.001% Triton X-100 solution. As Triton X-100 is a known interfering substance, additional dilutions of the protein standards were done using an identical concentration of the detergent. A calibration curve was constructed by calculating the 590/450 nm absorbance ratio using a micro-plate reader. The protein concentration of the cell lysates were determined as described by Zor and Selinger (see discussion section). A standard protein calibration curve is shown below.

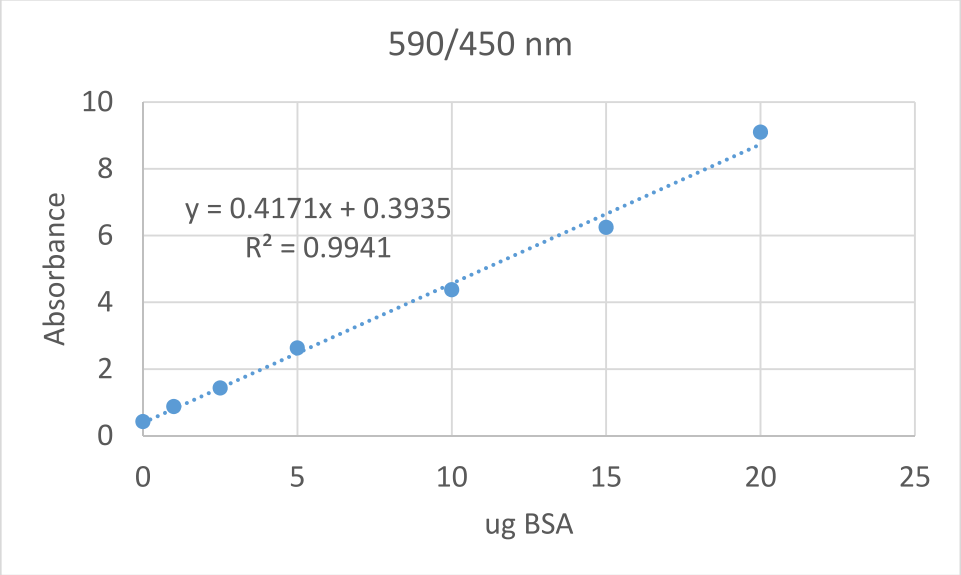

Figure 4.24. Standard calibration curve for Bradford Assay.

Determination of Iron Concentration: The lyophilized samples were dissolved in 230 μL of concentrated nitric acid and heated at 65°C for 6 h. The samples were then diluted to a total volume of 8 mL using 0.1% Triton X-100 and the iron concentration (ng/g) was determined by ICP-OES. The iron concentration was then related to the protein concentration to account for differences in biomass between separate flasks. Results are expressed as an average of three independent experiments.

F. Appendix 1 – NMR Spectra

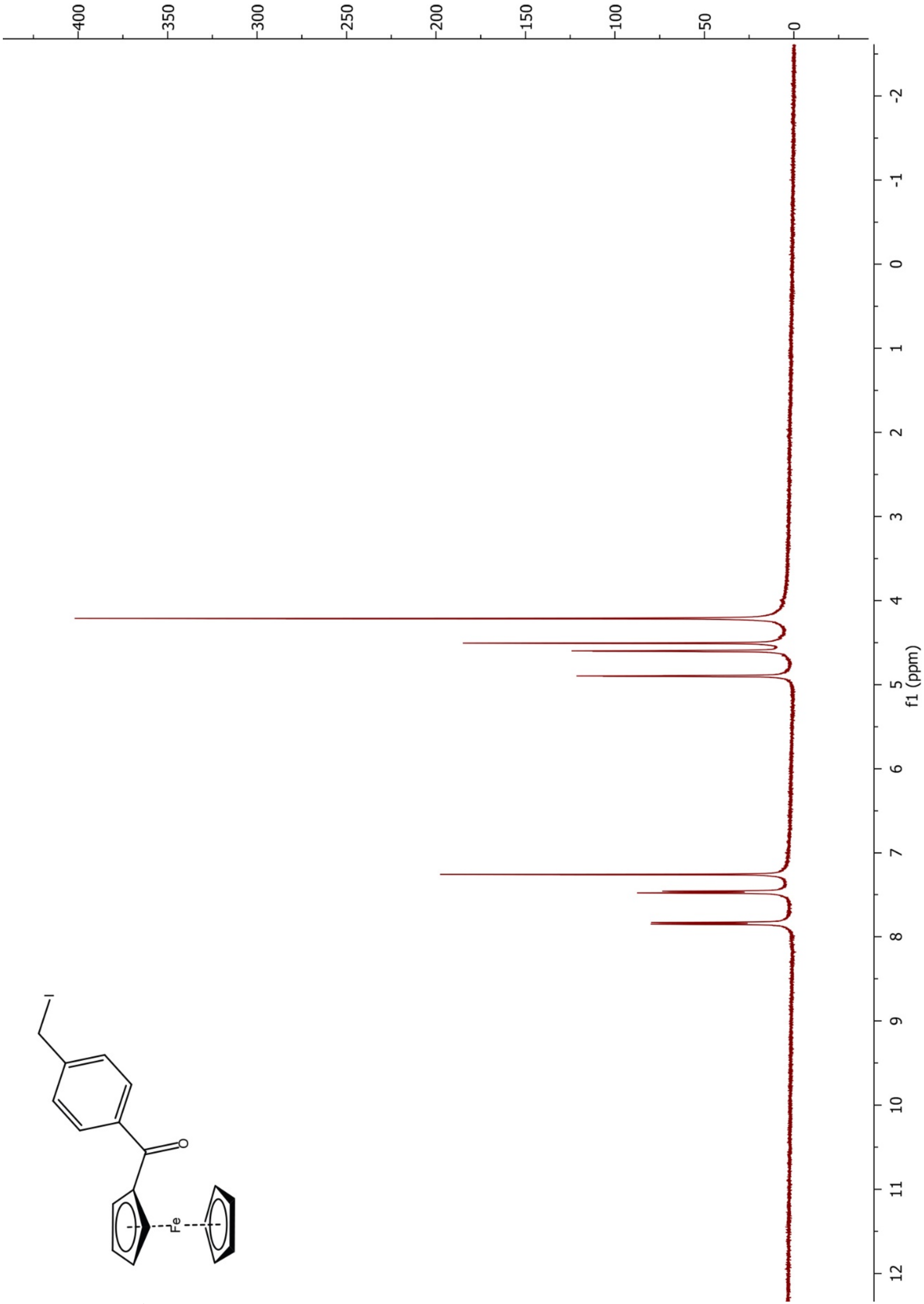

Figure 2.25. ^{1}H NMR of compound **14** (400 MHz, $CDCl_3$).

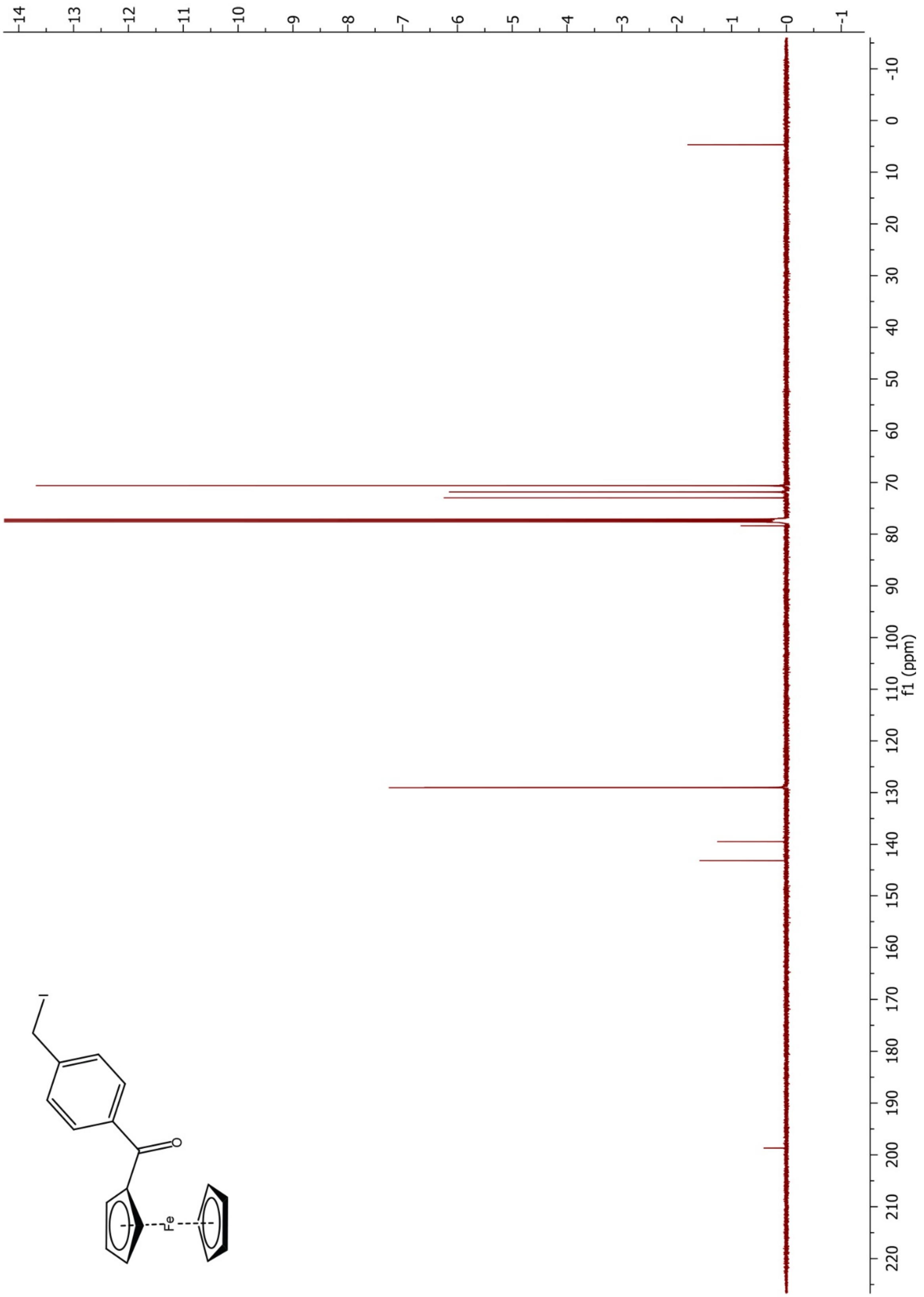

Figure 2.26. $^{13}C\{^1H\}$ NMR of compound **14** (126 MHz, $CDCl_3$).

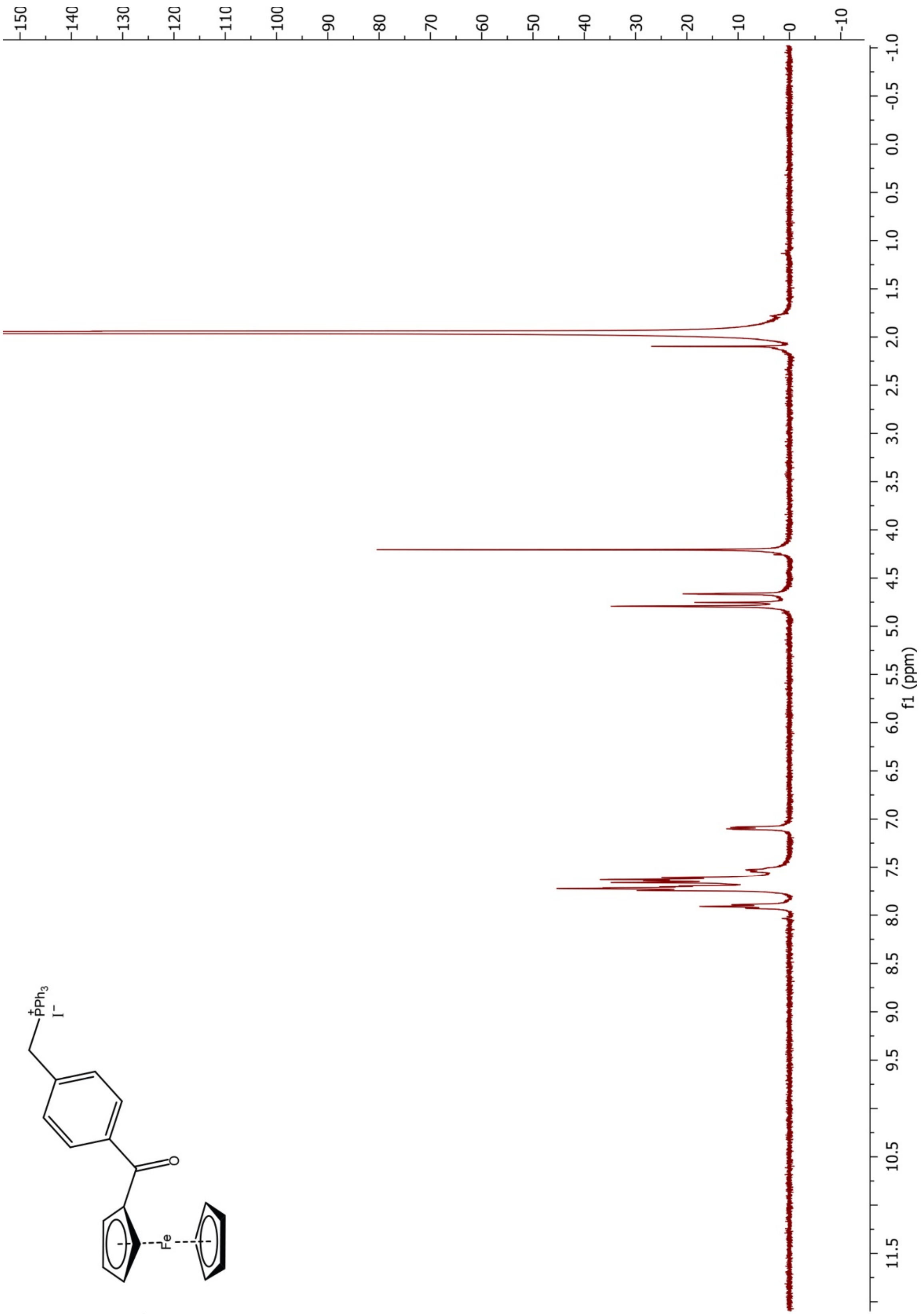

Figure 2.27. ^{1}H NMR of compound **15** (400 MHz, CD_3CN).

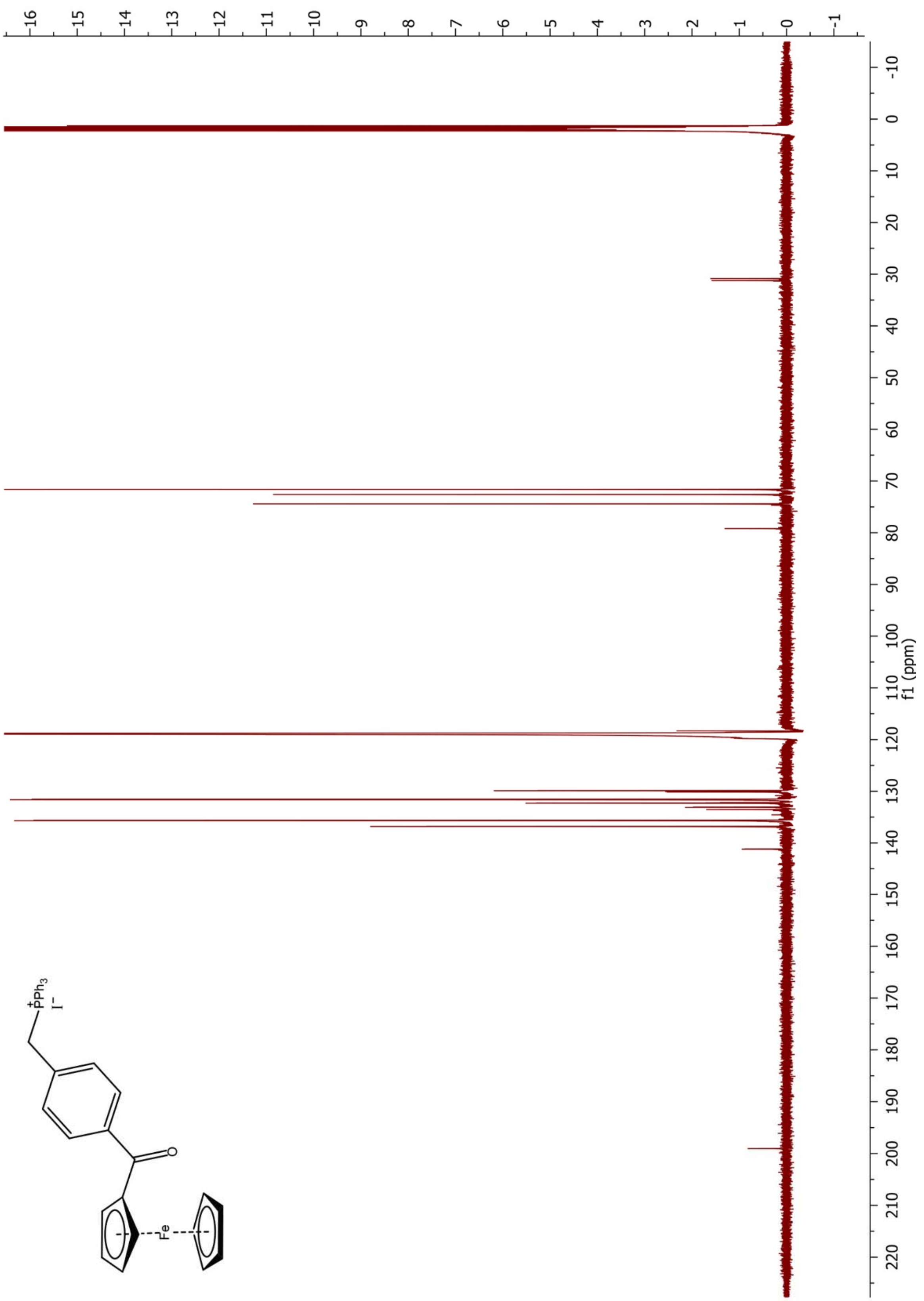

Figure 2.28. $^{13}C\{^1H\}$ NMR of compound **15** (126 MHz, CD_3CN).

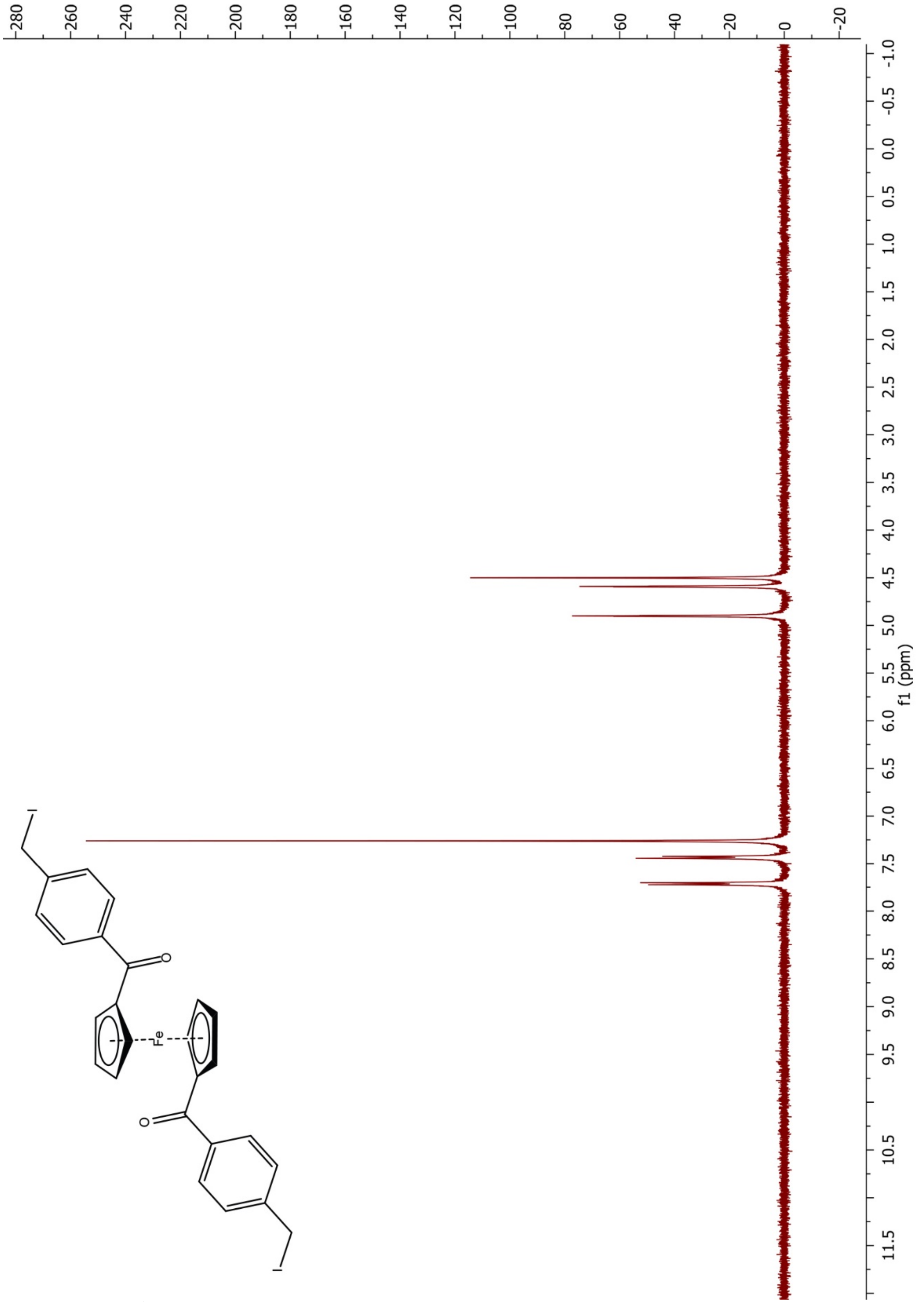

Figure 2.29. ^{1}H NMR of compound **18** (400 MHz, CDCl$_3$).

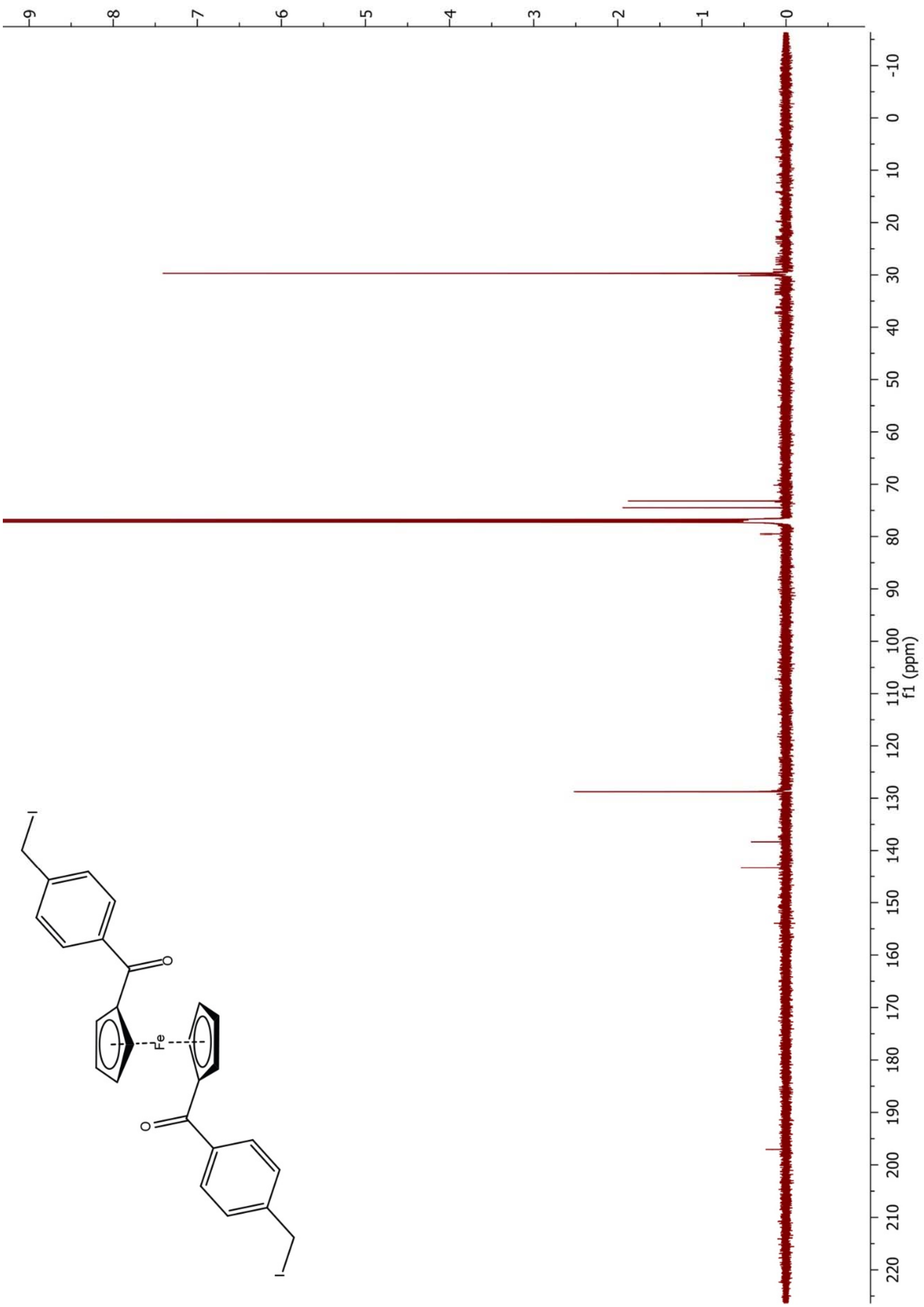

Figure 2.30. $^{13}C\{^1H\}$ NMR of compound **18** (126 MHz, $CDCl_3$).

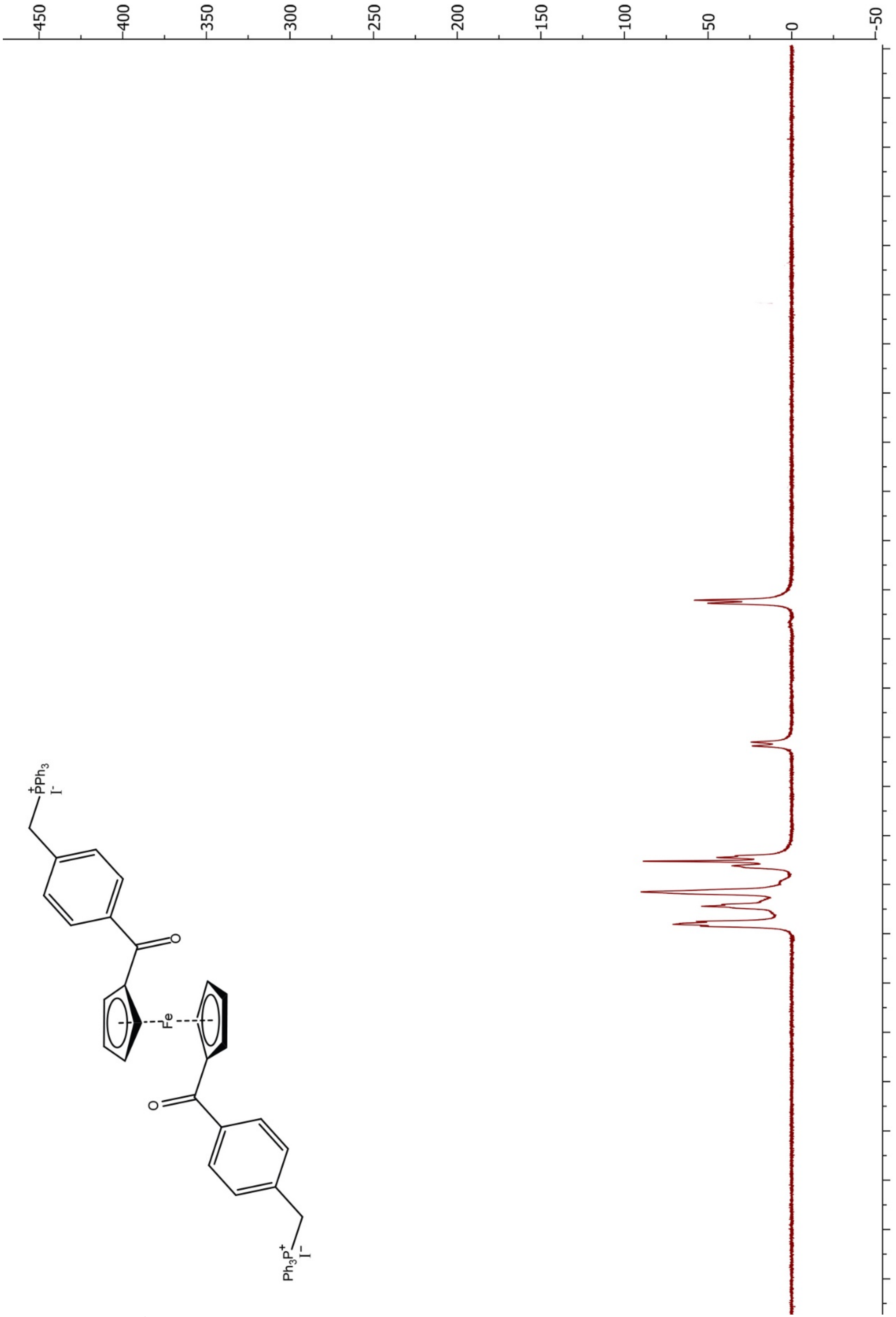

Figure 2.31. ^{1}H NMR of compound **19** (400 MHz, CDCl$_3$).

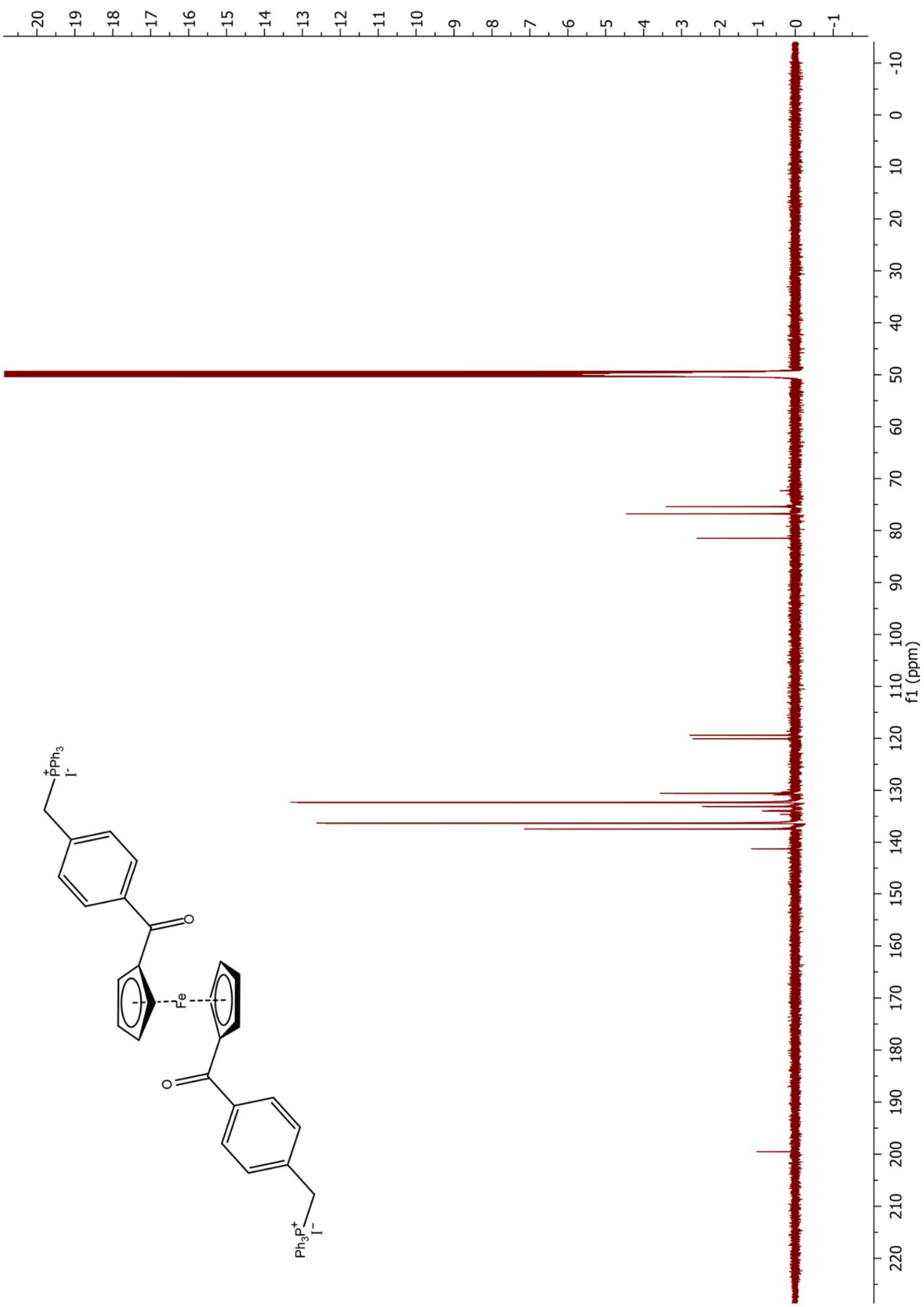

Figure 2.32. $^{13}C\{^1H\}$ NMR of compound **19** (126 MHz, CD_3OD).

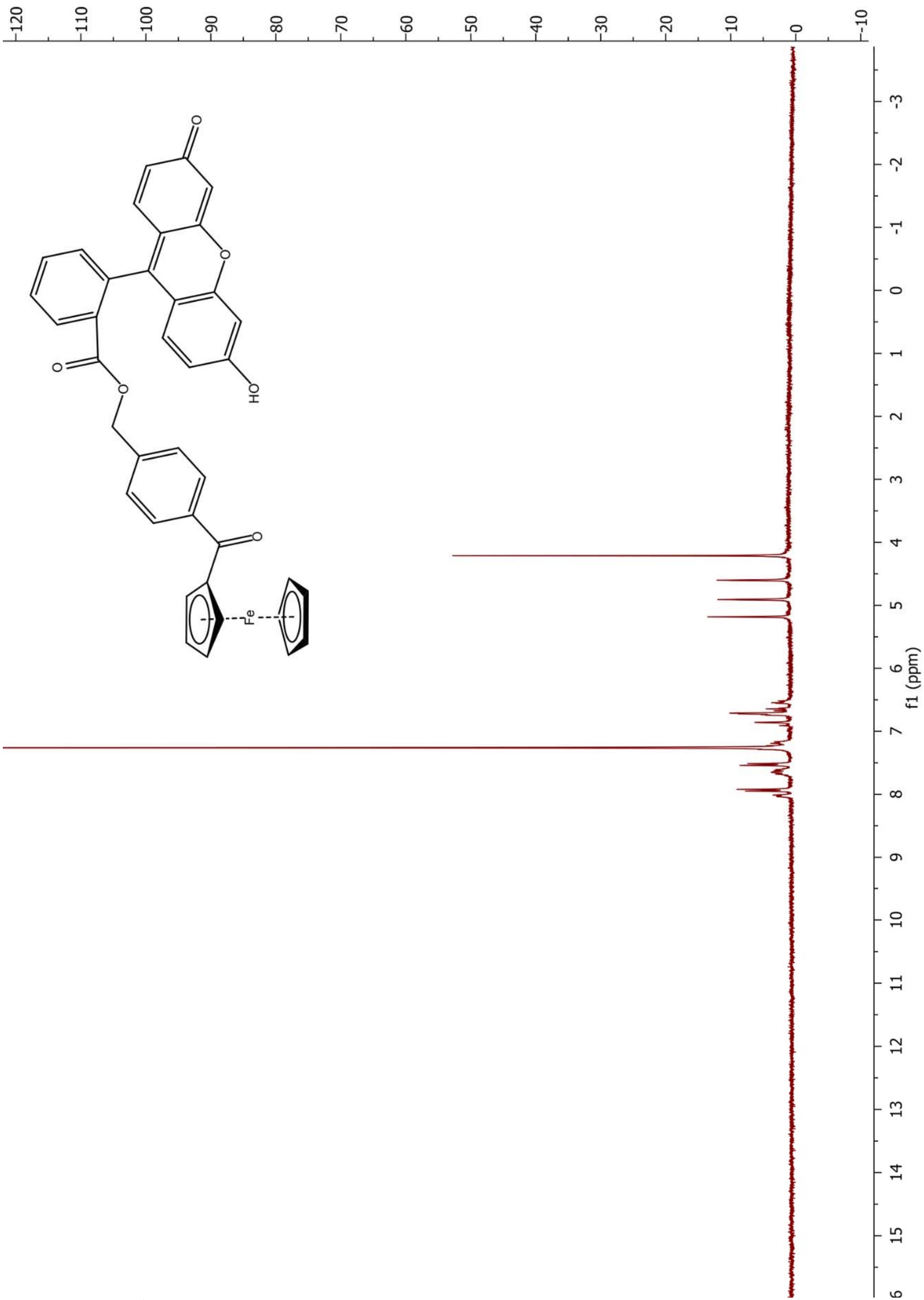

Figure 2.33. ^{1}H NMR of compound **20** (400 MHz, $CDCl_3$).

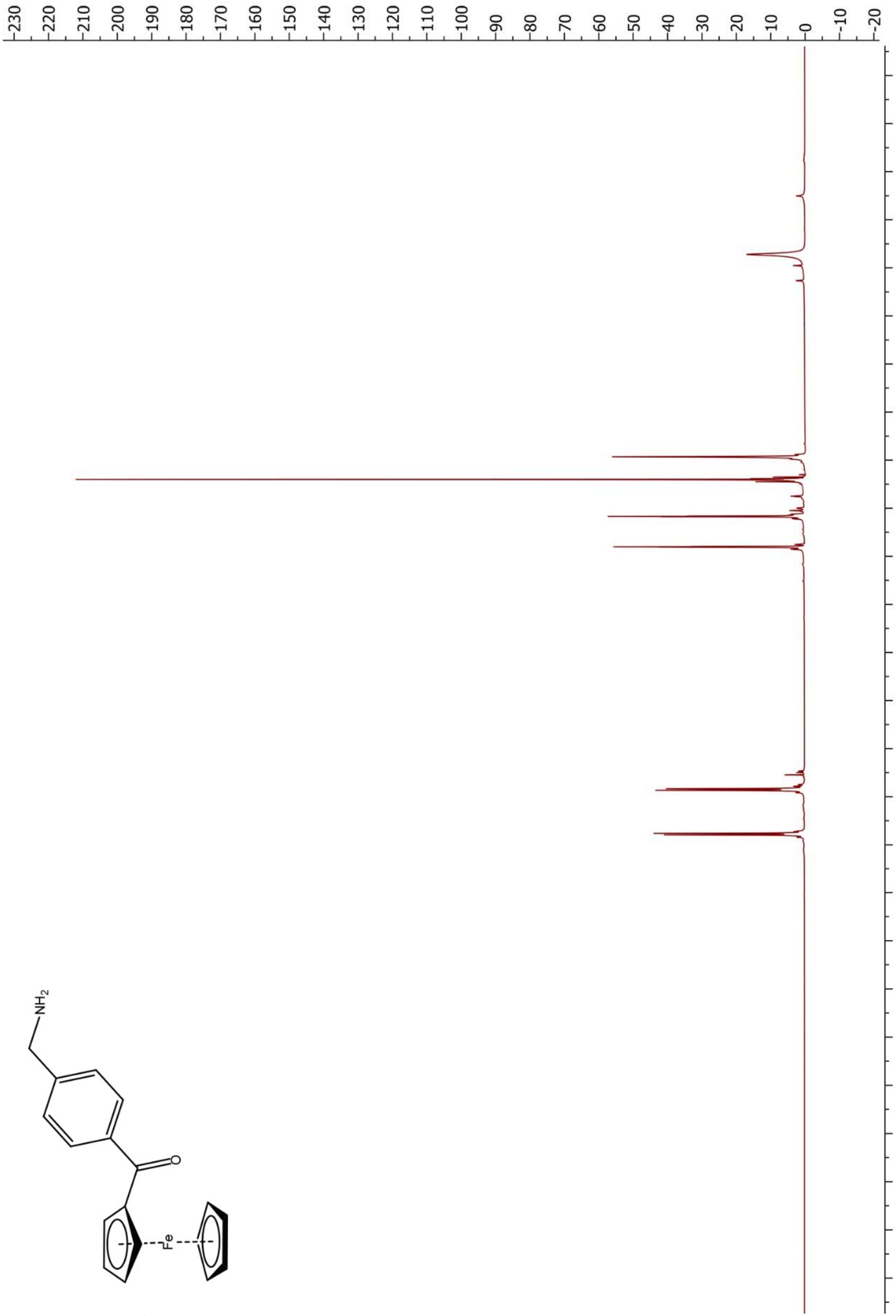

Figure 2.34. ^{1}H NMR of compound **21** (500 MHz; $CDCl_3$).

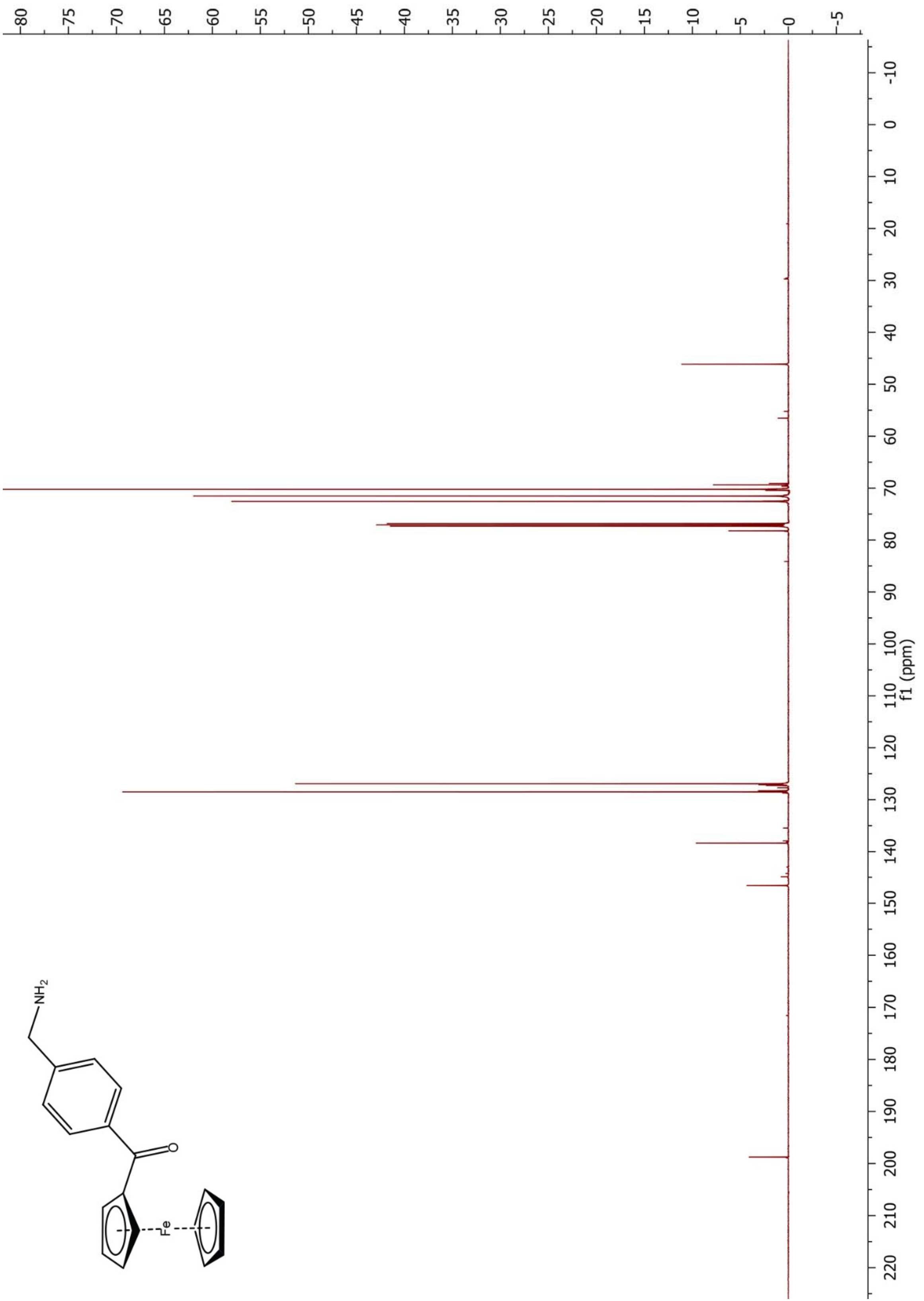

Figure 2.35. $^{13}C\{^1H\}$ NMR of compound **21** (126 MHz, $CDCl_3$).

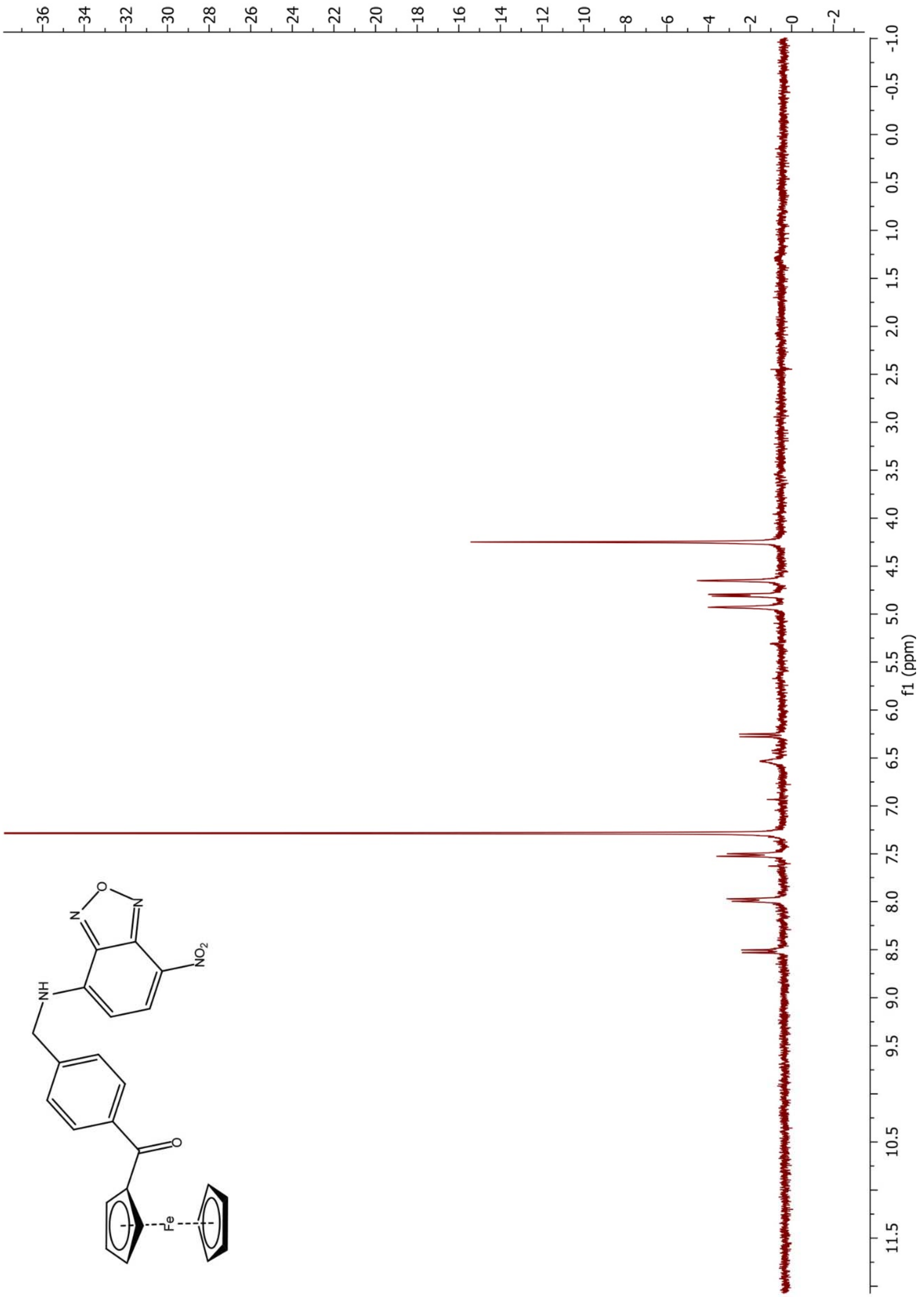

Figure 2.36. ^{1}H NMR of compound **22** (400 MHz, CDCl$_3$).

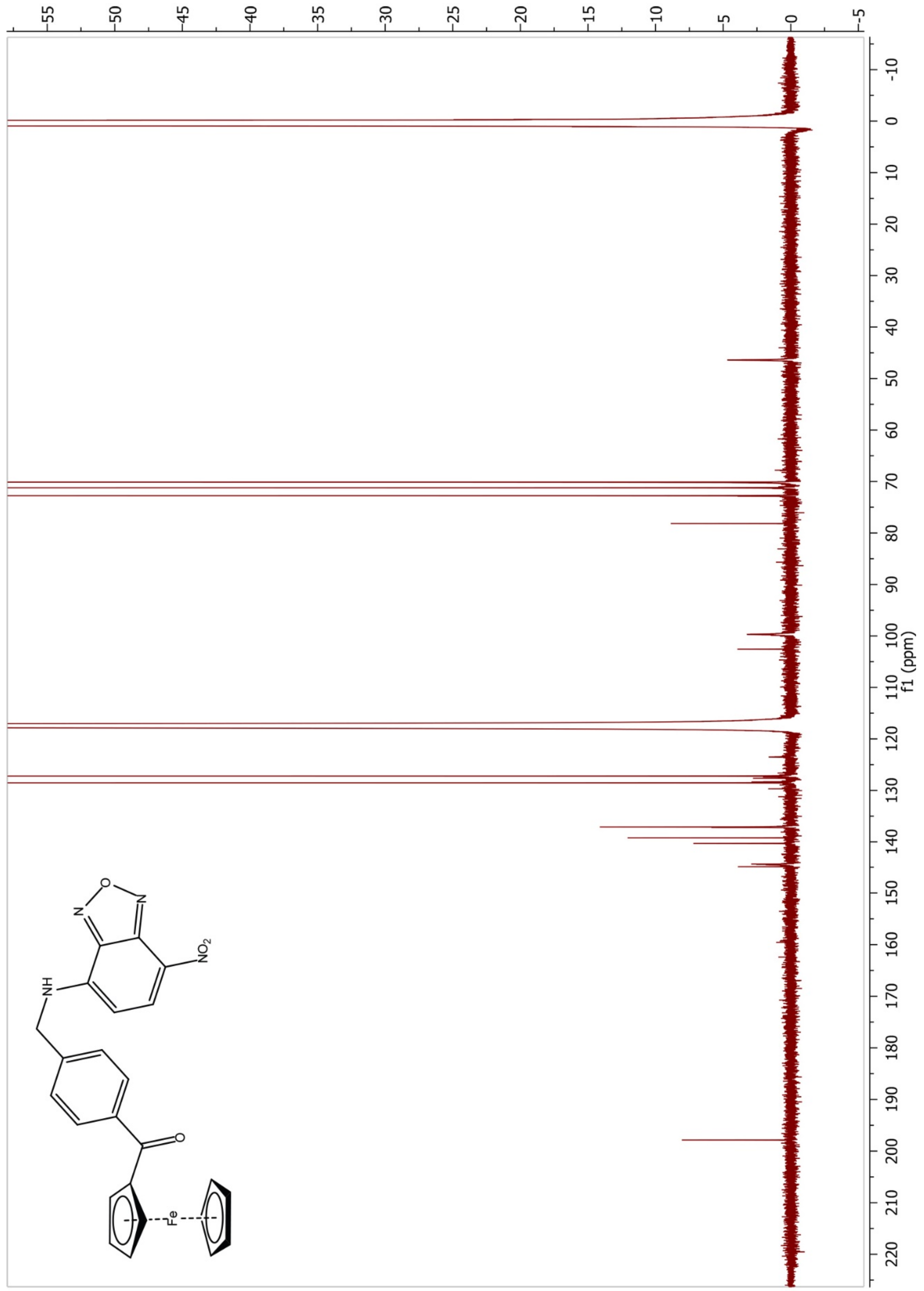

Figure 2.37. $^{13}C\{^1H\}$ NMR of compound **22** (126 MHz, CD_3CN).

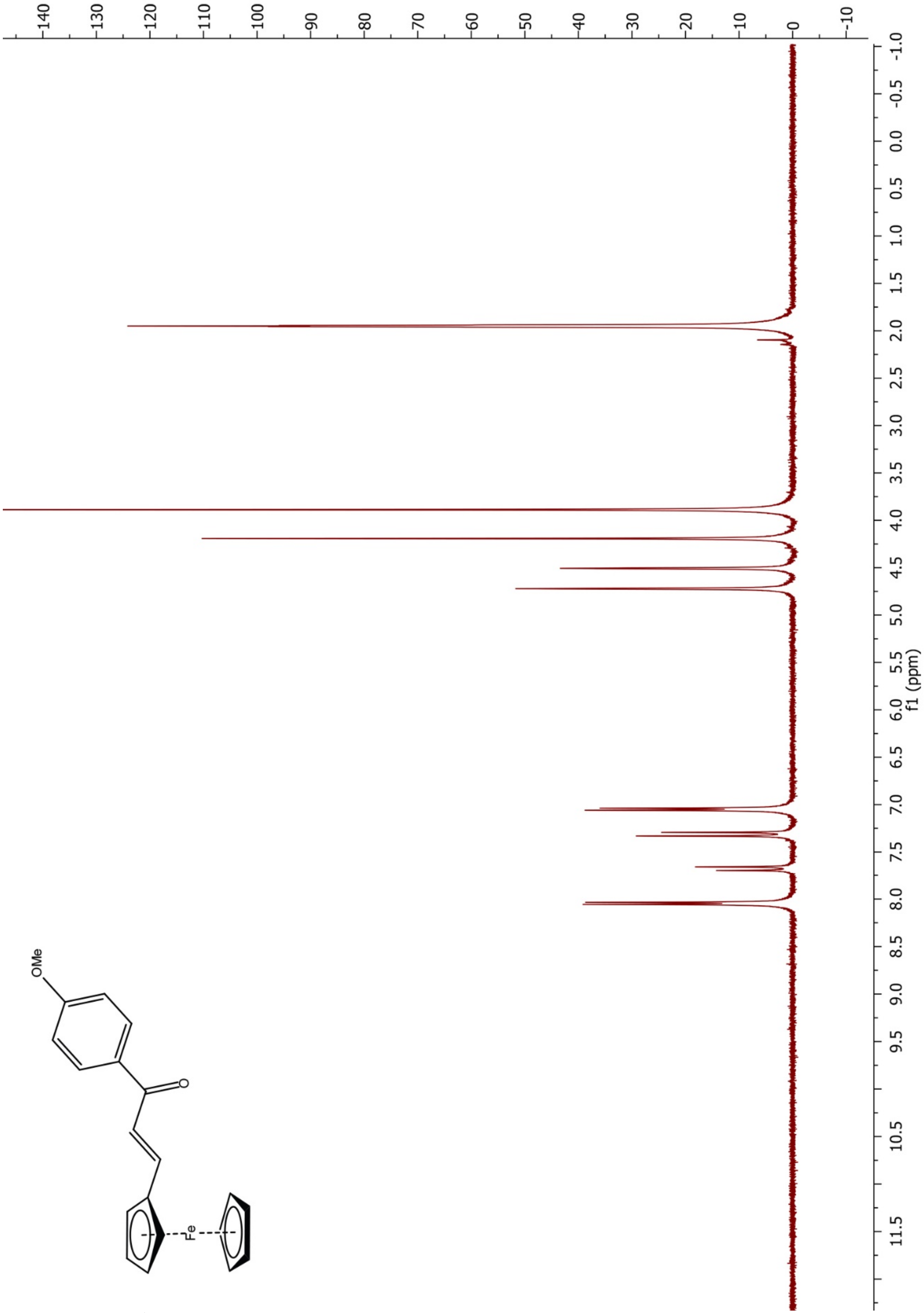

Figure 2.38. ^{1}H NMR of compound **25** (400 MHz, CD$_3$CN).

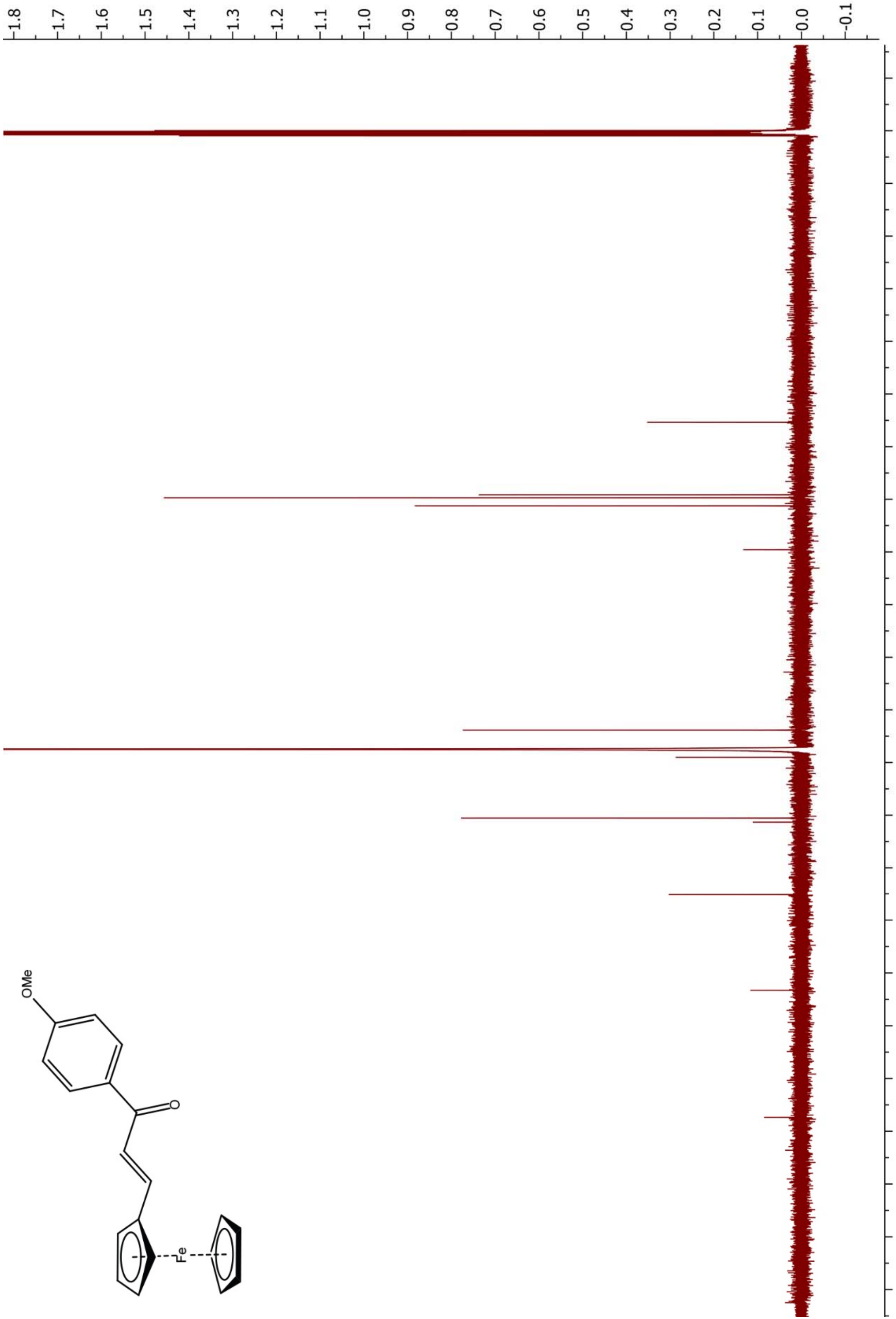

Figure 2.39. $^{13}C\{^1H\}$ NMR of compound **25** (126 MHz, CD_3CN).

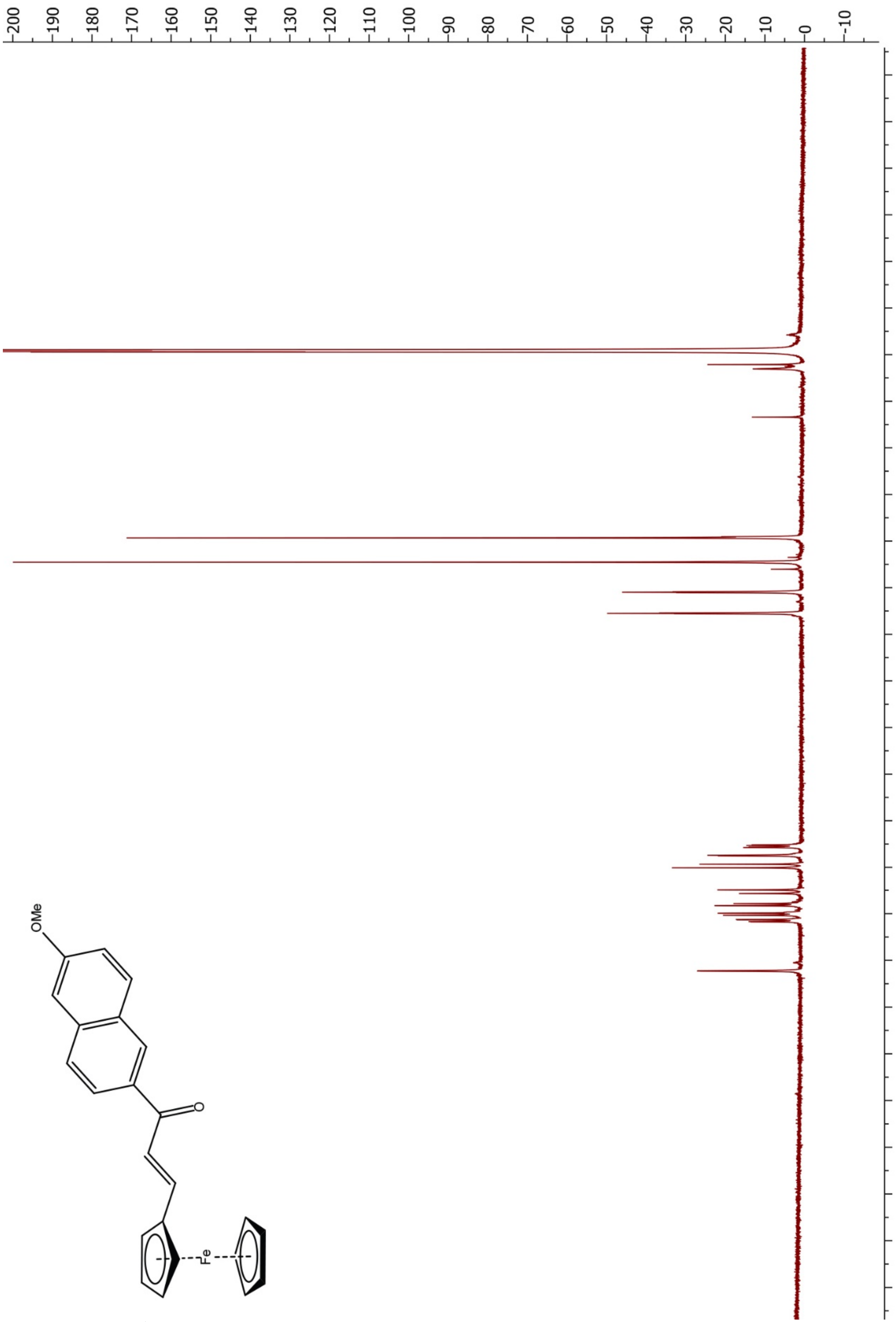

Figure 2.40. ^{1}H NMR of compound **26** (400 MHz, CD_3CN).

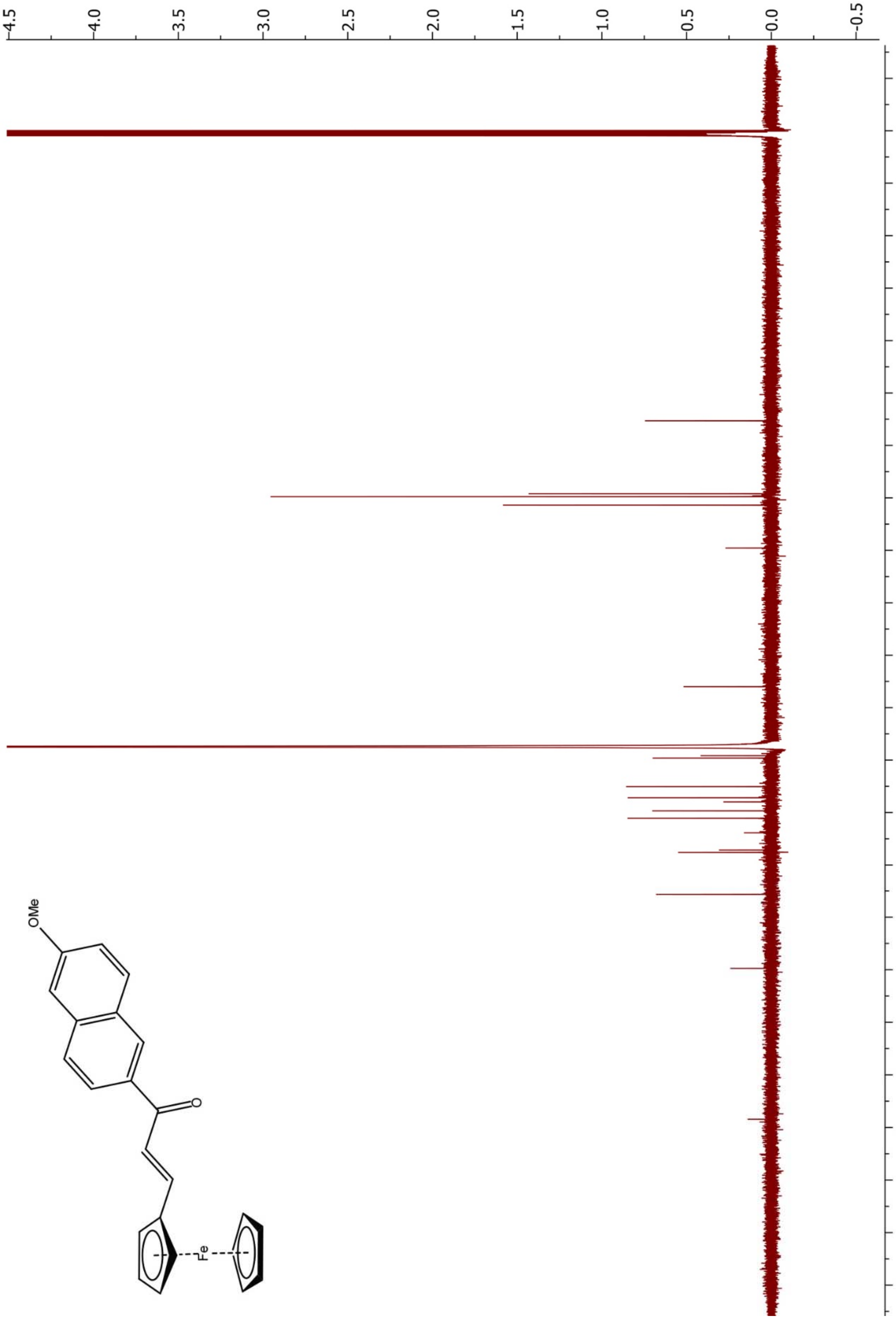

Figure 2.41. $^{13}C\{^{1}H\}$ NMR of compound **26** (126 MHz, CD_3CN).

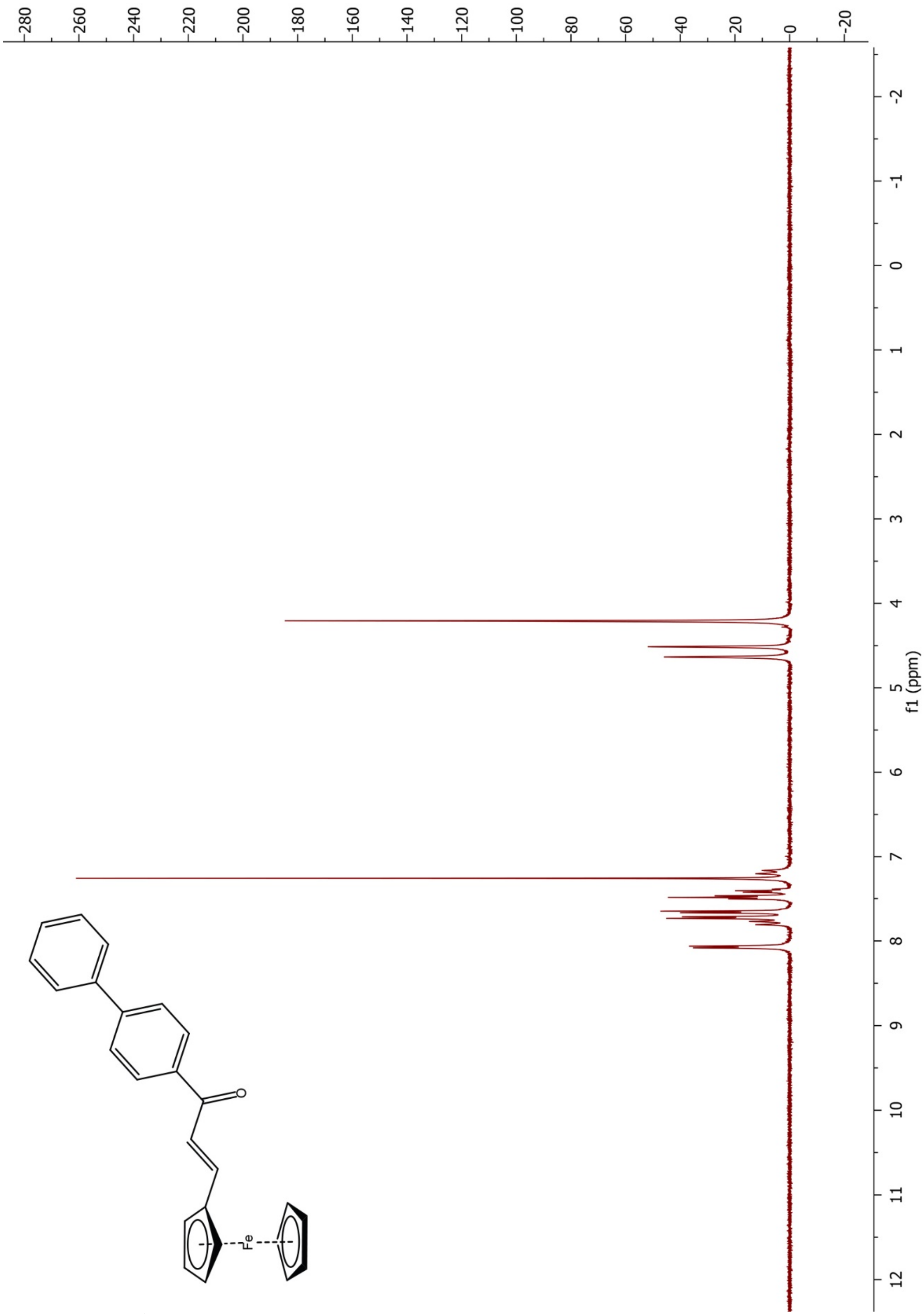

Figure 2.42. ^{1}H NMR of compound **27** (400 MHz, $CDCl_3$).

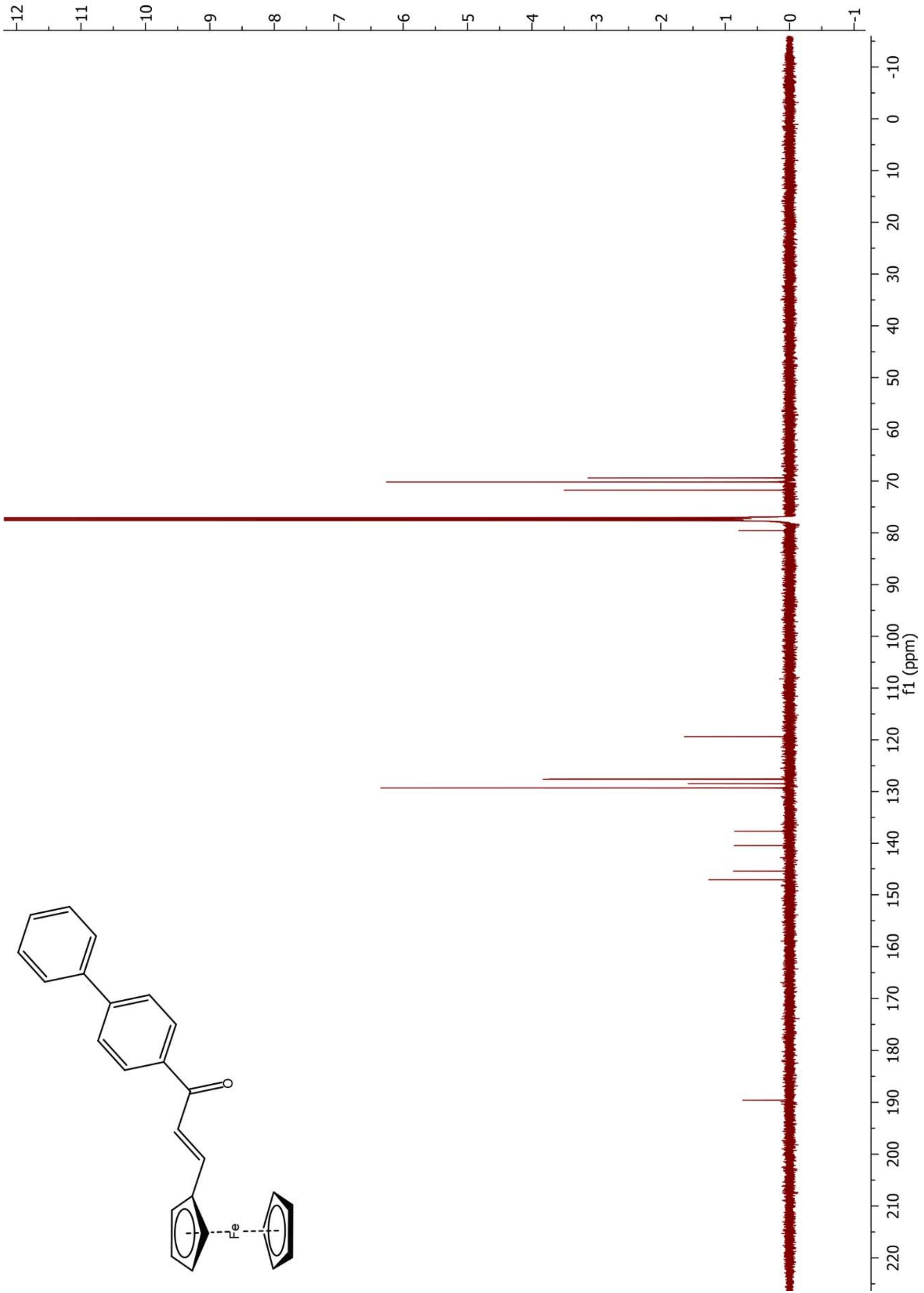

Figure 2.43. $^{13}C\{^1H\}$ NMR of compound **27** (126 MHz, $CDCl_3$).

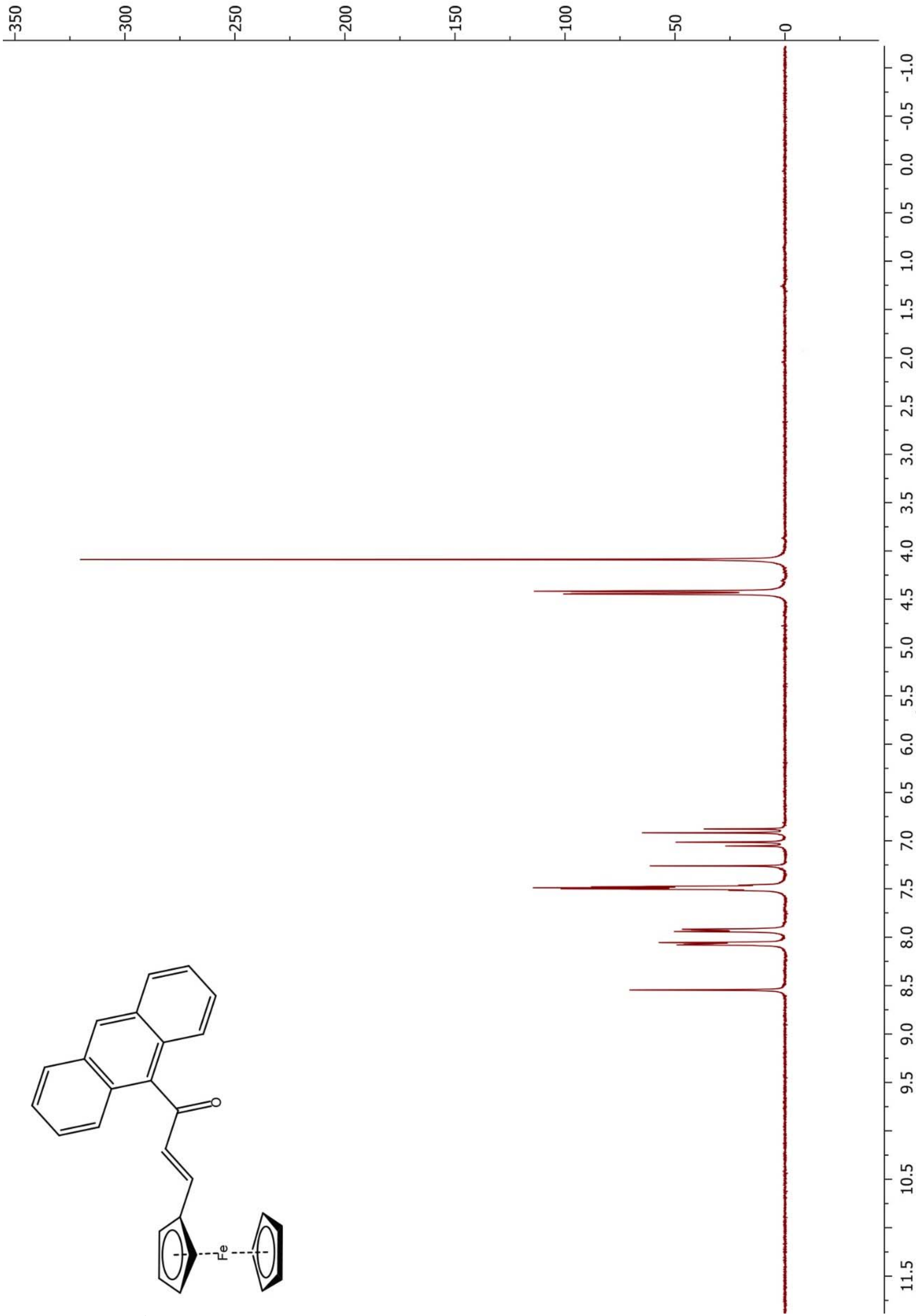

Figure 2.44. ^{1}H NMR of compound **28** (400 MHz, $CDCl_3$).

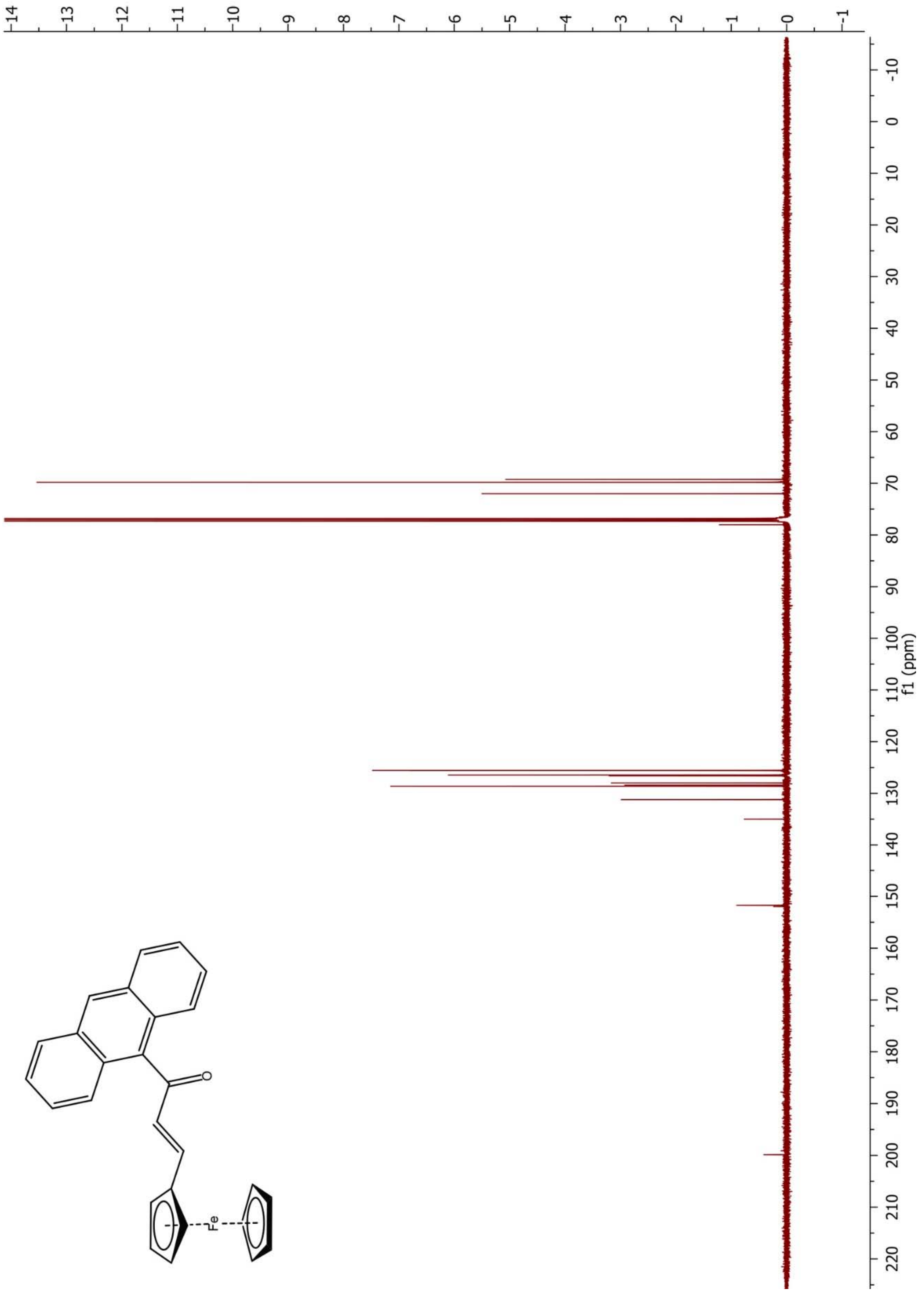

Figure 2.45. $^{13}C\{^1H\}$ NMR of compound **28** (126 MHz, $CDCl_3$).

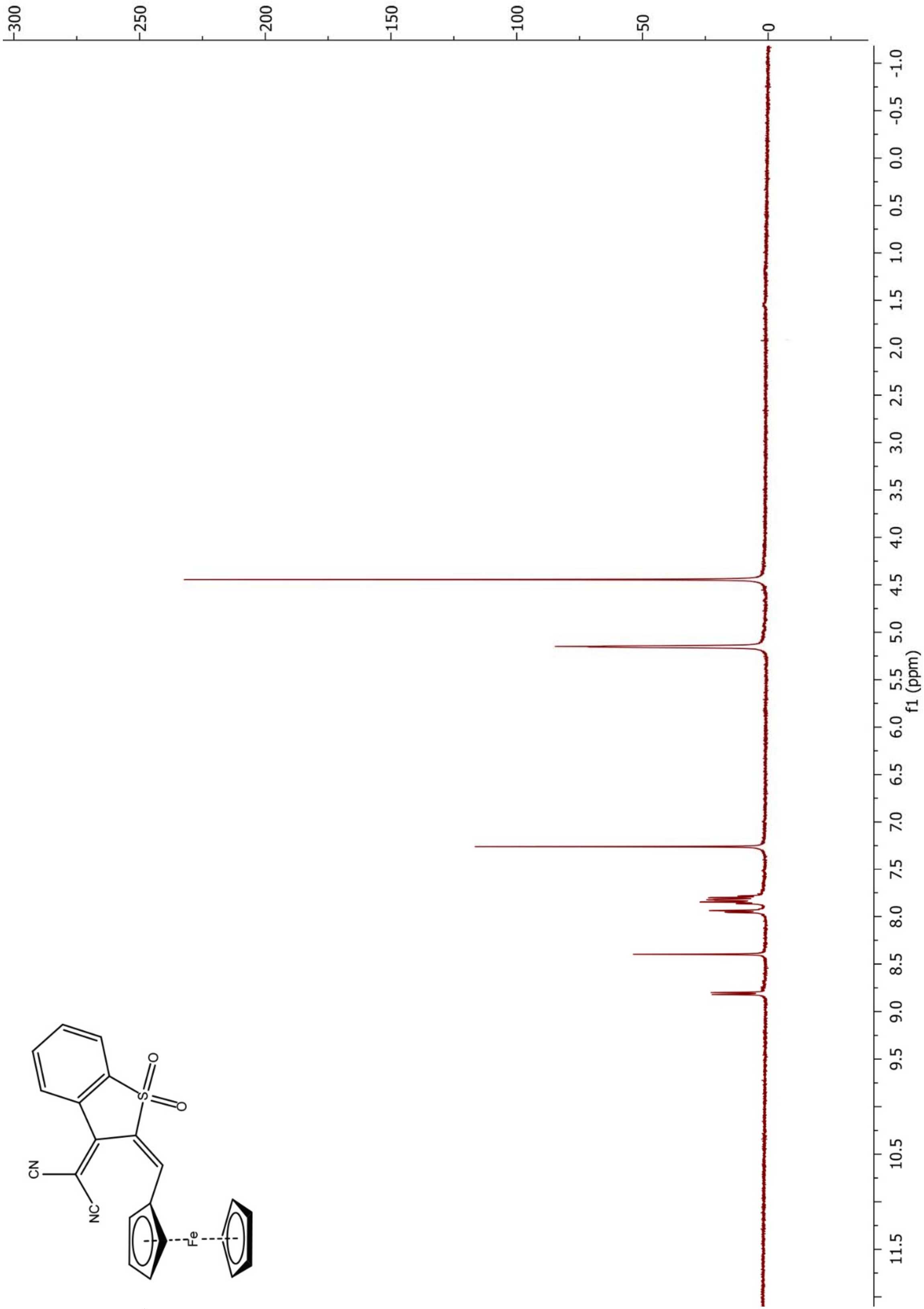

Figure 2.46. ^{1}H NMR of compound **29** (400 MHz, $CDCl_3$).

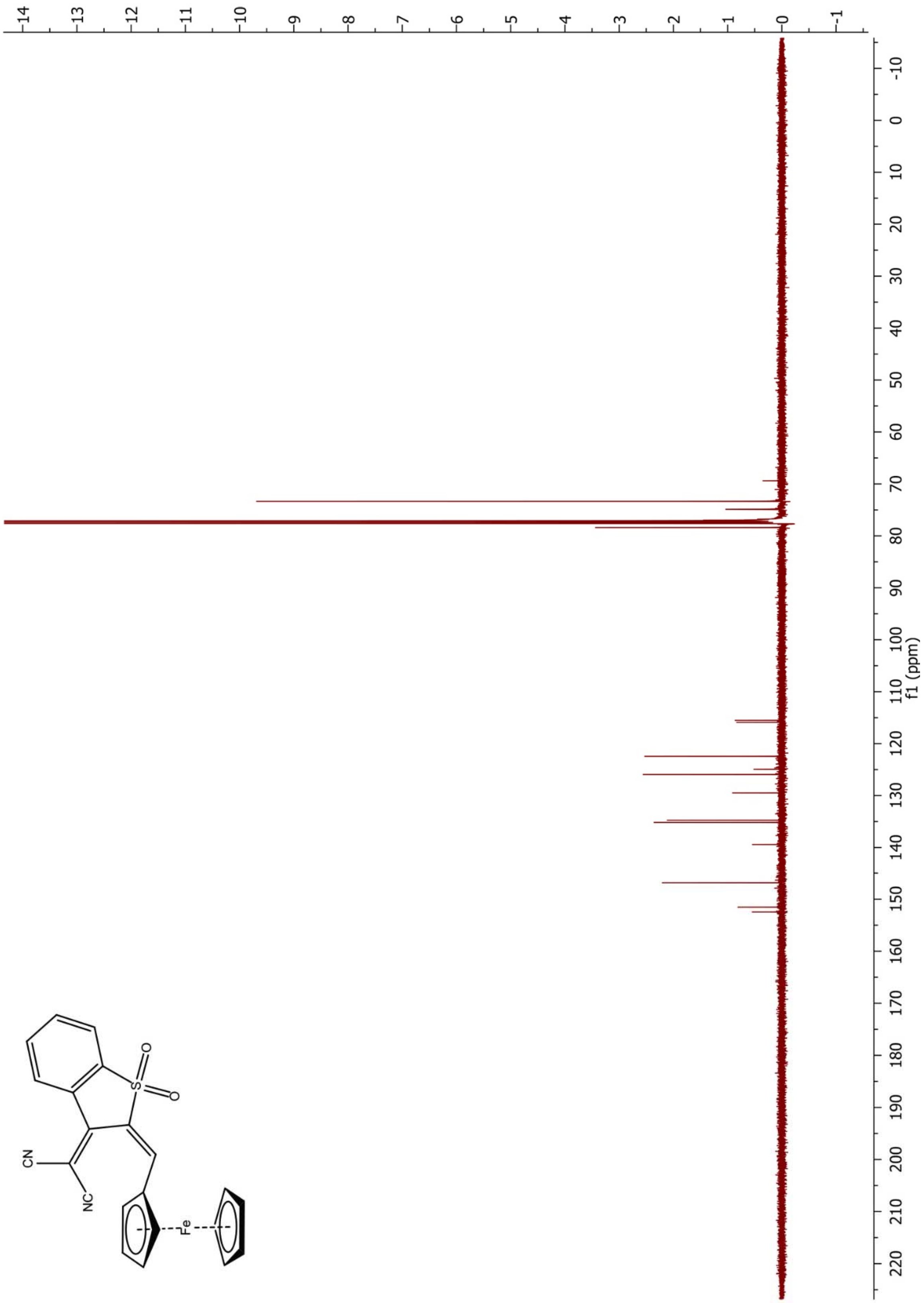

Figure 2.47. $^{13}C\{^1H\}$ NMR of compound **29** (126 MHz, $CDCl_3$).

G. Appendix 2 (Crystal Structures Refinement Data)

Table 2.12. Crystal data for **18**.

Identification code	oconn_ferro_a
Empirical formula	2 (C_{26} H_{20} Fe I_2 O_2)
Formula weight	2743.65
Temperature	100 (2) K
Wavelength	0.71073 Å
Crystal system	monoclinic
Space group	P 1 21 1
Unit cell dimensions	a = 6.0822(17) Å α = 90° b = 21.941(6) Å β = 101.100(10) ° c = 8.470(2) Å γ = 90°
Volume	1109.2(5) $Å^3$
Z	1
Density (calculated)	4.107 g/cm^3
Absorption coefficient	14.179 mm^{-1}
F(000)	1199
Crystal size	Not measured
Crystal color, habit	Reddish block
Theta range for data collection	2.450 to 25.766°
Index ranges	-7<=h<=6, -22<=k<=26, -10<=l<=10
Reflections collected	11092
Independent reflections	3464 [R(int) = 0.0219, R(sigma) = 0.0245]
Completeness to theta = 25.00°	99.7 %
Absorption correction	none
Max. and min. transmission	0.0921 and 0.0620
Refinement method	Full-matrix least-squares on F^2
Data / restraints / parameters	3464 / 1 / 81
Goodness of fit on F^2	1.035
Final R indices [I>2sigma(I)]	R1 = 0.0183, wR2 = 0.0419
R indices (all data)	R1 = 0.0189, wR2 = 0.0422
Largest diff. peak and hole	0.504 and -0.357 e. $Å^{-3}$

Table 2.13. Crystal data for **19**.

Identification code	Rlh3203
Empirical formula	C60 H46 Fe I2 O2 P2
Formula weight	1170.56
Temperature	100 (2) K
Wavelength	0.71073 Å
Crystal system	triclinic
Space group	P -1
Unit cell dimensions	a = 12.5824(13) Å α = 79.453(5)° b = 14.1169(2) Å β = 76.799(5) ° c = 17.8519(2) Å γ = 80.520(4)°
Volume	3009.9(5) Å^3
Z	2
Density (calculated)	1.292 g/cm^3
Absorption coefficient	1.366 mm^{-1}
F(000)	1168
Crystal size	Not measured
Crystal color, habit	Red block
Theta range for data collection	1.185 to 25.785°
Index ranges	-14<=h<=15, -16<=k<=17, 0<=l<=21
Reflections collected	18361
Independent reflections	11505 [R(int) = 0.1181]
Completeness to theta = 25.00°	100 %
Absorption correction	none
Max. and min. transmission	0.7452 and 0.6812
Refinement method	Full-matrix least-squares on F^2
Data / restraints / parameters	11505 / 606 / 580
Goodness of fit on F^2	2.3576
Final R indices [I>2sigma(I)]	R1 = 0.1803, wR2 = 0.4104
R indices (all data)	R1 = 0.2230, wR2 = 0.4329
Largest diff. peak and hole	11.254 and -3.597 e. Å^{-3}

Table 2.14. Crystal data for **28**.

Identification code	Ocon137
Empirical formula	C27 H20 Fe O
Formula weight	416.28
Temperature	100 (2) K
Wavelength	0.71073 Å
Crystal system	orthorhombic
Space group	P b c a
Unit cell dimensions	a = 11.1591(6) Å α = 90° b = 12.9909(8) Å β = 90 ° c = 26.3431(18) Å γ = 90°
Volume	3818.9(4) Å^3
Z	8
Density (calculated)	1.448 g/cm^3
Absorption coefficient	0.806 mm^{-1}
F(000)	1728
Crystal size	0.330 x 0.270 x 0.070 mm^3
Crystal color, habit	Red plate
Theta range for data collection	2.392 to 27.527°
Index ranges	-14<=h<=10, -16<=k<=15, -16<=l<=34
Reflections collected	15691
Independent reflections	4361 [R(int) = 0.0654]
Completeness to theta = 25.00°	99.8 %
Absorption correction	Multi-scan
Max. and min. transmission	0.939 and 0.777
Refinement method	Full-matrix least-squares on F^2
Data / restraints / parameters	4361 / 0 / 262
Goodness of fit on F^2	1.001
Final R indices [I>2sigma(I)]	R1 = 0.0425, wR2 = 0.1006
R indices (all data)	R1 = 0.0732, wR2 = 0.1194
Largest diff. peak and hole	0.566 and -0.412 e.Å^{-3}

H. References

1. Gasser, G.; Ott, I.; Metzler-Nolte, N. *J.Med.Chem.* **2011**, *54*, 3-25.

2. Martins, P.; Marques, M.; Coito, L.; Pombeiro, A. J. L.; Baptista, P. V.; Feranandes, A. R. *AntiCancer Agents Med. Chem.* **2014**, *14*, 1199-1212.

3. Jakupec, M. A.; Galanski, M.; Arion, V. B.; Hartinger, C.G; Keppler, B. K. *Dalton Trans*. **2008**, *2*, 183-194.

4. Wang, D.; Lippard, S. J. *Nat. Rev. Drug Discovery*.**2005**, *4*, 307-320.

5. Ornelas, C.; *New J. Chem.* **2011**, *35*, 1973-1985.

6. Patra, M.; Gasser, G. *Nature Rev. Chem.* **2017**, *1*, 1-12.

7. Fiorina, V. J.; Dubois, R. J.; Brynes, S. *J. Med. Chem.* **1978**, *21*, 393-395.

8. Köpf-Maier, P.; Köpf, H.; Neuse, E. W.; *J. Cancer Res. CLin. Oncol.* **1984**, *108*, 336-340.

9. Neuse, E. W. *J. Inorg. Organomet. Chem.* **2005**, *15*, 3-32.

10. Tamura, H.; Miwa, M. *Chem. Lett.* **1997**, 1177-1178.

11. Houlton, A.; Roberts, R. M. G.; Silver, J. *J. Organomet. Chem.* **2004**, *418*, 107-112.

12. Osella, D.; Ferrali, M.; Zanello, P.; Laschi, F.; Fontani, M.; Nervi, C.; Cavigiolio, G. *Inorg. Chim. Acta*, **2000**, *306*, 42-48.

13. Nguyen, A.; Vessières, A.; Hillard, E. A.; Top, S.; Pigeon, P.; Jaouen, G. *Chimia*, **2007**, *61*, 716-724.

14. Hillard, E. A,; Vessières, A.; Jaouen, G. *Top. Organomet. Chem*. **2010**, *32*, 81-117

15. Top, S.; Tang, J.; Vessières, A.; Carrez, D.; Provot, C.; Jaouen, G. *Chem. Commun.* **1996**, 955-956.

16. Vessières, A.; Corbet, C.; Heldt, J. M.; Lories, N.; Jouy, N.; Laïos, I.; Leclercq, G.; Jaouen, G.; Toillon, R. A. *J. Inorg. Biochem.* **2010**, *104*, 503.

17. Yamaguchi, Y.; Kutal, C. *Inorg. Chem.* **1999**, *38*, 4861.

18. Yamaguchi, Y.; Ding, W.; Sanderson, C. T.; Boden, M. L.; Morgan, M. J.; Kutal, C. *Coord. Chem Rev.* **2007**, *251*, 515.

19. Ding, W.; Sanderson, C. T.; Conover, R.C.; Johnson, M. K.; Amster, I. J.; Kutal, C. *Inorg. Chem*. **2003**, *42,* 1532.

20. Torti, S. V.; Torti, F. M. *Nat Rev Cancer*. **2013**, *13*, 342-355.

21. Haber, F.; Weiss, J. *Naturwissenschaften*. **1932**, *20*, 948-950.

22. Kehrer, J. P.; *Toxicology*. **2000**, *149*, 43-50.

23. Liou, G.-Y.; Storz, P. *Free Radic Res.* **2010**, *44*, 479-496.

24. Aubrey, M. Organoferrous Antitumor Agents, PhD Dissertation, University of California San Diego, San Diego, CA, 2015.

25. Frantz, M.-C.; Wipf, P. *Environ Mol Mutagen.* **2010**, *51*, 462-475.

26. Han, M.; Vakili, M. R.; Soleymani Abyaneh, H.; Molvai, O.; Lai, R.; Lavasanifar, A. *Mol Pharm*. **2014**, *11*, 2640-2649.

27. Yamaguchi, Y.; Kutal, C. *Macromolecules*. **2000**, *33*, 1152-1156.

28. Robertson, T. A.; Bunel, F.; Roberts, M. S. *Cells.* **2013**, *2*, 591-606.

29. Munishkina L. A.; Fink, A. L.; *Biochimica et Biophysica Acta.* **2007**, *1768*, 1862-1885.

30. Toyo'oka, T.; Watanabe, Y.; Imai, K. *Analytica Chimica Acta*. **1983**, *149*, 305-312.

31. Feoktistova, M.; Geserick, P.; Leverkus, M. *Cold Spring Harb Protoc*. **2016**, doi:10.1101/pdb.prot087379.

32. Shotton, D.; *J. Cell Science.* **1989**, 175-206.

33. Kapuscinski, J. *Biotech Histochem*. **1995**, *70*, 220-233.

34. Sigle, W. *Annu. Rev. Mater. Res.* **2005**, *35*, 239-314.

35. Bradford, M. M. *Anal. Biochem.* **1976**, *72*, 248.

36. Aron, A. T.; Loehr M. O.; Bogena, J.; Chang, C. J. *J. Am. Chem. Soc.* **2016**, *138*, 14338-14346.

37. Attar, S.; O'Brein, Z.; Alhaddad, H.; Golden, M. L.; Calderón-Urrea, A. *Bioorg. Med. Chem*. **2011**, *19*, 2055-2073.

38. Barlow, S.; Bunting, H. E.; Ringham, C.; Green, J. C.; Bublitz, G. U.;Boxer, S. G.; Perry, J. W.; Marder, S. R. *J. Am. Chem. Soc.* **1999**, *121*, 3715-3723.

39. Zhang, C.; *Protein Cell.* **2014**, *5*, 750-760.

40. Crichton, R. *Iron Metabolism*; 3rd ed.; Wiley: West Sussex U.K., 2009.

41. Halliwell, B.; Gutteridge, J. M. *Biochem. J.* **1984**, *219*, 1-14.

42. Pierre, J. L.; Fontecave, M. *BioMetals*. **1999**, *12,* 195-199.

43. McCord, J. M.; Fridovich, I.; *J. Biol. Chem.* **1969**, *244*, 6049-6055.

44. Lipson, R. L.; Baldes, E. J. *Arch. Dermatol.* **1960**, *82*, 508-516.

45. Lipson, R. L.; Baldes E. J.; Olsen, A. M. *J. Natl Cance Inst.* **1961**, *26*, 1-11.

46. Schwartz, S. K.; Abolin, K.; Vermund, H. *Univ. Minn. Med. Bul*. **1955**, *27*, 7-8.

47. Huang, Z. *Technol. Cancer Res. Treat.* **2005**, *4*, 283-293.

48. Golnick, K *Advanc.Photochem*. **1968**, *6*, 1-122.

49. Moan, J. Peng, Q. In *Photodynamic Therapy*; Patrice,T., Ed.; 2003; pp. 1-18.

50. Stacey, O. J.; Pope, S. J. *RSC Adv.* **2013**, *3*, 25550-255564.

51. Hu, J.; Dong, L.; Outten, C. *J. Biol. Chem.* **2008**, *283*, 29126-29134.

52. Acharya, A.; Das, I.; Chandhok, D.; Saha, T. *Oxid. Med. Cel. Longev.* **2010** *3,* 23-34.

53. Bingham, E.; Cohrssen, B.; Powell, C. H.; *Patty's Toxicology Volumes 1-9*; 5th ed.; John Wiley & Sons: New York, N.Y., 2001, p.4:189.

54. Zor, T.; Selinger, Z. *Anal. Biochem*. **1996**,*236*, 302-308.

55. Serbinova, E.; Kagan, V.; Han, D.; Packer, L *Free. Radic. Biol. Med.* **1991** *10* 263-275.

56. Dolmans D. E.; Fukumura, D.; Jain, R. K. *Nature Reviews Cancer*. **2003**, *3*, 380-387.

Chapter III

Ferroptosis and Benzoylferrocene Derivatives

A. Introduction

Ferroptosis is a relatively recent concept, originating in 2012 from the lab of Dr. Brent R. Stockwell, as a distinct form of regulated cell death.[1] Ferroptosis is an iron dependent, non-apoptotic, regulated form of cell death by lipid peroxidation that is genetically, biochemically, and morphologically distinct from other forms of regulated cell death.[1-4] It involves metabolic dysfunction that results in the production of both cytosolic and lipid reactive oxygen species (ROS). While ferroptosis is a recent area of study, ferroptosis inducers were discovered nearly a decade before. In 2003, Stockwell's group at Columbia University found erastin (**30**) to be synthetically lethal in engineered tumorigenic BJeLR cells but not the isogenic primary fibroblast cells.[5,6] BJeLR cells are genetically engineered from human foreskin fibroblast cells to express the *RAS* oncogene mutant HRAS^{G12V}. Later in 2008, they identified RSL3 (**31**) and RSL5 (**32**) in another high throughput small-molecule screening study that selectively killed BJeLR cells.[7] More recently, collaboration with Broad Institute's Schreiber and Munoz, led to the design of two new molecules, ML162 (**33**) and ML210 (**34**), which also exhibit selectivity for BJeLR cells, which express HRAS^{G12V}, over cells that do not express the RAS oncogenic mutation, BJeH-LT and BJeH (BJeH-LT, which are isogenic to BJeLR without HRAS^{G12V}, and BJeH which are immortalized background cell lines).[8] RAS proteins are essential components in signaling networks that control cellular proliferation, differentiation and survival. Mutations in the protein can lead to human tumor development, as they lead to an imbalance of cellular proliferation signaling pathways, leading to uninterrupted cell growth.[9]

Key regulators of ferroptosis remained unknown until Stockwell and Schreiber reported in 2014 that depletion of glutathione caused inactivation of glutathione peroxidases (GPxs), more specifically GPx4, resulted in ferroptosis.[10] GPx4 is an enzyme with antioxidant properties that protects the cell against lipid peroxidation by decreasing high ROS levels.[11] Studies have indicated that inhibition of GPx4 leads to lipid ROS and ferroptosis.[2,10]

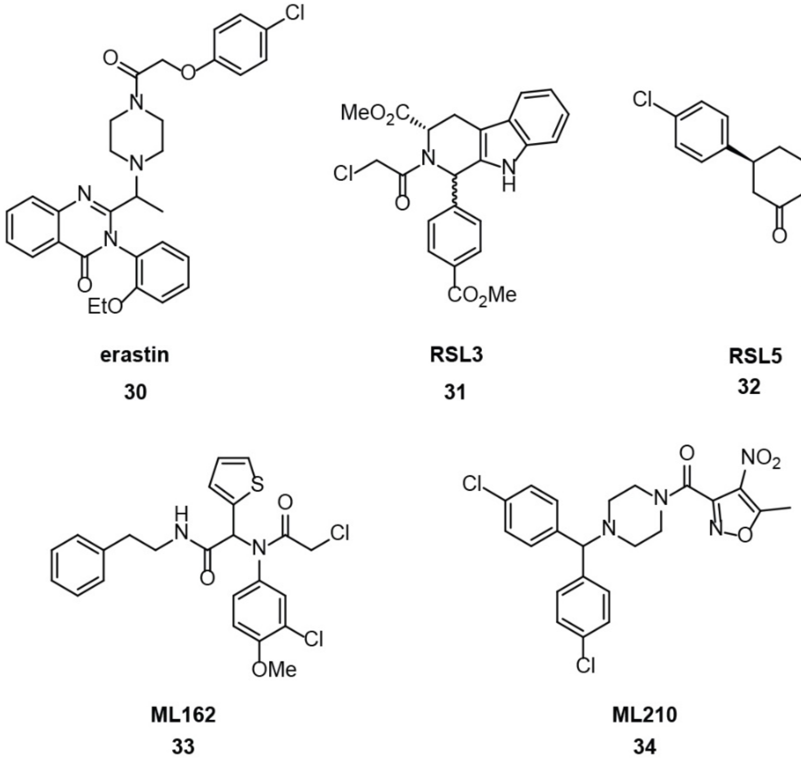

erastin
30

RSL3
31

RSL5
32

ML162
33

ML210
34

Figure 3.1. Structures of previously reported ferroptosis inducing compounds.

Initial mechanistic studies to further elucidate the mechanism of GPx4-regulated ferroptosis were performed on **30** and **31**.[10] Erastin (**30**) was found to inhibit system x_c^-,[1] the glutamate/cysteine antiporter which mediates the exchange of extracellular L-cystine and intracellular L-glutamate across the cell membrane.[12,13] This in turn would cause intracellular depletion of the cysteine pool, a precursor for glutathione synthesis.[10] The loss of glutathione results in a loss of cellular antioxidant capacity as well as inhibition of glutathione-dependent enzymes such as glutathione peroxidases.[10,11] In comparison, RSL3 (**31**) inhibits GPx4 directly.[2,10] Recent studies by Schreiber *et al*. also indicate that ML210 (**34**) inhibits GPx4 directly. Compound **34** was determined to be highly active in therapy-resistant cancer cells with a high-mesenchymal state.[13] A high mesenchymal cell state detected in human tumors and cancer cell lines has been associated with treatment resistance.[15-17] Compound **34** was found to be highly toxic in therapy resistant cancers by targeting the mesenchymal state acting on the lipid-peroxidase pathway and GPx4.

Based off these precedents, we wanted to design and synthesize an organoferrous analogue of compound **34** such that we could apply it to a broader spectrum of cancer cell lines, as their results were shown in human engineered BJ fibroblast cell transformations and high-mesenchymal state cancer lines. Studies have shown compound **34** to be intracellularly inhibiting GPx4, leading us to speculate that conjugating a ferrocenyl moiety to a derivative of compound **34** would induce ferroptosis. Photolysis of **41** (Scheme 3.1) would generate free iron(II), leading to higher intracellular ROS level, and simultaneously liberate a GPx4 inhibitor.

Our goals were to: (1) synthesize organoferrous analogue **41** and determine biological activity; (2) run cytotoxicity assays on **34**, as it has not been determined for our cell lines; and (3) run cytotoxicity assays with our lead compound from Chapter II, 1,1'-bis(4-pentyl)benzoyl ferrocene (**16**; Figure 3.2), in conjunction with **34** to determine if we could increase the cytotoxicity previously observed for **16**.

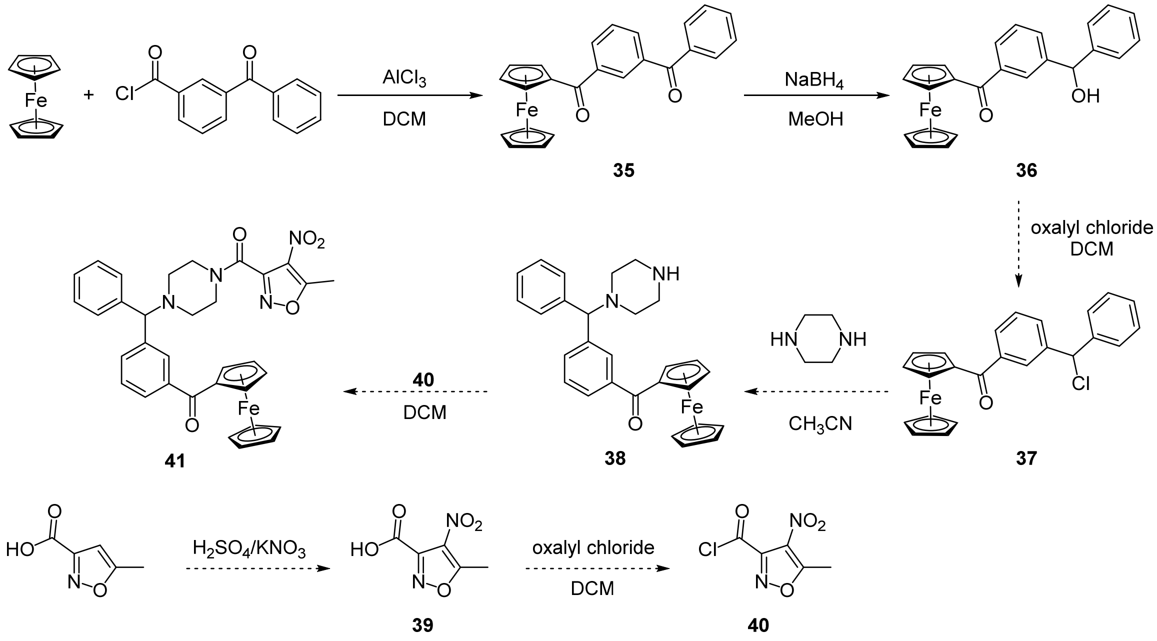

Scheme 3.1. Proposed synthetic scheme for organoferrous compound **41**.

The transformation from **35** to **41** of the proposed synthesis (Figure 3.2) is based on Schreiber's synthesis of **34**.[18]

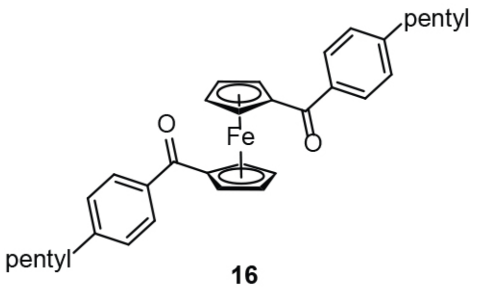

16

Figure 3.2. Lead compound **16**.

B. Results

1. Cytotoxicity Studies on 34 and 34 + 16 together

Cytotoxicity assays of compound **34** were first performed since it has not been reported for HeLa and Caov3 cancer cell lines. We were also curious if there would be a significant difference when treating **34** in combination with an iron source such as lead compound **16**. Cytotoxicity assays utilizing the same standard protocol developed for the organoferrous compounds listed in Chapter 2 were employed. With compound **34**, assays under light and dark conditions were performed as a control, with the assumption of no cytotoxicity difference between the two conditions. Comparison of cytotoxicity due to the combination of **34** and **16** to that cells independently treated with ML210 (**34**) and 1,1'-bis(4-pentyl)benzoyl ferrocene (**16**) could be therefore be performed.[19] Compound **34** exhibited no cytotoxicity in HeLa cells up to 200 µM under both light and dark conditions, while treatment in Caov3 resulted in an IC_{50} value of 42±6.4 µM in the light and 46.3±5.9 µM in the dark (Table 3.1). As both numbers were within the standard deviation range, we conclude there was no difference in light and dark toxicity for compound **34** in Caov3 cell lines. As the HeLa cell line displayed no cytotoxicity with compound **34**, we employed HeLa cells for our initial cytotoxicity studies using a combination of compounds **16** and **34**.

Table 3.1. Cytotoxicity of **16**, **34**, and **16+34**

	IC_{50} light values (µM)		**IC_{50} dark values (µM)**	
Compound	**HeLa**	**Caov3**	**HeLa**	**Caov3**
16	16.8±2.3	1.8±0.2	>100	>100
34	>200	>200	46.3±5.9	42±6.4
16 + 34*	7.1±0.5	n.d.	>100	n.d.

*values determined in relation to compound **16** as there was a constant concentration of 31.25 nM of **34**. n.d. – values have yet to be determined.

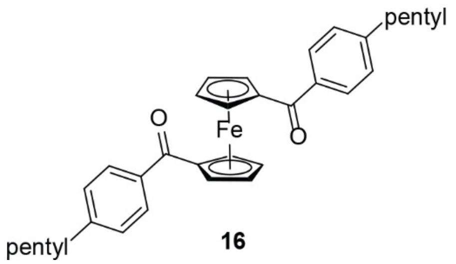

16

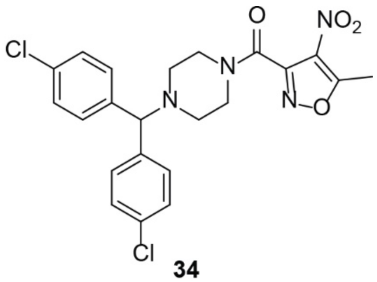

34

Cytotoxicity assays utilizing a combination of **16** and **34** were first run using six concentration of **34** between 1.0 µM and 31.25 nM in half concentration increments while keeping **16** constant at 50 μM. Assays run under light conditions resulted in complete cell death, while cells treated under dark conditions exhibited no cytotoxicity. We then chose to use six concentrations of **16** between 20 μM and 625 nm in half concentration increments and kept **34** at a constant 31.25 nM. We employed a constant concentration of 31.25 nM of **34** since varying the concentration of **34** did not influence cytotoxicity when used in conjunction with 50 μM of **16**. Treatment of HeLa cells with varying concentrations of **16** and 31.25 nM of **34** resulted in a light IC_{50} value of 7.1±0.5 μM. There was no dark cytotoxicity up to 100 μM **16**. For ease of comparison, Table 3.1 lists these values along with the independent values for compounds **16** and **34**. We have yet to determine IC_{50} values for Caov3 cells when treated with varying concentrations of **16** and 31.25 nM **34**.

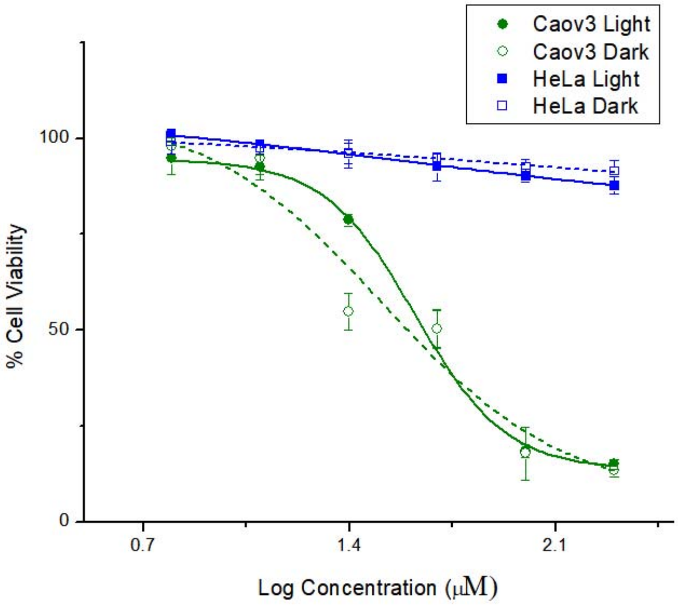

Figure 3.3. IC_{50} value graph of compound **34** in HeLa and Caov3 cells.

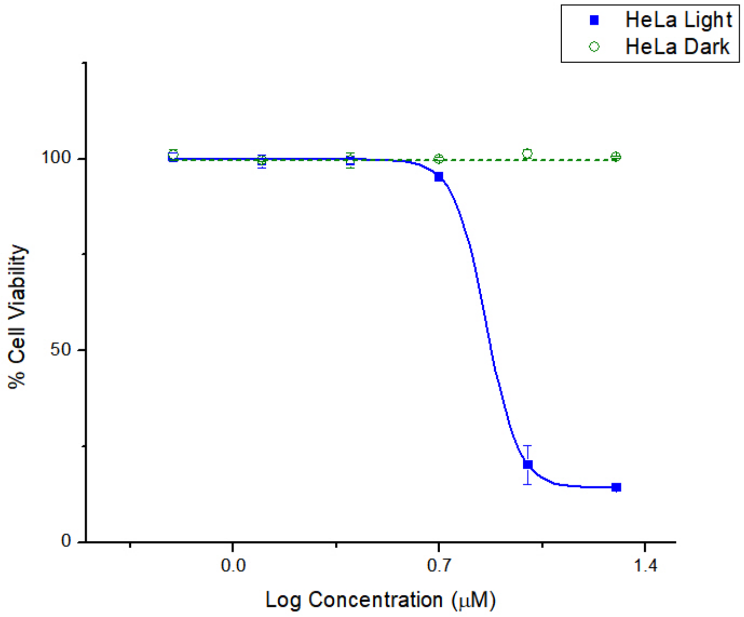

Figure 3.4. IC_{50} value graph of compounds **16** and **34** in HeLa cells.

2. Towards a synthesis of 41

The presence of a benzophenone moiety in compound **34** led us to first design a synthesis of **41** wherein the ferrocenoyl chloride would be conjugated to the benzophenone through a Friedel-Crafts reaction as shown in Scheme 3.2. Ferrocenecarboxaldehyde was converted to acid chloride in neat thionyl chloride (Δ_r, 6 h). After removal of excess thionyl chloride to afford an oil acid chloride product, the acid chloride was immediately treated with benzophenone and $AlCl_3$ in DCM under reflux conditions. TLC analysis indicated that no reaction had occurred, and a ^1H NMR spectrum of the crude reaction mixture exhibited resonances for starting material with no evidence for the presence of **35**. We therefore decided to use a benzophenone derivative as the acid chloride component in a Friedel-Crafts reaction with ferrocene, as shown in Scheme 3.1.

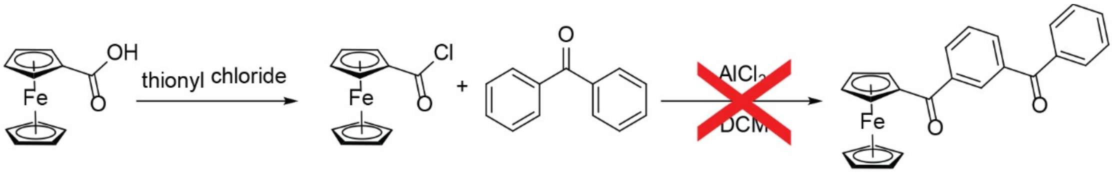

36

Scheme 3.2. Original failed synthetic route.

Treatment of 3-benzoylbenzoic acid with neat thionyl chloride (Δ_r, 6 h) afforded the 3-benzoyl benzoylchloride starting material shown in Scheme 3.1. Friedel-Crafts acylation with ferrocene using $AlCl_3$ in DCM resulted in compound **35**, as determined by ^1H NMR spectroscopic analysis of the product. Compound **35** has two carbonyl functional groups: one between a ferrocenyl and a phenyl ring, and one between two phenyls. Since ferrocene is more electron-donating than a phenyl, we believed that treatment with sodium borohydride would lead to selective reduction of the carbonyl bearing two phenyl groups. In order to minimize potential side reactions, such as reduction of the second ketone after the first ketone reduction, we employed a 0.8:1 ratio of $NaBH_4$ to **35**, and closely monitored the reaction by TLC. After $NaBH_4$ was added to a solution of **35** in ethanol at 0 °C, the reaction was immediately taken out of the ice bath and allowed to warm to room temperature for 30 minutes. The reaction mixture must be warmed to room temperature in order for the reaction to proceed, as determined by TLC analysis. When the reaction was allowed to proceed for more than 30 minutes at room temperature, the solution color turned to dark brown (after 1 h) and decomposition was observed by TLC analysis. The crude reaction mixture was then quenched with saturated NH_4Cl and extracted with DCM. After removal of excess solvent, the crude mixture was purified by preparatory TLC, with purity determined by ^1H NMR spectroscopic analysis of the isolated product. HMBC NMR spectroscopic analysis of **36** confirmed that compound **35** was selectively reduced at the carbonyl positioned between the two phenyl rings. Conversion of **36** to **41** is currently underway.

C. Discussion

Ferroptosis is an increasingly popular field of study even though it has been only recently characterized as a distinct form of cell death.[20] Current literature on ferroptosis is focused on small synthetic molecules that either directly target the antioxidant GPx4 enzyme or indirectly shut down the GPx4 enzyme in tumor cells which display the RAS mutation, which is found in approximately 30% of all tumors screened to date.[10,20-21] Recent studies have also demonstrate that targeting GPx4 inhibition of ROS represents a promising strategy to treat cancer cells that are resistant to current anticancer treatments.[22] The development of bioavailable GPx4 inhibitors is therefore a huge priority in anticancer research. It was reported that both erastin (**30)** and ML210 (**34**), direct inhibitors of GPx4, have very poor bioavailability (defined as extent and rate at which an active moiety enters systemic circulation).[22] Our reason for targeting the synthesis of compound **41** are twofold: (1) to increase bioavailability with the addition of a lipophilic ferrocenyl conjugate so that it may cross the cell membrane without difficulty,[23] and (2) to develop a novel photodynamic therapy approach toward cancer treatment based on the photochemical properties of benzoylferrocene derivatives. As highlighted in Chapter II, traditional photodynamic therapy uses non-toxic photosensitizers and visible light with intracellular oxygen to produce cytotoxic reactive oxygen species (ROS).[24] In this traditional method, a constant light source is needed for continuous generation of the cytotoxic ROS species, whereas our new methodology would generate free iron(II) that would operate in a catalytic cycle via the Haber-Weiss reaction, even after irradiation has ended (Figure 3.5). We speculated that, based on ferroptosis and photodynamic therapy literature precedents, we could develop a photoactivated drug for a general treatment of all cancer cell types instead of selectivey RAS mutation tumors.

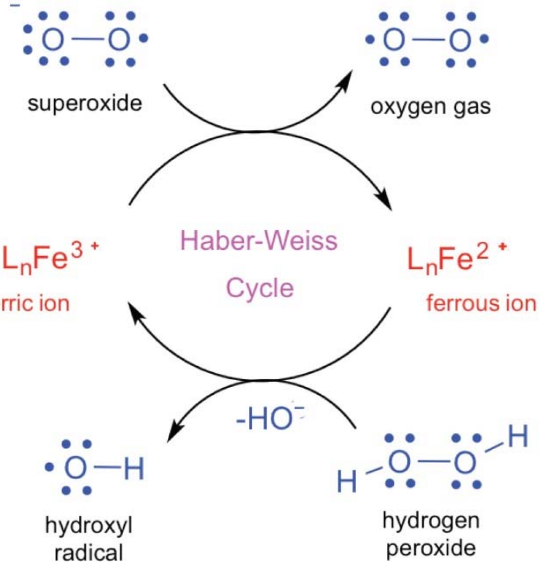

Figure 3.5. The Haber-Weiss catalytic cycle.

Independent treatment of ML210 (**34**) in HeLa and Caov3 indicated that **34** is more toxic to ovarian cancer Caov3 than to HeLa cells. Compound **34** exhibited an IC_{50} value of approximately 44 μM (average of light and dark cytotoxicity since is there is no significant difference between the light and dark cytotoxicity values), whereas no toxicity was seen in HeLa cells. The IC_{50} value of **34** in Caov3 was much higher than anticipated, as the IC_{50} was previously reported as 71 nM in the human engineered BJeLR cell lines.[8] We speculate that the higher literature cytotoxicity is due to the fact that the cell lines treated with **34** were humanly engineered to express RAS mutations. It has been hypothesized that RAS-transformed fibroblasts are under higher levels of oxidative stress,[25] which could explain the greater cytotoxicity in the engineered cells, especially when the antioxidant GPx4 enzyme is inhibited. HeLa cells treated with **34** exhibited no cytotoxicity, which we attribute to the lack of RAS mutation, as HeLa cells carry wild-type *RAS* genes.[26] The difference in cytotoxicity of **34** toward Caov3 and HeLa cell lines is most likely due to the p53 gene and protein mutation in Caov3.[27-28] In 2015, Jiang *et al.* reported that the mutations in tumor protein p53, a protein that regulates the cell cycle, can sensitize cells to ferroptosis by suppression of SLCA7AA, a component of system x_c^-.[29] As HeLa cells do not contain the p53 mutation,[30] we hypothesizes that treatment of p53 mutation cells, such as Caov3, with **34** could lead to ferroptosis by intracellular iron toxicity, explaining the lack of toxicity in HeLa cells.

As we are currently working towards the synthesis of compound **41**, we still wanted to test whether treatment of cells with **34** and a benzoylferrocene derivative would generate greater toxicity. Therefore, HeLa cells were treated with a combination of **34** and **16**. Cytotoxicity assays were run with HeLa cells first as no toxicity was observed when HeLa cells were treated with compound **34**, and **16** was less toxic in HeLa cells than in Caov3 cells. We hypothesized that since compound **34** would shut down the antioxidant pathway of cell reparation, and the generation of free iron(II) *in situ* would lead to elevated ROS levels, greater cytotoxicity would result. Our hypothesis is supported by the greater than 2-fold increase in HeLa cell cytotoxicity that was observed when cells were treated with a combination of **16** and **34** vs. only **16** under irradiation conditions (Table 3.1). There was no observed cytotoxicity under dark conditions, suggesting that our compound acts through a redox pathway involving free iron(II) instead of intact organoferrous compound **16**. We have yet to determine an IC_{50} value for treatment of the cells with a combination of **16** and **34** in Caov3 cells. This is due to difficulty in determining concentration points such that the cells are 90% viable at two concentrations, 90% death at two concentrations, and two points in between, such that we can generate an IC_{50} value graph.

The synthesis of **41** required starting material **35**. In our first attempt at the synthesis of **35**, we sought to couple a ferrocenoyl chloride to benzophenone under Friedel-Crafts acylation conditions, but no product was observed. This is possibly due to the electron-withdrawing nature of the phenyl ring, making the benzene less nucleophilic. We then decided to employ the more electron-rich ferrocene as the nucleophile in the substitution reaction. 3-Benzoylbenzoic acid was first treated with thionyl chloride to give 3-benzoyl benzoylchloride, which was then treated with ferrocene and $AlCl_3$ in DCM to afford **35** (43% yield over two steps). The structure of compound **35** was established by ^1H NMR analysis. In the ^1H NMR spectrum of 35, two triplets integrating to 2H each at δ 4.60 and 4.87 ppm are assigned to the substituted Cp ring hydrogens, and a singlet at 4.17 (5H) is assigned to the hydrogens of the unsubstituted cyclopentadienyl ring. The triplet at δ 7.51 ppm integrating to 2H corresponds to the two equivalent phenyl protons in the meta-position to carbonyl functional group. The multiplets at δ 7.61 ppm integrating to 2H is assigned to the one proton in the ortho-position (with a neighboring H) to the benzoyl ferrocene carbonyl and the other in the para position to the benzoyl ferrocene carbonyl. The 2H integration at δ 7.84 ppm and a doublet correspond to the two equivalent protons in the ortho-position from the carbonyl of the phenyl ring at the end. The proton at δ 8.08 ppm exhibits at doublet peak and was assigned as the proton in the para-position from the carbonyl of the phenyl rig at the end. The proton peak at δ 8.5 ppm is a singlet and assigned to the hydrogen at the other ortho-position of the benzoyl ferrocene carbonyl. We then synthesized compound **36** (Figure 3.6) by reduction of **35** using sodium borohydride (0.8 equiv) as the limiting reagent in order to reduce only one ketone. The reaction was left to stir for 30 minutes before TLC analysis. TLC analysis showed one major product, the presence of some starting material, and some decomposition product(s) at the baseline. The reaction was therefore quenched after 30 minutes by slow addition of a saturated ammonium chloride solution to the reaction mixture. After purification, a ^{1}H NMR spectrum of the sample exhibited a singlet at 5.87 ppm (1H, C*H*OH), which established that reduction of one of the ketones has occurred. However, the ^{1}H NMR data did not establish which carbonyl group had been reduced. We therefore carried out a Heteronuclear Multiple Bond Correlation (HMBC) NMR experiment, which gives correlations between carbon and proton nuclei that are separated by two or three bonds, sometimes even four in a conjugated system. As can be seen in the HMBC spectrum (Appendix, Figure 3.11), the proton at C13, with a ^{1}H NMR resonance at δ 5.87 correlates to three ^{13}C NMR resonances within the aromatic region between 120-150 ppm, with no observed correlation to ferrocenyl carbons C2 and C5 within the 70-80 ppm region. The HMBC analysis provides one form of proof of reduction ketone at C13. A full characterization including FTIR will be obtained in order to provide further support for the assigned structure.

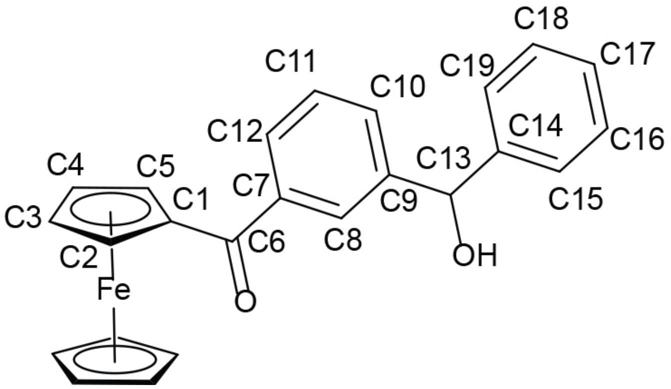

Figure 3.6. Numbered carbon of structure **36**.

While we currently have not finished the synthesis of compound **41**, and have only synthesized up to compound **36**, we believe that we can closely follow the Schreiber *et al.* synthetic route[21] as the ferrocenyl moiety is not too bulky to cause steric hindrance throughout the rest of the synthesis. A full characterization of compound **35** and **36** is needed if the synthetic route in **Scheme 3.1** does not contain any detrimental reactions such that we can successfully synthesize **41**. If the ferrocenyl moiety in the meta-position proves to be sterically hindering and a detriment to the synthetic scheme, we can modify it by starting with 4-benzoylbenzoic acid such that the ferrocenyl group is in the para-position and opposite from where any synthetic activity would occur (Figure 3.7). We hope that **41** will exhibit HeLa cell line cytotoxicity values in the nanomolar range under irradiation conditions, with no cytotoxicity in the dark.

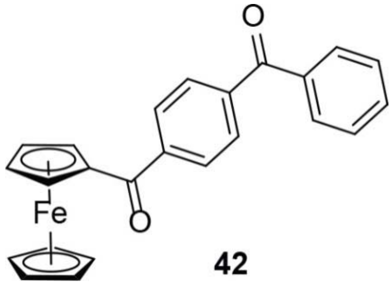

42

Figure 3.7. Alternative starting material **42** instead of **35**.

D. Conclusion

We speculate that the internalized cytotoxic organoferrous molecules used in Chapter II could be causing cell death by induction of ferroptosis. Interestingly, when HeLa cells are treated with ML210 (**34**), there was no observed cytotoxicity, as ferroptosis was not induced. However, treatment of **34** in combination with bis(pentyl) complex **16**, lead to a significant increase in cytotoxicity compared to independent treatment with **16**, which could be due to ferroptosis induction. Further studies are needed in order to show lipid ROS generation with those compounds **16** and **34**. In addition, higher quality TEM images are needed in order to determine if the observed morphological changes are in line with those previously reported.[1] As ferroptosis involves iron-dependent lipid peroxidation, we need to determine whether there is generation of higher lipid ROS in the cells. Pauline Olsen, another graduate student in the O'Connor lab, is currently working on determination of ROS species in cells and lipid peroxidation. Ferroptosis is characterized by decreased cell volume and mitochondrial shrinkage, as well as increased mitochondrial membrane density.[1,7] Additional high resolution TEM images of the cells are therefore needed in order to establish mitochondria size and membrane density.

In future studies, it would be interesting to run cytotoxicity assays with compounds **16** and **34**, independently and also in combination, for lung carcinoma A549 cell lines due to the known fact that A549 cell lines have KRAS protein mutations. While KRAS is different from the HRAS mutations, it would be interesting to compare the values to Stockwell's human engineered BJeLR HRAS mutation cell lines.[5,7,10] We hope to utilize the photochemical properties of our organoferrous complexes to create a generalized and broader approach to cancer treatment instead of selectively targeting *RAS* gene mutation that is found in 30% of all human tumors.[20] If we can utilize the adventitious properties of **34**, which is not cytotoxic across all tumor types but is known to shut down the antioxidant pathway of GPx4[1,2,10], and couple it to a ferrocenyl complex, as in **41**, it may be possible to overload tumor cells with ROS species generated by free iron(II). As cancer cells have a higher ROS state compared to normal cells[31], we speculate that shutting down the pathway to deal with cellular ROS would be more detrimental to cancer cells than to normal cells. It will therefore be interesting to test ML210 (**34)** and our synthesized compounds, such as lead compound **16**, in noncancerous cells to compare this difference.

E. Experimentals

General Methods

All synthetic reagents were purchased from Aldrich, Fisher Scientific, or Alfa Aesar, and were used without further purification. All solvents for anhydrous reactions were obtained from Fisher scientific and dried on alumina columns prior to use. All reactions were performed under N_2 or argon using standard Schlenk techniques unless otherwise noted. Solvents used for chromatography were ACS technical grade and used without further purification. Water (18.2 μΩ/cm) was filtered through a NANOPure DiamondTM (Barnstead) water purification system before use. All ^{1}H NMR and ^{13}C NMR spectra were recorded on a Varian Mercury Plus 400 MHz NMR spectrometer or a Varian VNMRS NMR spectrometer equipped with a 500MHz XSens Cold Probe. Deuterated solvents were purchased from Cambridge Isotopes. Chemical shifts are reported as δ in units of parts per million (ppm) referenced to the residual solvent peak. Coupling constants are reported as *J* value in Hertz (Hz).

Synthesis of Ferrocenyl Derivatives

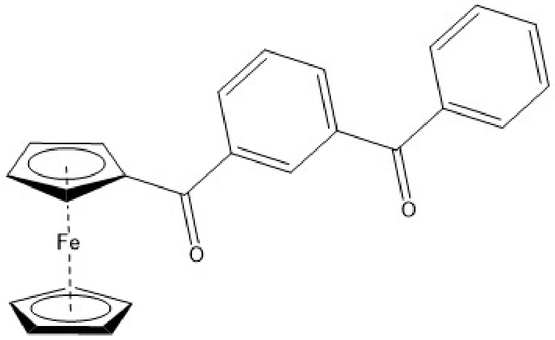

Compound 35. 3-Benzoylbenzoic acid (100 mg, 0.44 mol) was dissolved in 5 mL of neat thionyl chloride (8.2 g, 68.5 mmol, 156 equiv) in a round bottom flask equipped with a magnetic stir bar, and refluxed for 6 hours. The excess solvent was then evaporated and

the oily acid chloride was used without further purification. The acid chloride was dissolved in 5 mL of DCM, ferrocene (82 mg, 0.44 mol, 1 equiv) was added, and the reaction was heated at reflux for 24 h. After quenching the reaction mixture with 10 mL of 1M HCl, the organic layer was extracted with DCM (3 x 10 mL). The combined organic layers were then washed with brine and dried over $MgSO_4$, filtered, and the solvent was removed under reduced pressure. The crude product was purified by preparative TLC using PLC Silica gel 60 F254, 0.5mm plates with 85:15 hexanes:ethyl acetate as eluent to give 35 (75 mg) as an oil. The combined yield for the two steps was 43%. ^{1}H NMR (400 MHz, $CDCl_3$): δ 4.17 (s, 5H, CpH), 4.60 (t, $^3J_{HH}$ = 2.0 Hz, 2H, Cp'H), 4.87 (t, $^3J_{HH}$ = 2.0 Hz, 2H, Cp'H), 7.51 (t, $^3J_{HH}$ = 9.5 Hz, 2H, ArH) 7.61 (m, 2H, ArH), 7.84 (d, $^3J_{HH}$ = 9.5 Hz, 2H, ArH), 7.99 (d, $^3J_{HH}$ = 9.5 Hz, 1H, ArH), 8.08 (d, $^3J_{HH}$ = 9.5 Hz, 1H, ArH), 8.45 (s, 1H ArH). $^{13}C\{^1H\}$ NMR (100 MHz, $CDCl_3$): δ 68.24, 70.63, 71.85, 73.25, 128.57, 128.80, 128.85, 130.40, 131.25, 133.16, 133.50, 134.33, 137.35, 138.22, 196.21, 196.27. IR (KBr, cm^{-1}): 719, 974, 1252, 1444, 1599, 1657, 1718. HRMS-(ESI-TOF) (*m/z*): calcd for $[C_{24}H_{19}FeO_2]^+$, 395.0734; found, 395.0732.

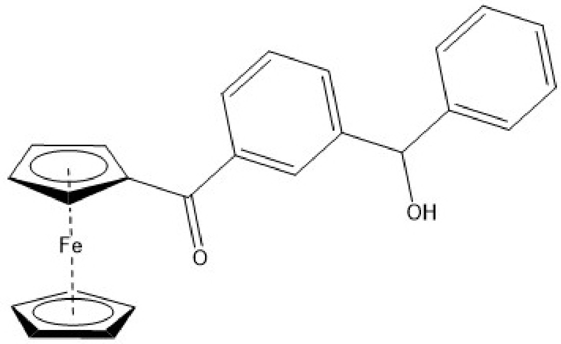

Compound 36. Compound **35** (75 mg, 0.19 mmol, 1 equiv), was dissolved in 3.8 mL of MeOH (0.05 M) in a round bottom flask equipped with a magnetic stir bar, and placed in an ice bath (0 °C). $NaBH_4$ (6 mg, 0.15 mmol, 0.8 equiv) was added and then the reaction

mixture was slowly brought to room temperature. The reaction mixture was quenched 30 minutes later by addition of 5 mL of saturated aqueous NH_4Cl. The organic products were extracted three times with 5 mL of DCM each time. The combined organic extracts were washed with brine and dried with $MgSO_4$, filtered, and the solvent was removed under reduced pressure. The crude product was purified by preparative TLC using PLC Silica gel 60 F254, 0.5mm plates with 80:20 hexanes:ethyl acetate as eluent. Yielded 31 mgs of product (41%). ^{1}H NMR (500 MHz, d_8-THF): δ 4.22 (s, 5H, Cp), 4.58 (t, $^3J_{HH}$ = 2.0 Hz, Cp'H), 4.83 (t, $^3J_{HH}$ = 2.0 Hz, Cp'H), 5.26, (br s, 1H, OH), 5.87 (s, 1H, CH), 7.22 (t, $^3J_{HH}$ = 7.8 Hz, 1H, ArH), 7.32 (t, $^3J_{HH}$ = 7.8 Hz, 2H, ArH), 7.41 (t, $^3J_{HH}$ = 7.6 Hz, 1H, ArH), 7.48 (d, $^3J_{HH}$ = 7.8 Hz, 2 H, ArH), 7.58 (d, $^3J_{HH}$ = 7.6 Hz, 1H, ArH), 7.76 (d, $^3J_{HH}$ = 7.6 Hz, 1H, ArH), 8.21 (s, 1H, ArH). $^{13}C\{^1H\}$ NMR (126 MHz, d_8-THF): δ 69.84, 71.09, 71.80, 74.94, 78.76, 126.33, 126.42, 126.47,126.76, 127.70, 127.96, 129.30, 139.66, 145.59, 145.73, 196.960. IR (KBr, cm^{-1}): 827, 908, 1019, 1047, 1138, 1290, 1371, 1443, 1577, 1627, 3417 (br). HRMS-(ESI-TOF) (*m/z*): calcd for $[C_{24}H_{21}FeO_2]^+$, 397.0886; found, 397.0884.

General Cell Culture Methods

Cell Lines and Growth Conditions: All cell lines were purchased from ATCC. HeLa, A549, and Caov-3 cells were cultivated as a monolayer cultures at 37 °C in a humidified atmosphere (95% air, 5% carbon dioxdie) in 25 cm^2 culture flasks using DMEM supplemented with FBS 5% (V/V), non-essential amino acids (1%), sodium pyruvate (1%), GlutaMax (1%), and antibiotics (penicillin/streptomycin, 1%) as growth medium. All cell seeding and manipulations were carried out in a sterile laminar flow hood unless noted otherwise. Passage into a fresh flask was done at 80-90% confluency as needed. At the time of passage, the old medium was removed by pipette and the cells were washed with 5 mL of sterile dPBS. Trypsin solution (1x) was washed gently over the cells and the flask was incubated for 10 min to detach the cells. Following treatment with trypsin, the cells were resuspended in fresh medium and a 0.2 mL aliquot of cell suspension was added to a fresh flask with new medium. All cells were passaged every 3-4 days, and no medium change was necessary.

All micro-plate UV-Vis data was collected using a PerkinElmer Health Sciences Inc., EnSpire multimode basic unit plate reader. Iron quantification was determined using a model 3000DV Perkin Elmer inductively coupled plasma-optical emission spectrometer (ICP-OES) in the laboratory of Dr. Paterno Castillo at the Scripps Institution of Oceanography. All TEM imaging was performed using a JOEL 1200EX II(JEOL, Peabody, MA) transmission electron microscope and photographed using a Gatan digital camera (Gatan, Pleasanton, CA), or viewed using a Tecnai G2 Spirit BioTWIN transmission electron microscope equipped with an Eagle 4k HS digital camera (FEI, Hilsboro, OR). Confocal microscopy images were obtained on the Olympus FV1000 Confocal with an Olympus IX81 inverted microscope incubated with CO_2 at the UCSD Microscopy Core managed by Jennifer Santini.

***In-Vitro* Cell Cytotoxicity Assays**: The cytotoxicity of the ferrocene complexes and their photoproducts were determined by the effect on growth rate as quantified by crystal violet staining at the end of drug exposure. Cells were seeded in 100 μL of DMEM media in 96-well plates at a density specific to the cell line: HeLa (3.5×10^4 cells/well), A549 (3.5×10^4 cells/well), and Caov-3 (3.5×10^4 cells/well). After incubation for 24 h at 37°C the cells were exposed to various concentrations of compounds in media for 24 h. At this time, the dark plate was left in the incubator and an identically prepared plate was illuminated with a Richee 2014-SLT-CW/WW 50W Flood Light (0.031 W) for 3 hours with a 455 nm long pass filter (Pol filter 152x100x3mm GG455) resting on top of the 96 well plate. Temperature during photolysis was kept constant at 37°C using a Denville Incubloc solid aluminum block. 48 h after photolysis, the cell cultures were fixed with 4% paraformaldehyde, washed three times with DPBS, and stained with crystal violet. The absorbance at 590 nm was measured for each well using a microplate reader scanning spectrophotometer. Cytotoxicity was then determined by dividing the average absorbance values of each concentration of the drug-containing wells by the average absorbance of the control wells. Each experiment was performed in at least triplicate. IC_{50} values were calculated using OriginPro 8.0 software.

F. Appendix

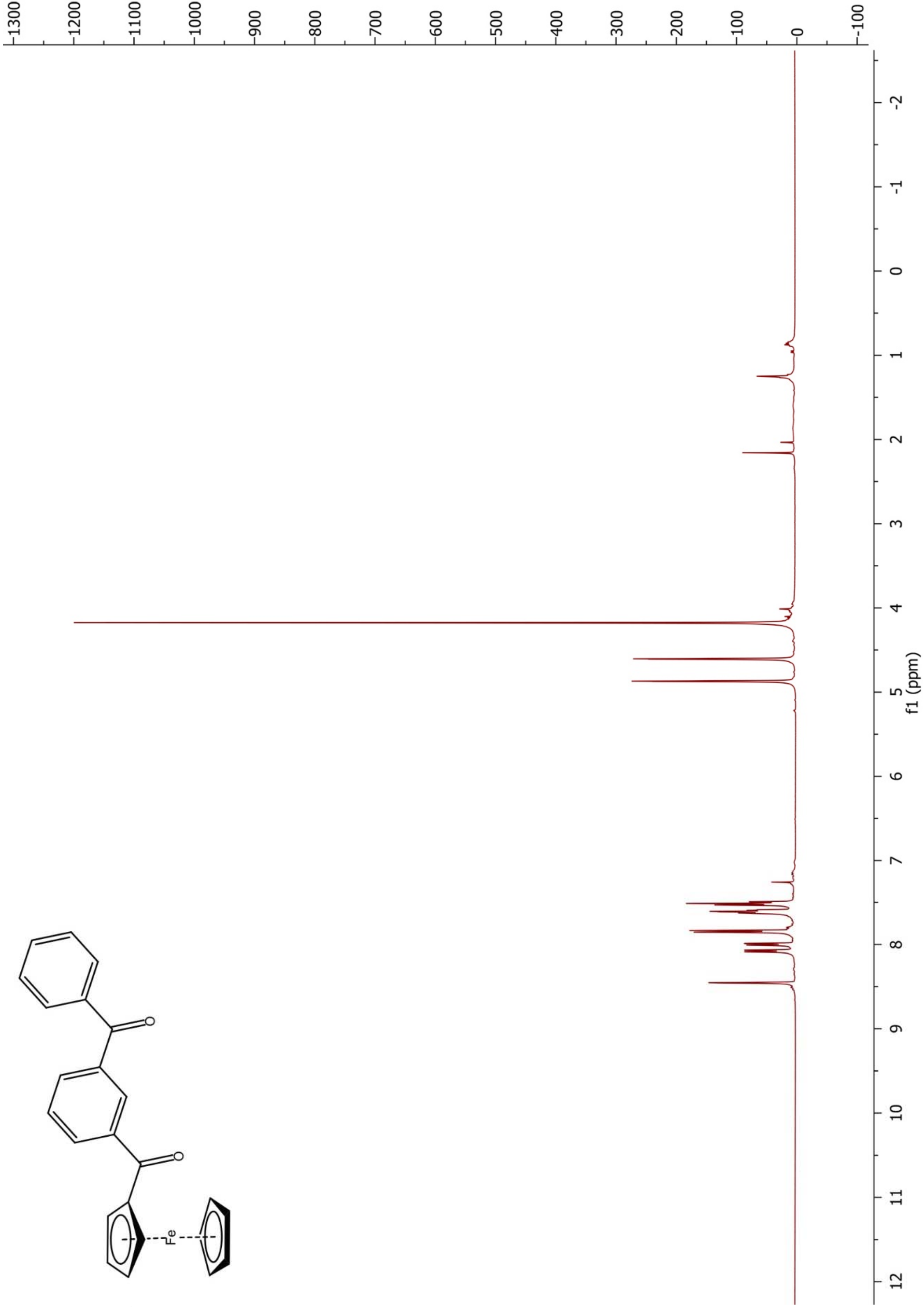

Figure 3.7. ^{1}H NMR of Compound **35** (400 MHz, $CDCl_3$).

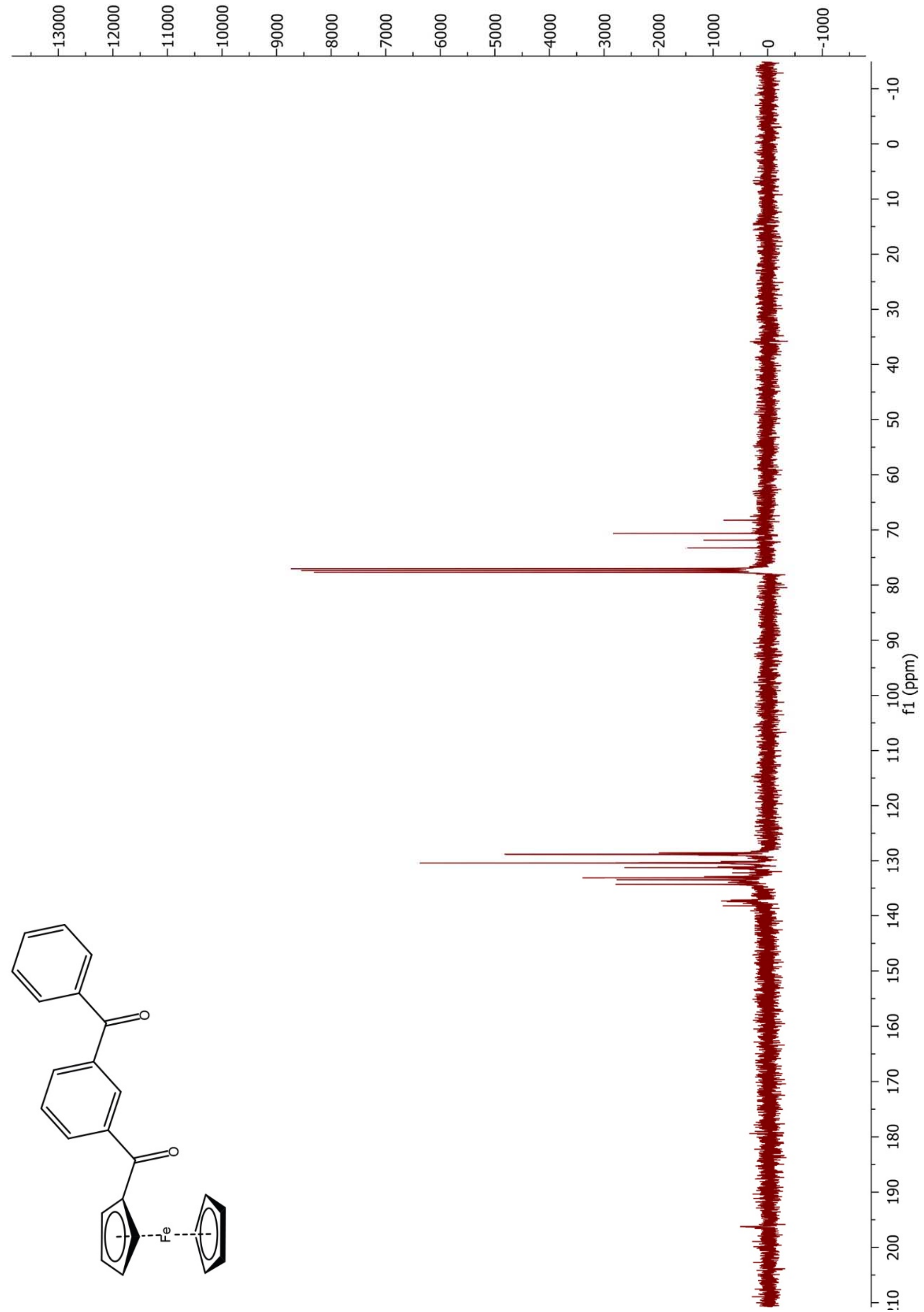

Figure 3.8. $^{13}C\{^1H\}$ NMR of Compound **35** (100 MHz, $CDCl_3$).

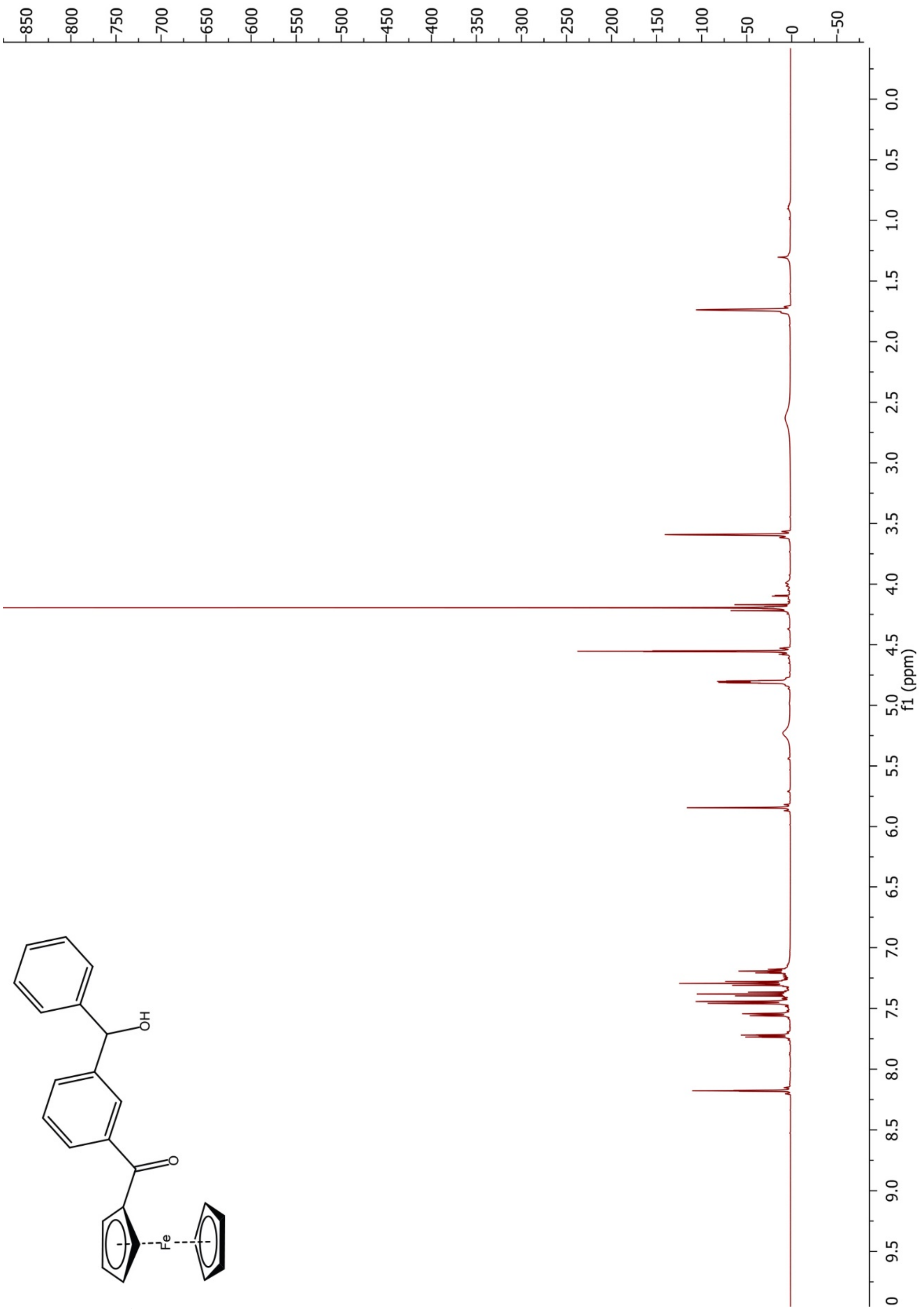

Figure 3.9. ^{1}H NMR of Compound **36** (500 MHz, d_8-THF).

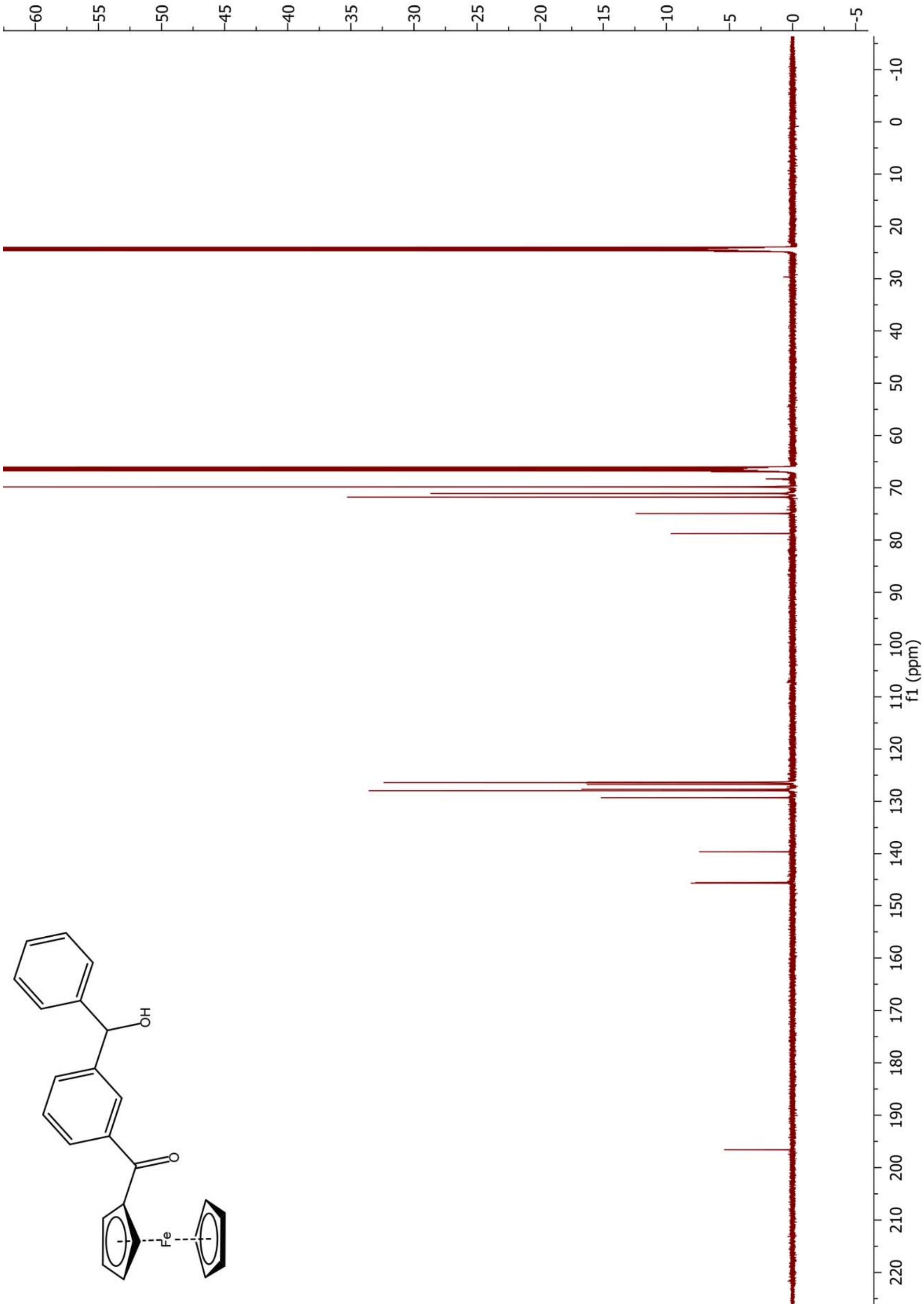

Figure 3.10. $^{13}C\{^{1}H\}$ NMR of Compound **36** (126 MHz, d_8-THF).

Figure

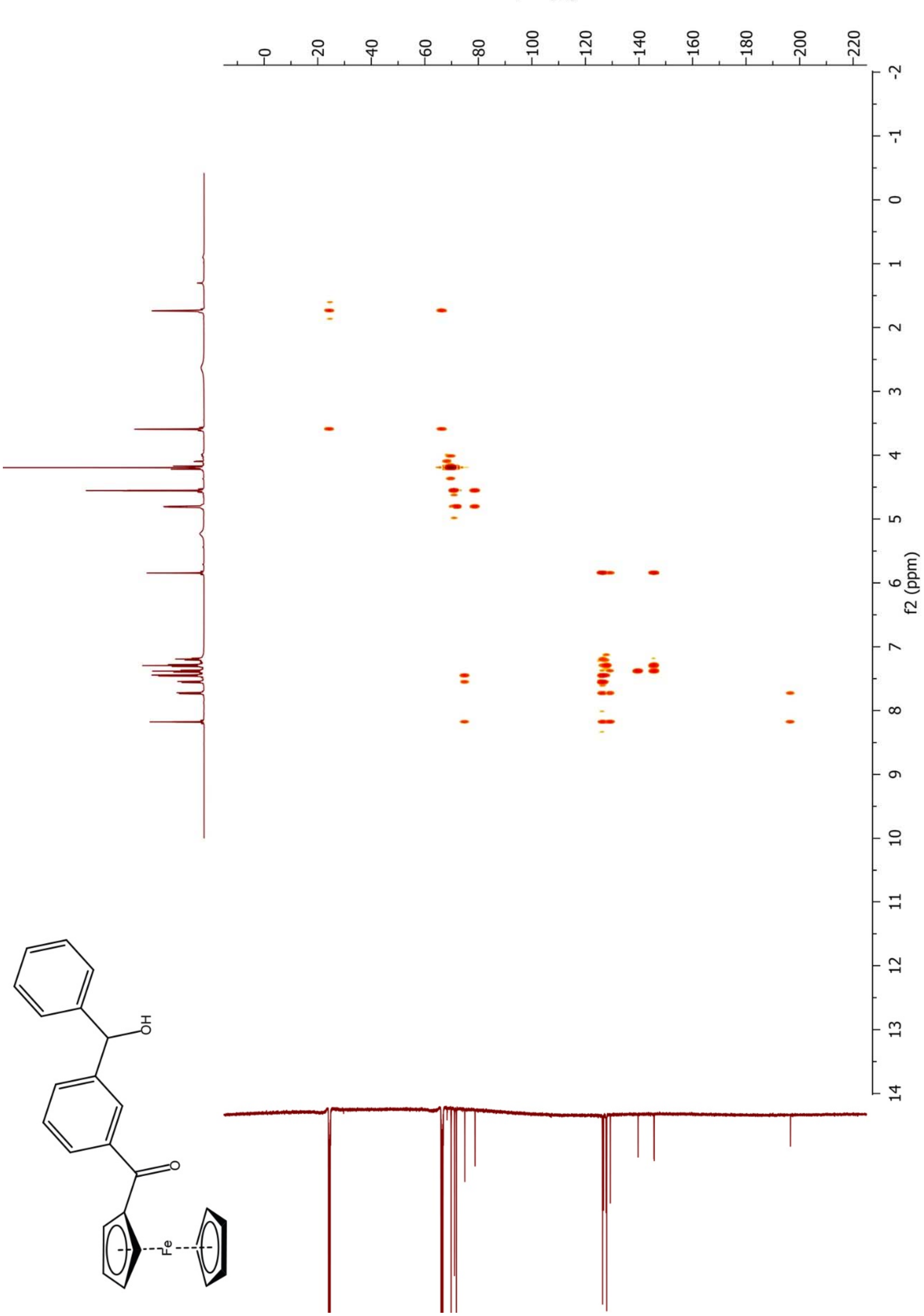

Figure 3.11. HMBC of Compound **36**.

G. References

1. Dixon, S. J.; Lemberg, K. M.; Lamprecht, M. R.; Skouta, R.; Zaitsev, E. M.; Gleason, C. E.; Patel, D. N.; Bauer, A. J.; Cantley, A. M.; Yang, W. S.; Morrison, B.; Stockwell, B. R. *Cell*. **2012**, *149*, 1060-1072.

2. Yang, W. S.; Stockwell, B. R. *Trends in Cell Biol*. **2016**, *26*, 165-176.

3. Xie, Y.; Hou, W.; Song, X.; Yu, Y.; Huang, J.; Sun, X.; Kang, R.; Tang, D. *Cell Death Differ*. **2016**,*23*, 369-379.

4. Angeli, J. P. F.; Shah, R.; Pratt, D. A.; Conrad, M. *Trends Pharmacol Sci.* **2017**, *38*, 489-498.

5. Dolma, S.; Lessnick, S. L.; Hahn, W. C.; Stockwell, B. R. *Cancer Cell*. **2003**, *3,* 285-196.

6. Hahn, W. C.; Counter, C. M.; Lundberg, A. S.; Beijersbergen, R. L.; Brooks, M. W.; Weinberg, R. A. *Nature*. **1999**, *400*, 464-468.

7. Yang, W. S.; Stockwell, B. R. *Chem. Bio.* **2008**, *15*, 234-245.

8. Weïwer, M.; Bittker, J. A.; Lewis, T. A.; Shimada, K.; Yang, W. S.; MacPherson, L.; Dandapani, S.; Palmer, M.; Stockwell, B. R.; Schreiber, S. L.; Munoz, B. *Bioorg. Med. Chem. Lett.* **2012**, *22*, 1822-1826.

9. Fernández-Medarde, A.; Santos, E. *Genes Cancer*. **2011**, *2*, 344-358.

10. Yang, W.S.; SriRamaratnam, R.; Welsche, M. E.; Shimada, K.; Skouta, R,; Viswanathan, V. S.; Cheah, J. H.; Clemons, P. A.; Shamji, A. F.; Clish, C. B.; Brown, L. M.; Girotti, A. W.; Cornish, V. W.; Schreiber, S. L.; Stockwell, B. R. *Cell*. **2014**, *156*, 317-331.

11. Brigelius-Flohé, R.; Maiorino, M. *Biochimica et Biophysica Acta*. **2013**, *1830*, 3289-3303.

12. Bannai, S.; Kitamura, E. *J. Biol. Chem.* **1980**, *255,* 2372-2376.

13. Bridges, R. J.; Natale, N.R.; Patel, S. A. *Br. J. Pharmacol*. **2012**, *165*, 20-34.

14. Viswanathan, V. S.; Ryan, M. J.; Dhruv, H. D.; Gill, S.; Eichhoff, O. M.; Seashore-Ludlow, B.; Kaffenberger, S. D.; Eaton, J. K.; Shimada, K.; Aguirre, A. J.; Viswanathan, S. R.; Chattopadhyay, S.; Tamayo, P.; Yang, W. S.; Rees, M. G.; Chen, S.; Boskovic, Z. V.; Javaid, S.; Huang, C.; Wu, X.; Tseng, Y-Y.; Roider, E. M; Gao, D.; Cleary, J. M.; Wolpin, B. M.; Mesirov, J. P.; Haber, D. A.; Engelman, J. A.; Boehm, J. S.; Kotz, J. D.; Hon, C. S.; Chen, Y.; Hahn, W. C.; Levesque, M. P.; Doench, J. G.; Berens, M. E.; Shamji, A. F.; Clemons, P. A.; Stockwell, B. R.; Schreiber, S. L. *Nature*. **2017**, *547*, 543-457.

15. Gröger, C. J.; Grubinger, M.; Waldhör, T.; Vierliner, K.; Mikulits, W. *PLoS ONE*. **2012**, *7*, e51136.

16. Byers, L. A.; Diao, L,; Wang, J.; Saintigny, P.; Girard, L.; Peyton, M.; Shen, L.; Fan, Y.; Giri, U.; Tumula, P. K.; Nilsson, M. B.; Gudikote, J.; Tran, H.; Cardnell, R. J. G.; Bearss, D. J.; Warner, S. L.; Foulks, J. M.; Kanner, S. B.; Gandhi, V.; Krett, N.; Rosen, S. T.; Kim. E. S.; Herbst, R. S.; Blumenschein, G. R.; Lee, J. J.; Lippman, S. M.; Ang, K.; Mills, G. B.; Hong, W. K.; Weinstein, J. N.; Wistuba, I, I.; Coombes, K. R.; Minna, J. D.; Heymach, J. V. *Clin. Cancer Res.* **2013**, *19*, 279-290.

17. Taube, J. H.; Herschkowitz, J. I.; Komurov, K.; Zhou, A. Y.; Gupta, S.; Yang, J.; Hartwell, K.; Onder, T. T.; Gupta, P. B.; Evans, K. W.; Hollier, B. G.; Ram, P. T.; Landers, E. S.; Rosen, J. M.; Weinberg, R. A.; Mani, S. A. *Proc. Natl. Acad. Sci. U.S.A.* **2010**, *107*, 15449-15454.

18. Bittker, J. A.; Weiwer, M.; Shimada, K.; Yang, W. S.; MacPherson, L.; Dandapani, S.; Munoz, B.; Palmer, M.; Stockwell, B. R.; Schreiber, S. L. Screen for RAS-Selective Lethal Compounds and VDAC Ligands – Probe 2. 2011 Feb 10 [Updated 2011 Dec 12]. In: Probe Reports from the NIH Molecular Libraries Program [Internet]. Bethsda (MD): National Center for Biotechnology Information (US); 2010-Available from: https://www.ncbi.nlm.nih.gov/books/NBK98919

19. Cytototoxicity values of compound **16** were obtained from Chapter II.

20. Yu, H.; Guo, P.; Xie, X.; Wang, Y.; Chen, G. *J. Cell Mol. Med.* **2017**, *21*, 648-657.

21. Forbes, S. A.; Bindal, N.; Bamford, S.; Cole, C.; Kok, C. Y.; Beare, D.; Jia, M.; Shepherd, R.; Leung, K.; Menzies, A.; Teague, J. W.; Campell, P. J.; Stratton, M. R.; Futreal, P.A. *Nucleic Acids Res.* **2011**, *39*, (Database issue): D945-D950.

22. Hangauer, M. J.; Viswanathan, V. S.; Ryan, M. J.; Bole, D.; Eaton, J. K.; Matov, A.; Galeas, J.; Dhruv, H. D.; Berens, M. E.; Schreiber, S. L.; McCormick, F.; McManus, M. T. *Nature* **2017**, published online Nov 1, 2017

23. Jaoen, G. *Bioorganometallics*; Jaouen, G.. Ed.; Wiley-VCH Berlab GmbH & Co: Weinheim, 2006.

24. Dolmans D. E.; Fukumura, D.; Jain, R. K. *Nature Reviews Cancer*. **2003**, *3*, 380-387.

25. Irani, K.; Xia, Y.; Zweier, J. L.; Sollott, S. J.; Der, C. J.; Fearon, E. R.; Sundaresan, M.; Finkel, T.; Goldschmidt-Cermont, P. J. *Science*, **1997**, *14*, 1649-1652.

26. Leblanc, V.; Delumeau, I.; Tocqué, B. *Oncogene*, **1999**, *18*, 4884-4889.

27. Yaginuma, Y.; Westphal H. *Cancer Res.* **1992** *52*, 4196-4169.

28. ATCC. ATCC Cell Lines by Gene Mutation. https://www.atcc.org (accessed November 4, 2017)

29. Jiang, L.; Kon, N.; Wang S. J.; Su, T.; Hibshoosh H.; Baer, R.; Gu, W. *Nature*. **2015**, *520*, 57-62.

30. Jia, L. Q.; Osada, M.; Ishioka, C.; Gamo, M.; Ikawa, S.; Suzuki, T.; Shimadaira, H.; Niitani, T.; Kudo, T.; Akiyama, M.; Kimura, N.; Matsuo, M.; Mizusawa, H.; Tanaka, N.; Koyama, H.; Namba, M.; Kanamaru, R.; Kuroki, T. *Mol. Carcinog.* **1997**, *19*, 243-253.

31. Liou. G.-Y.; Storz, P. *Free Radic. Res.* **2010**, *44*, 479-496.

Chapter IV

Delivery of Benzoylferrocene Using Nanoparticles and Peptide Recognition Targets

A. Introduction

The organoferrous compounds synthesized in Chapter II have a hydrophobic nature which makes them insoluble in water, but may allow the compound to more easily cross the cell membrane barrier. However, this trend is not absolute as illustrated with hydrophobic benzoyl ferrocene's lack of uptake *in vitro* in cancer cells.[1] We initially explored using porous silicon nanoparticles as a drug delivery carrier for benzoyl ferrocene since we previously determined that there was no cellular uptake of benzoyl ferrocene.[1] There has been major advancement in the field of nanotechnology in medicine with nanotechnology playing an important part in the development of anticancer therapeutics.[2-3] Utilization of porous silicon nanoparticles (pSiNPs) have emerged as promising versatile and multifunctional platforms for nanomedicine in drug delivery, diagnostics and therapy.[4] Porous silicon nanoparticles are of interest in biomedical research due to their low toxicity and high potential for successful focal and invasive therapies without conventional side effects.[5] Silicon is observed to be one of the most abundant trace metals in humans, with the average 70 kg human containing 1 g of silicon,[6] illustrating the biocompatibility and nontoxicity of silicon in living organisms. Porous silicon nanoparticles can be completely degraded and converted to silicic acid, a nontoxic bioavailable form in humans, which is efficiently excreted through renal clearance.[5,7-8] pSiNPs have received considerable attention due to the large surface area and pore volume to sufficiently load therapeutic drugs,[9] ease of surface modification,[10] and tunable size distribution[11] based on etching conditions. As a versatile carrier, pSiNPs are used for successful loading of conventional drug molecules, peptides, and small interfering RNA for drug delivery applications.[12-14] Functionalization of pSiNPs with an outer lipid coating can easily conjugate targeting moieties to actively target cancer cells.[15] Due to these reasons we decided to use pSiNPs as a drug delivery vehicle to target cancer cells with benzoyl ferrocene (**5**, Figure 4.1).

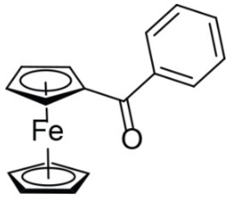

5

Figure 4.1. Structure of benzoyl ferrocene (**5**).

We wanted to synthesize two types of nanoparticles to determine if there was a difference in cellular internalization of our encapsulated benzoyl ferrocene (**5**). The first type of nanoparticle does not contain the internalized RGD (iRGD) targeting peptide while the second type of nanoparticle does (Figure 4.2). The RGD peptide sequence has previously been found to target the αβ-integrins which are highly expressed in tumor vasculature,[16-18] and has also been used as a successful targeting agent to deliver drugs, biologicals, imaging agents, viruses, and nanoparticles.[19-22] However, the RGD peptide targeting agents exhibited limited transport of the targeted payload into tumor cells, so studies were performed to overcome this limitation, and the iRGD peptide was developed.[23] Ruoslahti *et al*. has described an endocytic, transcytosis (a type of transcellular transport wherein macromolecules are transported across the interior of a cell) pathway in tumor cells that can be accessed by the iRGD peptides.

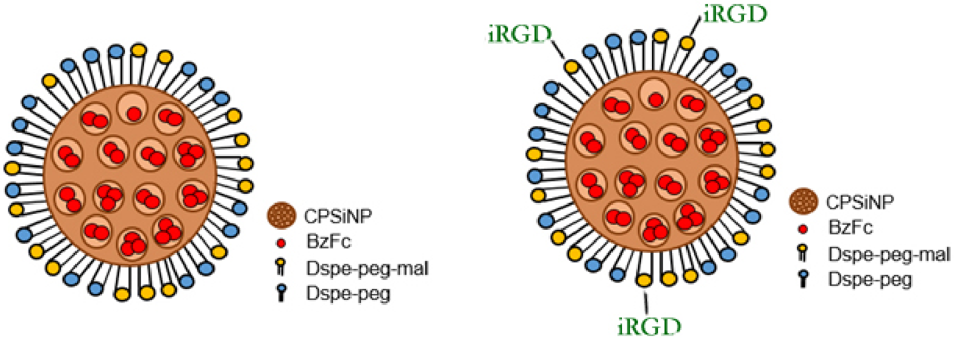

Figure 4.2. Two different types of nanoparticles, one with iRGD (right), and one without (left).

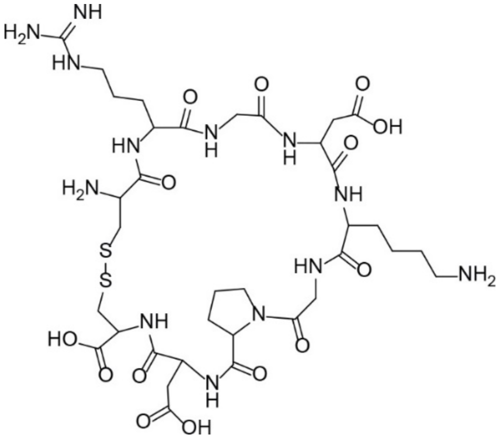

Figure 4.3. Structure of the cyclic iRGD peptide with sequence c(CRGDKGPDC).

The iRGD peptides are cyclic peptides consisting of the sequence CRGD[K/R]GP[D/E]C (Figure 4.3).[23] The iRGD peptide contains two critical sequences, one of which is the integrin RGD binding motif, while the other is a neuropilin-1 (NRP-1) binding motif.[24] NRP-1 binding leads to triggering of an endocytic transcytosis pathway that can assist drug and nanoparticle delivery, including small drug molecules, monoclonal antibodies, and nanoparticles.[25] The reason iRGD is a better targeting agent to internalize and increase the drug payload is due to a multistep process. The RGD sequence initially binds to either the $\alpha_v\beta_3$ or $\alpha_v\beta_5$ integrins, which are overexpressed in endothelial cells of tumor blood vessels and tumor cells.[26-27] Once the iRGD peptide is bound to the integrin, there is proteolytic cleavage, resulting in the release of the CRGD[R/K] sequence, also termed C-terminal rule (CendR) motif. This CendR moiety then binds to the NRP-1 receptor, leading to the endocytic transcytotsis pathway for drug delivery (Figure 4.4). Initial studies were performed with lung carcinoma A549 cells, which are known to have an overexpression of αβ-integrins.

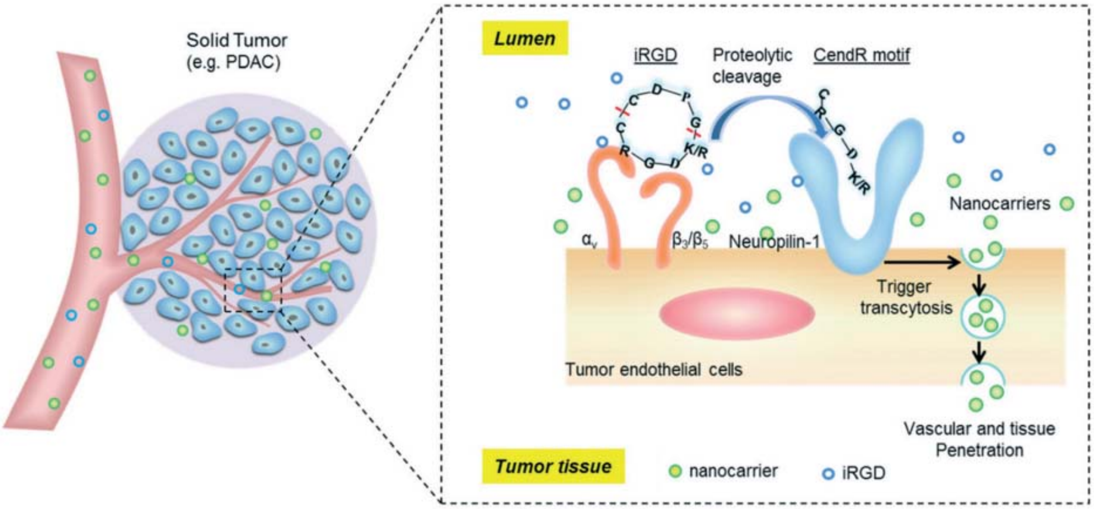

Figure 4.4. Figure from review article illustrating the iRGD-activated mechanism for carrier delivery in solid tumors.[24] The blue circles represent iRGD, which binds to the integrin protein, and is proteolytically cleaved. The CendR motif then binds to NRP-1, which triggers endocytosis of the green nanoparticle carriers.

While tuning the size of the nanoparticles can influence cellular internalization,[4] we wanted to ensure internalization of nanoparticles by using iRGD peptide. By using both types of nanoparticles to encapsulate **5** (Figure 4.2), we can compare the payload and cytotoxicity of internalized benzoyl ferrocene using our new approach to photodynamic therapy.[28] Our goals herein were to utilize nanoparticles and nanoparticles with iRGD targeting peptide to deliver benzoyl ferrocene **5** into lung carcinoma A549 cells, a cell line known to have the αβ integrins,[29] and compare cytotoxicity to free benzoyl ferrocene (Scheme 4.1). The pSiNP nanoparticles were coated with 1,2-disteraroyl-sn-glycero-3-

phosphoethanolamine-poly(ethylene glycol) (DSPE-PEG) lipid[30] to create a micelle nanoparticle hybrid as a versatile carrier to encapsulate our organoferrous agent for current studies.

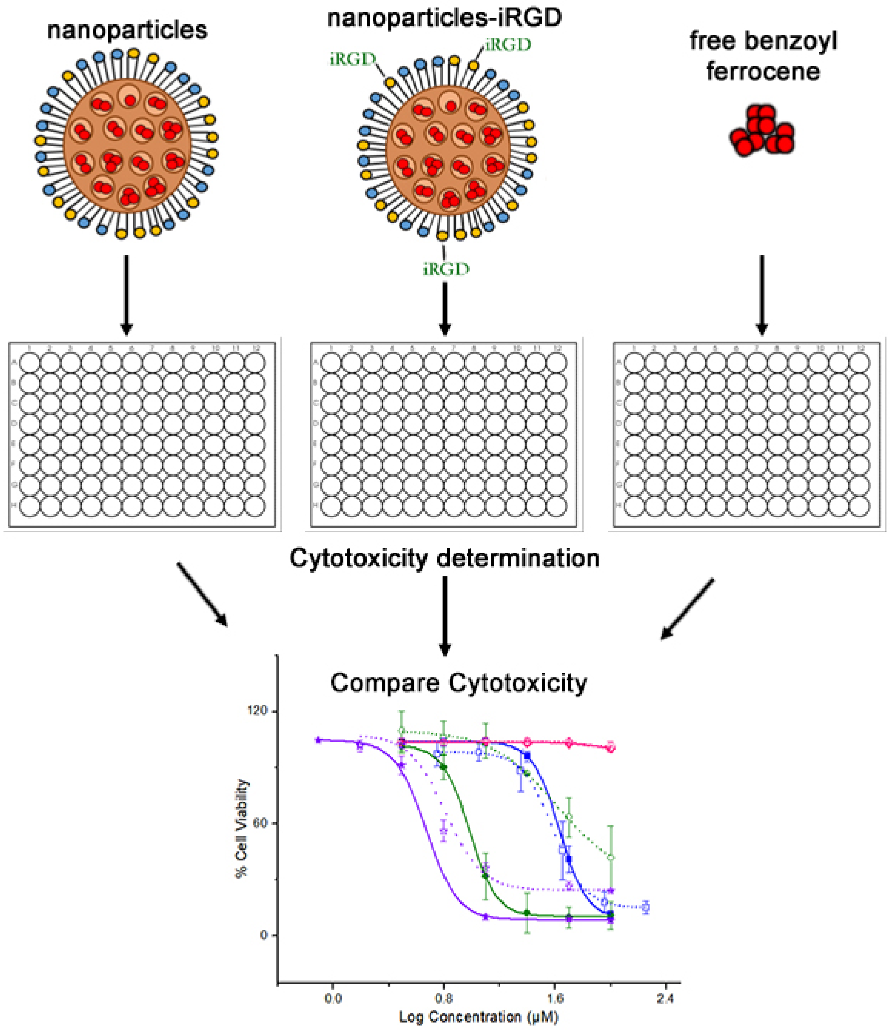

Scheme 4.1. Cartoon scheme showing different conditions for cytotoxicity assays we are testing for comparison. Left side shows nanoparticles without iRGD and containing **5** is added to A549 cells under standard protocol detailed in the Experimental section of this chapter. Middle show nanoparticles with iRGD containing **5** added to A549 cells. Right shows free benzoyl ferrocene added to cells. We then want to compare the IC_{50} values of these conditions to see if there is any difference in using nanoparticles and nanoparticles containing iRGD.

B. Results

1. Synthesis and Characterization of CPSiNP-PEG

Angie Kim from the Sailor lab at UCSD created porous Si nanoparticles (pSiNPs) coated with DSPE-PEG$_{2000}$ and DSPE-PEG$_{2000}$-Mal lipids to form micelle hybrid nanoparticles that can efficiently delivery hydrophobic drugs to cancer cells (Figure 4.4).[31] She first synthesized pSiNP from electrochemical etching of Si wafers. The crushed Si particles were then ultrasonicated with dodecene overnight to form Si-C bonds. This hydrosilylation of pSiNPs with dodecene is referred to as CPSiNPs. The CPSiNPs were then coated with DSPE-PEG lipids by a solid-oil-in-water (S/O/W) method detailed by Liu *et al.*[31] using both DSPE-PEG moieties shown in Figure 4.4.

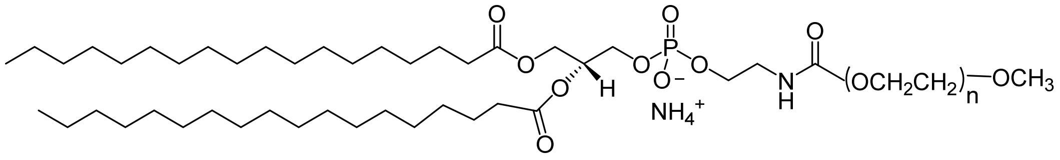

DSPE-PEG$_{2000}$

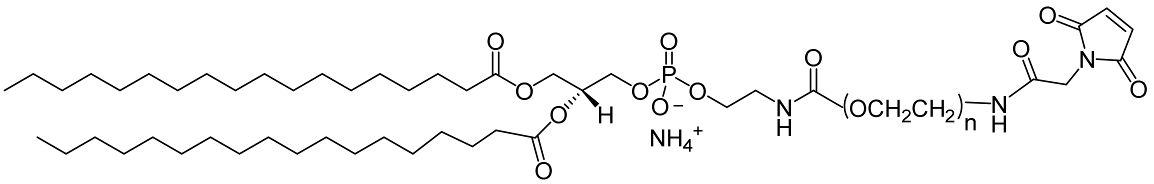

DSPE-PEG$_{2000}$-Mal

Figure 4.5. Structures of DSPE-PEG$_{2000}$ and DSPE-PEG$_{2000}$-Mal.

These CPSiNPs coated with DSPE-PEGs (also known as CPSiNP-PEG) were then analyzed, by Angie Kim, in terms of their size and morphology using transmission electron microscopy (TEM) and dynamic light scattering (DLS) measurements shown in Figures 4.6 and **Table 4.1** respectively. In order to increase efficiency in cellular uptake of CPSiNP-PEG, nanoparticles with a size between 200-300 had to be prepared, as it was known to be an effective size for internalization of tumor cells.[32] TEM imaging showed the nanoparticles were within the optimal range of 200-300 nm. DLS measurements[33] found the hydrodynamic diameter of pSiNP-PEG in aqueous solution was approximately 232 nm, whereas pSiNP-PEG loaded with benzoyl ferrocene was approximately 283 nm. DLS measurements also found a net negative zeta potential, due to the presence of the DSPE-PEG lipids on the surface of the porous silicon nanoparticles. The zeta potential measures the electric surface charge,[33] and is one confirmation of the DSPE-PEG lipids forming a micelle nanoparticle hybrid around the porous silicon nanoparticles (Figure 4.8). We use two types of lipids, DSPE-PEG$_{2000}$ and DSPE-PEG$_{2000}$-Mal, so we can utilize the lipids containing maleimide to conjugate it to the iRGD peptide (Figure 4.7). The iRGD peptide can be conjugated to the lipid by using the thio-functional group (Figure 4.7, blue structure). The iRGD peptide contains a 6-Carboxyfluorecein (6-FAM) fluorescent group (Figure 4.7, green structure). The iRGD functionalized lipid will herein be referred to as CPSiNP-PEG-iRGD.

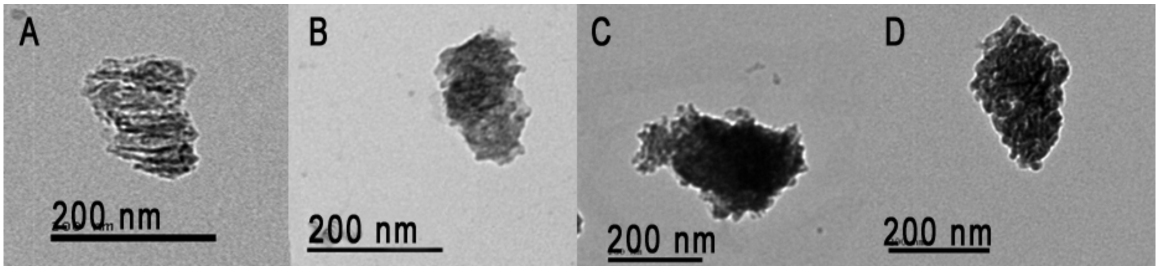

Figure 4.6. TEM imaging of nanoparticles. A. CPSiNP, B. CPSiNP-PEG, C. CPSiNP-PEG+**5**, D. CPSiNP-PEG-iRGD + **5**.

Table 4.1. DLS measurements for size and zeta potential.

Compound	Size (diameter, nm)	Zeta Potential (mV)
CPSiNP	183.8 (0.184)	-14.3 ± 7.8
CPSiNP-PEG	232 (0.174)	-21.1 ± 8.1
CPSiNP-PEG + 5	283 (0.232)	-28.4 ± 10.0
CPSiNP-PEG-iRGD + 5	277 (0.205)	-25.3 ± 10.3

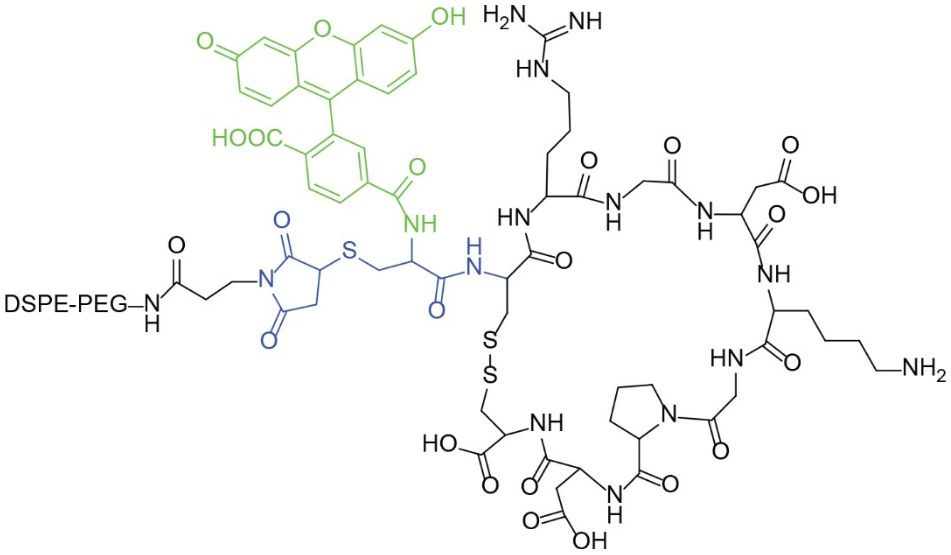

Figure 4.7. iRGD conjugated to maleimide.

Benzoyl ferrocene was loaded into CPSiNPs by addition of benzoyl ferrocene to a mixture of hydrosilylated silicon nanoparticles and DSPE-PEG lipids in chloroform. The solution was mixed for 24 h before the mixture was left open to air for a slow evaporation of chloroform. This results in formation of benzoyl ferrocene (**5**) encapsulated in the micelle nanoparticle (known as CPSiNP-PEG) as illustrated in Figure 4.8. Treatment of DPSE-PEG-Mal with the iRGD peptide afforded benzoyl ferrocene **5** encapsulated in CPSiNP-PEG-iRGD.

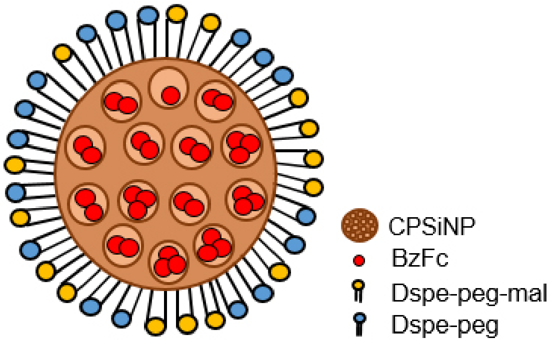

Figure 4.8. Cartoon illustration of a micelle nanoparticle hybrid.

2. Cellular Internalization of Micellar Hybrid Nanoparticles

To demonstrate the cellular uptake of CPSiNPs by lung carcinoma A549 cells, we encapsulated 6-FAM fluorescent dye into the CPSiNP-PEG nanoparticles using the same methods for benzoyl ferrocene as mentioned in section 1. We then imaged the cells utilizing confocal microscopy techniques to image the green fluorescence of 6-FAM and blue fluorescence of the cells' nucleus stained with 4,5-Diamidino-2-phenylidole dihydrochloride (DAPI) dye. For nanoparticles containing the iRGD peptide (CPSiNP-PEG-iRGD), Rhodamine 6G red fluorescent dye was used. The iRGD peptide fragment contains fluorescein, a similar dye to 6-FAM with similar fluorescent properties. We could then compare the confocal images of cells treated with nanoparticles containing the iRGD peptide and without the targeting peptide. Figure 4.9 illustrates that both nanoparticles are internalized by A549 cells.

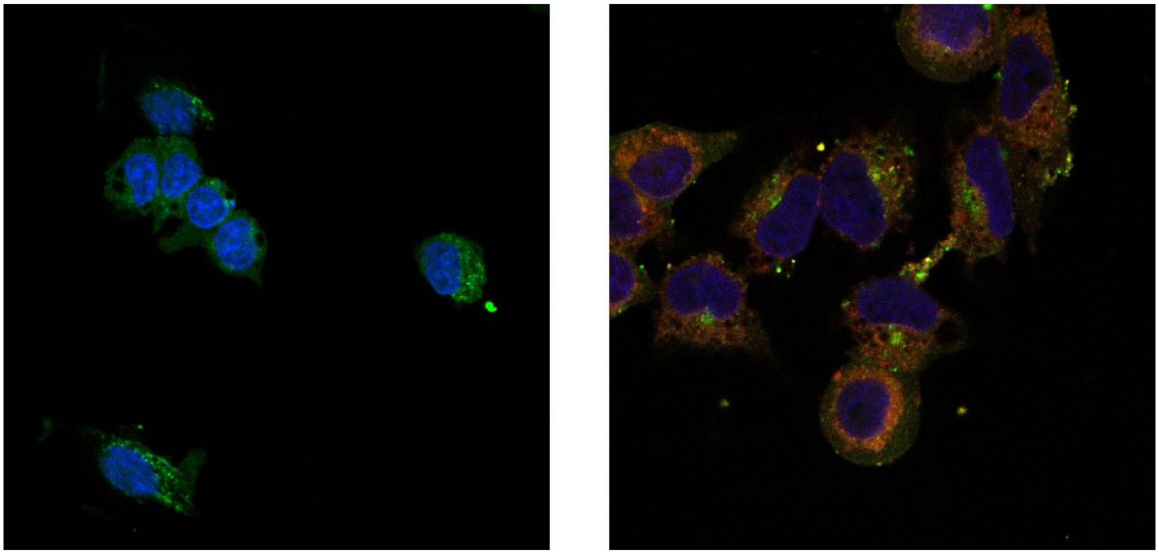

Figure 4.9. Confocal imaging of A549 cells treated with nanoparticles containing no iRGD (left) and nanoparticles containing iRGD (right) after 24 h. Green fluorescence on the left indicates internalization of the 6-FAM dye using nanoparticles as a carrier. The green and red fluorescence on the right indicate internalization of CPSiNP-PEG-iRGD and Rhodamine 6G respectively.

The confocal images of Figure 4.9 show that incubating the cells for 24 hours with the nanoparticles results in cellular internalization of both CPSiNP-PEG and CPSiNP-PEG-iRGD. After 24 h incubation period, the fluorescent dyes and the lipid containing iRGD peptide are still internalized, even after degradation of porous silicon nanoparticles (See section 3 for silicon nanoparticle degradation). After using confocal imaging to show the nanoparticles containing dye were entering the tumor cells, we decided to use TEM imaging to determine whether the CPSiNP-PEG and CPSiNP-PEG-iRGD containing benzoyl ferrocene was uptaken in the cells. TEM images shown in Figure 4.10 illustrate that both CPSiNP-PEG and CPSiNP-PEG-iRGD containing benzoyl ferrocene are uptaken by the cells independently. Interestingly, the uptake of nanoparticles without iRGD shows what we hypothesize is the compound in a vacuole approximately 2-3 μm in length in the cytoplasm (Figure 4.10, left). The CPSiNP-PEG-iRGD containing benzoyl ferrocene shows something causing deformation of the nucleus (Figure 4.10, right).

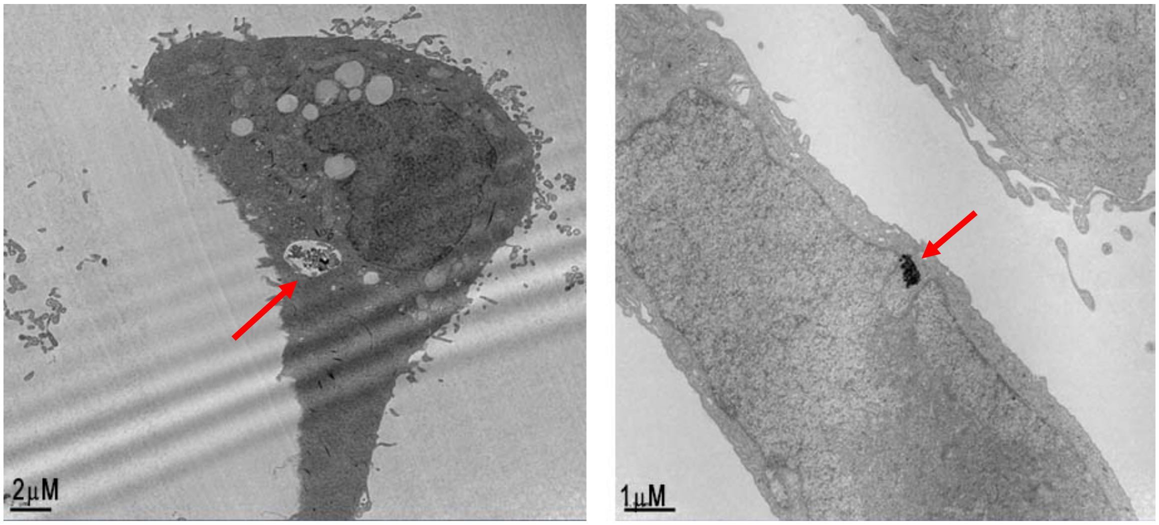

Figure 4.10. TEM images of CPSiNP-PEG (left) and CPSiNP-PEG-iRGD (right) containing benzoyl ferrocene.

3. Iron Concentration Determinations

In order to confirm drug loading efficiency and release of benzoyl ferrocene from the silicon nanoparticles, inductively coupled plasma-optical emission spectroscopy (ICP-OES) was used at the UCSD-SIO facility run by Pat Castillo and Chris Macisaac. Angie Kim utilized ICP-OES to measure the concentration of iron from benzoyl ferrocene as it is released from the CPSiNP-PEG nanoparticles during degradation in solution.

Iron release and silicon degradation is measured and plotted against time in DPBS solution (Figure 4.11). Silicon nanoparticles were placed in an eppendorf tube in a DPBS solution. After every time point at 2, 5, 8, 11, 13, 24 and 27 h, the solution of CSiNP-PEG containing **5**, was centrifuged. The supernatant containing the degraded silicon nanoparticles and released benzoyl ferrocene (**5**) was collected and separated from the intact solid silicon nanoparticles. The iron and silicon concentrations were measured at teach timepoint using ICP-OES and plotted in a graph (Figure 4.11). The release of benzoyl ferrocene was determined to be 50% after 6 h, with greater than 90% release at 24 h, and all the benzoyl ferrocene is released within 30 h. The release of benzoyl ferrocene and degradation of Si nanoparticles confirmed that photolyzing the cells 24 hours after incubation of CPSiNP-PEG and CPSiNP-PEG-iRGD containing compound **5** is optimal in order to generate free iron(II) from photolysis of A549 cells.

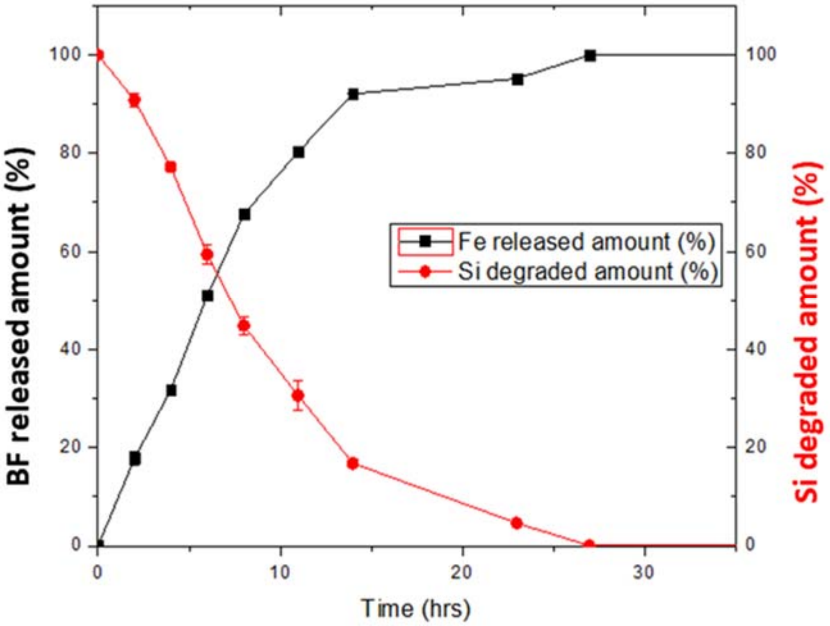

Figure 4.11. Release of benzoyl ferrocene compared to degradation of Si nanoparticles in relation to time.

ICP-OES studies were also used to determine the iron uptake in lung carcinoma A549 cells. The cells were treated with CPSiNP-PEG loaded with **5**, CPSiNP-PEG-iRGD loaded with **5**, and free compound **5** independently. The ratio of the iron concentration from ICP-OES to the cellular protein concentration gave approximate iron accumulation in cells. Two controls were set up, A549 cells that were treated with the same DPBS concentration used for nanoparticles containing **5**, and A549 cells that were treated with the same DMSO concentration used to dissolve benzoyl ferrocene. All cells treated with the iron containing compound were related back to the appropriate control as the standard. Table 4.2 lists the average ratio of iron concentration using nanoparticles compared to control and no use of nanoparticles. The iron accumulation studies were run under similar conditions to those detailed in Chapter II (Section B2 and E). For further details see the Experimental section of this chapter (Section E).

Table 4.2. Average ratio if iron accumulation compared to control.

Compound	**Avg Ratio to Control (Std Dev)**
Control	1
Control (DMSO)*	1
5*	1.3 (0.4)
CPSiNP-PEG + 5	22.3 (3.2)
CPSiNP-PEG-iRGD + 5	40 (4.8)

*__5__ is compared to control containg DMSO whereas everything else is compared to the top control.

As can be seen from Table 4.2, using an iRGD targeting peptide on the nanoparticles resulted in nearly a two-fold increase in iron accumulation compared to nanoparticles without the iRGD targeting peptide. Utilization of nanoparticles without iRGD targeting peptide led to a 20-fold increase in benzoyl ferrocene uptake, whereas incubation with free benzoyl ferrocene led to no cellular uptake.

4. Cell Viability Studies

We performed cytotoxicity assays using the standard procedures in Chapter II (Section B2 and E), which is also listed in the Experimental section of this chapter, on both types of nanoparticles containing benzoyl ferrocene (**5**) in order to compare their cytotoxicity to that of free benzoyl ferrocene in A549 cells. Interestingly, CPSiNP-PEG containing **5** showed a light IC_{50} value of 11.1 (2.7) μM of compound **5**, with an undetermined dark IC_{50} value as we could not get the concentration where it caused greater than 90% cell death. This was due to the solubility limit of 100 μM of **5** when encapsulated in nanoparticles. At the solubility limit of 100 μM, compound **5** exhibited an average of

42% cell viability (Table 4.3). The cytotoxicity of benzoyl ferrocene using CPSiNP-PEG increased toxicity in the light, and decreased the toxicity in the dark, compared to cells treated with free compound **5**, as shown in Table 4.3. When compound **5** was encapsulated within CPSiNP-PEG-iRGD, the light IC_{50} value increased by two-fold, with a value of 6.4±0.6 μM. However, the dark cytotoxicity also drastically increased with IC_{50} value of 12.4±0.5 μM. This dark cytotoxicity is very surprising as it is two-fold less toxic compared to the light toxicity, but significantly more toxic in the dark compared to CPSiNP-PEG containing **5**. Utilization of the iRGD targeting peptide increases cytotoxicity of benzoyl ferrocene significantly in the light and dark compared to CPSiNP-PEG containing **5** and free benzoyl ferrocene. Assays were also performed on nanoparticles with no compound inside, which demonstrated no cytotoxicity.

Table 4.3. Cytoxicity of **5**, CPSiNP-PEG containing **5**, and CPSiNP-PEG-iRGD with **5**.

Compound	A549 IC_{50} light (μM)	A549 IC_{50} dark (μM)
5	43.5±2.0	41.3±2.7
CPSiNP-PEG + 5	11.1±2.7	Approx. 100
CPSiNP-PEG-iRGD + 5	6.4±0.6	12.4±0.5

5. Using a RGD conjugate on a benzoyl ferrocene derivative

Besides using an iRGD peptide sequence on nanoparticles to target tumor cells, we also wanted to synthesize and test a benzoyl ferrocene derivative that contained the peptide sequence CRGDK, since it is a known NRP-1 binding peptide sequence.[25] We hypothesized that by adding the peptide targeting sequence to a ferrocenyl derivative, we could evade detection of cellular regulatory mechanisms for iron and deliver a sandwiched iron complex into the cells. Since we had access to a peptide synthesizer with the Gianneschi group, who was previously at UCSD, we wanted to design a ferrocenyl derivative with a carboxylic acid end in order to utilize the peptide synthesizer to form new peptide bonds. After much trial and error, the final ferrocenyl derivative synthesized was compound **43** (Figure 4.12). The synthesis of compound **43** is fairly straightforward, wherein we utilize aldol condensation chemistry. Treatment of ferrocene carboxaldehye and compound **42** with NaOH in an ethanol/water solution lead to formation of compound **43**. After acidification, the precipitate was collected and washed with cold ethanol. The compound was then used without further purification, as ^{1}H NMR spectroscopic analysis confirmed purity. Compound **43** was then conjugated to the peptide CRGDK with the assistance of Dr. Matt Thompson in the Gianneschi lab to form the final compound **44** (Figure 4.13). However, after using TFA to remove the compounds from the peptide resin, the compound turned from a red color solution to blue, indicating that this last step may have oxidized the product from iron(II) to iron(III). A NMR spectra was not obtainable, so we obtained a LRMS which confirmed the mass of **44**. Future studies into cleavage of the product from the peptide resin will need to be pursued.

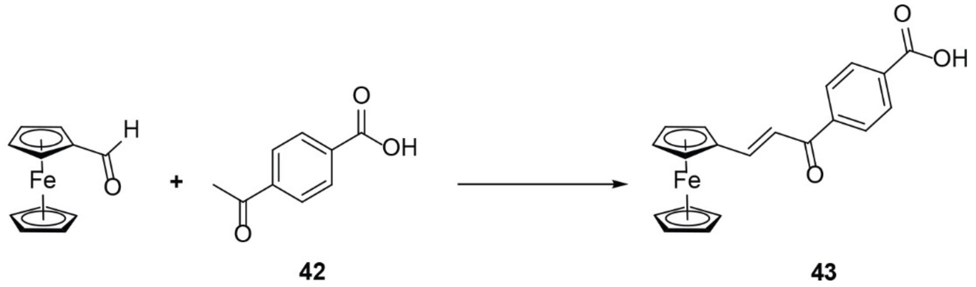

Figure 4.12. Synthesis of compound **43**.

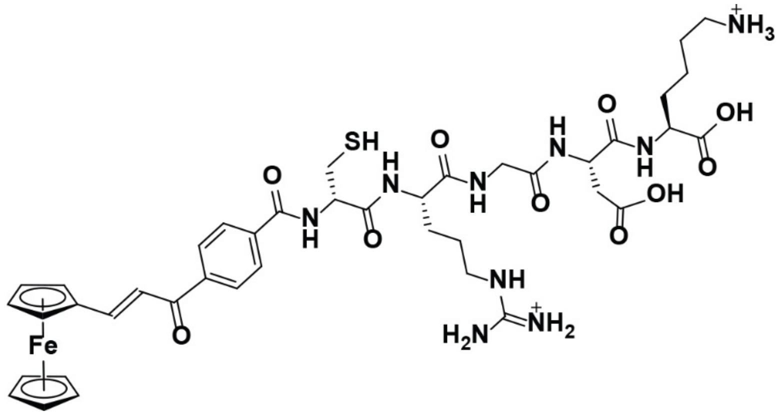

Figure 4.13. Structure of compound **44**.

C. Discussion

The use of nanoparticles in the field of biological medicine has become an important tool in the development of anticancer therapeutics.[34] In particular, the use of porous silicon nanoparticles (pSiNPs) have emerged as a promising platform for drug delivery, diagnostics and therapeutics.[34] This is in part due to the biodegradability of silicon, lending itself to low toxicity in humans. The ease of surface modification, tunable size distribution, and large surface area and pore volume also lends itself to its importance in anticancer research.[2-3] By utilizing these versatile modifications, pSiNPs can be used for successful loading of small molecule drugs, peptides, and RNA for antitumor applications. In our project, we have modified pSiNPs by engineering a micelle hybrid nanoparticle (CPSiNPs) using DSPE-PEG$_{2000}$ lipids and hydrosilylation of silicon with dodecene in order to encapsulate our hydrophobic ferrous drug for tumor drug delivery. Since the passage of nanoparticles into tumor cells relies on a passive diffusion across the leaky, hyperpermeable tumor vasculature,[35] we wanted to test if there would be greater cytotoxicity if the nanoparticles are conjugated to tumor-homing peptides such as iRGD.

We decided to run initial tests on lung carcinoma A549 cells, as they are known to overexpress the αβ-integrins,[36] which the iRGD peptide can target. The iRGD peptide was discovered and developed as a way to deal with the limited transport and payload into tumor cells of the RGD peptide sequence.[23] The cyclic iRGD peptide was found to contain two critical sequences to insure delivery of a higher payload into tumor cells. One was the RGD sequence which can target the αβ-integrins, and the other was the CendR moiety (CRGD[R/K]) that can bind to the NRP-1 receptor, leading to endocytosis of the drugs.[23] This knowledge led to initial studies into the synthesis of a ferrocenyl derivative conjugated to a CRGDK sequence (Figure 4.13), the CendR fragment which binds to NRP-1.

By encapsulating an organometallic compound such as benzoyl ferrocene **5** within porous silicon nanoparticles, we can possibly generate a longer lifetime catalyst in the form of free iron (II) for a new method to photodynamic therapy (PDT) treatment. [37] We speculate that generation of this catalyst would be much more favorable compared to traditional photodynamic therapy methods wherein the photosensitizer has to constantly be excited by light. The photosensitizer stays in the excited for a short amount of time before being quenched either by reaction with oxygen to form singlet oxygen or cellular products to form oxygenated species.[38] We hypothesize that we could create a more optimal method to PDT because our organometallic drug only needs an initial light source to trigger free iron(II) that can operate without a continuous light source (Figure 2.3, Figure 2.23). In these studies, we have explored a unique mechanism of antitumor photodynamic therapy compounds and cellular response to iron(II) with a greater iron payload into tumor cells using nanoparticles as a delivery vehicle.

Benzoyl ferrocene was encapsulated in the CPSiNPs by dissolving benzoyl ferrocene in chloroform and mixing with the hydrosilylated nanoparticles and DSPE-PEG lipids to form a micelle. This micelle was able to form during evaporation of chloroform in a similar fashion that membrane lipids are formed. The hydrophobic ends of the dodecenyl functional group in the hydrosilylation product and DSPE-PEG lipids come together to form a micelle encapsulating benzoyl ferrocene inside the silicon nanoparticles (Figure 4.14).

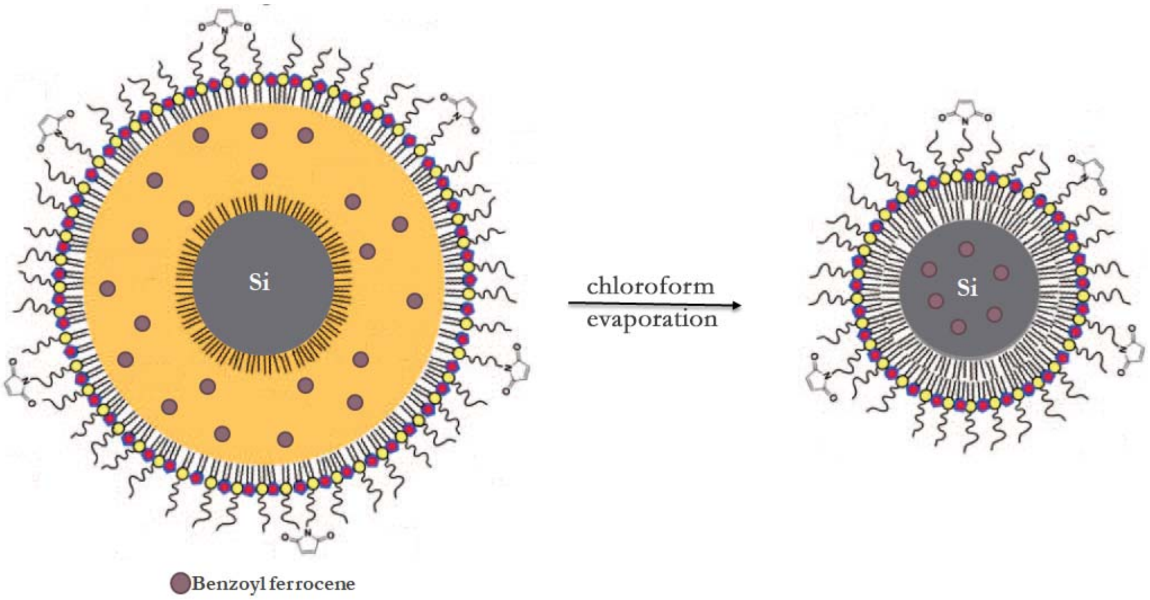

Figure 4.14. Formation of the micelle encapsulating benzoyl ferrocene **5**.

After formation of the various nanoparticles listed in **Table 4.1**, the nanoparticle sizes were determined to ensure that the size range was optimal for cell uptake of the nanoparticles.[32] After determining the nanoparticle sizes by DLS measurements, which fel within the optimal range of 200 – 300 nm, we sought to confirm those results by employing TEM imaging. The TEM imaging results (Figure 4.6) for both types of nanoparticles (without the fluorescent dyes) confirmed that the nanoparticle sizes were within the desired

200 – 300 nm range. With this confirmation of optimal nanoparticle size for cellular uptake, internalization and cytotoxicity studies were undertaken. Confocal imaging using fluorescent dyes encapsulated in the CPSiNPs-PEG and CPSiNPs-PEG-iRGD nanoparticles confirmed internalization. As can be seen in Figure 4.9, CPSiNPs-PEG encapsulating 6-FAM dye established that the nanoparticles were located in the cytosol surrounding the blue fluorescent DAPI-labeled nucleus. The green fluorescently labeled CPSiNPs-PEG-iRGD containing rhodamine 6G also showed internalization of the nanoparticles and fluorescent dye in the cytosol of the cells surrounding the DAPI-labeled nucleus. Cell internalization was confirmed using TEM imaging of A549 cells treated with the nanoparticles. TEM imaging of CPSiNP-PEG containing **5** showed the internalization of what we speculate is our compound in a vacuole within the cells. We therefore concluded that the cytotoxicity of **5** is due to cellular internalization instead of extracellular activities. Interestingly, the TEM imaging if CPSiNP-PEG-iRGD shows that the nuclear membrane is affected by nanoparticles containing the iRGD targeting peptide, so it is possible the iRGD peptide target is targeting or somehow adversely affecting the nucleus, thereby causing increased cytotoxicity under both irradiation and dark conditions.

The results of cytotoxicity assays using CPSiNP-PEG and CPSiNP-PEG-iRGD containing **5**, were compared to those for free benzoyl ferrocene **5** (**Table 4.3**). We had originally hypothesized that since benzoyl ferrocene **5** was not internalized by the cells, there could be an extracellular mode of action, possibly on the extracellular membrane, leading to similar cytotoxicities under irradiation and dark conditions. The cytotoxicity of CPSiNP-PEG containing **5** under irradiation conditions has an IC_{50} value of 11.1 μM, which is approximately four times more toxic than treatment of the cells with free benzoyl ferrocene **5** (43.5 μM). We previously ran a control with just the CPSiNP-PEG, with no compound inside, to determine that the nanoparticles were not a source of toxicity. ICP-OES studies were also performed to determine that benzoyl ferrocene was freed from the nanoparticles as detailed in the Results section 2. This was to ensure that the cytotoxicity was due to benzoyl ferrocene freed from the nanoparticles, as the nanoparticles were degrading in cells. The dark toxicity of CPSiNP-PEG containing **5** was approximately 100 μM; the exact value was unable to be determined using the OriginsPro software as we had reached our solubility limit and could not get greater than 90% cell death at the highest limit. This result was expected, as we had noticed the trend in Chapter II that benzoyl ferrocene derivatives that are internalized exhibited a significant difference between light and dark toxicity values. We previously suspected that this phenomenon was due to the generation of free iron(II) under irradiation conditions, which can participate in potentially destructive redox chemistry in cells. The dark toxicity could be explained by the fact that it is possible for cells to oxidize the iron in benzoyl ferrocene (**5**) as it has an $E_{1/2}$ = 0.250 V compared to the redox potential of ferrocene,[39] which is similar to the potential reported for 4-pentylbenzoyl ferrocene (**10**, Figure 4.15) with an $E_{1/2}$ potential of 0.251 V. Compound **10** also exhibits dark cytotoxicity.[39-40]

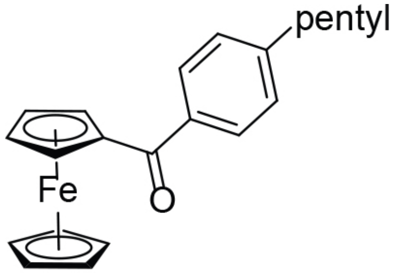

10

Figure 4.15. Figure of compound **10**.

The cytotoxicity results for CPSiNP-PEG-iRGD containing **5** were intriguing. The IC_{50} value in the light was 6.4 µM, which was almost twice as toxic compared to CPSiNP-PEG containing **5**. However, the dark toxicity of CPSiNP-PEG-iRGD containing **5** was at 12.4 µM, which is almost a 10-fold increase compared to the dark toxicity of the nanoparticles without the iRGD target. We speculated that this increase in cytotoxicity is due to a much greater concentration of iron in the cells, since we used a peptide targeting agent. Another hypothesis is that it's possible the iRGD conjugate is somehow affecting the nucleus, leading to the greater toxicity values. The cytotoxicity graph of free benzoyl ferrocene **5**, CPSiNP-PEG + **5**, and CPSiNP-PEG-iRGD + **5** are illustrated together in Figure 4.16, with IC_{50} values listed in **Table 4.3**.

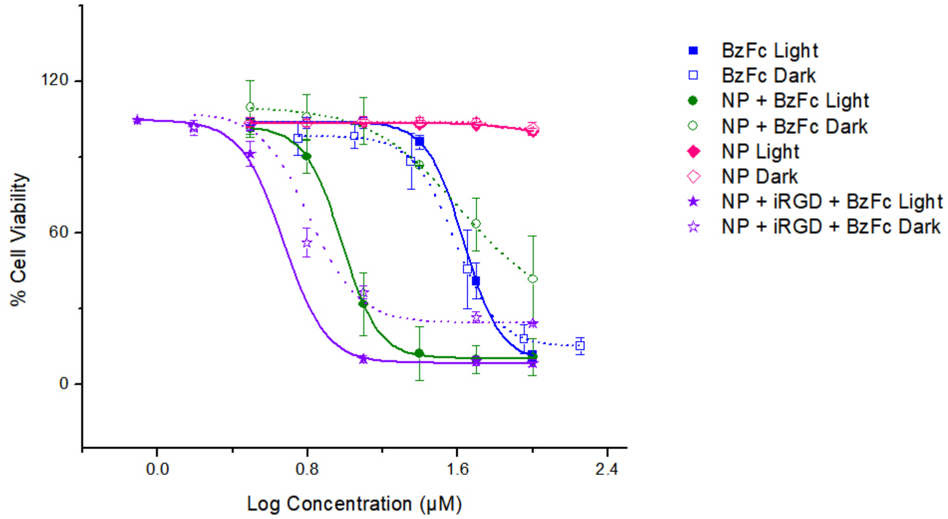

Figure 4.16. IC_{50} graph of benzoyl ferrocene **5** under different treatment conditions.

We hypothesized that if we could determine how much iron is internalized in cells when **5** is encapsulated in CPSiNP-PEG compared to CPSiNP-PEG-iRGD, it may shed some light into the interesting cytotoxicity trend that we have observed. ICP-OES studies were performed on A549 cell lysates containing benzoyl ferrocene **5**, CPSiNP-PEG + **5**, and CPSiNP-PEG-iRGD + **5** to determine iron uptake. ICP-OES studies indicated that free compound **5** was not uptaken by the cells, whereas nanoparticles carriers allowed internalization of benzoyl ferrocene. The iron concentration of cells treated with CPSiNP-PEG + **5** has about 22 times more iron compared to normal cellular concentration, while CPSiNP-PEG-iRGD + **5** has about 40 times higher iron concentration. This huge difference of iron concentration could explain why there is greater cytotoxicity when compound **5** is encapsulated in an iRGD targeting nanoparticle than without the peptide targeting agent. Since it is possible for benzoyl ferrocene (**5**) to perform redox chemistry in the cells as exhibited by the dark cytotoxicity for CPSiNP-PEG containing benzoyl ferrocene, it is possible that this huge concentration of iron in cells is undergoing redox chemistry which the cells do not have a mechanism to deal with.

After these nanoparticle studies, and based on the results, we wanted to synthesize a ferrocenyl derivative with a peptide target without use of nanoparticles. We speculate that using a peptide targeting agent appended to a ferrocenyl derivative would allow uptake of iron in cells by binding to the NRP-1 receptor using the CRGDK target,[25] so we worked to synthesize compound **44**. We planned to compare the uptake of iron with compound **44** to an analogous structure, such as **43**, encapsulated in nanoparticles in order to observe any differences in cellular uptake. We were able to successfully synthesize compound **43** with a carboxylic acid end for peptide conjugation. We used the peptide synthesizer, with the help of Dr. Matt Thompson in the Gianneschi group, to loaded the resin with amino acids cysteine, arginine, glycine, aspartic acid, lysine, and compound **43** to synthesize compound **44**. However, after trying to cleave the compound off the resin with TFA, our compound turned from a red color to a blue color, which we speculate is iron(II) oxidizing to iron(III).

The compound was dissolved in $CDOD_3$ to obtain a NMR, but there was a huge broadening of peaks, which we attribute to iron(III) formation. We speculate that it's possible we were able to conjugate the peptide target onto compound **43** due to the low-resolution mass spectrometry analysis confirming compound **44**'s molecular weight.

D. Conclusion

We are able to take advantage of the versatility of porous silicon nanoparticles to encase benzoyl ferrocene **5** for cellular internalization such that the cytotoxicity values between light and dark conditions have a difference, which confirms that free iron(II) is more toxic than its sandwich complex. However, the cytotoxicity difference between irradiation and dark conditions is more significant when using CPSiNP-PEG compared to CPSiNP-PEG-iRGD. ICP-OES data illustrates the uptake of iron compound encapsulated in the nanoparticles is uptaken 22 times more with CPSiNP-PEG and 40 times more using an iRGD peptide target. This could suggest that this extra increase in iron with iRGD is extremely toxic to cells, and benzoyl ferrocene could easily be oxidized. TEM imaging suggests that the iRGD-containing nanoparticles could also be affecting the nucleus. Our next steps should be to encapsulate a benzoyl ferrocene derivative, such as 1,1'-bispentylbenzoyl ferrocene **16** (Figure 4.17), which has a greater oxidation potential to determine whether **5** is easily oxidized in the intracellular environment. If there is less or no toxicity under dark conditions, it would indicate that the redox potential of the organoferrous agents are extremely important. This vital information would assist in synthetic attempts to optimize design of a highly cytotoxic drug under irradiation conditions and bioinactive under dark conditions.

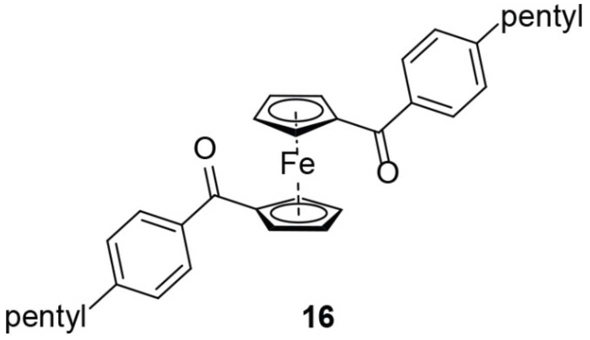

16

Figure 4.17. Structure of compound **17**.

The ICP-OES results using iRGD targeting peptide also led to an interest the CRGDK peptide sequence as a small molecule peptide target. Since nanoparticles can deliver a high payload, which ended up with non-ideal dark cytotoxicity results when conjugated to the iRGD peptide targeting agent, we wanted to see if we could target tumor cells without using nanoparticles by directly conjugating the targeting unit onto an organoferrous agent. We hypothesize that compound **44** was synthesized based on LRMS, however, we believe iron was oxidized due to the blue colored solution, and inability to obtain sharp peaks in proton NMR. In future studies, we will need to look into other ways to cleave the peptides off the resin without oxidizing iron.

E. Experimentals

Materials: 1,2-Distearoyl-sn-glycero-3-phosphoethanolamine-N-[methoxy(poly(ethylene glycol))-2000] (DSPE-PEG) and 1,2-distearoyl-sn-glycero-3-phosphethanolamine-N-[maleimide-(poly(ethylene glycol))2000] (DSPE-PEG-Mal) were purchased from Avanti Polar Lipids. Silicon wafers (100)-oriented single side polished p-type (<0.0015mΩ resistivity) were obtained from Virginia Semiconductor, Inc. Dodecene (>99%) was purchased from Aldrich. Chloroform was purchased from Fisher Scientific, Inc. Dulbecco's Phosphate Buffered Saline (DPBS) without calcium and magnesium was purchased from Mediatech, Inc. The cyclic RGD (5FAM-Cys-Arg-Gly-Asp-Lys-Gly-Pro-Asp-Cys-(Cys&Cys Bridge) was synthesized at a purity of 95% by CPC Scientific.

Synthesis of Porous Si Nanoparticles: Porous Si nanoparticles were prepared from the electrochemical etching of highly doped, (100)-oriented, p-type Si wafers (boron-doped, 1mΩ resistivity) in a 3:1 solution of 48% aqueous hydrofluoric acid (HF) in ethanol (HF from Fisher, Inc.). A Si wafer with an exposed area of 60 cm^2 was contacted on the back side and mounted in a Teflon etching cell with a platinum counter electrode. Etching waveforms were generated in a computer program written in Labview (National Instruments, Inc.) and etching was driven by a Keithley 2651A SourceMeter power supply interfaced to the Labview program. The wafer was etched at 2804.7 mA for 1.818 second and 10,000 mA for 0.363 second with 1700 repeats. The resulting porous layer was then lifted off by electropolishing in 3.33% HF in ethanol solution for 500 second at a current density of 250 mA. The resulting porous layer was crushed into small particles with a mortar.

Hydrosilylation of Porous Si Nanoparticles: 20 mg of porous Si particles as prepared above in 1 mL of dodecene purged with N_2 gas for 10 min were placed in a 10 mL Pyrex beaker and heated in a commercial consumer microwave oven (Sears Kenmore 700W) for 4 min at 280 W twice. The particles were then ultrasonicated overnight. Porous Si nanoparticles after ultrasonication were then rinsed with hexane and ethanol twice to remove excess dodecene. In order to obtain nanoparticles in a size range of 20-200 nm, particles in ethanol solution were left for 2 h, and supernatant was collected to be used. . Particles without settlements were centrifuged at 5000 rpm for 4 min and supernatants were collected.

Physical Characterization of Porous Si Nanoparticles: Dynamic light scattering (Zetasizer Nano ZS90, Malvern Instruments) was used to determine hydrodynamic size and zeta potential of CPSiNP. To analyze pore structure, TEM experiments were carried out on a JEOL instrument at an acceleration voltage of 80 kV. The TEM samples was prepared by administering the NP suspension onto a 300 mesh copper grids. Samples were dried prior to imaging. The Fourier-transform infrared (FTIR) spectra of as-etched porous silicon films and CPSiNP were obtained in the absorption mode using a Thermo Scientific Nicolet 6700 FTIR spectrometer equipped with a diamond Attenuated Total Reflectance (ATR) accessory.

Loading and Release of Benzoyl Ferrocene into Porous Si Nanoparticles: Approximately 6 mg of porous Si nanoparticle was suspended in 1 mL of chloroform, and 20 mg of Benzoyl Ferrocene (Sigma Aldrich, ≥ 98%) was mixed in rotatory for 24 h at room temperature. The solution was centrifuged at 15000 rpm for 15 min, and excess benzoyl ferrocene was removed. The solution in chloroform was dropped into 5mL of

DPBS solution while stirring vigorously at 120 °C to remove chloroform for 1 h. The solution was washed with DPBS to remove excess lipids by centrifugation at 15000 rpm for 15 min twice. Around 1.25 mg of CPSiNP-PEG containing benzoyl ferrocene in 1 mL of DPBS solution was incubated at 37°C. An aliquot of 1mL of supernatant incubated in 1 mL of DPBS at 37°C was removed at different time points after spinning 14,000 rpm for 10 min. The solution was diluted with HNO_3 (2% (v/v)) and subjected to analysis by inductively coupled plasma optical emission spectroscopy (ICP-OES, Perkin Elmer Optima 3000DV). Release kinetics of benzoyl ferrocene from CPSiNP-PEG was measured based on wavelength corresponds to elements (Si and Fe) for five different trials.

In vitro Confocal Imaging: Cell internalization of fluorescent dyes loaded in the CPSiNP was inspected by confocal fluorescence microscopy. A549 cells were seeded into 4-well chamber glass slides (Lab-Tek) and incubated overnight. A 100 µg per well quantity of CPSiNP-PEG and CPSiNP-PEG-iRGD loaded with 6-FAM dye or Rhodamine 6G dye was added and the cells incubated for 24 h at 37°C in the presence of 10 % fetal bovine serum (FBS). The cells were then rinsed three times with cell medium, fixed with DAPI mounting agent for 20 min and then observed in the fluorescence microscope (370 nm or 488 nm excitation and 650 nm long pass emission filter) and in the Radiance 2100/AGR-3Q BioRad Multi-photon Laser Point Scanning Confocal Microscope. For confocal fluorescence microscopy, the cells treated with CPSiNP-PEG were imaged using 488 nm Ar ion laser excitation and a 650 nm long pass emission filter. The DAPI and pSiNP signals were separated using 495 nm dichroic filter and 560 nm long pass filter.

Fixation and Plastic Embedding for TEM: Samples were immersed in modified Karnovsky's fixative (2.5% glutaraldehyde and 2% paraformaldehyde in 0.15 M sodium cacodylate buffer, pH 7.4) for at least 4 hours, postfixed in 1% osmium tetroxide in 0.15 M cacodylate buffer for 1 h and stained en bloc in 2% uranyl acetate for 1 hour. Samples were dehydrated in ethanol, embedded in Durcupan epoxy resin (Sigma-Aldrich), sectioned at 50 to 60 nm on a Leica UCT ultramicrotome, and picked up on Formvar and carbon-coated copper grids. Sections were stained with 2% uranyl acetate for 5 min and Sato's lead stain for 1 min. Grids were viewed using a JEOL 1200EX II (JEOL, Peabody, MA) transmission electron microscope and photographed using a Gatan digital camera (Gatan, Pleasanton, CA), or viewed using a Tecnai G2 Spirit BioTWIN transmission electron microscope equipped with an Eagle 4k HS digital camera (FEI, Hilsboro, OR).

Cell Toxicity Assay: Lung carcinoma A549 cells were seeded in 100 μL of media in 96-well plates at a density of 3.5×10^4 cells/well. After incubation for 24 h at 37°C the cells were exposed to various concentrations of CPSiNP-PEG, benzoyl ferrocene in CPSiNP-PEG, benzoyl ferrocene in CPSiNP-PEG-iRGD, or free benzoyl ferrocene for 24 h. After this time, the dark plate was left in the incubator and an identically prepared plate was illuminated with a Richee 2014-SLT-CW/WW 50W Flood Light (0.031 W) for 3 hours with a 455 nm long pass filter (Pol filter 152x100x3mm GG455) resting on top of the 96 well plate. Temperature during photolysis was kept constant at 37°C using a Denville Incubloc solid aluminum block. 48 hours after photolysis, the cell media was discarded and the cells were fixed with 4% paraformaldehyde, washed three times with DPBS, and stained with crystal violet. The absorbance at 590 nm was measured for each well using a microplate reader scanning spectrophotometer. Cell viability was expressed as percentage of viable cells compared with controls.

Determination of Iron Concentration: A549 cells were cultivated as a monolayer in 150

cm^2 flasks. The CPSiNP-PEG carrier was then diluted with water and added to FBS-free cell growth medium. The A549 cells were exposed to the drug containing media for a period of 2 h then the media was removed by pipette and the cell monolayer was washed gently three times with 10 mL of warm dPBS. The cells were then treated with 3 mL of 1x trypsin for ten min and resuspended in 10 mL of fresh FBS-free media. The cell suspension was subsequently centrifuged at 1200 rpm (4 °C) for 5 min, and the pellets were washed twice with 10 mL of dPBS between additional centrifugation cycles. The pellets were drained for 10 min then stored at -18 °C until analysis.

Determination of Protein Concentration: The cell pellets were homogenized in 5 mL of 0.001% Triton X-100 solution by vortex followed by sonication (5 x 5 s). 1 mL was removed for protein quantification and the remaining 4 mL were lyophilized in preparation for iron quantification. Protein concentration was determined by the Bradford method using the commercially available Bio-Rad Protein Assay Dye Reagent Concentrate #500-0006 prepared per the manufacturer's instructions. Protein standards were prepared using bovine serum albumin (BSA) in 0.001% Triton X-100 solution. As Triton X-100 is a known interfering substance, additional dilutions of the protein standards were done using an identical concentration of the detergent. A calibration curve was constructed by calculating the 590/450 nm absorbance ratio using a micro-plate reader. The protein concentration of the cell lysates were determined as described by Zor and Selinger (See Chapter II experimentals).[39-40]

Determination of Iron Concentration: The lyophilized samples were dissolved in 115 μL of concentrated nitric acid and heated at 65°C for 6 h. The samples were then diluted to a total volume of 4 mL using 0.1% Triton X-100 and the iron concentration (ng/g) was determined by ICP-OES. The iron concentration was then related to the protein concentration to account for differences in biomass between separate flasks. Results are expressed as an average of three independent experiments.

Synthesis of Compounds

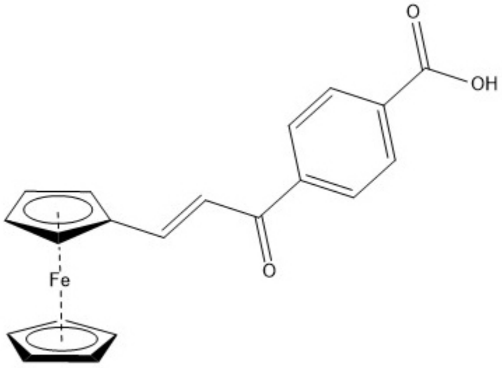

Compound 43. Ferrocenecarboxaldehyde (100 mg, 0.47 mmol, 1 equiv) and 4-acetylbenzoic acid (0.52 mmol, 1.1 equiv) was dissolved in EtOH (4 mL, 0.12 M) under magnetic stirring. NaOH (38 mg, 0.94 mmol, 2 equiv) dissolved in 0.6 mL of water was added via syringe. The reaction was allowed to proceed for 12 h at room temperature. The reaction mixture was acidified with 1 mL of HCl. The solution was then filtered and the solid was collected and dried for 12 h in a desiccator with drierite. Product was determined to be pure by ^{1}H NMR spectroscopy and used without further purification. Obtained an orange-red solid in 98 mg (58% yield). ^{1}H NMR (400 MHz, $CDCl_3$): δ 4.20 (s, 5H, CpH), 4.54 (s, 2H, Cp'H), 4.62 (s, 2H, Cp'H), 7.10 (d, $^3J_{HH}$ = 15.6 Hz, 1H, =CH), 7.80 (d, $^3J_{HH}$ = 15.6 Hz, 1H, =CH), 8.04 (d, $^3J_{HH}$ = 8.3 Hz, 2H, ArH), 8.22 (d, $^3J_{HH}$ = 8.3 Hz, 2H, ArH). $^{13}C\{^1H\}$ NMR (126 MHz, $CDCl_3$): δ 68.58, 69.28, 71.14, 118.16, 127.67, 127.67, 129.74, 129.75, 142.31, 147.74, 151.96, 188.57. IR (KBr, cm^{-1}): 810, 1016, 1218, 1588, 1652, 1680.

HRMS-(ESI) (*m/z*): calcd for $[C_{20}H_{15}FeO_3]^-$, 359.0371; found, 359.0374. UV-Vis (50:50 DMF:H_2O) λ_{max}, nm: 506.

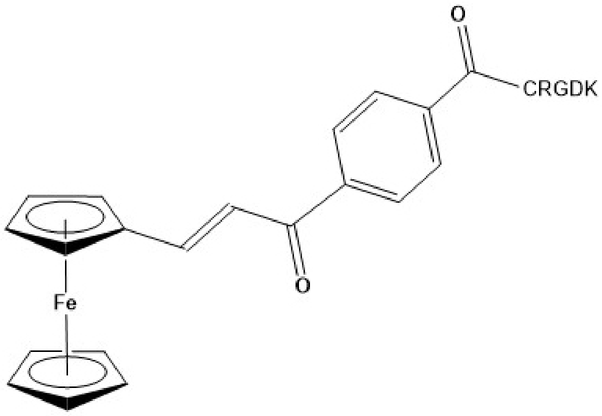

Compound 44. An AAPPTec Peptide Synthesizer was used for solid phase synthesis of the CRGDK peptide. Individual peptides were obtained from AAPPTec with N-Boc protecting groups and common side chain protecting groups. Rink Amide MBHA resin was used, and the general peptide synthesizer protocol from AAPPTec was followed using a 3-fold excess of each amino acid. The only deviation is in the 6th peptide slot, **Compound 43** was added to couple to the cysteine end with 1 equivalence with respect to the resin loading amount. After using the peptide synthesizer, the resin with our compound was collected into a plastic peptide vessel with yellow cap. The resin was then treated with 5 mL of a solution of 95% TFA, 2.5% trisopropylsilane, and 2.5% water and placed on a shaker for 45 minutes to cleave peptide chain off the resin. The supernatant was then collected and concentrated to afford what we believe is our compound. Unfortunately, the compound turned from a red color solution to blue, so we believe that the last step with TFA oxidized our compound from iron(II) to iron(III) and a NMR spectrum was not able to be obtained. We believe we were able to synthesize our peptide target based on low-

resolution mass spectrometry analysis indicating a compound with the correct molecular weight. LRMS-(ESI) (*m/z*): calcd for $[C_{41}H_{55}FeN_9O_{10}S]^+$ 921.31; found, 921.30.

F. Appendix

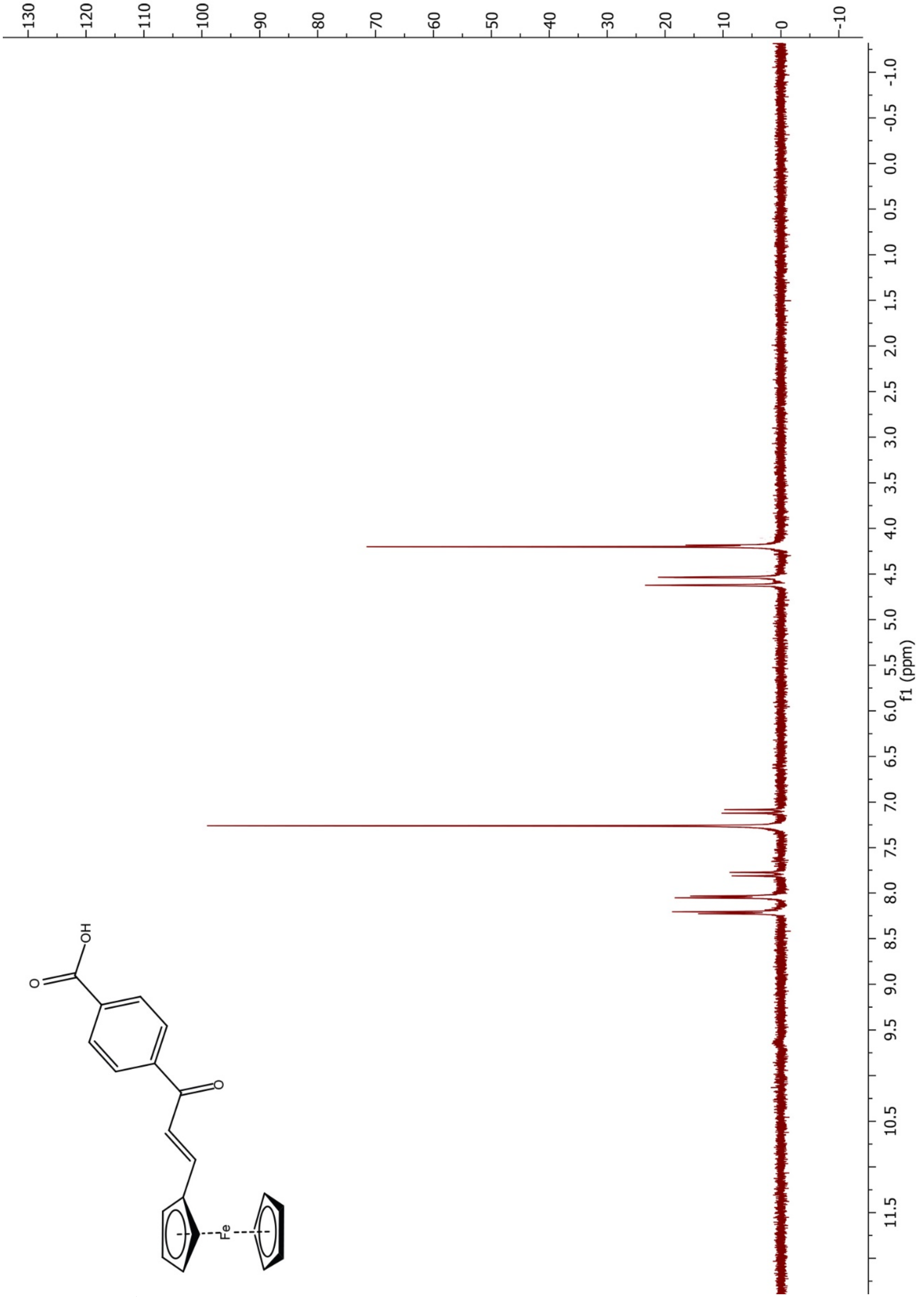

Figure 4.18.^{1}H NMR of compound **43** (400 MHz, CDCl3).

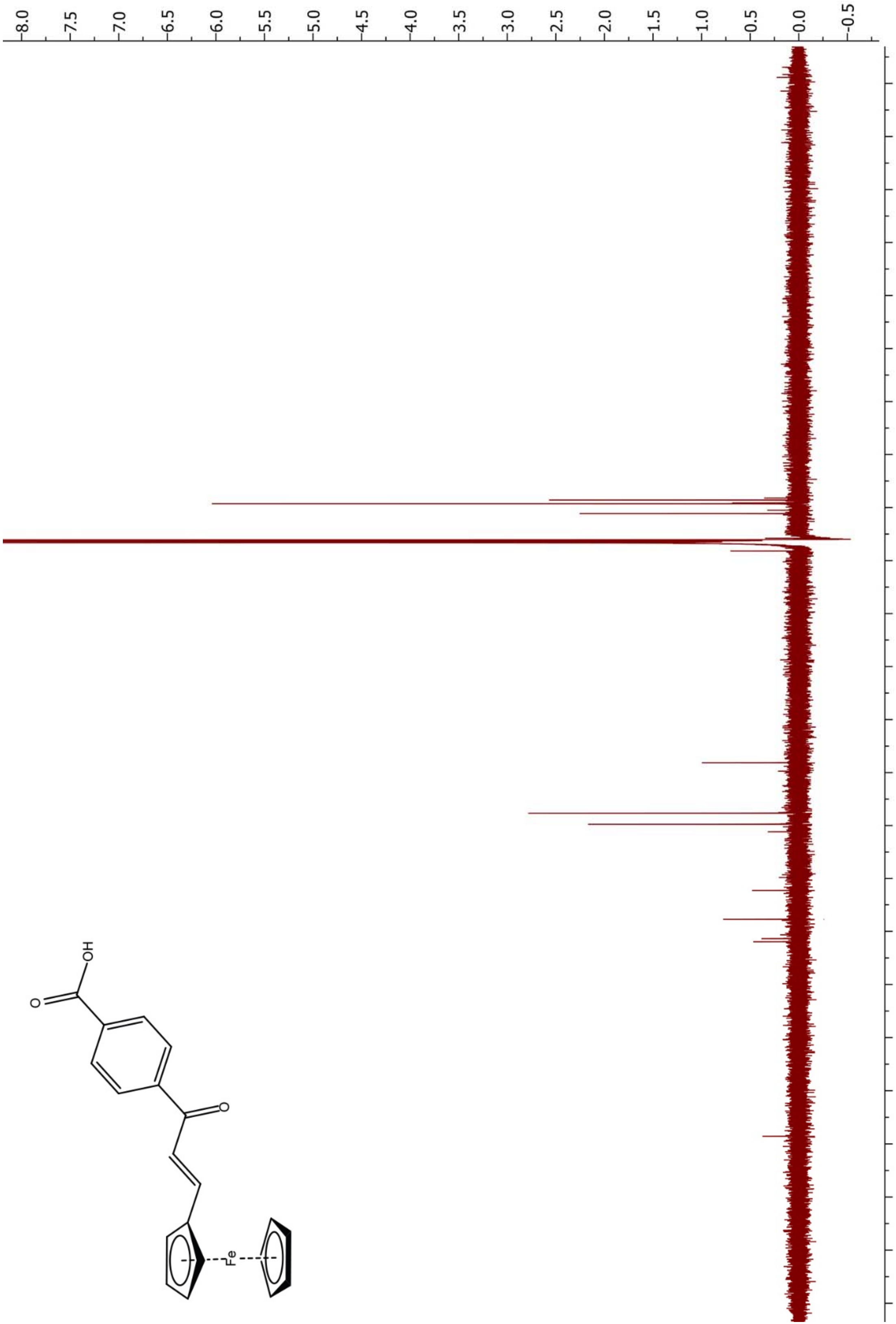

Figure 4.19. ^{13}C{1H} NMR of compound **43** (126 MHz, CDCl3).

G. Acknowledgements

The material in Chapter IV was performed in collaboration with Angie Kim, from the Mike Sailor Lab at UCSD, who worked on encapsulating benzoyl ferrocene inside porous silicon nanoparticles, determination of optimal nanoparticle size and release kinetics of iron complex and degradation of silicon nanoparticles.

The material in Chapter IV contains unpublished material with co-authors: Hoong, Christina; Kim, Angie; O'Connor, Joseph. "Delivery of Benzoylferrocene Using Nanoparticles and Peptide Recognition Targets." The dissertation author was the primary researcher and author of this material.

H. References

1. Chapter II of thesis demonstrates that benzoyl ferrocene is not uptaken in the cells.

2. Serda, R. E.; Godin, B.; Blanco, E.; CHiappini, C. Ferrari, M.; *Biochim. BIophys. Acta, Ge. Subj.* **2011**, *1810*, 317-329.

3. Ferrari, M. *Nat Rev. Cancer*. **2005**, *5*, 161-171.

4. Stojanovic, V.; Cunin, F.; Durand, J. O.; Garcia, M.; Gary-Bobo, M. *J. Mater. Chem. B.* **2016**, *4*, 7050-7059.

5. Park, J. H.; Gu, L.; von Malzah, G.; Rouslati, E.; Bhatia,S. N.; Sailor, M. J. *Nat. Mater*. **2009**, *8*, 331-336.

6. Osminkina, L. A.; Tamarov, K. P.; Sviridov, A. P.; Galkin, R. A.; Gongalsky, M. B.; Solovyev, V. V.; Kudryavtsev, A. A.; Timoshenko, V. Y. *Biophotonics*, **2012**, *5*, 529-535.

7. Canham, L. T. *Nanotechnology*. **2007**, *18*, 185704.

8. Tzur-Balter, A.; Gilert, A.; Massad-Ivanir, N.; Segal, E. *Acta Biomater*. **2015**, *213*, 188-191.

9. Bimbo, L. M.; Sarparanta, M.; Santos, H. A.; Airaksinen, A. J.; Mäkilä, E.; Laaksonen, T.; Peltonen, L.; Lehto, V.-P.; Hirvonen, J.; Salonen, J. *ACS Nano*. **2010**, *4*, 3023-3032.

10. Gaspar, M. M.; Radomska, A.; Gobbo, O. L.; Bakowsky, U.; Radomski, M. W.; Ehrhardt, C. *J. Aerosol Med.Pulm Drug Deliv*. **2012**, *25*, 310-318.

11. Hamoir, J.; Nemmar, A.; Halloy D, Wirth, D.; Vincke, G.; Vanderplasschen, A.; Nemery, B.; Gustin, P. *Toxicol Appl Pharmacol*. **2003**, *190*, 278-285.

12. Kinsella, J. M.; Ananda, S.; Andrew, J. S.; Grondek, J. F.; CHien, M.-P.; Scadeng, M.; Gianneschi, N. C.; Ruoslahti, E.; Sailor, M. J. *Adv. Mater*. **2011**, *23*, H248-H253.

13. Kasalainen, M.; Rytkönen, J.; Mäkilä, E.; Närvänen, A.; Salonen, J. *Langmuir*. **2015**, *31*, 1722-1729.

14. Hasanzadeh Kafshgari, M.; Alnakhli, M.; Delalat, B.; Apostolou, S.; Harding, F. J.; Mäkilä, E.; Salonen J. J.; Kuss, B. J.; Voelcker, N. H. *BIomater. Sci*. **2015**, *3*,1555-1565.

15. Salonen, J.; Kaukonen, A. M.; Hirvonen, J.; Lehto, V.-P. *Pharm. Sci.* **2008**, *97*, 632-653.

16. Pierschbacher, M. D.; Ruoslahti, E. *Nature*. **1984**, *309*, 30-33.

17. Eliceiri, B. P.; Cheresh, D. A. *Curr Opin Cell Biol.* **2001**, *13*, 563-568.

18. Rouslahti, E. *Matrix Biol.* **2003**, *22*, 459-465.

19. Curnis, F.; Gasparri, A.; Sacchi, A. Longhi, R.; Corti, A. *Cancer Res*. **2004**, *64*, 565-571.

20. Sipkins, D. A.; Cheresh, D. A.; Kazemi, M. R.; Nevin, L. M.; Bednarski, M. D.; Li, K. C. *Nat Med*. **1998**, *4*, 623-626.

21. Wickham, T. J. *Gene Ther*. **2000**, *7*, 110-114.

22. Murphy, E. A.; Majeti, B. K.; Barnes, L. A.; Makale, M.; Weis, S. M.; Lutu-Fuga, K.; Wrasidlo, W.; Cheresh, D. A. *Proc. Natl. Acad. Sci. U S A.* **2008**, *105,* 9343-9348.

23. Sugahara, K. N.; Tessalu, T.; Karmali, P. P.; Kotamraju, V. R.; Agemy, L.; Girard, O. M.; Hanahan, D.; Mattrey, R. F.; Ruoslahti, E. *Cancer Cell*. **2009**, *16*, 510-520.

24. Liu, X.; Jiang, J.; Ji, Y.; Lu, J.; Chan, R.; Meng, H. *Mol. St. Des. Eng.* **2017**, *2*, 370-379.

25. Tessalu, T.; Sugahara, K. N.; Kotamraju, V. R.; Rouslahti, E. *Proc. Natl. Acad. Sci. U S A.* **2009**, *106,* 16157-16162.

26. Ruoslahti, E.; Pierschbacher, M.; *Science*, **1987**, *238*, 491-497.

27. Hanahan, D.; Weinberg, R. A. *Cell*, **2000**, *100*, 57-70.

28. As discussed in Chapter II.

29. Guo, L.; Zhang, F.; Cai, Y.; Liu, T. *Pathol. Res. Pract.* **2009**, *205*, 847-853.

30. Che, J.; Okeke, C. I.; Hu, Z. B.; Xu, J. *Curr. Pharm. Des.* **2015***, 21*, 1598-1605.

31. Liu, D.; Mäkilä, E.; Zhang, H.; Herranz, B.; Kaasalainen, M.; Kinnari, P.; Salonen, J.; Hirvonen, J.; Santos, H. A. *Adv. Funct. Mater*. **2013**, *23*, 1893-1902.

32. Qin, Z.; Joo, J.; Gu, L.; Sailor, M. J. *Part. Part. Syst. Charct.* **2014**, *31*, 252-256.

33. Xu, R. *Particuology*. **2008**, *6*, 112-115. Schmut, R. *Ind. Eng. Chem.* **1964**, *56*, 28-33.

34. Brigger, I.; Dubernet, C.; Couvreur, P. *Adv. Drug Deliv. Rev*. **2012**, *64*, 24-36.

35. Yuan, F. *Semin. Radiat. Oncol.* **1998**, *8*, 164-175.

36. Guo, L.; Zhang, F.; Cai, Y.; Liu, T. *Pathol. Pract*. **2009**, *205*, 847-853.

37. New photodynamic therapy method as detailed in Chapter II.

38. Torti, S. V.; Torti, F. M. *Nat Rev Cancer*. **2013**, *13*, 342-355.

39. Aubrey, M. ‘Organoferrous Antitumor Agents’, PhD thesis, University of California San Diego, San Diego, CA.

40. Zor, T.; Selinger, Z. Anal. Biochem. 1996,236, 302-308.